Dissertation

submitted to the

Combined Faculties of the Natural Sciences and Mathematics

of the Ruperto-Carola-University of Heidelberg, Germany

for the degree of

Doctor of Natural Sciences

Put forward by

Mag. rer. nat. Leonard Fister,

born in: Cologne, Germany

Oral examination: October 18, 2012

On the Phase Diagram of QCD with Dynamical Quarks

Referees: Prof. Dr. Jan M. Pawlowski
Prof. Dr. Michael G. Schmidt

Abstract

In this dissertation the phase diagram of hadronic matter is studied. One of its characteristic features is confinement, which denotes the absence of particles with non-zero colour-charge in experimental observations. The fundamental mechanism for confinement is unknown yet, however, there is significant evidence that it is primarily driven by the dynamics of gluons. The interacting system of gluons is called Yang–Mills theory. It is the main focus of this thesis. Functional continuum methods describe the physics via correlation functions, whose thermal behaviour is investigated in this thesis in the framework of the functional renormalisation group. In particular, the temperature-dependent two-point functions are important, since the thermodynamics can be directly accessed by the knowledge of the propagators. In this work this allows for a quantitatively accurate computation of the pressure of Yang–Mills theory. Furthermore, confinement of static quarks is investigated via the Polyakov loop, which is calculated for the gauge groups $SU(2)$ and $SU(3)$ by means of low-order Green functions. Moreover, the effects of dynamical quarks onto the gauge sector are studied. All results are directly compared with findings from other continuum methods and lattice gauge theory.

Kurzfassung

In dieser Dissertation werden ausgewählte Aspekte des Phasendiagramms hadronischer Materie untersucht. Eine charakteristische Eigenschaft ist der Farbeinschluss. Er bezeichnet das Fehlen von Teilchen mit nichtverschwindender Farbladung in experimentellen Beobachtungen. Bis heute ist der grundlegende Mechanismus für den Farbeinschluss nicht bekannt, wenngleich es starke Hinweise darauf gibt, dass dieser Effekt in erster Linie durch die Dynamik der Gluonen erzeugt wird, welche Yang–Mills Theorie genannt wird. Deren Analyse bildet den Fokus dieser Doktorarbeit. In funktionalen Kontinuumsmethoden wird die Physik durch Korrelationsfunktionen beschrieben. Das thermische Verhalten derselben wird in der vorliegenden Abhandlung mittels der funktionalen Renormierungsgruppe erforscht. Vornehmlich die Zweipunktfunktionen haben eine fundamentale Rolle, da man anhand der Propagatoren sämtliche thermodynamische Größen der Theorie bestimmen kann. In dieser Dissertation wird der Druck der Yang–Mills Theorie mit quantitativer Präzision berechnet. Des Weiteren wird der Farbeinschluss statischer Quarks anhand der Polyakovschen Schleife studiert, welche für die Eichgruppen $SU(2)$ und $SU(3)$ rein durch die Kenntnis von Greenschen Funktionen niedriger Ordnung berechnet wird. Zudem werden Effekte dynamischer Quarks im Eichsektor der Theorie untersucht. Alle Resultate werden direkt mit Ergebnissen anderer Kontinuumsmethoden und der Gittereichtheorie verglichen.

Contents

1. Introduction

1.1. Introduction

The majority of the observable matter in the universe is made up by hadrons, which themselves are composite particles. The fundamental constituents are quarks, which are bound together by the strong interaction mediated by gluons. Quantum Chromodynamics (QCD) [1–7] has emerged as the proper theoretical framework to capture the nature of the strong interaction. QCD is embedded in the Standard Model (SM) of elementary particle physics, which combines the strong and weak nuclear forces as well as electromagnetism in a single theory. So far, the SM has proven to be the best approach to elementary particle physics, as it describes and predicts processes at very high energies with amazing accuracy.

QCD has very peculiar properties at different scales. For very small distances, or equivalently high momentum transfers, the coupling of quarks and gluons is weak. This feature is known as asymptotic freedom [8, 9]. In the limit of infinite momenta the coupling even vanishes, i.e. quarks and gluons form an ideal gas. For non-vanishing but very small coupling it is a fair assumption that the system remains almost free, but is affected mildly by the interaction. The theoretical approach is the expansion around small couplings, which is called perturbation theory.
Clearly, the coupling is not small on all scales because of the existence of hadrons, where the coupling is strong. The coupling increases with decreasing energy scale, and in fact, perturbation theory finds that the coupling diverges around the intrinsic scale Λ_{QCD}. This is not the correct physical situation, but rather indicates that perturbation theory fails in its predictive power. Therefore, at the latest where the coupling is of order 1 it breaks down. Actually, speaking from the human experience point of view, under normal circumstances the coupling is strong as the scale of QCD is $\Lambda_{\mathrm{QCD}} \approx 10^{12}\mathrm{K}$.

Strongly coupled QCD is governed by two characteristic effects, called confinement and dynamical chiral symmetry breaking, both of which are truly non-perturbative and cease to exist at scales where either the temperature or the quark chemical potential renders the coupling small. Confinement accounts for the experimental fact that although quarks are the fundamental building blocks of hadrons, individual quarks have not been observed so far, but they are always bound into mesons or baryons. On the other side, dynamical chiral symmetry breaking is the mechanism that generates quark masses via the interactions of quarks and gluons among themselves, giving actually most of the observed mass

of the universe in terms of binding energy in protons and neutrons. Although large effort has been invested for decades, neither the origin of confinement nor dynamical chiral symmetry breaking, nor a potential relation of these effects to each other is understood yet.

The reasoning above implies that the state of hadronic matter varies with temperature and chemical potential: With increasing temperature and/or chemical potential it changes from the hadronic phase, where quarks are confined and chiral symmetry is broken dynamically, to another phase, where quarks can exist individually, and chiral symmetry is restored. In practice, the investigation of physics close to the phase transition is challenging on the experimental as well as theoretical side. Consequently, the phase diagram of QCD can only be conjectured from the limits of the hadronic physics and asymptotic freedom yet, which leads to a picture that is sketched in fig. (2.1). As the further exploration of the phase diagram of QCD is the main motivation for the work presented in this thesis, I dedicate chapter 2 to a more detailed summary of the phase diagram and the methods that are used to unravel the mysteries of it.

There is good evidence that chiral symmetry breaking is generated in the matter sector of QCD, but confinement is supposedly triggered by gluon dynamics, which are described by Yang–Mills theory [10]. Gluons arise from the gauge symmetry of QCD; thus, the gluon dynamics is also called pure gauge theory. Being responsible for confinement, theoretical studies of Yang–Mills theory and its phase transition provide direct information about the phase diagram of QCD. At the time, the most profound insights about Yang–Mills theory are obtained from lattice QCD. Unfortunately, lattice QCD suffers from conceptual problems concerning simulations of quarks. Thus, direct investigations of full QCD are hampered in the latter method, in particular at non-vanishing quark chemical potential. Non-perturbative continuum methods provide exact equations for full QCD. As a consequence, they are applicable without restriction in all regions of the phase diagram. Furthermore, they allow to study the mechanisms in a more direct way than it is possible in lattice QCD; thus, for not only computing QCD but understanding its physical mechanisms functional methods are inevitable. However, with only few exceptions, the functional equations can not be solved without making approximations, and the complexity of the system limits the extend of the truncations in practical applications severly. This complicates studies in pure gauge theory already. In this sense, continuum and lattice methods are complementary, as the limitations of both approaches are such that they can be tested with the other method.

In this work functional methods are employed, in particular the functional renormalisation group (FRG) and Dyson–Schwinger equations (DSEs). Starting from the path integral, both approaches provide an exact description of QCD in terms of Green functions. Like in any continuum description of a quantum field theory the propagators play a predominant role. Their behaviour can be directly related to the phase transitions of QCD, and appropriate order parameters for the deconfinement-confinement phase transition as well as the chiral phase transition can be defined. Therefore, during the last two decades, the

propagators of low-energy QCD, in particular of Yang–Mills theory have been studied. However, most of the studies were done in the vacuum.
In this thesis this approximation is extended in such a way that the full momentum-dependent propagators of Yang–Mills theory are studied in the presence of temperature. Apart from being a quantitative improvement of previous results, the thermal behaviour of correlation functions turns out to be crucial for the thermodynamics of pure gauge theory, which is seen in this work in the computation of the pressure. Taking into account the implicit temperature dependence of the propagators, for the first time within functional continuum methods the behaviour of the pressure of Yang–Mills theory is captured correctly for all temperatures, even on a quantitative level: Below the phase transition the pressure is suppressed due to the mass gap, at the phase transition temperature it sharply increases, and above the critical temperature it slowly approaches the limit of the ideal gas of gluons. The behaviour is consistent with results from lattice QCD at all temperatures. In addition to confinement in pure Yang–Mills theory, confinement of quarks can be studied within functional methods. The corresponding order parameter is derived from the Polyakov loop. It can be computed from the propagators in Yang–Mills theory. In previous works [11, 12] it was computed by the help of the FRG. In this thesis the Polyakov loop is computed in the framework of DSEs. The orders of the phase transitions and the critical temperatures found in both approaches are consistent with results from lattice QCD.

Yang–Mills theory is a complex system in functional continuum approaches, however, the inclusion of quarks is comparatively simple. In this thesis n-point functions of full QCD are addressed. Preliminary results for propagators in the presence of dynamical quarks are obtained in the framework of the FRG. These results compare well with findings from DSEs and lattice QCD. At the time being, the results are obtained in the vacuum, but they are going to be extended to non-vanishing temperature and quark chemical potential in the near future. This advancement is conceptually straightforward, and is sketched at the end of this thesis. This paves the way for quantitative studies of the phase diagram of QCD from first principles within non-perturbative functional continuum methods.

Parts of the content of this thesis are already published in [13, 14].

1.2. Outline

The outline of this thesis is as follows. In chapter 2 I review those aspects of QCD that are particularly relevant for the work presented in this thesis. Section 2.1 is concerned with the different phases of QCD. The focus lies on the non-perturbative effects as well as the characteristic features of the low-energy regime and on the methods that are used to explore the phase diagram. In the subsequent section 2.2 I recapitulate the construction

of the QCD action, which encodes all the complexity of QCD under various conditions. In section 2.3 more information is given about the limit of pure gauge theory, which is supposed to trigger confinement in full QCD as well. In continuum methods there are possible scenarios for the mechanism of confinement that are based on the correlation functions of Yang–Mills theory. They are sketched in section 2.3.1. In connection to this I briefly summarise the present knowledge about Green functions in the non-perturbative regime in section 2.3.2. These Green functions are not only sensitive to quantum fluctuations, but also to the temperature. Naturally, the thermal behaviour of correlation functions encodes the full thermodynamics. The determination of the pressure is one main topic of this thesis. Thus, I recapitulate in section 2.3.3 what is known about Yang–Mills thermodynamics at the end of this introductory chapter.

In chapter 3 the theoretical tools that are used in this thesis are introduced. At first, the Matsubara formalism is discussed, which is one conceptual way of formulating a quantum field theory in equilibrium at non-vanishing temperature, see section 3.1. This formalism will be employed within two non-perturbative functional continuum methods, especially the FRG and DSEs. The FRG is the prevailing tool in this thesis. Therefore, it is described in detail in section 3.2. Its general idea is introduced, and the algorithmic derivation of equations for correlation functions in this approach is summarised. As most work in this thesis is concerned with Yang–Mills theory, the characteristics of the FRG in gauge theories are described in more detail, before I specify technical elements of this method that are needed in the proceeding chapter 4. At the end of section 3.2 I comment on thermal flows, i.e. particularities of the FRG at non-vanishing temperature. Section 3.3 is dedicated to DSEs. In fact, these two approaches are not independent of each other. Their relation and the structural similarities and differences are sketched in section 3.4.

In chapter 4 the results for Yang–Mills theory at finite temperature are presented. The results are achieved in the framework of the FRG. At first, the approximation in use is given in section 4.1. Then, thermal effects on the momentum-dependent correlation functions, in particular the gluon and ghost propagators are studied in section 4.2. These results are directly compared to lattice gauge theory. The two-point functions are the key ingredient to the flow equation for the effective action, which encodes the full theory. Therefore, in section 4.3 the thermodynamics of Yang–Mills theory is extracted from its propagators.

In chapter 5 the deconfinement-confinement phase transition is studied, again from the continuum point of view. However, in addition to an analysis within the formalism of the FRG, also DSEs as well as 2-particle irreducible actions are used to compute the Polyakov loop potential to study quark confinement.

Chapter 6 deals with full QCD, i.e. quarks are included in a dynamical way. The emphasis is on the back-coupling of the quarks onto the gauge sector. In section 6.1 I present the method that is applied here. Furthermore, results for low-order correlation functions are presented. As this is work in progress, in section 6.2 I outline the strategy that is going to

be followed to study full QCD at non-vanishing temperature and quark chemical potential in the FRG approach.

In chapter 7 I summarise the important aspects and results of the work presented in this thesis.

Conventions, additional information, notes on numerical techniques and lengthy results can be found in several appendices.

2. Aspects of the Phase Diagram of QCD

In this section I summarise those aspects of the phase diagram of quantum chromodynamics (QCD) that are of prior importance in this thesis. At first I summarise the QCD phase diagram. The focus lies on the transition from the hadronic phase to the quark-gluon plasma. Thus, I detail in particular the deconfinement-confinement phase transition as well as dynamical chiral symmetry breaking.
Then I recall the construction of the Lagrangian of QCD and its intrinsic symmetries. These symmetries play an important role in the understanding of the phase diagram.
The main part of this thesis is focused on the pure gauge part of QCD. Singling out the parts of Yang–Mills theory[1] that are important in this work, I emphasise this sector of QCD separately in this introductory section. The gluon dynamics is supposed to be responsible for confinement. The signatures of this characteristic feature of QCD must be found in the long distance physics, thus, the infrared limit of pure gauge theory is the relevant region to study confinement. At the end of this section I comment on results of thermal Yang–Mills theory, which are directly referred to in section 4.

2.1. The Phase Diagram of QCD

The phase diagram of QCD is a very active area of research on both the experimental as well as the theoretical side. Nevertheless, the precise phase structure of the phases of QCD is not known yet.
In equilibrium QCD depends on the external parameters temperature and quark chemical potential[2]. In this two-dimensional parameter space QCD is believed to show a non-trivial phase spectrum of at least three distinct states of matter. This conjecture is based on the features of QCD that are implied from asymptotic freedom at high energies, at which QCD behaves qualitatively different compared to the state of matter that is observed at low energies. However, technical limitations complicate interphaseal studies and the corresponding transitions in experiments as well as in theory.

After a short comment on the methods that are employed to study the phase diagram, in this section I summarise the phases of QCD, the assumptions that suggest the existence

[1] There is no strict definition for the term Yang–Mills theory as it is used for any non-Abelian gauge theory. However, within this thesis Yang–Mills theory is synonymous with QCD without dynamical quarks, i.e. quarks with infinite masses. In other words, effectively $N_f = 0$, leaving the pure gauge part of the action.
[2] The quark chemical potential is related to the baryon chemical potential by simply $\mu_q = \mu_B/3$.

of phase transitions, and in addition their orders as well as the corresponding order parameters. The focus lies on low-energy QCD. Thus, the deconfinement-confinement phase transition and the chiral phase transitions. For extensive reviews on the phase diagram of QCD see e.g. [15–20].

2.1.1. Approaches to the QCD Phase Diagram

Experiments

From the experimental side very high energy densities must be reached in order to scan the region where other phases different from the hadronic phase are expected. As it is in fact not the energy but really the energy density that matters, these high scales can be reached by collisions of particles, either charged elementary particles or heavy ions that have been accelerated to ultrarelativistic velocities. The increase of particle momenta is realised via strong electromagnetic fields, and as the field strengths are technically limited the distance that the particle has to travel to reach high energies is long. So in practice either these tracks are very long or they are closed in a ring. In the latter case the particles lose the more energy by synchrotron radiation the smaller the radius of the ring is. Thus, also in the latter case, the spatial extent of the experiments is necessarily large.

Therefore, there are only few research facilities that run experiments at these energies. The most efficient ones in the recent past, present and near future are the *Relativistic Heavy-Ion Collider* (RHIC) at *Brookhaven National Laboratory* (BNL), USA, the *Large Hadron Collider* (LHC) at *Conseil Européen pour la Recherche Nucléaire* (CERN), Switzerland, the *Facility for Antiproton and Ion Research* (FAIR) at *Gesellschaft für Schwerionenforschung* (GSI), Germany, the *Nuclotron-based Ion Collider Facility* (NICA) at *Joint Institute for Nuclear Research* (JINR), Russia and the *Japan Proton Accelerator Research Complex* (J-PARC) at the *Japan Atomic Energy Research Institute* (JAERI), Japan.

Apart from that, even if energies are high enough it is a highly non-trivial task to extract the information of a different phase than the hadronic one because there is no rigorous signal that uniquely shows the presence of a different phase. Typically, a collision experiment of heavy ions happens as follows: First, the two ultrarelativistic ions collide in a preferably central way and the inelastic scattering happens. In this "little bang", in which strong fields emerge, a fireball forms, whose energy density is high enough that other phases than the hadronic phase can occur, i.e. where quarks and gluons are not confined into hadrons but are active degrees of freedom. At this stage the system can be described well by viscous hydrodynamics. Then, the fireball expands and equilibrates to thermal and chemical equilibrium, which can be approximated by ideal hydrodynamics. In the course of further expansion, at the phase transition hadronisation sets in, i.e. the system returns to the phase where hadrons are the active degrees of freedom. However, the hadrons still interact in such a way that the hadronic content can change. The point in the evolution

where the energies are so low that the hadrons are fixed is called chemical freeze-out. This temperature is outstandingly important for theoretical considerations because it can be extracted from experiment and sets a lower bound for the hadronisation temperature. These are the particles that are observed in the detectors. But elastic scatterings can still change the momentum distribution of the particles. This can be described well by kinetic theory. These scatterings vanish at the thermal freeze-out, which is the last stage in the expansion of a fireball.

Unfortunately, technical and physical limitations are such that the experimentally observable particles are the final states only, so exclusively the states of the system after the thermal freeze-out. As a consequence, the physics that happen in the fireball can only be reconstructed. For a review on experimental data from heavy-ion collisions see e.g. [21–27].

Lattice QCD

Lattice QCD yields very profound information about the phase diagram of QCD [28–43], in particular about its pure gauge part [44–49], also for different values of N_c [47,48,50,51]. The idea of lattice gauge theory is to discretise spacetime and perform the functional integral over the residual finite amount of paths straighforwardly, which is possible in a Euclidean formulation due to the correspondence to a statistical theory[3]. This method is genuinely non-perturbative and it does not rely on any approximations or truncations, but solves the discretised theory from first principles. However, from this discretisation lattice artefacts can occur, i.e. effects from both, finite volume of the lattice or finite lattice spacing. In fact, modern computing capabilities only allow for spanning about two orders of magnitude. Nevertheless, extrapolations to the continuum limit give reliable results if done properly. Therefore, the discretisation does not pose conceptual problems.

Unfortunately, there are other, even more severe hardships when it comes to simulations of full QCD, due to the fermionic nature of quarks. The implementation of fermions on the lattice is a hard task, especially on a dynamical level for realistically small quark masses. For reviews see e.g. [20, 57–60]. Furthermore, at non-vanishing quark chemical potential there is the so-called sign problem [61] that hinders computations. The sign problem is due to the fact that a non-vanishing quark chemical potential renders the fermion determinant in the integral measure of the functional integral complex. Therefore, only the region of small chemical potential $\mu/T < 1$ can be simulated on the lattice, which is done by means of reweighting techniques [62–66], Taylor expansions [67–71] with real quark chemical potential, or extrapolations from imaginary chemical potential [72–77]. For a recent review on the QCD phase diagram from lattice methods see e.g. [20].
Another approach to learn about the sign problem is to investigate theories that are similar to QCD, but do not suffer from a sign problem. One example herefore is QC_2D, which

[3] Although the Euclidean signature appears to be indispensable in lattice QCD, also non-equilibrium physics that necessitate a Minkowski metric can be studied on the lattice [52,53], e.g. using stochastic quantisation [54–56].

is standard QCD but with two colours instead of three. The sign problem is not present there, as the fundamental representation is a pseudo-real representation. Furthermore, the (colour-singlet) baryons are states that are built up from two quarks only. Thus, QC_2D is a good model for testing actually more than the problems related to the sign problem and in fact various questions and methods for full QCD. This system has been studied extensively on the lattice [78–87], but also with functional methods [88, 89], chiral effective field theory and random matrix models [90–100], and the Nambu–Jona-Lasinio model [101–110].

Continuum Methods

In addition to lattice gauge theory there are various continuum methods. Unfortunately, the standard technique perturbation theory is not applicable in all regions of the phase diagram, in particular at low energies, i.e. with a momentum transfer that is smaller than $\approx 1\text{GeV}$, as the coupling becomes large. Thus, the radius of convergence is not sufficient to investigate the deconfinement-confinement phase transition or the chiral phase transition, which are the characteristic and genuinely non-perturbative effects of low-energy QCD. Both are described below in more detail.
So one has to resort to truly non-perturbative methods. With those approaches, studying full QCD for all values of quark chemical potential and temperature is possible from first principles, in a Euclidean as well as a Minkowski metric. However, in comparison to lattice gauge theory, the gauge sector is usually the harder part in these applications, but the inclusion of quarks comparatively simpler. Thus, these methods are complementary in the sense that the lattice can serve as a benchmark for continuum methods in Yang–Mills theory which in contrast allow for studies at non-vanishing real chemical potential.

One prominent continuum method is the functional renormalisation group, which has been successfully applied to study the phase diagram [17, 111–113]. Furthermore, also Dyson–Schwinger equations have provided valuable insights [114–117]. In addition to real chemical potential also imaginary chemical potential has been studied [17, 112, 113]. In these studies dual order parameters [114, 118–122] were employed which are constructed from quark correlators to study the phase transition.

Continuum methods are in principle straightforward but suffer from practical limitations too, as truncations are inevitable. The reliability of these methods depends on the adequate choice of the approximation, see section 3.2.2 for further details. It has turned out that sophisticated truncations are inevitable to describe the non-perturbative physics of QCD, not only because the system is complex in each phase individually, but also because the relevant degrees of freedom change at the phase transition(s). To make things even more troublesome, the phase transitions are probably not sharp phase transitions but rather smooth crossovers, see section 2.1.2. At least in some regions, e.g. for small chemical potential, there is very clear evidence from the lattice as well as continuum methods

that the chiral phase transition as well as the deconfinement-confinement phase transition are crossovers. In chapter 3 I detail those non-perturbative functional methods that are used in this work.

In continuum methods models serve to study selected features of full QCD. Based on the Nambu–Jona-Lasinio (NJL) model [123–125] one can study the breaking of chiral symmetry. By the inclusion of the Polyakov loop the model can be improved to the PNJL model [126–140], which shows the chiral phase transition as well as confinement. A variant thereof is the Polyakov-Quark-Meson model [141–148]. Actually, at least for non-vanishing chemical potential most of the information from continuum methods about the phase transitions in QCD was obtained from model computations[4]. For a review see e.g. [149].

2.1.2. Phases of QCD

The qualitative picture of the phase diagram of QCD is based on the knowledge of the theory in the two limits of very low and high energies. In the low energy region the hadronic physics can be studied directly by experiments. At high energies the feature of asymptotic freedom [8, 9] of QCD should dominate the physical situation at hand.

At low temperatures and densities the relevant degrees of freedom are hadrons, like it is observed in the every-day life. Hadrons themselves are bound states of quarks, either quark-antiquark pairs, called mesons, or three-quark bound states, called baryons. Interestingly, these constituent particles have never been observed individually. The fact that individual quarks, or in general any particles that carry colour, have not been observed yet is called confinement[5], and it is one of the two characteristic features of low energy QCD. Confinement is a non-perturbative effect, it occurs only in regions of the phase diagram where the coupling is strong.
However, the situation is different at very large temperatures where the temperature raises the energy scale so high that the coupling becomes weak. In this limit the constituents of hadrons are not bound any more, but form the so-called quark-gluon plasma[6], for reviews see [154–158].

This necessitates that in between these limits a phase transition[7] or at least a change in the

[4] Note however, that also in models baryons have not been included dynamically yet.

[5] Note that the definition of confinement is not unambiguous, see e.g. [150]. In this thesis I simply refer to confinement as the absence of coloured particles from the observed particle spectrum.

[6] The fact that the hadronic description necessarily breaks down can be seen also from a different viewpoint, which has already been pointed out very early [151]. The idea is that the density of states grows exponentially with the mass m of the hadron divided by the Hagedorn temperature T_H, which is known from experiments. A Boltzmann-factor of $\exp\{-m/T\}$ compensates this exponential growth of statistics. But above $T > T_H$ the suppression is not sufficient and a divergent partition sum invalidates a hadronic picture.
The value of the Hagedorn temperature is still being measured. Interestingly, the value of $T_H \approx 174\,\mathrm{MeV}$ obtained in [152] with data from [153] is actually about the temperature where the deconfinement-confinement phase transition occurs.

[7] For simplicity I refer to a crossover as being a phase transition, although this is not correct in a strict

relevant degrees of freedom must occur, which deconfines the quarks and gluons in a way that they can occur individually and not only as bound states. This phase transition is referred to as deconfinement-confinement phase transition. It is expected that the energy scale at which this transition occurs is set by Λ_{QCD}, as it is the only intrinsic scale of QCD.

At infinite temperatures the quark-gluon plasma is actually a gas of free quarks and gluons, due to the vanishing coupling. So at least for large temperatures the picture of a weakly coupled gas should persists. Surprisingly, this holds only up to very large temperatures compared to the energy Λ_{QCD}. In contrast, experiments at RHIC and the LHC advocate that in the vicinity of the phase transition from the hadronic phase to the quark-gluon plasma the latter one behaves rather like a liquid of strongly coupled quarks and gluons [22–27, 159–161].

The transition from the quark-gluon plasma to the hadronic phase took place in the evolution of the early universe. The standard picture is such that the trajectory of the universe as a function of time in the phase diagram started at large temperatures and entered the hadronic phase, both stages happened at small quark chemical potential.

In addition to that, there is another aspect that suggests a phase transition which is in principle independent of the deconfinement-confinement phase transition. The masses of hadrons that consist of light quarks are far above the straightforward sum of the masses of the quarks, like they are extracted from high-energy experiments. The light quark masses are of the order of a few MeV, the quark masses are given in tab. (2.1) [162]. In contrast to this, the proton, which consists of two up and one down quarks, has a mass of $m_{\mathrm{proton}} \approx 938\mathrm{MeV}$. So actually, most of the mass comes from the binding energy in the gauge fields and the sea quarks. Therefore, also this attribute of the masses of the

up	down	strange	charm	bottom	top
$2.5^{+.6}_{-.8}$ MeV	$5.0^{+.7}_{-.9}$ MeV	100^{+30}_{-20} MeV	$1.25^{+.05}_{-.11}$ GeV	$4.19^{+.18}_{-.06}$ GeV	$172.9^{+.6}_{-.8}$ GeV

Table 2.1.: Quark masses [162].

fundamental particles must change at some point, i.e. at the phase transition the (almost) massless up, down and also the strange quark effectively receive a much higher mass. This phase transition is called the chiral phase transition. Also, here the relevant scale is supposed to be Λ_{QCD} and the phase transition is supposed to happen in this energy region. The other quarks, the charm, bottom and top quark, are much heavier than this scale. Thus, they are not dynamical any more at the chiral phase transition but dominated by their mass scale, which they obtain from the Higgs mechanism. In contrast to this, the masses of the light quarks are well below the scale Λ_{QCD}, in particular the mass of the up and down quark should not play a dominant role. For the light quarks the effect of chiral

sense.

symmetry breaking is therefore crucial, and in fact most of the constituent quark mass of the up and down quarks in hadrons is not triggered by the Higgs mechanism, but by dynamical chiral symmetry breaking. For the strange quark both effects contribute with roughly half of the mass.

It is worth to mention that it is not clear yet whether the deconfinement-confinement phase transition and the chiral phase transition are independent of each other. It may well be that they are related to each other, or even that they are one single phase transition. This statement would be supported by the fact that these phase transitions occur at approximately the explored regions of the (μ, T)-plane, at least for vanishing chemical potential [34, 72]. Although both effects should be set by the scale Λ_{QCD}, this is an unexpected result.

In the hadronic phase there is another phase transition which is called nuclear phase transition. It is the transition of the liquid self-bound ground state of baryonic matter to the state where the baryons form a gas. This transition happens at low temperatures and baryon chemical potentials of $\mu_B \approx 924\mathrm{MeV}$. At vanishing temperature it is a first order transition which turns into a second order critical point with increasing temperature. For even larger temperatures it becomes a crossover.

Another interesting phase that is reasonable by the argument of asymptotic freedom is that at low temperatures but high baryon densities the state of matter should exhibit colour superconductivity, i.e. quarks form Cooper pairs [163]. For instance, in neutron stars or in the still hypothetical objects of quark stars this phase is likely to be realised. As this is not of particular importance for the work presented in this thesis, I do not discuss this phase in detail, for further information see [163–169].

Motivated by the phase diagram of QCD in the theoretical limit of many colours, i.e. $N_c \to \infty$, another phase for low and intermediate temperatures and intermediate quark chemical potential has been proposed, called the quarkyonic phase [170–173]. In this state the quarks are still confined but chiral symmetry is restored. However, the existence is more questionable than the other phases described in this section.

The arguments can be put into a sketch of the conjectured phase diagram which is given in fig. (2.1). In particular the deconfinement-confinement phase transition and the chiral phase transition are of interest in this thesis. I detail them in the subsequent sections.

A natural question is the order of the phase transition from the hadronic phase to the quark-gluon plasma. For vanishing quark chemical potential the situation is summarised in the so-called Columbia plot [175], which is given in fig. (2.2). The order strongly depends on the quark masses. In fig. (2.2) the axes label the quark masses, the abscissa shows the two almost degenerate light quarks whereas the ordinate indicates the mass of the strange quark. In this plot the chiral limit corresponds to the lower left corner

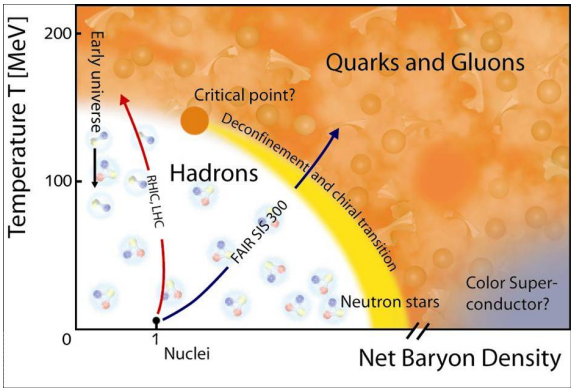

Figure 2.1.: Sketch of the (conjectured) phase diagram of QCD. For high temperature and net baryon density quarks and gluon are the relevant degrees of freedom. For low temperatures and quark chemical potential the fundamental particles appear only in bound states, called hadrons. Between these two phases the deconfinement-confinement phase transition and the chiral phase transition occur. Both transitions happen at about the same parameter sets in the phase diagram. At low temperature but high baryon densities the system shows signs of superconductivity, as quarks form Cooper pairs. This illustration is taken from the homepage of GSI Darmstadt [174].

where the solid line is the critical line of the chiral phase transition. For small masses the phase transition is of first order [176] which turns into a crossover for larger masses of the quarks. In the other extreme, the limit of large quark masses, Yang–Mills theory is theoretically realised in the upper right corner, where the solid line denotes the critical line of the deconfinement-confinement phase transition in pure gauge dynamics. The phase transition of Yang–Mills theory is of first order[8] [177], but with dynamical quarks it gets smeared out to become a crossover as well. The measured quark masses are such that the physical point lies in the crossover region [34–36, 41, 42, 178–180].

Turning now to non-vanishing quark chemical potential, lattice simulations are hampered. Thus, the information about the phase transition is not as profound as in fig. (2.2). As a function of chemical potential in addition to the temperature the critical line in fig. (2.2) is a critical surface. Model studies show [144, 181–184] that this critical surface bends towards the physical point. Thus, for large values of the quark chemical potential the phase transition from the hadronic phase to the quark-gluon plasma is a first order transition. For decreasing chemical potentials it occurs on the critical surface, which yields a second order transition. Beyond this point the transition becomes a crossover, like it is observed for $\mu_q = 0$ in fig. (2.2).
So far, lattice results are consistent with the existence of a critical point. However, these results suffer from the technical and conceptual limitations of the lattice. Moreover, recent

[8] Actually, the order of the deconfinement-confinement phase transition depends on the gauge group, for a recent analysis see [11, 12, 48]. For $SU(3)$ the phase transition is of first order, in $SU(2)$ it is of second order. Confinement and the order of the deconfinement-confinement phase transition are studied further in chapter 5.

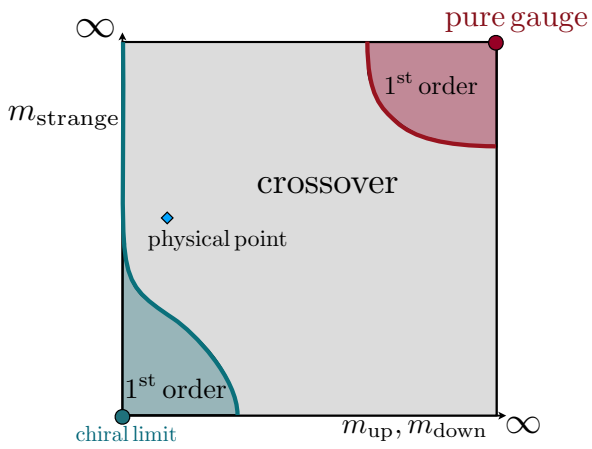

Figure 2.2.: This so-called Columbia plot shows the order of the phase transition from the hadronic phase to the quark-gluon plasma as a function of the quark masses. In the chiral as well as pure gauge limit the transition is first order, both end at critical lines where the transition is of second order. For quark mass configurations that do not satisfy these limits the transition is a crossover. The physical point is situated in the crossover region.

lattice results indicate that this picture may have to be revised, as in these extrapolations from the region of imaginary chemical potentials the critical surface bends away from the physical point at small chemical potentials [74, 75]. This leaves two different scenarios: Either the transition remains a crossover, or the critical surface bends back towards the physical point. In the latter case the critical point in the phase diagram, see fig. (2.1), would be at much larger values of μ_q/T than expected. The exact location of the critical point is of great interest because fluctuations at this point are enhanced [185, 186], which would yield clear signals in experiments.

Aspects of Confinement

Since the acceptance of QCD as a fundamental theory, it has been a pressing question why coloured particles are absent in observations[9]. I refer to the lack of colour non-singlets[10] as confinement, although there is no rigorous definition for this term. For further details of definitions and signatures of confinement see e.g. [187, 188]. The feature of confinement is also observed in lattice simulations. By the time, it has become accepted, although a satisfactory explanation or derivation of this property is not known yet.

Quarks interact very weakly at short distances. However, if the constituents of say a me-

[9] In fact, experimentally the search is not for coloured particles but for particles that have fractional electric charge, which is the case for quarks.

[10] Note that the signal of the absence of coloured particles is not a clear signal for confinement either, since it mixes the notions of confinement in a strict sense and colour screening. For further details see e.g. [187].

son are pulled apart, the attractive force between them increases with the distance. For infinitely heavy (anti-)quarks this growth is unbounded, i.e. it would require an infinite amount of energy to separate the quark from the antiquarks. This is confirmed by lattice simulations of pure gauge theory, i.e. static quarks. Here, a linearly rising static quark potential signals the confining phase, for a review see [189]. At finite quark masses the energy between the quark-antiquark pair at some point surpasses the threshold for pair creation from the vacuum. At this point the initial particles bind with one particle of the created pair. Therefore, for finite quark masses the energy does not tend to infinity but settles at a finite value. Nevertheless, the remaining particle content is colour neutral.

There are many signals of confinement like the Wilson loop or the Polyakov loop, respectively, the 't Hooft operator or the vortex free energy. For a detailed discussion see [187]. In this work, in particular in chapter 5, the order parameter for quark confinement is the Polyakov loop [190, 191] which is defined by

$$L(\vec{x}) = \frac{1}{N_c}\mathrm{tr}\,\mathcal{P}e^{ig\int_0^{1/T} dx_0\, A_0(x)}\,, \tag{2.1}$$

where N_c is the number of colours, tr is the trace and $\mathcal{P}$ denotes path ordering, g is the unrenormalised gauge coupling and A_0 is the temporal component of the gluon at temperature T. The Polyakov loop is a Wilson loop in time direction with periodic boundary conditions, i.e. at finite temperature, which winds around the compactified time direction at least once.
The Polyakov loop L has very peculiar properties related to the centre of the gauge group $SU(N_c)$. The elements z_k of the centre Z_{N_c} commute with all group elements. For $SU(N_c)$ it is proportional to the unit matrix $\mathbb{I}$, with the proportionality factor being the N_c roots of 1. Thus, under a gauge transformation

$$U = \left(z_k \mathbb{I}^{N_c\times N_c}\right)^{x_0 T}\,, \tag{2.2}$$

see eq. (2.8), the gauge field is simply shifted by a constant, but is still periodic in the temporal direction. Therefore, it leaves the purely gluonic action invariant. This is only the case if the z_k is an element of the centre of the group. Thus, this invariance is called centre symmetry [192, 193].
However, L is sensitive to this transformation because $L \to z_k L$, so its expectation value $\langle L\rangle$ over all gauge transformed L vanishes if centre symmetry is immanent but is non-zero if centre symmetry is broken [187].
This can be related to an order parameter for quark confinement, because $\langle L\rangle$ can be related to the free energy F_q of a static quark [194–196],

$$\langle L\rangle = \exp\left\{-F_q/T\right\}\,. \tag{2.3}$$

$\langle L\rangle$ serves as an order parameter for quark confinement for the following reason: If confine-

ment prevails, bringing an infinitely heavy quark-antiquark pair into the system and then sending the antiquark to spatial infinity requires an infinite amount of energy. This infinite free energy of the static quark corresponds to $\langle L \rangle = 0$. In contrast to this, the needed amount of energy is finite in the deconfined phase and therefore $\langle L \rangle \neq 0$. Consequently, the expectation value of the Polyakov loop is a true order parameter: It is strictly zero in the confined phase $T < T_c$ and non-zero in the deconfined phase $T > T_c$. The full information is encoded in the effective potential of the gluons. As the quarks are infinitely heavy, i.e. static, confinement is generated by gluon dynamics. This suggests that confinement in QCD is indeed an effect that is driven by the pure gauge sector.
The centre transformation eq. (2.2) leaves the action of Yang–Mills theory invariant. However, dynamical quarks break the centre symmetry explicitly, thus $\langle L \rangle \neq 0$ in both phases, the deconfined but also the confined phase. As a result, the phase transition in full QCD becomes a crossover, but still the sharp rise of $\langle L \rangle$ at the phase transition gives a clear signal.

Aspects of Chiral Symmetry Breaking

Chiral symmetry is an exact symmetry of the Lagrangian of QCD, eq. (2.12), in the case of massless quarks, see section 2.2, with the symmetry group $U(1)_V \times U(1)_A \times SU(N_f)_L \times SU(N_f)_R$, stemming from vector rotations and axial-vector transformations on the quark fields. If this symmetry is realised, quarks q_f^a can be split in left- and right-handed Weyl spinors, ψ_L and ψ_R, whose components do not mix under chiral transformations. In the physical situation quark masses break this symmetry explicitly, they mix left- and right-handed spinors, and the $SU(N_f)_L \times SU(N_f)_R$ is broken the to the $SU(N_f)_V$. But due to the small quark masses for the light flavours, for those the symmetry remains as an approximate symmetry. In addition, the $U(1)_A$ symmetry is broken to $Z(N_f)$ by quantum fluctuations. The latter effect is called axial anomaly.
In addition to this explicit breaking, chiral symmetry gets spontaneously broken in the hadronic phase. An order parameter that is sensitive to this spontaneous breaking is the chiral condensate $\langle \bar{q}_i^a q_i^a \rangle = \langle \bar{\psi}\psi \rangle = \langle \bar{\psi}_\mathrm{R}\psi_\mathrm{L} + \bar{\psi}_\mathrm{L}\psi_\mathrm{R} \rangle$, as it is zero if the components do not mix, i.e. in the chirally symmetric phase, but acquires a non-vanishing value in the phase of spontaneously broken chiral symmetry, even for initially massless quarks.

2.2. The Action of QCD

In the standard model of particle physics, the strong interaction is described as a relativistic quantum field theory called QCD. It is the force between quarks and gluons, which are the fundamental particles in the theory.
In the functional integral formulation the microscopic action of the theory is the important

ingredient. It can be described as the spacetime integral over the Lagrangian density[11]. As QCD bares local gauge symmetry the classical Lagrangian must be gauge invariant. A gauge transformation acting on a quark can be written as

$$q(x) \to q'(x) = U(x)q(x) = e^{ig\theta^a(x)t^a} q(x)\,, \quad \text{with} \quad U(x) \in SU(N), \tag{2.4}$$

where the t^a are the generators of the group of special unitary transformations $SU(N)$, i.e. (in a matrix representation) unitary matrices with determinant +1. These transformations themselves form a Lie algebra $\left[t^a, t^b\right] = if^{abc}t^c$, where the f^{abc} are the structure constants of the group. For $SU(2)$ they are simply the entries of the Levi-Civita symbol. In the following, the normalisation is chosen such that $\mathrm{tr}\,\{t^a t^c\} = +\frac{1}{2}\delta^{ab}$. For the case of $SU(2)$ the generators t^a are proportional to the standard Pauli matrices, in $SU(3)$ they are called Gell-Mann matrices.
As the gauge transformation does depend on spacetime itself, the kinetic part containing a normal spacetime derivative would not transform covariantly, because the derivative would act on $U(x)$ as well

$$\partial_\mu U(x)q(x) = U(x)\partial_\mu q(x) + (\partial_\mu U(x))\, q(x). \tag{2.5}$$

This can be cured via the construction of a covariant derivative which guarantees covariance of the kinetic part in the action. The covariant derivative is defined as

$$\mathcal{D}_\mu = \partial_\mu - ig\, t^a A^a_\mu(x)\,, \tag{2.6}$$

where the $A^a_\mu(x)$ are the gluons, and g is the unrenormalised coupling. In order to ensure covariance, the transformation of the gluonic field must cancel the term $\sim \partial_\mu U(x)$ in eq. (2.5). This leads to the requirement that

$$(\partial_\mu U(x))\, q(x) - ig(A')_\mu(x)U(x)q(x) = -ig\,(U(x)A_\mu(x))\, q(x)\,, \tag{2.7}$$

with the sum abbreviation for a coloured object $\mathcal{C}^a t^a = \mathcal{C}$. Thus, the gluons transform according to

$$A_\mu(x) \to (A')_\mu(x) = U(x)A_\mu(x)U^{-1}(x) - \frac{i}{g}\,(\partial_\mu U(x))\, U^{-1}(x). \tag{2.8}$$

Due to the unitary of the $SU(N)$: $U^{-1}(x) = U^\dagger(x)$.
The gluons are fundamental particles, therefore, a kinetic term in the action must be included as well. The four-dimensional curl is not appropriate, because it does not ensure the correct transformation property. Instead, the commutator of two covariant derivatives is a gauge invariant

$$\frac{i}{g}\left[\mathcal{D}_\mu, \mathcal{D}_\nu\right] = \frac{i}{g}F_{\mu\nu} = \partial_\mu A_\nu(x) - \partial_\mu A_\nu(x) - ig\,\left[A_\mu(x),\, A_\nu(x)\right]\,, \tag{2.9}$$

[11] In the following I employ an abbreviation common in the literature, as I refer to the Lagrangian density simply as the Lagrangian.

so for its components spanned via the generators $F_{\mu\nu} = F^a_{\mu\nu} t^a$ the field strength tensor $F^a_{\mu\nu}$ is defined by

$$F^a_{\mu\nu}(x) = \partial_\mu A^a_\nu(x) - \partial_\nu A^a_\mu(x) + g f^{abc} A^b_\mu(x) A^c_\nu(x). \tag{2.10}$$

For applications at non-vanishing temperature, see especially chapter 4, the spatial components of $F^a_{\mu\nu}(\mathrm{x})$ are grouped in analogy to electrodynamics. The differentiation is done for chromoelectric fields $E^a_i(x)$ and chromomagnetic fields $B^a_i(x)$, defined as

$$E^a_i(x) = F^a_{0i}(x)\,, \quad B^a_i(x) = \frac{1}{2}\epsilon_{ijk} F^a_{jk}\,, \quad \text{with } i = 1,2,3\,. \tag{2.11}$$

Finally, constructing the non-trivial kinetic term for the gluons by the Lorentz-scalar quantity $\left(F^a_{\mu\nu}\right)^2$,gives the classical Lagrangian for QCD

$$\mathscr{L}_{\text{classical}} = \frac{1}{4} F^a_{\mu\nu} F^a_{\mu\nu} + \sum_f \bar{q}^a_f \left(-\gamma_\mu \mathcal{D}_\mu + m_f\right)^{ab} q^b_f\,. \tag{2.12}$$

Actually, this simple looking Lagrangian is sufficient to describe QCD in all situations, even though the theory has such diverse properties in different regions which lead to a rather complex phase structure, see section 2.1.

One interesting aspect of non-Abelian gauge theory is that the pure gauge part is an interacting theory on its own, already on a classical level. In the square of the field strength tensor also cubic and quartic terms in the gluon fields arise, which are interaction terms for gluons among themselves. They are illustrated by the help Feynman diagrams as the last two terms in fig. (2.3(a)).

In view of a quantum theory the classical Lagrangian eq. (2.12) is yet inappropriate. This is due to the fact that the measure of the functional integral respects all possible configurations, but there is a redundancy in the physically different configurations as one is free to perform a gauge transformation. The set of physically similar configurations that are related by a gauge transformation is called gauge orbit $[A^U]$

$$[A^U] := \left\{A^U \;=\; UAU^\dagger + (\partial_\mu U)U^\dagger\,,\; U \in SU(N)\right\}\,. \tag{2.13}$$

This freedom results in an (infinite) overcounting of the physical states, which can be circumvented by fixing the gauge: The aim is to count only one representative of each gauge orbit by imposing the gauge fixing condition $\mathcal{G}[A] = 0$. At first, I employ the Faddeev–Popov gauge fixing method [197] postponing potential problems connected to this gauge fixing procedure in non-Abelian gauge theories for the moment.
The idea of the Faddeev–Popov trick is to insert a multiplicative factor of 1 in the path integral, written in the form

$$1 = \int \mathscr{D}U\, \delta\mathcal{G}[A]\, \Delta_{\text{FP}}[A^U]\,, \tag{2.14}$$

where $\mathscr{D}U$ is the Haar measure of the group manifold, which is invariant under gauge

transformations. The $\delta\mathcal{G}[A]$ takes out only one configuration of each gauge orbit, and $\Delta_{\mathrm{FP}}[A^U] = \det M$ is the Faddeev–Popov determinant arising due to the normalisation. The Faddeev–Popov determinant is the determinant of the Faddeev–Popov operator

$$M^{ab}(x,y) = \left.\frac{\delta\mathcal{G}[A^a(x)]}{\delta\theta^b(y)}\right|_{\theta=0} . \tag{2.15}$$

In linear covariant gauges the latter quantity can be written as

$$M^{ab} = -\partial_\mu \mathcal{D}^{ab}_\mu . \tag{2.16}$$

The Faddeev–Popov determinant itself can be transformed by the help of additional, auxiliary fields called Faddeev–Popov ghosts. As the determinant is in the numerator the transformation into a path integral,

$$\det M = \int \mathscr{D}c\,\mathscr{D}\bar{c}\, \exp\left\{\int_{x,y} \bar{c}^a(x) M^{ab}(x,y) c^b(y)\right\} , \tag{2.17}$$

requires that the ghosts c^a and antighosts $\bar{c}^a$ are Grassmannian fields. Nevertheless, ghosts have spin 0. However, there is no conflict with the spin-statistics theorem as these fields are not part of the physical state space, but rather a pure mathematical trick. Thus, they are not subject to the spin-statistics theorem. Note that ghosts carry colour themselves, which is intuitively reasonable as they cancel the redundant gluonic degrees of freedom.
Also the gauge-fixing condition $\delta\mathcal{G}[A]$ can be raised to be a term $\frac{1}{2\xi}(\partial_\mu A_\mu)^2$ in the action directly, where ξ is the gauge parameter. Here, Landau gauge is employed $\xi \to 0$, i.e. only those configurations contribute that satisfy the condition $\partial_\mu A_\mu = 0$, whereas all others are suppressed in the functional integral.
The gauge fixing gives the quantum formulation of the non-Abelian gauge theory in terms of the generating functional

$$\begin{aligned} Z[Q,\bar{\eta},\eta,\bar{\sigma},\sigma] = \int \mathscr{D}[A\,q\,\bar{q}\,c\,\bar{c}] \quad \exp\Bigg\{ - \int_x \Bigg(\mathscr{L}_{\text{classical}} + \frac{1}{2\xi}(\partial_\mu A_\mu)^2 + \bar{c}^a \partial_\mu \mathcal{D}^{ab}_\mu c^b \Bigg) \\ + \int_x \left(Q\cdot A + \bar{\eta}\cdot q + \bar{q}\cdot\eta + \bar{\sigma}\cdot c + \bar{c}\cdot\sigma \right) \Bigg\} , \end{aligned} \tag{2.18}$$

with the path integration over the particle content $\mathscr{D}[A\,q\,\bar{q}\,c\,\bar{c}] = \mathscr{D}A\mathscr{D}q\mathscr{D}\bar{q}\mathscr{D}c\mathscr{D}\bar{c}$. The arguments of the partition function, $Q, \bar{\eta}, \eta, \bar{\sigma}$ and σ, are the sources of the corresponding fields. The proper field affiliation of a source can be read off from the couplings of these quantities in the exponent given in the second line of eq. (2.18).
The interaction terms that appear in the QCD action are illustrated best with Feynman diagrams. The seven primitively divergent n-point functions that are present in the action of QCD are illustrated in fig. (2.3). In a quantum theory they are modified by quantum effects. In addition to the interactions given in fig. (2.3) further interactions can be triggered by quantum fluctuations.

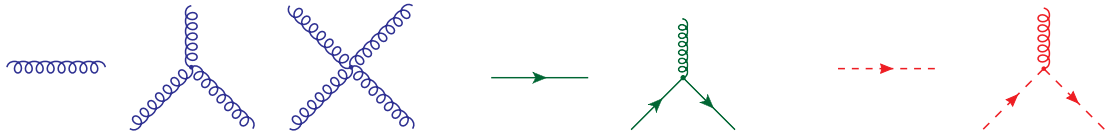

(a) Purely gluonic n-point functions.

(b) n-point functions with quark contributions.

(c) n-point functions with ghost contributions.

Figure 2.3.: Primitively-divergent vertex functions of QCD.

The action of QCD bares symmetries, i.e. the exponent of eq. (2.18) is invariant under certain transformations, although the local gauge symmetry discussed above is not present any more due to gauge fixing. Nevertheless, there are also gauge symmetries left.
First of all, there is the freedom for global gauge rotations, i.e. invariance under a gauge transformation whose parameter in eq. (2.4) does not depend on spacetime. Though, it is not clear if this symmetry is realised in full QCD. Phrased in other words, the existence of a global colour charge associated with this symmetry of QCD due to the Noether theorem is not guaranteed. However, the existence of a global colour-charge is crucial for the Kugo–Ojima confinement scenario, cf. section 2.3.1.

Furthermore, there is another symmetry related to gauge invariance called BRST symmetry [198–201]. It means that the action is invariant under the gauge transformations with the product of the ghost field and a Grassmann valued number as transformation parameter. The transformations of the fields are given by

$$\begin{aligned} s\,A^a_\mu &= \mathcal{D}^{ab}_\mu c^b\,, \quad & s\,q &= -igt^a c^a q\,,\\ s\,c^a &= -\frac{1}{2} g f^{abc} c^b c^c\,, \quad & s\,\bar{c}^a &= \frac{1}{\xi}\partial_\mu A^a_\mu\,, \end{aligned} \tag{2.19}$$

where s is the BRST-operator, sc. the symmetry generator. In the confinement scenario of Kugo and Ojima described in section 2.3.1 it is crucial that s is a nilpotent operator, i.e. in abuse of notation $s^2 = 0$.
Due to the Noether theorem there is a conserved charge associated with BRST symmetry, the BRST charge Q_B. However, in the formulation above this holds for the perturbative treatment only. So similar to the global colour charge, also for Q_B it is not clear if it is well-defined also on the non-perturbative level.

The global gauge symmetry and the BRST symmetry are related to the gauge symmetry, but there is a symmetry also in the matter sector. The matter part of the Lagrangian, given explicitly as the second term in eq. (2.12), contains two terms: the covariant derivative and the quark masses. From experiments it is known that the quark masses are non-zero, which is (most likely) due to the Higgs mechanisms. However, if the quarks are taken to be massless, i.e. in the chiral limit $m_f \to 0$, chiral symmetry is exact. In this case quarks

can be decomposed into left- and right-handed Weyl-spinors, whose components do not mix under chiral transformations, i.e. global unitary transformations $U(N_f)_L \times U(N_F)_R$. Finite quark masses break chiral symmetry explicitly. However, as the quark masses of the three lightest quarks up, down and strange are very light, for large energy scales well above the quark masses it is expected that the chiral symmetry remains as an approximate symmetry for these three flavours, which should be reflected in low-energy QCD as well. But in addition to the explicit breaking there is also a dynamical spontaneous breaking of chiral symmetry, which is detailed in section 2.1.2.

To conclude this section I sketch the problems that arise in the Faddeev–Popov gauge-fixing procedure.
The gauge-fixing must single out the physical configurations only. However, this is not satisfied by the Faddeev–Popov gauge fixing. This can be seen easily in Landau gauge by the help of the Faddeev–Popov operator, eq. (2.16). As well it is also immanent in other gauges like Coloumb gauge [202] or maximal Abelian gauge [203]. In fact it is present in all local gauge-fixings procedures, because it is due to the topological structure of the gauge group [204]. However, here it is only shown for Landau gauge.
For a gauge configuration that fulfills the Lorenz condition,

$$\partial_\mu A_\mu = 0\,, \tag{2.20}$$

a gauge transformation, eq. (2.8), can yield another configuration that still fulfills the Lorenz condition if the Faddeev–Popov operator eq. (2.16) has zero modes, thus

$$\partial_\mu A_\mu = 0 \;\longrightarrow\; \partial_\mu A_\mu + M\Theta\,. \tag{2.21}$$

The presence of these gauge copies is known as the Gribov problem [205], for a recent review see [206].

Consequently, the gauge-fixing needs a refinement which is done in first place by the definition of the (first) Gribov region. Actually, the configuration space can be separated by the Faddeev–Popov operator. Writing the determinant by the product of its eigenvalues,

$$\det M = \prod_i \lambda_i\,, \tag{2.22}$$

it is obvious that the Gribov horizon is where an eigenvalue vanishes. Therefore, at every zero mode an eigenvalue changes its sign, and therefore the Faddeev–Popov operator changes its sign. By the zeroes the space is separated into regions, the first of which is around the origin with the Faddeev–Popov operator being positive definite. This defines the Gribov region Ω by

$$\Omega = \{\,\{A_\mu(x)\}\,|\,\partial_\mu A_\mu(x) = 0 \wedge M > 0\}\,. \tag{2.23}$$

The Gribov region contains the origin[12] [207] and is bounded in all directions [207]. Furthermore, it is complex, i.e. two consecutive gauge transformations in the Gribov region combine to a gauge transformation which stays itself in the Gribov region [207]. In addition, it can be shown that all gauge orbits intersect the Gribov region [208], therefore no physical configurations are neglected. Thus, integrating only over the Gribov region in the functional integral circumvents the problems of zero modes in the Faddeev–Popov operator.

Unfortunately, even within the Gribov region there are still gauge copies left [208–211]. A full gauge fixing would be obtained by restricting the integration to the Fundamental Modular Region, but a construction of this object in the continuum is not know yet. Also resorting to the lattice formulation is not satisfactory because fixing the gauge uniquely would mean to find the global maximum of the gauge-fixing functional, which is numerically too costly to allow for a proper solution.

2.3. Yang–Mills Theory

2.3.1. Confinement in Yang–Mills Theory

As outlined in section 2.1.2 confinement means the absence of colour-charged objects in the physical particle spectrum. Yang–Mills theory shows confinement for low temperatures. For the gauge group of QCD, $SU(3)$, and larger temperatures it undergoes a first order phase transition to a deconfined phase. This is expected from the fact that like QCD also Yang–Mills theory is asymptotically free.
As confinement in full QCD is driven by the gluon dynamics, see section 2.1.2 and chapter 5, Yang–Mills theory on its own provides direct insight into the phase diagram of full QCD.

Confinement is a large distance phenomenon. Thus, in momentum space confinement of Yang–Mills theory must be reflected in the correlation functions in the infrared regime. As expected, it turns out that the perturbative description fails. A perturbative gluon propagator would diverge in the infrared as gauge invariance does not allow for a constant gluonic mass term. In Landau gauge[13], however, in both, continuum as well as lattice studies, this is not observed. Quite the contrary, the gluon propagator at zero momentum approaches a constant or may even vanish. The different solutions are detailed below in section 2.3.2. The other particle, the Faddeev–Popov ghost, does diverge at zero momentum. In some possible explanations for the confinement mechanism the infrared behaviour of the propagators is crucial. In the following I detail these scenarios, namely the Kugo–

[12] The fact that the origin lies within the Gribov region is crucial for perturbation theory, which is an expansion around the origin. The point where complications due to insufficient gauge-fixings occur is where quantum effects are too large as to allow for a perturbative approach in first place.
[13] Throughout this thesis Landau gauge is used.

Ojima scenario and the Gribov–Zwanziger scenario, respectively.

Kugo–Ojima Scenario

Confinement in Yang–Mills theory can be explained by the help of the Kugo–Ojima scenario [212]. It relies on the existence of BRST symmetry, which was already introduced in section 2.2, the existence of a global colour charge and the violation of the cluster decomposition property in total state space but not in the physical state space.
In Landau gauge the state space $\mathcal{W}$ has an indefinite metric, i.e. not only physical states occur, but also unphysical ones, e.g. single gluon or ghost states. If BRST symmetry is unbroken, it allows for a construction of the physical state space $\mathcal{W}_{\text{phys.}}$ starting from the full state space[14]. Although the symmetry is a global symmetry[15], the non-perturbative existence of a global BRST charge is not guaranteed. However, the Kugo–Ojima scenario assumes that this charge is well-defined. By the help of the nilpotent BRST charge-operator Q_B, i.e. the generator of the symmetry, the state space $\mathcal{W}$ of all states $|\psi\rangle$ is divided in three parts of which the cohomology of Q_B constitutes the physical state space, i.e. $\mathcal{W}_{\text{phys.}} = \operatorname{Ker} Q_B / \operatorname{Im} Q_B$. The physical states are therefore in the kernel of Q_B, i.e. BRST invariant $Q_B|\psi_{\text{phys.}}\rangle = 0$, but not in the image of it, i.e. not a BRST daughter state $|\psi_{\text{phys.}}\rangle \neq Q_B|\psi\rangle$. A BRST daughter state is also called BRST exact state. Herein, the nilpotency Q_B is crucial as all BRST exact states are BRST invariant as well. If this were not fulfilled, the definition of the physical subspace as cohomology of Q_B would not hold. BRST states that are exact and non-invariant BRST states always come in quartets. In the S-matrix the contributions from the states that constitute a quartet always cancel, thus, these states do not appear as physical states. In contrast to this, physical states are BRST singlets. Note that the BRST quartet mechanism is not only investigated in pure Yang–Mills theory, but also in QCD, see e.g. [215]. As Kugo and Ojima showed, under the assumption of the existence of a global colour charge Q^a, the physical state space only contains colour neutral states. Herefore, the Q^a is expressed as spatial integral over the divergence-free Noether current J^a_μ, which is obtained from the equation of motion for the gluon, thus,

$$Q^a_\mu \;=\; G^a + N^a \;=\; \int d^3x \left\{ \partial_\nu F^a_{\mu\nu} + \left\{ Q_B, \mathcal{D}^{ab}_\mu \bar{c}^b \right\} \right\} . \tag{2.24}$$

The individual terms stemming from the field strength tensor and the anti-commutator, respectively, may yield individual charges, each of which can be spontaneously broken. This allows for a classification. Note that the anti-commutator in eq. (2.24) is BRST exact. In Abelian gauge theories the ghosts always decouple, i.e. the charge N^a stemming involving the covariant derivative of the ghost is always broken. Furthermore, also the

[14] In the superficial sense, the Kugo–Ojima scenario in Yang–Mills theory resembles the Gupta-Bleuler mechanism of QED [213, 214]. There, the unphysical states do not appear in S-matrix elements, i.e. only transversally polarised photons occur as physical particles. However, single gluon states are always unphysical asymptotic states, even if they are transversal. Thus, the Kugo–Ojima mechanism has to cancel those states as well in addition to negative norm states.

[15] The BRST symmetry is gauge transformation with the (spacetime-dependent) ghost as gauge-parameter. Nevertheless, it is a global symmetry as different points in spacetime must be treated similarly.

charge from the field strength G^a is broken due to massive gauge modes. However, the combination of these two breaking terms always cancels in such a way that the global charge Q^a is conserved. In non-Abelian gauge theories massless gauge bosons yield a vanishing colour charge G^a. But N^a is always broken, so in this case the global charge Q^a is broken. In the confining case both G^a as well as N^a are unbroken. Consequently, also Q^a is conserved.

The requirements for the case in which both charges are unbroken is the relevant one for the confinement mechanism for Yang–Mills theory. The relations translate to direct signatures in the propagators of the gluon and the ghost. The charge G^a vanishes iff the theory has a mass gap, which is realised if the gluon propagator is less singular than a simple pole[16]. N^a is unbroken if the ghost propagator is enhanced in comparison to the trivial propagator. If these conditions are fulfilled, the global colour charge is well-defined. From this follows the absence of coloured particles from the physical spectrum of $\mathcal{W}_{\text{phys.}}$. The last condition for confinement is linked to the cluster decomposition property. Cluster decomposition is connected to the locality of the quantum field theory. It states that clusters that are separated in space can be divided and observed individually. Obviously, this property has to be violated in the full state space as otherwise coloured objects could be observed. But for physical states only it needs to be fulfilled, i.e. all physically observable states are local in the sense that the substructures can not be resolved in the experiment. Therefore, observable states can not scatter into colour singlet states that consist of two coloured constituents which are well separated in position space, and thus, it would be observable individually, cf. behind-the-moon problem.

Gribov–Zwanziger Scenario

Another confinement scenario is based on considerations of the gauge fixing that are explained in section 2.2.

The Gribov–Zwanziger scenario [205, 207, 216, 217] states that the infrared relevant configurations are close to the boundary of the first Gribov region as due to the high dimensionality most configurations are at the boundary. The Gribov–Zwanziger action is a way to restrict the integration to the horizon of the Gribov region. In Landau gauge, again, this restriction translates to requirements for the infrared behaviour of the Yang–Mills propagators. In fact, for the ghost the same condition as in the Kugo–Ojima scenario is met, sc. the ghost propagator has to diverge more strongly than a simple pole. For the gluon the requirement is even stricter than in the Kugo–Ojima scenario, as the propagator must vanish at zero momentum.

In Coulomb gauge the importance of the configurations at the horizon is directly visible at the hand of the Coulomb potential. The colour Coulomb potential is a renormalisation group invariant potential, which is an upper bound for the gauge invariant potential of the Wilson loop, thus, there is no confinement without Coulomb confinement [218]. But the

[16] Note that the order of the pole relates to momentum squared, so the propagator must be less singular than the trivial one p^{-2}.

Coulomb potential is also related to the Faddeev–Popov operator. This potential is almost linearly rising [219–225], which is generated from the horizon. In Landau gauge, however, a corresponding potential has not been identified yet, but, nevertheless, the application in Coulomb gauge supports the relevance of the horizon.

Positivity Violations

If a Euclidean correlator shall have a particle interpretation in the Gårding–Wightman relativistic field theory, it needs to fulfill the Osterwalder-Schrader axioms [226–228]. One of these constraints on the propagators is reflection positivity, which is related to the positive definiteness of the norm of the physical state space. For unphysical particles, in the case of Yang–Mills theory in particular the gluon, it is sufficient to show that reflection positivity is violated in order to prove that the particle is not in the physical state space. Or in other words it does not have a Källén–Lehmann representation.
Actually, this is not a strict condition for confinement because although particles are absent in the spectrum, positivity violation itself is not required. Furthermore, it only provides information for the field, but not of bound states that may carry non-zero colour. Besides that subtlety, the Källén–Lehmann representation of a propagator $G(p)$ is given by

$$G(p) \;=\; \int_0^\infty dm^2 \, \frac{\rho(m^2)}{p^2+m^2} \,, \tag{2.25}$$

with the spectral function ρ being positive semi-definite. The Fourier-transformation of this gives

$$G(t,\vec{p}^{\,2}) \;=\; \int_{\sqrt{p^2}}^\infty d\omega \, \rho\left(\omega^2-\vec{p}^{\,2}\right) \exp\left\{-\omega t\right\} \;, \text{ for } \omega = \sqrt{\vec{p}^{\,2}+m^2} \,. \tag{2.26}$$

For a non-negative spectral function ρ it is therefore necessary that the propagator is positive. A propagator with negative norm contributions has no Källén–Lehmann representation and, therefore, can not be interpreted as an asymptotic particle state.
Reflection positivity can be studied by the help of the Schwinger function $\Delta(t)$, given by

$$\Delta(t) = \frac{1}{\pi} \int_0^\infty dp_0 \, \cos\left\{t\, p_0\right\} G(p_0, \vec{p}=0) \,, \tag{2.27}$$

where $G(p_0,\vec{p})$ is the propagator of the field, which also signals the mass and width of a field. E.g. for a massive asymptotic field the Schwinger function would show an exponential decay. In contrast to this, the Schwinger function for an unstable particle would oscillate with a period that is related to its decay width. For the gluon none of these statements is fulfilled as the Schwinger function goes to zero at some point, however, above that point it does not oscillate as an unstable particle would. Further, the Schwinger function becomes negative above a certain scale. In addition, no exponential decay is seen. Therefore, the gluon is neither a stable nor an unstable particle, and consequently it has no Källén–Lehmann representation.

2.3.2. Yang–Mills Correlation Functions at Vanishing Temperature

In section 2.3.1 possible mechanisms for confinement, the Gribov–Zwanziger scenario and Kugo–Ojima scenario, are described. These scenarios can be tested by studying the infrared behaviour of Yang–Mills correlation functions in the infrared. To summarise, both scenarios require a ghost propagator that is more divergent than a simple pole and, in addition to that, an infrared finite value of the gluon propagator. Note that the ghost enhancement is limited from background Landau gauge [229]. In this section I shortly review results from different methods for the Yang–Mills propagators at vanishing temperature. The situation at non-vanishing temperature is detailed in chapter 4, where it serves as direct comparison for the results obtained in this thesis.

In contradistinction to the requirements from the confinement scenarios above, early continuum studies with truncations that were built on arguments from perturbation theory found an infrared divergent gluon propagator [230–232]. This situation was called infrared slavery. It appeared to be a reasonable scenario as a linearly rising potential between static quarks can be constructed via one-gluon exchange. However, this solution was already ruled out by early lattice results [233–236] where a finite gluon propagator was found. In the following, enormous effort has been invested to clarify the infrared behaviour of Yang–Mills propagators with various methods. In continuum approaches especially the frameworks of DSEs [237–268], the FRG [13, 14, 248, 249, 269–281], stochastic quantisation [207, 282–284] and the Gribov–Zwanziger approach [285–290] have provided information about the Yang–Mills system and its structure, which can directly be tested on the lattice [115, 291–332]. In addition to that, a wide range of approaches has been successfully applied to the system, like the mapping of ϕ^4 theory to the infrared sector of Yang–Mills theory [333–335], the epsilon expansion [336] or the massive extension of the Faddeev-Popov action [337, 338].

In most studies Landau gauge is chosen because it simplifies the treatment due to several reasons. Most importantly, all terms that emerge from the gauge condition term in the action do not contribute in Landau gauge, as $\xi \to 0$. This constrains the gauge boson propagator such that the only possible tensor structure is the purely transversal one, given by

$$\Pi^{\mathrm{T}}_{\mu\nu} = \delta_{\mu\nu} - \frac{p_\mu p_\nu}{p^2}\,, \tag{2.28}$$

as the longitudinal structure is proportional to the (inverse) gauge parameter. Therefore, the gluon can be described with only one (non-trivial) wave-function renormalisation Z_A that encodes all quantum effects. The ghost is even simpler, as it is a Lorentz scalar, i.e. it carries a trivial tensor structure. Consequently, the full two-point functions in Landau gauge can be parametrised as

$$\Gamma^{(2)}_{A,\mu\nu}(p) = Z_A(p)\, p^2\, \Pi^{\mathrm{T}}_{\mu\nu}(p)\,, \tag{2.29}$$

$$\Gamma^{(2)}_{c}(p) = Z_c(p)\, p^2\,, \tag{2.30}$$

where the identity in colour space δ^{ab} is suppressed, and the wave-function renormalisations, i.e. the Z's, are scalar functions that actually only depend on the squared momentum p^2. The dependence of the Z's on a non-vanishing field expectation value is neglected for the moment, although in general the wave-function renormalisations depend on it[17].
In order to get the full propagator G_A for the gluon and G_c for the ghost the two-point function must be inverted[18]. If there are other tensor structures in addition, in particular structures that mix longitudinal and transversal components, this is a non-trivial task in general. However, the inverse of the transversal projector $\Pi^{\mathrm{T}}_{\mu\nu}$ is the transversal projector itself and no further structures can emerge[19].
In addition to this simplification on the level of the two-point functions, the transversality of the gluon facilitates the study of all higher n-point functions as well. In section 3.2.4 it becomes clear that the functional equations for a purely transversal n-point function depend on purely transversal n-point functions only. Thus, it is sufficient to exclusively compute the transversal structures to cover the full dynamics of the system. In other words, any observable can be constructed from these transversal n-points functions[20].
Another nice feature of Landau gauge is that the ghost-gluon vertex stays (almost) bare in the infrared limit [241, 248, 249, 294, 339–343].

In the continuum the deep infrared of Yang–Mills theory shows two qualitatively different types of solutions, the so-called scaling solution and the decoupling solution. In order to discuss the features of these two solutions it is convenient to introduce exponents $\kappa_{A/c}$ to describe the qualitative infrared behaviour of the propagators. Considering only the

[17] Taking into account the dependence of the wave-function renormalisation on the field expectation can be useful in finding proper truncations in functional methods, see e.g. the BMW method in section 3.2.2.

[18] In the framework of DSEs the standard notation in the literature is chosen such that the propagators $G_{A/c}$ are proportional to a (scalar) dressing function Z for the gluon and G for the ghost. Thus,

$$G_{A,\mu\nu}(p) = \Pi^{\mathrm{T}}_{\mu\nu}(p)\frac{Z(p^2)}{p^2}\,, \tag{2.31}$$

$$G_c(p) = -\frac{G(p^2)}{p^2}\,, \tag{2.32}$$

where the trivial colour-tensor is omitted. In Landau gauge the relation of the dressing functions $D_{A/c}$ and the wave-function renormalisations $Z_{A/c}$ is straightforward as they are simply the inverse quantities of each other, viz.

$$Z_A = \frac{1}{Z}\,, \quad Z_c = \frac{1}{G}\,. \tag{2.33}$$

[19] This holds also in the presence of a regulator in the FRG if the regulator is chosen to be transversal as well, cf. section 3.2.4.

[20] Note that, although the dynamics can be described by purely transversal n-point functions, this does not imply that the longitudinal parts do not contribute at all, but rather they stay bare up to finite corrections. E.g. in perturbation theory the pressure the longitudinal mode gives half of the Stefan–Boltzmann pressure, which cancels one ghost-mode, cf. section 4.3. A similar cancellation of one ghost mode by the gauge mode happens in the Weiss potential, the perturbative limit of the Polyakov loop potential, see chapter 5.

Lorentz scalar parts in the propagators this is done according to

$$\lim_{p^2\to 0} G_A(p) \sim \frac{1}{(p^2)^{1+\kappa_A}}, \tag{2.34}$$

$$\lim_{p^2\to 0} G_c(p) \sim \frac{1}{(p^2)^{1+\kappa_c}}. \tag{2.35}$$

The $\kappa_{A/c}$ are the anomalous dimensions that account for the non-trivial scaling that emerges in addition to the canonical dimension, which is the 1 in the exponent of the denominator.
For the scaling solution it turned out that the behaviour of all n-point functions can be solved exactly in the infrared limit [248, 249, 254], even in dimensions $d \neq 4$. An arbitrary Green function scales according to

$$\lim_{p^2\to 0} \Gamma^{(m,n)}(p) \sim \left(p^2\right)^{(n-m)\kappa+(1-n)(d/2-2)} \tag{2.36}$$

where n is the number of external ghost-antighost pairs that enter the vertex and m is the number of external gluon legs. Note that the scaling eq. (2.36) is actually a function of only one infrared scaling exponent κ as the anomalous dimensions of the propagators are not independent of each other

$$\kappa = \kappa_c = -\frac{\kappa_A}{2} + \frac{d-4}{4}. \tag{2.37}$$

The requirements concerning the propagators in the infrared stemming from the Kugo–Ojima or Gribov–Zwanziger confinement scenarios are met if the exponent fulfills the relation

$$\frac{d-2}{4} \leq \kappa < \frac{d}{4}, \tag{2.38}$$

as in eq. (2.34) this corresponds to a vanishing wave-function renormalisation Z_c ($\Leftrightarrow$ divergent dressing function) for the ghost, which implies an additional enhancement.
In four dimensions this exponent was computed, the most precise results [241, 272, 273, 282] give a numerical value of $\kappa \approx 0.5953$. This is consistent with the bound which is obtained in an FRG study [229]. Eq. (2.36) is self-consistent, and in fact it is even the unique scaling solution for Green functions in the infrared [248, 249, 254].

The scaling solution is unique in the sense that it satisfies the scaling relation, eq. (2.36). In addition, another type of solution is found which shows a ghost propagator that diverges as $(p^2)^{-1}$ and a finite gluon[21]. In terms of anomalous dimensions this corresponds to $\kappa_c = 0\,, \kappa_A = -1$. Clearly, this configuration does not satisfy the scaling relation, eq. (2.37). In fact, the solution of propagators in the infrared is such that there is a whole family of solutions. A particular solution is determined by fixing one value which is the renormalisation condition for the ghost at vanishing momentum [276]. Iff this value is set to be

[21] Note that a finite gluon propagator can not be described as a "massive" propagator with a momentum-independent mass. This can be seen trivially via going to high momentum, where perturbation theory is applicable. Perturbatively a gluonic mass term would violate gauge-invariance.

zero, the scaling solution is obtained, however, for any larger value a decoupling solution is obtained.
The fact that there is a family of solutions suggests that the dominating effects in the scaling as well as decoupling solution come from the same contributions. It is one strength of continuum methods that the individual contributions of the diagrams/fields can be investigated separately. In the case of infrared Yang–Mills theory it turned out that closed ghost-loops are the prevailing effects. Therefore, the situation is referred to as ghost dominance. The effect of ghost dominance is seen in the ghost as well as the gluon-propagator in both types of solutions[22]. The feature of ghost dominance is important in later chapters for the construction of a proper truncation for higher n-point functions, see section 4.1.4. Interestingly enough, at least in four dimensions lattice results show the decoupling solution only, even on lattices large enough to exclude the possibility of lattice artefacts spoiling the qualitative behaviour. Therefore, it is yet unclear whether the scaling solution is a purely mathematical solution or a physically realised solution. For a discussion of the discrepancy between the lattice and continuum results see e.g. [344]. However, for physical observables the deep infrared sector should not drive the relevant physics[23], but the mid-momentum sector is the important region. For example, this has been shown explicitly for the Polyakov potential [11] and is supported by the results presented in chapter 5.

Results for the two-point correlators of Yang–Mills theory from different methods can be found in fig. (2.4)[24]. In fig. (2.4(a)) the gluon propagator is given, the corresponding dressing function Z defined in eq. (2.29) with $Z = 1/Z_A$ is given in fig. (2.4(b)). The ghost dressing function G, cf. eq. (2.29) with $G = 1/Z_c$, is shown in fig. (2.4(c)). The Schwinger functions of the two solutions are given in fig. (2.4(d)).

The classification of the different types of solutions does not seem very spectacular, and for physical observables it is irrelevant, even quantitatively. However, for the mechanism of colour confinement the implications of the difference in the qualitative behaviour are crucial. One important difference is that the scaling solution respects BRST symmetry. In contrast to this, decoupling solutions break BRST symmetry. As the Kugo–Ojima scenario relies on a well-defined BRST charge, i.e. the existence of BRST symmetry, only the scaling solution is consistent with this picture. Furthermore, as the Gribov–Zwanziger scenario does not allow for a trivial ghost propagator, this explanation fails as well.

The statements above refer to the mechanism for confinement of Yang–Mills theory, but not for the question whether confinement is realised or not. Naturally, both types are confining which can be seen in the Schwinger function of the solutions in fig. (2.4(d)).

[22] Actually, it were the contributions of the ghosts that were underestimated in the studies that yielded infrared slavery.
[23] This conjecture is supported by the fact that in loops the infrared is suppressed with a factor of at least p^2 coming from the integration measure of the loop integral, see appendix D.1.
[24] Figures are taken from [276] and printed with permission of Elsevier, license number 2924051409272.

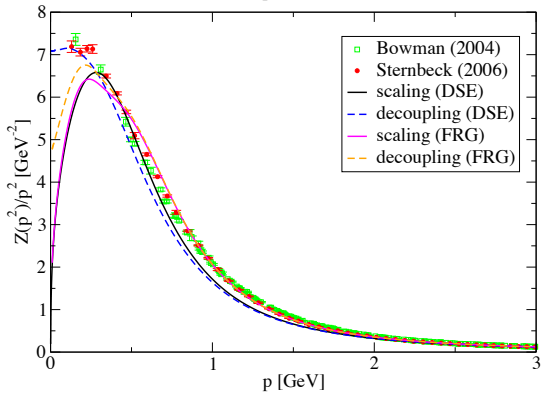

(a) Gluon propagator, $G_A = \frac{Z(p^2)}{p^2} = \frac{1}{Z_A(p)p^2}$.

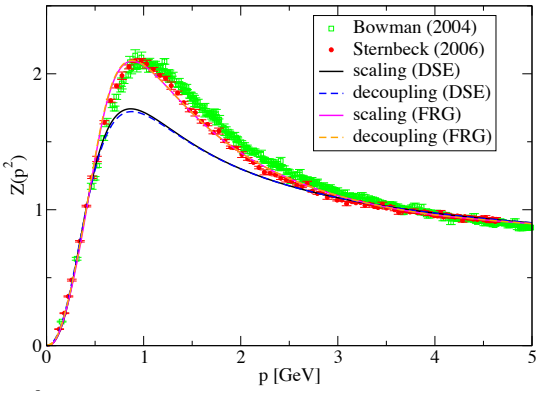

(b) Gluon dressing function, $Z = 1/Z_A$.

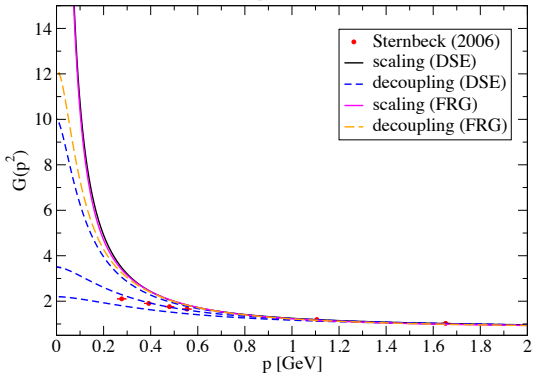

(c) Ghost dressing function, $G = 1/Z_c$.

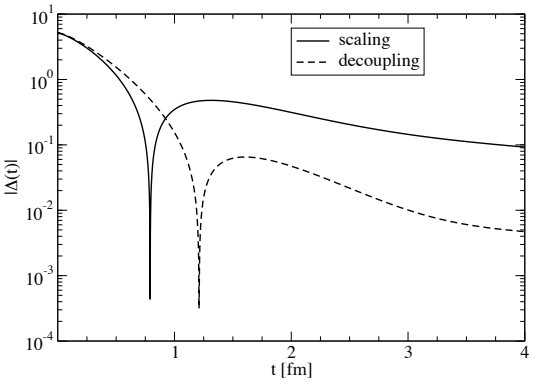

(d) Schwinger function of the scaling and decoupling solutions, cf. eq. (2.27).

Figure 2.4.: Results for the propagators in Yang–Mills theory [276] at vanishing temperature.

2.3.3. Thermodynamics of Yang–Mills Theory

For high temperatures perturbation theory is supposed to be applicable. This statement is based on the feature of asymptotic freedom of QCD, which persists also in the limit of Yang–Mills theory. Indeed, the coupling becomes weak and allows for a perturbative treatment, but only at very high temperatures, which are well above the deconfinement-confinement phase transition temperature. In a strict sense perturbation theory is applicable for $T = 10^4 - 10^5\ T_c$. In this region even the approximation by a free gas of quarks and gluons provides quantitatively good results. For small and intermediate temperatures ordinary perturbation theory becomes unreliable. This is due to the fact that the convergence radius is too small as to reach this domain, at least up to already high order in the coupling g^5. At this point I want to mention that, in contradistinction to this, there are results from weak coupling expansions for QCD up to order $g^6 \ln 1/g$ [345] that provide suprisingly good agreement with lattice data for significantly smaller temperatures down to $\approx 4\,T/\Lambda_{\overline{\text{MS}}}$.

But the fact that the naive perturbative treatment fails, does not rule out a perturbative treatment in general as perturbation theory can be refined. For reviews on perturbative investigations on thermodynamics in Yang–Mills theory and beyond see for example [346, 347]. There are several mathematical methods that allow to widen the region of convergence to much lower temperatures, e.g. Padé approximants [348–350], self-similar approximants [351] or Borel resummations [352, 353]. Also, other schemes have proven to be successful, not only in Yang–Mills theory but even in full QCD, especially hard thermal loop (HTL) resummations, where modes with momenta far above the temperature scale are resummed, but the soft contributions are fully taken into account. There are different ways of how to order these resummations, the most successful ones are either based on a Φ-derivable HTL resummation [354–357] or HTL perturbation theory [347, 358–362].
Continuum approaches based on (improved) perturbation theory do allow for a study of thermodynamic quantities in the full temperature range above $3\,T_c$, where they give accurate results in quantitative agreement with lattice data [44, 49]. Unfortunately, temperatures around $0 \leq T \lesssim 3\,T_c$ are out of reach also in these approaches, basically because perturbation theory can only yield logarithmic corrections to the pressure of a free gas, so the Stefan–Boltzmann limit. In contrast to this, lattice data shows that for low temperatures there is a qualitatively different behaviour which is rather a quadratic term in the temperature that dominates up to $\approx 3\,T_c$.

In order to study physics around the deconfinement-confinement phase transition non-perturbative methods are inevitable, of which in particular the FRG is suited as it gives an expression for the free energy[25] directly, eq. (3.15). From the free energy all other thermodynamic quantities can be computed. The free energy of Yang–Mills theory has already been studied within the FRG [11, 363], and it is one of the major topics in this thesis as well. From the free energy the pressure, energy density and trace anomaly can be computed. For first results which are in good agreement with lattice data at temperatures very close to the deconfinement-confinement phase transition temperature see [363].
In this work the FRG approach is applied to compute thermodynamic observables, see section 4.3. The results for the pressure agree qualitatively with lattice data, but furthermore, even quantitative agreement up to $\approx 12\%$ for the investigated region $0 < T < 4\,T_c$.

In conclusion, perturbative methods fail at describing the system at the deconfinement-confinement phase transition but non-perturbative functional approaches are applicable and very promising in this region. However, the study of thermodynamics in Yang–Mills theory is very intricate within these methods, so the results need to be cross-checked with other theoretical methods as no experiments can be conducted in the limit of pure gauge theory. Fortunately, for pure Yang–Mills theory lattice gauge theory is applicable for all temperatures because it does not suffer from problems emerging from the matter sector. For reviews on lattice gauge theory, see e.g. [20, 57–60]. Thus, the lattice is actually the

[25] Basically, what is called effective action in a field theoretical description is the free energy.

method that provides the quantitatively most accurate insight into this region of Yang–Mills theory, and in principle the thermodynamics are well understood [44, 49], even as a function of N_c [364–366]. Actually, for $N_c \to \infty$ analytical solutions can be found again [367]. This limit is an important ingredient for employing the AdS/CFT conjecture [368], for a review see e.g. [369]. However, if one wants to address not only Yang–Mills theory but proceeds the study with full QCD, the lattice suffers from two severe problems. Firstly, adding (dynamical) quarks is a hard task in general, and secondly, the sign problem hinders computations at finite quark chemical potential at least in the region where $\mu/T \gtrsim 1$, see also section 2.1.2. Therefore, it is desirable to have an alternative description of the physics in terms of a continuum functional method that allows for arbitrary values of the temperature and quark chemical potential in order to fully study the phase diagram. By comparison of different methods the potential weaknesses of each approach can be tested, e.g. finite volume or finite size artefacts on the lattice, or truncation insufficiencies in the continuum. It is an appealing situation that functional continuum methods and the lattice are complementary in the sense that the pure gauge part of QCD is comparatively easy on the lattice but the hard part in the continuum, and in turn the matter sector is the easier part of QCD in the continuum whereas it is hard on the lattice.

3. Non-Perturbative Functional Methods

Perturbation theory is an expansion around small amplitudes[1]. Thus, at the latest where the coupling becomes of order 1 perturbative computations become unreliable. As a consequence, for a description of the full momentum range of QCD within a unique setting one has to apply non-perturbative methods[2]. After a short comment on the formulation of thermal field theory in this chapter I describe two formalisms, the functional renormalisation group (FRG) as well as Dyson-Schwinger equations (DSEs), that are able to treat strongly coupled systems. Both methods are directly derived from the functional integral of the quantum field theory. Thus, they are exact methods, and capable to study non-perturbative physics. Another exact non-perturbative method are nPI effective actions, however, they are not the main approach in this work. Due to this I delay the discussion to section 5.1.3, in which they are utilised.
The focus is on the FRG as most of the results that are presented in this thesis have been derived within this framework. However, I sketch the derivation of DSEs as well as highlight the aspects that are relevant for the thesis. In fact, both methods are related to each other, however, dependent on the system that is studied one or the other may be more suited to tackle the problem at hand. Therefore, I conclude this chapter with a direct comparison of both methods, their relationship to each other and their merits.

3.1. Thermal Quantum Field Theory

In a relativistic field theory, due to particle–anti-particle creation and annihilation processes, particle number is not conserved. Further, energy can be exchanged with a heat reservoir. Therefore, the appropriate statistical ensemble for this physical situation is the grand canonical partition function. The temperature T, the volume V and the chemical potential μ are conserved, which determine the mean values for the energy and conserved charges, i.e. the mean number of particles. These constraints are satisfied by the help of Lagrangian multipliers, i.e. $\beta = 1/(k_B T)$ and μ_i are added to the Hamiltonian in the exponent of density matrix, one μ_i for each conserved number operator N_i. In the following, natural units are introduced, thus, $k_B = 1$. By the help of the density matrix ρ the

[1] Often perturbation theory is said to be applicable for weak interactions. In general this is not true as quantum effects can render the effective couplings strong.

[2] In principle a strong coupling itself is not an inevitable problem for perturbation theory as in such cases resummation techniques may be successful. In QCD, however, confinement requires the generation of a physical mass-scale Λ at low energies. The Λ-dependence is not included in a perturbative expansion. Thus, such a series or a resummation thereof is not capable of describing QCD in the infrared.

ensemble averages $\langle \mathscr{O} \rangle$ for arbitrary observables $\mathscr{O}$ can be computed according to

$$\rho = \exp\left\{-\beta\left(H - \mu_i N_i\right)\right\}, \quad \langle \mathscr{O} \rangle = \frac{\mathrm{Tr}\left\{\rho \mathscr{O}\right\}}{\mathrm{Tr}\left\{\rho\right\}}. \tag{3.1}$$

From this the partition function Z is constructed via

$$Z = \mathrm{Tr}\left\{\rho\right\}. \tag{3.2}$$

The partition function comprises the entire information of the physical system, i.e. all physical observables can be calculated from it, e.g. in the thermodynamic infinite volume limit the (thermodynamic) pressure P, entropy S, charge densities N_i and energy $\mathcal{E}$

$$\begin{aligned} P &= T\frac{\partial \ln\left\{Z\right\}}{\partial V} = \frac{T}{V}\ln\left\{Z\right\}, \\ S &= \frac{\partial\left(T\ln\left\{Z\right\}\right)}{\partial T} = \frac{\partial P}{\partial T}, \\ N_i &= T\frac{\partial \ln\left\{Z\right\}}{\partial \mu_i} = \frac{\partial P}{\partial \mu_i}, \\ \mathcal{E} &= \frac{\langle H \rangle}{V} = -\frac{1}{V}\frac{\partial \ln\left\{Z\right\}}{\partial \beta}. \end{aligned} \tag{3.3}$$

The trace in the partition function is equivalent to a sum over all states in Fock space, thus,

$$Z = \mathrm{Tr}\; e^{-\beta(\hat{H} - \mu_i \hat{N}_i)} = \sum_j \langle \phi_j | e^{-\beta(\hat{H} - \mu_i \hat{N}_i)} | \phi_j \rangle. \tag{3.4}$$

In order to make the connection of the statistical description with the quantum field theory the element $\langle \phi_j | e^{-\beta(\hat{H} - \mu_i \hat{N}_i)} | \phi_j \rangle$ is written as a transition amplitude, but, working in terms of an imaginary time[3] variable $t \to i\tau$. This is why this formalism is also called imaginary time formalism or also Matsubara formalism. Note that this is effectively an analytical continuation to the Euclidean metric, however with a finite time interval. The temperature only enters via the interval range.

For statistical purposes in equilibrium the system returns to its initial state after a certain time. This should be reflected by the description in terms of the path integral. Thus, the integration in the time direction is not from negative infinity to infinity any more but rather over a finite interval. This suffices to describe the system within this time. Fur-

[3] There is also another formulation of a field theory at non-zero temperature which does not introduce an imaginary time. In analogy this method is called the real-time approach. Actually, in systems that are not in equilibrium this formalism is to be chosen as the Matsubara formalism is not applicable. This is due to the fact that one needs to specify the initial state at time t_0 by its density matrix $\rho_{\mathrm{non-eq}}(t_0)$. Then, one is interested in the (real-)time evolution of the system. But, this initial state is generally not in equilibrium, i.e. the identification of the transition amplitude with the time-evolution does not hold as $\rho_{\mathrm{non-eq}}(t_0) \neq \exp\left\{\beta H\right\}$. This invalidates the Matsubara formalism for out-of-equilibrium physics. Note that this also refers to the standard lattice formulations for the functional integral, as in Minkowksi space the probability interpretation is lost. Nevertheless, the lattice is still possible to simulate these systems, however within other formulations, e.g. with stochastic quantisation [54–56].

ther, one demands (anti-)periodic boundary conditions for the (fermionic) bosonic fields as the system can evolve at earlier or later times as well. However, the behaviour of the system at these times can be described equivalently to this one time interval, again due to the fact that the equilibrated system returns to the same state after some time. Thus, the system is determined via the integration over the time region $[0, \beta]$ with the proper boundary conditions. This has changed the space on which the fields live. At vanishing temperature the space is infinite in time direction as well as in spatial direction, thus, the space is an $\mathbb{R}^4$. At non-zero temperature the time direction is compactified, i.e. the space is $[-\frac{1}{T}, \frac{1}{T}] \times \mathbb{R}^3$ (after symmetrisation), so it has the topology of $S^1 \times \mathbb{R}^3$.

The fields can be expanded in a Fourier series. Therefore, the spectrum of the 0-component is not continuous anymore but it has become discrete, which is naturally just the generical property for particles in a finite volume. By this analogy it is clear that the number of possible modes is infinite. The discrete modes are called Matsubara modes. Thus, e.g. a bosonic field $\phi(\tau, \vec{x})$ can be Fourier expanded and Fourier transformed as

$$\phi(\tau, \vec{x}) \sim \sum_{n=-\infty}^{\infty} \int d\vec{p}\; e^{i(\vec{p}\vec{x}+\omega_n \tau)} \phi_n(\vec{p}) \,, \tag{3.5}$$

where the normalisation is omitted. The $p_0 = \omega_n$ are the Matsubara modes, and the $\phi_n(\vec{p})$ are the different modes of the field, which are labelled by n. The field continuously depends on spatial momentum as the volume is supposed to be infinite.
The integration over spacetime is affected by this discrete spectrum: The integration over infinite Euclidean space $\mathbb{R}^4$ turns into an integral over the infinite spatial subspace and a sum over the Matsubara modes, thus, for an arbitrary function f the integral over spacetime is performed by

$$\int \frac{d^4p}{(2\pi)^4}\; f(p) \quad \xrightarrow{T\neq 0} \quad T \sum_{n=-\infty}^{\infty} \int \frac{d^3p}{(2\pi)^3}\; f\left(\omega_n, \vec{p}\right) . \tag{3.6}$$

The length of the time interval is $\beta = 1/T$, thus, the bosonic modes are given by $\omega_n^{(b)} = 2\pi T n$, with $n \in \mathbb{Z}$. For fermions, due to the anti-periodic boundary conditions, the modes are spanned by $\omega_n^{(f)} = 2\pi T(n + \frac{1}{2})$. Note that although the ghost is a Grassmann particle it has bosonic statistics[4]. Therefore, both types of fields in Yang–Mills theory have bosonic statistics, i.e. gluons and ghosts have periodic boundary conditions. Naturally, the quarks are anti-periodic as they are fermions. For the loop integrations and summations in this thesis I use the abbreviations

$$\int_p = \int \frac{d^4p}{(2\pi)^4} \,, \quad \text{and} \quad \sum\!\!\!\!\!\!\int_p = T \sum_{n\in\mathbb{Z}} \int \frac{d^3p}{(2\pi)^3} \,, \tag{3.7}$$

with $p_0 = 2\pi T n$.

[4]The Faddeev–Popov ghost is a Grassmann particle with spin zero, i.e. it has the wrong statistics. But, this does not contradict to the spin-statistics theorem [370] as this theorem holds for physical particles only, whereas the ghost is an auxiliary field that is introduced only for mathematical convenience.

The finiteness of the interval shows that temperature is an infrared phenomenon, where "infrared" does not refer to Λ_{QCD}, but the temperature. Modes with momenta much larger than the temperature do not feel the change of the boundary conditions, therefore, they behave as in the zero-temperature case. If the momentum of the mode is low, i.e. of the order of the interval length, temperature effects grow in size.

Interestingly, in the limit of $T \to \infty$ only the zero mode can contribute, because higher Matsubara modes are suppressed in the functional integral. As a result, the originally four-dimensional system becomes an effectively three-dimensional one. Thus, this transition is also called "dimensional reduction".

In the work presented later the notion of the rest frame of the heat bath is introduced, which relates to Lorentz invariance. The rest frame of the heat bath singles out a preferred frame that breaks Lorentz symmetry manifestly. However, full Lorentz symmetry is not really broken but obscured. To see it explicitly one can introduce a vector that points in the direction of the heat bath, and define the path integration to be constrained to the hypersurface that is orthogonal to this vector. In this formulation Lorentz symmetry is seen directly. For practical computations this formulation is usually not utilised, because the construction of the path integral is complicated. Instead of that most calculations are done in the rest frame of the heat bath. This is justified by the knowledge that, in principle, the explicit restoration of Lorentz invariance can be done at any time. Later this manifest breaking of gauge-invariance has an effect on the parametrisation of the gluon, which needs to be done differently at vanishing and non-vanishing temperature, as explained in section 4.1.1.

In the rest of this thesis the formulation is done in this Matsubara formalism and in the rest frame of the heat bath. Further, I refer to the imaginary time τ simply as t.

3.2. The Functional Renormalisation Group

In this section 3.2 I give a short introduction into the powerful tool of functional flow equations. I sketch the properties of the flow equation in section 3.2.2 and further I give details on the flow equation in gauge-theories in section 3.2.4. Flow equations can be derived algorithmically, which is described in detail in section 3.2.3. In section 3.2.5 I describe field reparametrisations in such a way that (part of) the dependence on the renormalisation group scale is put directly into the fields. This is crucial in the investigations of the thermal aspects of Yang–Mills theory in chapter 4.

3.2.1. The Idea behind the Renormalisation Group

The exact treatment of a real physical system is usually not possible. Thus, the general strategy is to simplify the system such that solutions for this model system are possible. But, it is crucial not to neglect relevant aspects of the system, which typically can only be satisfied if profound knowledge about the system is given. This is often the case if the system contains just a small number of degrees of freedom and a short correlation length. Needless to say there are other cases. At critical phase transitions the correlation length diverges. In quantum field theory the number of degrees of freedom is infinite, even in finite systems. Both are typical cases for which the functional renormalisation group offers a framework to describe the system. The idea is to look at the system at various scales, reducing the degrees of freedom such, that only the relevant aspects persist.

There are two important steps in the reasoning of the FRG: It builds on a coarse-graining procedure which is followed by a rescaling of the system afterwards. Suppose there is a system with many degrees of freedom, but a finite interaction length, even though the correlation length may be large. First, the coarse-graining divides the system in many subsystems of approximately the size of the interaction length. Then, one averages over the elements in the subsystem and beholds the averaged system only. This averaging reduces the number of degrees of freedom of the full system[5]. However, these subsystems interact with each other, but as the averaged regions are larger than the elements over which has been averaged within this particular region the interaction length has increased, or in other words, the scale was changed artificially by the averaging procedure. The second step in the FRG is to undo this change, thus, to *re*scale the interaction length to its original value measured in terms of the size of the single interacting parts. This twofold transformation tells how the system has changed under a change of scale in the sense that one learns which mechanisms are still there, whereas others become more irrelevant if the system is looked at a different scale. Thus, by iteration of renormalisation group transformations one can learn about the basic interactions and structures of the system at hand, namely those that persist and those that have extincted in the iteration.
Scale-invariance means that the long-range fluctuations can be treated similarly to the ones in the bare action, so the description of the system is similar after an arbitrary amount of renormalisation group transformations[6]. This is also referred to as a fixed point, as the theory does not change under further renormalisation group transformations. It has far-reaching meanings. Firsty, for critical phenomena, as there is no scale to which the cor-

[5] In a quantum field theory the number of degrees of freedom is infinite. This seems to disqualify the idea for these systems. However, the interactions are local which allows for a infinitesimal coarse-graining. This is reasoned further in the context of the momentum shell-integration.

[6] Note that the system does not necessarily look similar in a literal sense. E.g. for a ferromagnet at the phase transition the net magnetisation vanishes. However, it is still possible to find a region whose magnetisation is non-zero, say positive, thus, more constituents would be positive than negative. But, this would hold on all scales, i.e. each region itself consists of smaller regions with positive magnetisation. Thus, the non-zero magnetisation would persist either averaging and going to larger scales, but also by looking at smaller scales. This would signal the system not being at the phase transition. Thus, the trivial interpretation of scale-invariance that the system looks similarly at all scales is not correct in a strict sense.

relation length can be compared, correlation lengths up to infinite range can be included. Secondly, and maybe even more importantly for the content of this thesis, scale-invariance is closely related to renormalisability of a theory. Again due to the fact that there is no scale a cutoff of modes in momentum space is not fixed to a scale, thus, it can be sent to infinity. But this implies that the theory is (trivially) renormalisable. Furthermore, even for scale-dependent theories, as it is encountered in this work, one can impose renormalisation if the ultraviolet behaviour is determined by a fixed point.

This idea can be translated in a field theoretical language. The classical action encodes the full information of a classical theory, i.e. in our case a relativistic field theory without quantum fluctuations. In a quantum theory the effective action[7] is the analoguous quantity to the classical action, i.e. it contains all details of the quantum theory. The FRG does the following: One starts with a (renormalised) theory about which one has full knowledge at a certain microscopic scale Λ. In fact, one can either start with the classical action directly or with an action computed by resummation techniques or perturbation theory, the important point is that the starting action describes the system well at the energy scale Λ. But in contrast to other methods, e.g. DSEs, one does not integrate out all quantum fluctuations at once, but following the idea of Wilson [371–373] in a step by step procedure. This corresponds to the coarse-graining of a theory with local interactions. At the initial scale Λ only quantum fluctuations of a momentum scale around the initial scale are considered, so from the region $\Lambda - \Delta k$. These contributions are finite as all quantum fluctuations below that scale are suppressed. After integration of the action in the presence of the quantum effects one knows the effective action at the lower scale $\Lambda - \Delta k$. This step corresponds to an renormalisation group transformation. Integrating quantum fluctuations sequencially and infinitesimally until all fluctuations are included in the effective action, i.e. integrating down to the scale $k = 0$, one ends up with the effective action of the full theory, involving all quantum effects[8].
In the following sections I introduce the flow equation in more detail, especially for gauge theories. Further, I sketch the idea of constructing thermal flows.

3.2.2. Flow Equations

In this section 3.2.2 I highlight those aspects of flow equations that are of importance in the work presented here. For reviews on the functional renormalisation group see e.g. [277–279, 374–391].

The aim in a theoretical description of a quantum field theory is to get the hands on the

[7] The effective action generates 1-particle irreducible Green functions. Although other formulations are possible, see e.g. [278], I only discuss the functional flow equation for the scale-dependent effective action, as this framework is applied later in this thesis.

[8] Generally, the flow equation covers all fluctuations, not only quantum fluctuations. Actually, the effect of thermal fluctuations is a major topic in this thesis. Thus, I delay a discussion of thermal effects to a separate section 3.2.6 in order not to confuse the special aspects of thermal fluctuations with the general features of the flow equation, that are to be presented in this chapter.

effective action Γ_k, as it comprises the entire information of the quantum theory at a scale k. In the high energy limit, where all quantum effects are suppressed, the scale-dependent effective action approaches the classical action $S[\varphi]$, where φ is a field multiplet that contains the the fields of the theory.

On the other side, the scale-dependent effective action turns into the full quantum effective action if one sends the infrared cutoff parameter k to zero, so

$$\Gamma_k[\varphi] \overset{k\to\Lambda}{\to} S[\varphi],\ \Gamma_k[\varphi] \overset{k\to 0}{\to} \Gamma[\varphi]. \tag{3.8}$$

The suppression of infrared fluctuations is implemented via the cutoff function, which is hard to do consistently on the level on the Greens functions. Instead, the better choice is to directly modify the generating functional. Here, a regulator term is added to the action which suppresses low momentum modes

$$e^{W_k[J]} := e^{-\Delta S_k\left[\frac{\delta}{\delta J}\right]} Z[J] \ = \ \int_\Lambda \mathcal{D}\varphi e^{-S[\varphi]+\Delta S_k[\varphi]+J\cdot\varphi}. \tag{3.9}$$

General fields φ and sources J carry indices. The coupling to the external sources must enter the exponential as a scalar quantity. As the possible tensorial structures are not relevant for the discussion here, neither for the fields and their sources, nor for the regulation procedure, I omit them by using the condensed notation: The dot-product in eq. (3.9) indicates dummy summation of all types of indices as well as integration over spacetime or momentum, respectively, when Fourier transformation in momentum space has been done.

The generating functional for connected n-point functions $W_k[J]$ eq. (3.9) is also called Schwinger functional[9]. These quantities are renormalised, i.e. finite quantities, due to the regulator insertion. This renormalisation is k-dependent, because the regulator is k-dependent. Here, also the regulator ΔS_k receives regularisation. For reasons of convenience in practical computations that are detailed below, the regulator term that is used here is defined to be quadratic in the fields, although in principle higher orders would be possible. Due to its quadratic structure it acts like a mass-term $\sim k^2$ for the propagator. This effectively cuts off contributions from fluctuations below that artificial mass scale. The regulator quadratic in the fields looks like

$$\Delta S_k[\varphi] = \frac{1}{2}\,\varphi\cdot R_k\cdot\varphi. \tag{3.10}$$

The fields may carry indices. In this case the regulator R_k for the specific field type must have a non-trivial tensor structure as the action as well as its modification is a scalar quantity.

The requirements that the theory has the limits of the classical and the full quantum effective action for very high and low momenta, respectively, and that the infrared fluctuations are suppressed directly translate into constraints for the scalar part of the regulator

[9] Functional flow equations can be derived not only for the effective action, but also for the Schwinger functional, see e.g. [278].

function R_k. Neglecting possible tensor structures it must respect the relations

$$\begin{aligned}
\lim_{\frac{p^2}{k^2}\to 0} R_k(p) &> 0 \text{ (infrared finiteness of propagator)} \\
\lim_{\frac{k^2}{p^2}\to 0} R_k(p) &= 0 \text{ (full quant. theory at } k = 0) \\
\lim_{k^2\to\Lambda\to\infty} R_k(p) &\to \infty \text{ (reduction to classical action).}
\end{aligned}$$

Apart from that the form of the regulator is free to choose[10].
Actually, the form of the regulator guarantees the regularisation of both momentum limits. In the infrared the regulation is due to the mass-like term whereas in the ultraviolet the vanishing of the scale derivative $\partial_t R_k$ for $\frac{p^2}{k^2} \gg 1$ ensures the finiteness of the contributions coming from this region. The scale derivative $\partial_t R_k$ is peaked around $p \approx k$. Thus, the integral is dominated by the values around k, i.e. it is local in momentum space. This shows the Wilsonian idea of integrating over small momentum shells. The finiteness facilitates numerical computations as no divergencies appear and no further (numerical) renormalisation must be done.

Taking a regulator function like eq. (3.11) for scalar theories is trivially possible. In gauge theories the introduction of a regulator term is a little bit more subtle as a mass-term for the gluon breaks gauge invariance manifestly. This problem can be circumvented in different ways: either by keeping track of the breaking of gauge invariance via so-called modified Ward–Takahashi- and Slavnov–Taylor-identities or by a construction of gauge-invariant flow itself. I explain the issue of gauge-invariance in more detail in section 3.2.4.

Conveniently, the regulator function is written in terms of a dimensionless shape function $r(p^2/k^2)$ and the tensor and momentum structure of the particle that shall be regulated, so usually p^2 for a real boson or $\not{p}$ for a fermion. For more complex systems the regulator R may carry other indices. E.g., for the gauge boson in Yang–Mills theory the regulator carries Lorentz and Colour indices. These generalisations are straightforward, thus, here it is sufficient and most illustrative to consider a real scalar particle only. In this case

$$R_k(p) = p^2 \; r(p^2/k^2). \tag{3.11}$$

[10] Albeit the shape of the regulator can be chosen freely as long as the constraints given in eq. (3.11) are satisfied, some forms may be unsuited for practical computations. As an example that is of particular importance in the following sections, the sharpness of the regulator in thermal computations can be in the primary focus. For thermal flows only the difference between the Matsubara sum and the 4-dimensional integral of the temporal component is relevant. Although the direct thermal effects are limited to low scales $k \lesssim 2\pi T$, for regulators that fall off very fast the difference oscillates also in a momentum region far above this scale. In fact, the steeper the regulator the wider is the region in which these oscillations are of quantitative importance. Thus, in the limit of a sharp regulator the initial scale for the start of the flow would have to be $\Lambda \to \infty$. In a numerical treatment this choice can not be implemented. Therefore, the choice of an infinitely steep regulator may be inappropriate, although it satisfies the limits in eq. (3.11) and is therefore theoretically correct.

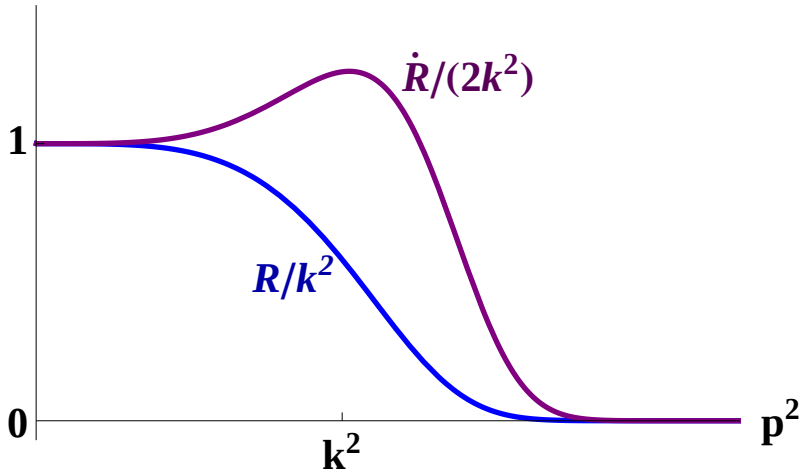

Figure 3.1.: Plot of a typical regulator $R_k(p)$, and the scale derivative $\dot{R}_k(p) \equiv k\partial_k R_k(p)$. For low momenta the regulator acts like a mass-term $\sim k^2$. Thus, it suppresses contributions from fluctuations with momentum $p^2 \lesssim k^2$.

Typical regulators that are applied in this work are the exponential regulator

$$r^m(x) = \frac{x^{m-1}}{e^{x^m} - 1}, \tag{3.12}$$

and the optimised regulator [392]

$$r^{\text{opt}}(x) = (k^2 - p^2)\Theta\left(k^2 - p^2\right), \tag{3.13}$$

the shapes of these choices are plotted in fig. (3.2). So, an infrared-divergent massless bosonic propagator is rendered infrared-finite via the regulator

$$G(p) = \frac{1}{p^2} \quad \rightarrow \quad G_k(p) = \frac{1}{p^2\,(1 + r\,(p^2/k^2))}. \tag{3.14}$$

In fig. (3.1) the shape of the exponential regulator $R_k^m(p)$ and the dimensionless derivative $\dot{R}_k^m(p) = k\,\partial_k\,R_k^m(p)$ is given. The latter is a direct ingredient of the flow equation as well.

The different choices of the regulator are given in fig. (3.2). The locality of the flow in momentum space is directly related to the steepness of the regulator. The faster the regulator falls off for momenta $p > k$ the more local turns the flow. As locality is a basic concept of the flow equation the regulator should in general not be smeared over a region too wide in p-range, as then the picture of momentum shells is not satisfied any more. In this case fluctuations from large scales, that are far above the scale k, can affect lower scales.

The effect on a bare massless propagator is sketched in fig. (3.3). For large momenta it appoaches the perturbative propagator whereas for small momenta it automatically re-

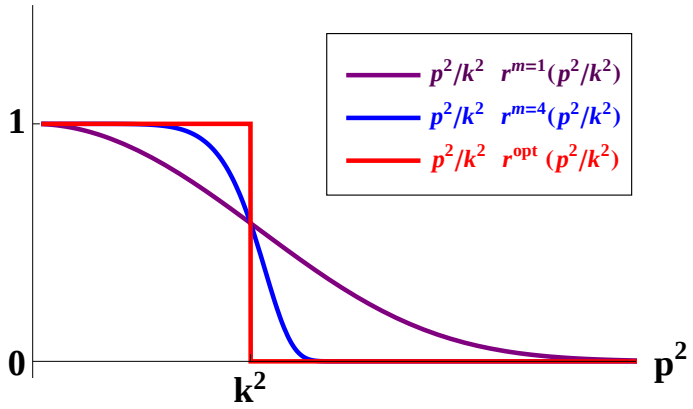

Figure 3.2.: Different choices for the regulator function $R_k(p)$. The purple and blue curves are exponential regulators of different steepness controlled by the power in the exponential, the red curve gives the optimised regulator shape function.

ceives an infrared regularisation, so it tends to a finite value. In this plot it is evident that

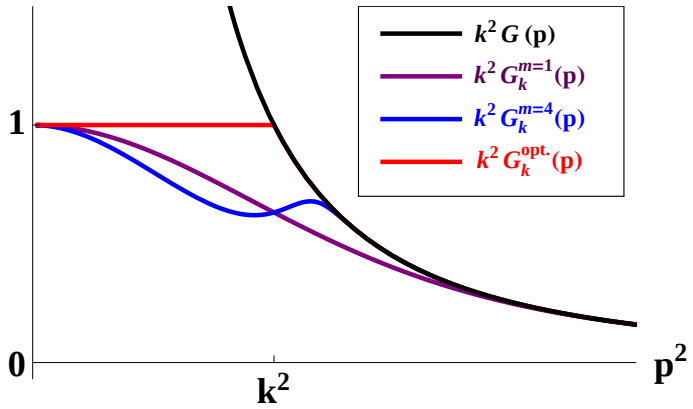

Figure 3.3.: The black curve shows the Feynman propagator of a massless boson, which diverges at $p \to 0$. The blue and purple curve shows the regulated propagator with an exponential shape function with the steepness factor $m = 1$ and $m = 4$, respectively, and the red curve is the regulator propagator with an optimised regulator. The regulator acts like a mass term in the infrared and suppresses fluctuations from this region.

different shape function treat the infrared behaviour differently at non-vanishing k. Thus, the flow itself is specific to the regulator, and hence regulator dependent. It is important to note that this ambiguity is only present for non-vanishing k, in the limit of $k \to 0$ both flows yield the full (unique) effective action. The concept of optimisation in the sense of minimising the flow by the choice of the regulator plays an important role in the practical applications.

The functional flow equation was first derived by Wetterich [393]. It is given by

$$\partial_t \Gamma_k[\varphi] \;=\; \frac{1}{2}\,\mathrm{STr}\left\{\left(\Gamma_k^{(2)}[\varphi] + R_k\right)^{-1} \partial_t R_k\right\}, \tag{3.15}$$

with the frequently used abbreviations $\partial_t \mathcal{O}_k \equiv \dot{\mathcal{O}}_k \equiv k\partial_k \mathcal{O}_k$. The supertrace STr comprises integration of the loop momentum as well as the summation over internal indices of the fields in the loop. Further, it assigns correct signs for Grassmann fields. How these signs emerge is sketched in section 3.2.3. The inverse of the second derivative of the modified action is referred to as the propagator.

The flow equation, eq. (3.15), is a differential equation for the scale-dependent effective action. By infinitesimal variation of the scale k it interpolates between the classical action and the quantum effective action. The idea of this can be visualised by the help of the theory space which is an infinitely dimensional space spanned by all possible orthogonal operators and couplings. Each point in theory space describes a different theory. The flow equation describes the transition of the classical action to the effective action as a trajectory/flow in theory space. Reminding of the discussion of different regulators, the trajectory in theory space is regulator-dependent, besides the limits $k \to \infty$ and $k \to 0$ are unambiguous[11]. An illustration is given in fig. (3.4), which shows that different trajectories end in the same quantum action. Later, especially in section 3.2.6, this picture is refined such that thermal effects are considered in addition to quantum fluctuations.
For illustration of the flow equation, eq. (3.15) can also be expressed diagrammatically. For the example of a real scalar field this more illustrative representation is given in fig. (3.5). The propagator is given by a solid line where the shaded-circle indicates that it is the full propagator. In the rest of the thesis the circles are dropped for clarity. All internal propagators are to be seen as full propagators. The scale-derivative of the regulator is illustrated by white circle with the cross. The closed loop involves integration and summation over internal momenta and indices.

I want to stress two important points. Firstly, no approximation has been made in the derivation of the functional flow equation. Thus, this equation is exact, although it is of one-loop structure[12], however with fully non-perturbative Green functions in the loop. Therefore, it is a proper tool to study non-perturbative physics[13]. Secondly, the one-loop structure contains full n-point functions. This is directly seen in the closed loop at the propagator, which is not the perturbative one but the full non-perturbative propagator. So the scale-dependent effective action depends on the two-point function.

It is a generic feature of the FRG that a flow equation for an n-point function depends

[11] Stricly speaking the point moves in theory space due to the regulator, but that does not alter the physics at this point.

[12] Note that this one-loop structure would be lost if regulator terms in orders in the field of higher than two were introduced.

[13] Although the FRG is a non-perturbative method, perturbation theory can be easily reproduced by doing an expansion in $\hbar$.

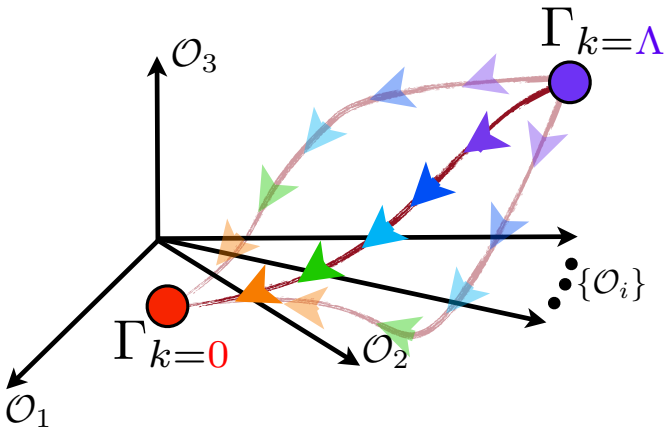

Figure 3.4.: The flow equation interpolates between the classical action at the renormalisation group scale Λ and the full quantum effective action at $k = 0$. The flow is a trajectory in the space of all possible theories which are spanned by orthogonal operators/couplings $\mathcal{O}_i$, and serve as expansion coefficients, e.g. $\mathcal{O}_1 = \Gamma^{(2)}(p = 0)$. For different implementations of the regulation procedure the flow varies at non-vanishing k, but the end-points of the flow are unambiguous. Furthermore, the trajectory depends on the chosen truncation, as may the quantum effective action. By choosing satisfying truncations the limit $k \to 0$ must be rendered independent of the truncation.

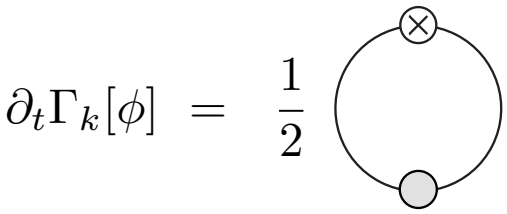

Figure 3.5.: Graphical representation for the flow equation of a real scalar particle given in eq. (3.15). The solid line with the shaded circle represents the full non-perturbative propagator of the scalar field. The crossed circle indicates the insertion of the scale derivative of the regulator $\partial_t R_k(p)$.

explicitly on higher n-point functions up to $n + 2$, which in turn can be derived from the Wetterich equation eq. (3.15) by taking functional derivatives with respect to the fields that are external to the particular n-point process. Note that herein all off-shell contributions must be taken into account in the course of the derivation. Only after the last functional derivative they can be dropped to get the physical contributions. However, the dependence on higher n-point functions holds at arbitrary order. So accordingly, the flow equation generates an infinite tower of coupled differtial equations. Thus, for most practical applications truncations are inevitable, which means that the set of contributing

n-point functions is rendered finite. Although eq. (3.15) is exact truncations of the flow equation only approximate the exact result. Thus, the approximation must respect important aspects of the physical system, e.g. symmetries or relevant operators. The main point is to find an approximation that covers the physics of the systems to a satisfactory extend, but further allows for the solution of the set of coupled flow equations on the technical level. Besides, consistency is a key issue of truncations which means that once one has chosen a specific order in the expansion one should keep all the terms of that order in the flow equation. Unfortunately, the quality of the approximation can not be estimated a priori but must be tested after the computation by comparison with other truncations as well as other methods.
Furthermore, the truncation may also rule out certain choices for the regulator. In any case, the approximation introduces a manifest dependence of the final result on the shape function, even at $k \to 0$. Consequently, at the end of the computation it is not only necessary to investigate the truncation itself but in combination with the dependence on the regulator[14].

The situation becomes clear by looking at the theory space fig. (3.4) again. The trajectory does not only depend on the regulator but furthermore on the truncation. Each choice of approximation excites a different flow. Also the effective action potentially moves. The task to find a satisfying truncation is to guarantee that the theory flows into the exact quantum effective action in the limit of vanishing renormalisation group scale.

There are various constructions for truncations. The method that is used predominantly in the work presented here is the vertex expansion of the effective action,

$$\Gamma_k[\varphi] \quad = \quad \sum_{n=0}^{\infty} \frac{1}{n!} \int d^d x_1 \dots d^d x_n \; \Gamma_k^{(n)}(x_1, \dots, x_n) \varphi(x_1) \dots \varphi(x_n),$$

that is inserted into the flow equation and allows for a solution of the system of equations for a closed subset of the $\Gamma_k^{(n)}$. Flow equations for $\Gamma_k^{(n)}$ can be obtained from the flow equation for the effective average action Γ_k by taking n function derivatives with respect to the fields φ. It is a systematic expansion. This means that by adding more terms in a systematic way, i.e. adding more vertices to the non-trivial part of the truncation, the result improves qualitatively and quantitatively.

A further systematic truncation scheme was designed by J. P. Blaizot, R. Méndez-Galain and N. Wschebor, commonly referred to as BMW method [394, 395]. Up to some truncation order n it keeps momentum dependence of the propagators and vertices. However, for higher n the momentum dependence is approximated by making use of generic features of the FRG. The momentum q of the fluctuations is bounded from above due to the regulator, which means that the relevant scale for $p > k$ is p, but not the generic term that carries $p + q$ in the momentum argument. So this dependence on the loop momentum is

[14] In the literature the regulation procedure is often considered to be part of the truncation. For clarity I do not make this fusion of these two aspects here.

neglected. In this case the higher n-point functions can be obtained by taking functional derivatives of lower n-point functions. Thus, the knowledge of the functions up to order n suffices to close the hierachy of flow equations, e.g. restricting to two-point functions, the three-(four-)point function is obtained by taking one (two) derivative(s) with respect to the field. Unfortunately, this powerful method is expensive when it comes to applications as the price to be paid for reliable approximations of higher n-point functions is the explicit field dependence, which has to be resolved in addition to the momentum-dependence. As a consequence, for complex systems like Yang–Mills theory of QCD this method is not feasible yet.

Another truncation scheme is the derivative expansion, as initiated by T. R. Morris [396]. Here, the focus is on resolving small momenta, i.e. long wavelengths.

The great power of the flow equation as a computational tool is due to two charateristics of the approach. Firstly, no further renormalisation must be done. Secondly, the flow equation eq. (3.15) has a stabilising form, which is in particular convenient for numerical computations. If the $\Gamma_k^{(2)}$ in the denominator is large the flow becomes small. In the other case, for potentially small values of $\Gamma_k^{(2)}$ at low momenta, the regulator part becomes dominant and guarantees a relatively small flow as well. Thus, numerically one has to deal with contributions that are finite in the first place due to the regulator form, but futhermore, they are even small. In the evolution of the differential equation moderate changes can be resolved with little numerical efforts, and in many applications standard differential equations solvers can be used.

3.2.3. Algorithmic Derivation of Flow Equations

As there is a strict algorithm for the derivation of functional flow equations it can be conveniently done by the help of a computer. The algorithmic derivation of the general form of functional equations has been put forward for DSEs as well as FRGEs in [397, 398], and recently even programs have been developed that directly solve functional equations [399, 400].

The derivation of functional flow equations of Yang–Mills theory is a tedious but not very illuminating task. For purely bosonic theories the derivation is simplified by the possibility of diagrammatic derivations, as it is known from DSEs, see e.g. [397]. While this is possible for fermionic theories, in principle, the derivation is very complex due to the anti-commutativity of fermionic fields and derivatives. Therefore, for the computations to be presented below, in the course of this work, on the basis of previous codes [269, 401], the program *fleq* was developed that derives the general form of flows of n-point functions in an arbitrary quantum field theory. For Yang–Mills theory the code was devised further in the way that the general expressions are replaced by the corresponding expressions in the chosen truncation, and contractions of colour and Lorentz indices are done automatically

by the help of *FeynCalc* [402], for both cases, zero and non-zero temperature. For more details on the numerics used here see section 4.1.6. Later the program was extended to QCD for non-zero temperatures and/or chemical potential.
In this thesis I only sketch the general approach to the algorithmic derivation of flow equations.

The generating equation for flow equations is the Wetterich equation eq. (3.15). It is a renormalisation group equation for the scale-dependent effective action $\Gamma_k[\varphi]$, which depends on the fields that are collected in the field multiplet φ, e.g. for Yang–Mills theory $\varphi = (A, \bar{c}, c)$. An arbitrary n-point function is defined by taking functional derivatives of the effective action Γ with respect to n fields in the field multiplet (φ_i), viz.

$$\Gamma^{(n)}_{k,\varphi_{i_1}\varphi_{i_2}\ldots\varphi_{i_n}} = \frac{\delta^n \Gamma_k}{\delta\varphi_{i_1}\delta\varphi_{i_2}\ldots\delta\varphi_{i_n}}, \tag{3.16}$$

where the index i is a multiindex containing not only the field type but also all indices of this field. Note that all derivatives act from the left to the right. The order of the derivatives acting on the effective action is important. Particles with fermionic statistics anti-commute and so do their derivatives, thus, for two fermions[15] ψ, $\bar{\psi}$

$$\Gamma^{(2)}_{k,\psi\bar{\psi}} = -\Gamma^{(2)}_{k,\bar{\psi}\psi}. \tag{3.17}$$

In the flow equation (3.15) the trace on the right hand side involves the inverse of the second derivative of the modified action as well as a scale derivative of the regulator function R. The latter one is obtained via taking derivatives of the term $\partial_t \Delta S_k[\varphi]$ with respect to the fields,

$$\partial_t R_{\varphi_i\varphi_j} = \frac{\partial_t \Delta S_k}{\delta\varphi_i \delta\varphi_j}. \tag{3.18}$$

For the inverse two-point function one has to be careful with the fermionic content. Firstly, recall that the Schwinger functional $W[J]$ is related to the effective action $\Gamma[\varphi]$ via a Legendre transformation. This holds also in the presence of the regulator term,

$$\Gamma_k[\varphi] = \sup_J \left(J \cdot \varphi - W_k[J]\right) - \Delta S_k[\varphi]\,. \tag{3.19}$$

The integration over spacetime is absorbed in the summation over dummy indices. Note that the indices are all subscripts as the field space metric used here is the unity matrix. From (3.19) one can derive the relation

$$\delta_{\varphi_a}\left(J \cdot \varphi\right) = \eta^{ab} J_b = \delta_{\varphi_a}\left(\Gamma + \Delta S\right)\,, \tag{3.20}$$

where the functional derivatives of an operator $\mathcal{O}$ with respect to a field φ_a or source J_a,

[15] In Euclidean spacetime there is no Dirac conjugation. Therefore, I want to stress that the $\bar{\psi}$ and the ψ are two distinct particles, so the degrees of freedom are effectively doubled compared to Minkowski space. This can be redone unambiguously, therefore, it does not pose fundamental problems.

respectively, are abbreviated by

$$\delta_{\varphi_a}\mathscr{O} = \frac{\delta}{\delta\varphi_a}\mathscr{O}\,, \quad \text{and} \quad \delta_{J_a}\mathscr{O} = \frac{\delta}{\delta J_a}\mathscr{O}\,. \tag{3.21}$$

Furthermore, the factor η_{ab} is introduced,

$$\eta_{ab} = \begin{cases} -1\,\delta_{ab} & \text{if } \varphi_a \text{ and } \varphi_b \text{ are Grassmann fields,} \\ 1\,\delta_{ab} & \text{else,} \end{cases} \tag{3.22}$$

i.e. (η_{ab}) is a diagonal matrix in field space with +1 in the bosonic subspace and −1 in the fermionic subspace. This definition allows to treat commutations of fermionic and bosonic quantities, respectively, in a unified manner. With $\varphi_a = \delta_{J_a} W$ the inverse of the two-point function can be identified from the relation

$$(\delta_{J_a}\delta_{J_c}W)\,(\delta_{\varphi_c}\delta_{\varphi_b}\Gamma) = (\delta_{J_a}\varphi_c)\,\eta_{db}\,(\delta_{\varphi_c}J_d) = \eta_{ab}\,. \tag{3.23}$$

The factor η_{ab} accounts for the correct minus sign in fermionic loops. Relating the propagator $G_{\varphi_a\varphi_b} \equiv \delta_{J_a}\delta_{J_c}W$ to the two-point function via

$$\eta_{ab}\,G_{\varphi_a\varphi_c}(\Gamma + \Delta S)_{\varphi_c\varphi_b} = 1 \tag{3.24}$$

shows that the inverse of the matrix $(\Gamma + \Delta S)_{\varphi_a\varphi_b}$ is not given by pure inversion of the Hessian matrix but obtains an additional minus sign for fermions. Therefore, the flow equation in the matrix notation is given by

$$\partial_t\Gamma_k = \frac{1}{2}\mathrm{Tr}\left\{\eta\cdot G\cdot(\partial_t R)\right\}\,, \tag{3.25}$$

which is equivalent to eq. (3.15) where the η was absorbed into the supertrace. In order to derive the flows of higher n-point functions from this equations one takes functional derivatives with respect to fields. The only two structures that emerge are $\delta_{\varphi_a}\Gamma^{(n)}_{k,\varphi_{i_1}\varphi_{i_2}\ldots\varphi_{i_n}}$ and $\delta_{\varphi_a}G_{\varphi_b\varphi_c}$, of which the first relation is implicitly given in eq. (3.16). By further use of $\delta_\varphi(G\cdot G^{-1}) = 0$ the latter quantity yields in matrix notation

$$\delta_\varphi G = -\,\eta\cdot G\cdot\eta\cdot\left(\delta_\varphi\Gamma^{(2)}\right)\cdot\eta\cdot G. \tag{3.26}$$

3.2.4. Flow Equations in Gauge Theories

In section 3.2.2 and section 3.2.3 I detailed the general derivation of flow equations. One major part of this thesis deals with Yang–Mills theory. Therefore, in this section I concretise the formalism of the preceeding sections to the pure gauge part of QCD. For reviews on the FRG in gauge theories see e.g. [277–279, 378, 403].
In continuum methods it is necessary to choose a gauge, see section 2.2. In this work Yang–

Mills theory in Landau gauge is investigated, which is not a ghost-free gauge. Therefore, the theory under investigation is an interacting theory of gluons and ghosts.

In the framework of the FRG the suppression of infrared fluctuations below the renormalisation group scale k is done by modifying the quadratic part of the action eq. (3.10). This regulation is done individually for each field, thus, the modification involves a term quadratic in the gluon fields and another one quadratic in the ghosts

$$\Delta S_k[A,\bar{c},c] = \frac{1}{2}\int_p A^a_\mu(-p)R^{ab}_{k,\mu\nu}(p)A^b_\nu(p) + \int_p \bar{c}^a(p)R^{ab}_k(p)c^b(p). \tag{3.27}$$

The regulator functions themselves have a non-trivial tensor structure. The proper derivation of the Wetterich equation, eq. (3.15), for Yang–Mills theory is straightforward. Noting that a negative sign in the ghost loop emerges due to the Grassmann nature of the ghosts the flow equation for the scale-dependent effective action in Yang–Mills theory is given by

$$\partial_t\Gamma_k[A,c,\bar{c}] \;=\; \frac{1}{2}\int_p \; G^{ab}_{\mu\nu}[A](p,p)\,\partial_t R^{ba}_{\nu\mu}(p) - \int_p \; G^{ab}[c,\bar{c}](p,p)\,\partial_t R^{ba}(p)\,, \tag{3.28}$$

where $t = \ln k$, $G^{ab}_{\mu\nu}[A](p,p)$ ($G^{ab}[c,\bar{c}](p,p)$) is the gluon (ghost) propagator. Again the flow equation can be illustrated in a diagrammatic manner[16] which is given in fig. (3.6).

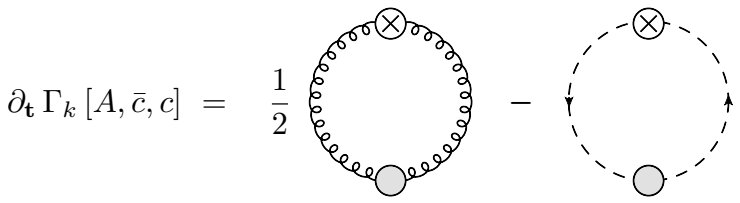

Figure 3.6.: Flow equation for Yang–Mills theory. The Γ_k is the scale-dependent effective action that depends on the field content of the theory, in Landau gauge Yang–Mills theory gluon and (anti-)ghosts. On the right hand side, the wiggly line with the shaded blob represents the full gluon propagator, the dashed line is the ghost. The crossed circle denotes the insertion of the scale-derivative of the regulator $\partial_t R$. The factor of 1/2 of the gluon loop is the natural factor that emerges in the flow equation for bosons. For Grassmann fields, however, there are two routings which yield the same contributions to the flows of arbitrary n-point functions. Therefore, this is combined in just one loop with the combinatorical factor 1. Furthermore, the sign of the loop of fermionic particles is negative. This holds for ghosts and later on also the quarks.

From eq. (3.28) arbitrary n-point functions of Yang–Mills theory can be derived by taking functional derivatives with respect to the attached fields. For the propagators this results in the equations to be given here in the diagrammatic way in fig. (3.7) and fig. (3.8), the corresponding equation for the ghost-gluon vertex is given in fig. (3.9) and for the trigluon

[16] All illustrations of functional equations in this thesis have been produced with *JaxoDraw* [404].

vertex in fig. (3.10). These diagrammatic expressions contain the full information in an unambiguous way. The explicit expressions are given in appendix A. In the graphical representations in this thesis the internal propagator are to be seen as full propagators, but I omit the blobs for clarity. The flow equations for Yang–Mills theory were generated with the algebraic program *fleq* to derive flow equations that is described in section 3.2.3 and compared with the alternative program *DoFun* [398] that derives arbitrary flow equations as well as DSEs.

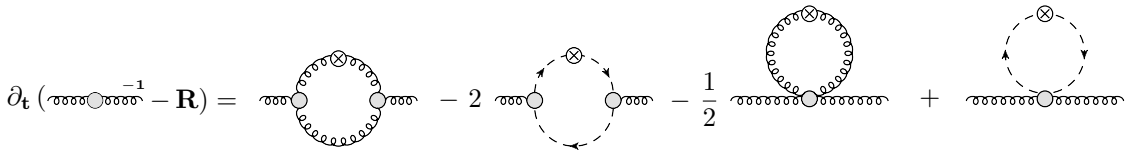

Figure 3.7.: Flow equation for the gluon propagator.

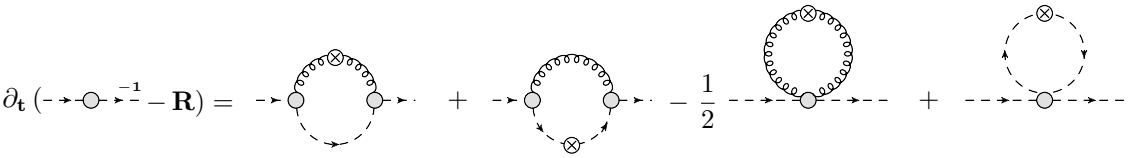

Figure 3.8.: Flow equation for the ghost propagator.

In section 2.3.2 I argued that the transversality of the gluon field in Landau gauge facilitates the investigation enormously. On the level of the functional equations this becomes clear: The propagators and vertices are purely transversal due to the transversality of the gauge field.

The purely transversal correlation functions vanish by contracting one of the Lorentz indices with its momentum, $(p_i)_{\mu_i}\Gamma^{(n)\,T}_{\mu_1\cdots\mu_i\cdots\mu_m} = 0$ for $i = 1, ..., m$. Note that in general $n \neq m$ due to the ghosts. Since the propagators are purely transversal in the Landau gauge the purely transversal correlation functions in the Landau gauge form a closed system of flow equations: The flow of a purely transversal correlation function only depends on purely transversal correlation functions and carry the whole dynamics. Any observables can be built up from the purely transversal correlation functions.

In turn the flow of correlation functions with at least one longitudinal direction, $\Gamma^{(n)\,L}$, depends on both, $\Gamma^{(n)\,T}$ and $\Gamma^{(n)\,L}$. Moreover, they also obey modified Slavnov–Taylor

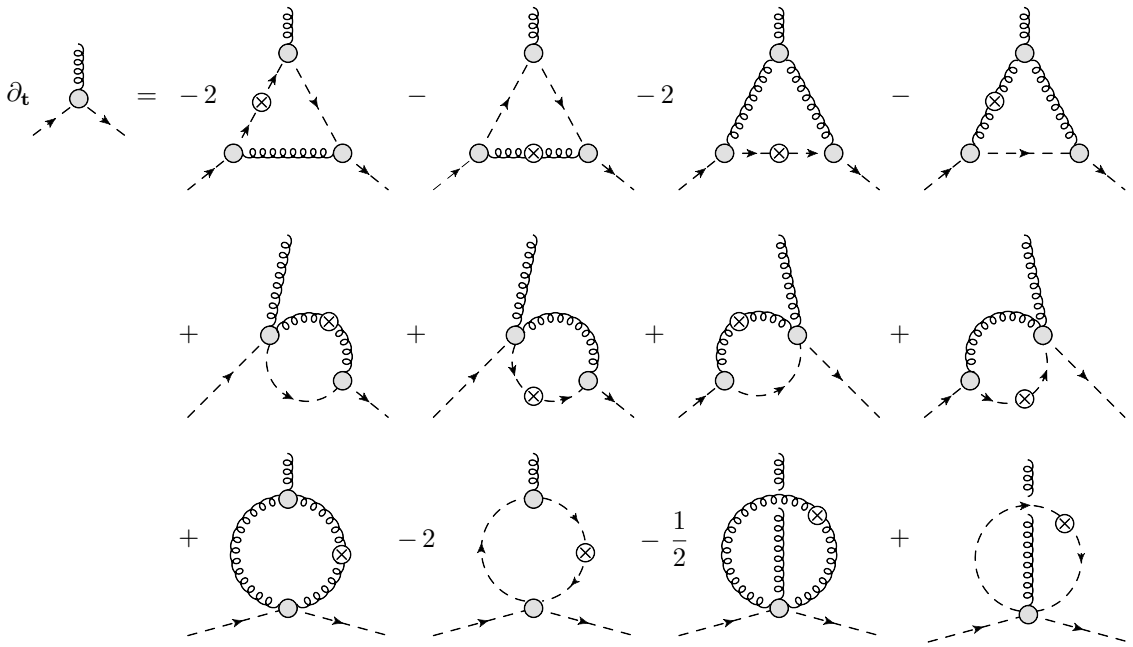

Figure 3.9.: Flow equation for the ghost-gluon vertex. Note that also the last two diagrams are of one-loop order, the break in the wiggly line denotes that there is no four-point interaction.

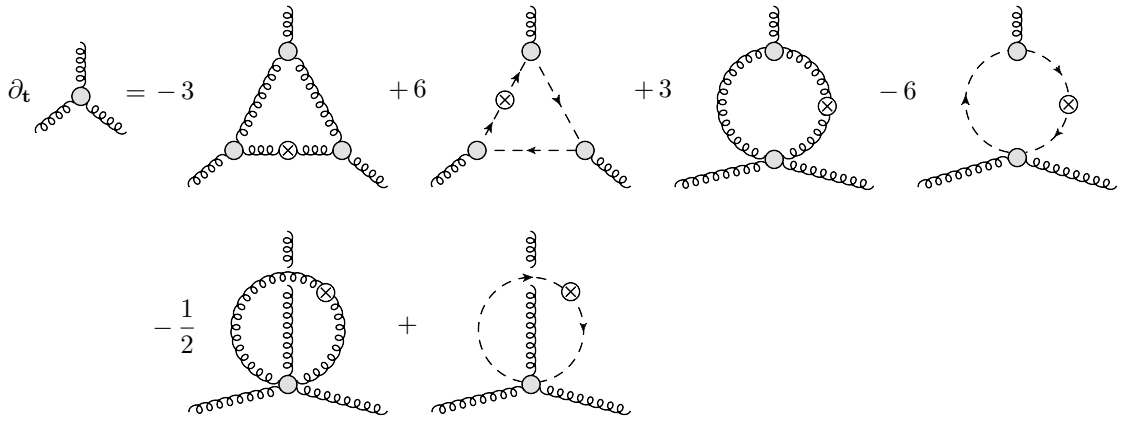

Figure 3.10.: Flow equation for the trigluon vertex. Note that also the last two diagrams are of one-loop order, the break in the wiggly line denotes that there is no four-point interaction.

identities, see [278, 279, 405, 406] and references therein. This situation is summarised in

$$\begin{aligned} \partial_t \Gamma^{(n)\,T} &= \mathrm{Flow}_n^T[\{\Gamma^{(m)\,T}\}]\,, \\ \partial_t \Gamma^{(n)\,L} &= \mathrm{Flow}_n^L[\{\Gamma^{(m)\,T}, \Gamma^{(m)\,L}\}]\,, \\ (p)_\mu \Gamma^{(n)\,L}_{\mu\mu_2\cdots\mu_m} &= \mathrm{mSTI}_n[\{\Gamma^{(m)\,T}, \Gamma^{(m)\,L}\}]\,, \end{aligned} \tag{3.29}$$

where $m \leq n+2$. The modified Slavnov–Taylor identities are introduced below. They converge to the standard ones for vanishing cutoff scale $k = 0$. The above system comprises the full information about the correlation functions in the Landau gauge. Interestingly, the hierarchy of flow equations for the purely transversal correlation functions can be solved independently and carries the full dynamics of Yang–Mills theory. Therefore, vertex constructions aided by Slavnov–Taylor identities implicitly utilise an assumed uniformity of correlation functions, that is

$$\partial_{p_\mu} \Gamma^{(n)} < \infty \quad \text{for all } (p_1, ..., p_n)\,. \tag{3.30}$$

This works well in perturbation theory but has to be taken with a grain of salt in the non-perturbative regime.

It is also worth emphasising that eq. (3.29) does not depend on the way how the Landau gauge is introduced. The Landau gauge can be also represented as the limit of covariant gauges with the gauge action $1/(2\xi)\int_x (\partial_\mu A^a_\mu)^2$ and gauge fixing parameter ξ. Here $\xi \to 0$ signals the Landau gauge. In this case in general one also introduces a regularisation for the gauge mode, which is schematically given by

$$R^{\mathrm{L}}_{\mu\nu} = \lim_{\xi\to 0} \frac{1}{\xi} \Pi^{\mathrm{L}}_{\mu\nu}\, p^2 r(p^2/k^2)\,, \tag{3.31}$$

with the longitudinal projection operator $\Pi^{\mathrm{L}}_{\mu\nu}(p)$ given by

$$\Pi^{\mathrm{L}}_{\mu\nu}(p) = p_\mu p_\nu / p^2\,. \tag{3.32}$$

Still, the longitudinal mode does not play any role for the flow of correlation functions as $G \cdot \partial_t R^{\mathrm{gauge}} \cdot G \to 0$ for $\xi \to 0$ and $\lim_{\xi\to 0} G$ is purely transversal. Note however that $1/2\,\mathrm{Tr}\, R^{\mathrm{gauge}} \cdot G$ does not vanish and is of importance in the study of thermodynamics. Upon t-integration it gives the thermal pressure for the gauge mode, namely the Stefan–Boltzmann pressure of $N_c^2 - 1$ fields, see [407].

The regulator term for the gluons acts like a mass term. Thus, for non-vanishing[17] k it breaks gauge invariance explicitly. However, this does not necessarily mean that the theory is ill-defined. In a gauge-fixed setting physical gauge-invariance is not observed on the level of an invariant effective action directly. Rather, if the classical action and the path integral measure are gauge-invariant, gauge-invariance for the effective action is encoded via constraints for n-point functions. These constraints involve terms that stem from the gauge-fixing term and the ghost term. In Abelian gauge theories, for physical Green functions, i.e. for on-shell quantities, these are the so-called Ward identities (WIs). They can be generalised to the Ward–Takahashi identities (WTIs) for off-shell Green functions and further to Slavnov–Taylor identities (STIs) for non-Abelian theories, which is

[17] Note that if truncations are done the limit of vanishing k does not necessarily provide a gauge-invariant effective action.

the appropriate relation for Yang–Mills theory. These relations keep gauge-invariance by implementing constraints for the longitudinal parts of the vertices. If a regulator term is introduced these relations are different, as they receive contributions that originate from the regulation in the scale-dependent effective action[18]. The resulting expressions are called modified Slavnov–Taylor identities (mSTIs) [405, 408–411] and describe gauge-invariance at the energy scale k. As the mSTIs constitute a fixed point under renormalisation group transformations they guarantee that a gauge-invariant quantity at some scale k stays gauge-invariant. Thus, gauge-invariance also holds for $k \to 0$, and furthermore, the mSTIs turn into the usual STIs at vanishing scale k as the regulator term quadratically goes to zero with the renormalisation group scale. However, one has to keep track of the terms originating from the regulation which is done by an appropriate choice of the initial condition of the flow at $k = \Lambda$. Here, counterterms are added to the classical action which cancel gauge-symmetry breaking contributions from the regulator at some k.

Another approach to ensure gauge-invariance is to construct flows that are gauge-invariant themselves. In particular, this would be desireable because the implementation of the modified Slavnov–Taylor identities in order to ensure gauge invariance is a hard task as it necessitates the solution of another loop equation, i.e. an additional equation of a similar complexity as the flow equation itself. Especially in numerical computations this is hard to get under control, as small numerical errors in the flow of the mSTI can destroy gauge-invariance crucially if they occur in relevant operators. Therefore, the construction of gauge-invariant flows via a gauge-invariant regularisation itself facilitates the ensuring of gauge-invariance. However in all suggestions for manifestly gauge-invariant flows made so far the construction itself is rather complex. Thus, it has not been applied in any realistic physical system. On the other hand, promising proposals have been made recently [277, 412–414]. Other ways to construct gauge invariant flows are via the geometric approach [415, 416], where the regularisation only acts on gauge-invariant fields, or the background field approach [406, 417, 418] which ensures a gauge-invariant effective action itself, see also chapter 5.

3.2.5. Locality of Flows and Field Reparametrisation

In this section I detail the issue of locality of the flow equation. This property is crucial for applications at non-vanishing temperature, thus, it is of great importance in section 4. Furthermore, I introduce a reparametrisation of the theory which is done in precisely such a way that the flows of the two-point functions are strictly local.

[18] Note that these algebraic constraints get modified in a non-trivial way, i.e. loop terms emerge from the regulation.

Locality of Flow Equations

By construction the flow equation needs to be local, otherwise contributions from scales much larger than the considered renormalisation group scale k would affect the region around k in an uncontrolled way. In the cases presented below the flow is in principle local but still the behaviour is not very well suited for computations. This section concerns locality and techniques that can be employed to improve the locality in flow equations.

The loops on the right hand side of fig. (3.7) and fig. (3.8) only receive contributions from momentum fluctuations with $p^2 \lesssim k^2$ due to the regulator insertion $\partial_t R$, see fig. (3.1). However, the external momenta are not limited by such a constraint. Indeed, for large external momenta $p^2/k^2 \gg 1$ the flow factorises at leading order: The tadpole diagram with the four-gluon vertex tends to a constant. The other tadpole diagrams vanish with powers $\lesssim k^2/p^2$. The related four-point functions are not present on the classical level. Hence they decay at least with k^2/p^2. This intuitive statement can be proven easily with the help of the respective flows and the factorisation present there. Here, the factorisation is sketched at the relevant example of the three-point function diagrams, see also fig. (3.11), for the example of the flow of the ghost propagator. These diagrams factorise for large external momenta, one factor being the uncutted internal line evaluated at p^2. For $p^2/k^2 \to \infty$,

$$\begin{aligned} &\mathrm{Tr}\left[\left(G\dot{R}G\right)(q)\cdot\Gamma^{(3)}(q,p+q)\cdot G(p+q)\cdot\Gamma^{(3)}(q+p,q)\right] \\ \to\quad &\mathrm{Tr}\left[\left(G\dot{R}G\right)(q)\cdot\Gamma^{(3)}(0,p)\cdot G(p)\cdot\Gamma^{(3)}(p,0)\right] \\ &\quad + \text{higher order terms}\,, \end{aligned} \tag{3.33}$$

where the trace also integrates over loop momenta q. In eq. (3.33) it is assumed that all

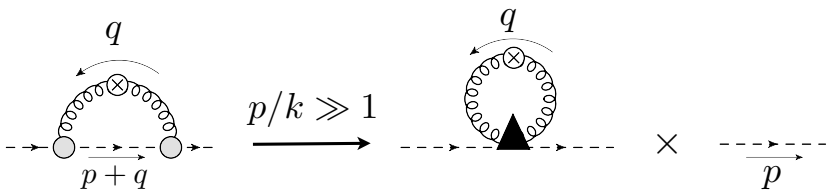

Figure 3.11.: Factorisation in leading order for large momenta for the first diagram (cutted gluon line) in the flow of the (inverse) ghost propagator in fig. (3.8). The triangle stands for the product of the two vertices at $q = 0$ and reads $-p_\mu p_{\mu'} f^{acd} f^{bc'd'}$, cf. appendix E.

momentum components are suppressed by the regulator: R is a function of p^2 and not e.g. of solely spatial momentum squared, $\vec{p}^{\,2}$. Note also that for kinetic and/or symmetry reasons the leading order in line two of eq. (3.33) may vanish. This even supports the factorisation. The interchange of integration and limit, and hence the factorisation works as the diagram is still finite with the uncutted line being removed.

The general factorisation in eq. (3.33) can be nicely illustrated diagrammatically at the example of the flow of the ghost propagator, fig. (3.8). In fig. (3.11) the factorisation of the first diagram in fig. (3.8) is displayed. The terms in the second line of eq. (3.33) or on the right hand side of fig. (3.11) are already subleading as the flow is usually peaked at momentum scales $p^2 \lesssim k^2$. However, they are already quantitatively relevant at vanishing temperature, but turn out to be crucial for the correct thermodynamics, in particular for the slow approach to the Stefan–Boltzmann limit for large temperatures. Potentially, they also play an important role for the thermodynamics in non-relativistic systems, where they supposedly relate to the Tan relations [419–421] in the context of many-body physics. For FRG-reviews on non-relativistic systems see e.g. [384, 386, 391].

Still, one needs to reconcile the above polynomial decay with external momenta p with the well-known exponential decay of thermal fluctuations with the standard suppression factor $\exp(-m/T)$ in the presence of a mass scale m. In the present case this mass scale can be either the cutoff scale k or the physical mass scale of Yang–Mills theory, Λ_{QCD}, which is directly linked to the critical temperature T_c of the deconfinement-confinement phase transition. The exponential thermal damping factor originates from the full Matsubara sum, and is strictly not present if only the lowest Matsubara frequencies are taken into account. A four-dimensional regulator depending on four-dimensional loop momentum $q^2 = (2\pi T n)^2 + \vec{q}^{\,2}$ cuts the Matsubara sum. Hence, it only leads to the polynomial decay of the flow. The exponential suppression is then built up successively with the flow. The above properties can be already very clearly seen and understood at the example of perturbative one-loop flows.

The full Matsubara sum is reintroduced for regulators only depending on $\vec{p}^{\,2}$. They are frequently used in finite temperature applications of the FRG as they allow for an analytic summation of the Matsubara sums if only the trivial frequency-dependence is taken into account, see e.g. [277, 407, 422, 423]. However, in the present work full propagators and vertices are considered, so the Green functions have a non-trivial frequency- and momentum-dependence. Moreover, as lower-dimensional regulators introduce an additional momentum- or frequency-transfer in the flow, only four-dimensional regulators are used for the study of Yang–Mills theory at non-vanishing temperature in chapter 4.

Apparently, the large momentum contributions also weaken the locality of the flow present in the loop momenta as they induce a momentum transfer: The flows at a given cutoff scale k carry physics information about larger momentum scales. In turn this entails that any local approximation does not fully cover this momentum transfer.

Field Reparametrisations

The problems that potentially occur in non-local flows can be circumvented by a reparametrisation of the fields of the theory along the computation. At the end of the solution of the flow this reparametrisation must be undone in order to express the correlation functions in terms of the physical fields. This technique is sketched in this section.

In a vertex expansion the dependence on the renormalisation group scale k does not need to be put into the n-point functions $\Gamma^{(n)}$ only. Instead, one is free to reparametrise the effective action as well as the regulator such, that a part of the dependence on k is put into the fields. In the computation of thermal correlation functions as well as thermodynamic quantities of Yang–Mills theory the locality of the flow is crucial as it minimises the systematic error of a given truncation [278]. By the help of this reparametrisation of the fields locality of the flow of n-point functions can be restored in cases where it is not present.
The starting point is to rewrite the regulator term in eq. (3.27) as follows,

$$\Delta S_k = \frac{1}{2}\int_p A^\mu_{k,a}\,\hat{R}^{ab}_{\mu\nu}\,A^\nu_{k,b} + \int_p \bar{c}_{k,a}\,\hat{R}^{ab}\,c_{k,b}\,. \tag{3.34}$$

The fields $\phi = (A_k, c_k, \bar{c}_k)$ in eq. (3.34) relate to the cutoff-independent fields $\varphi = (A, c, \bar{c})$ in the classical action via a cutoff- and momentum-dependent rescaling,

$$\phi(p) = \hat{Z}^{1/2}_{\phi,k}(p)\varphi(p) \quad \text{with} \quad \partial_t\phi(p) = \hat{\gamma}_\phi(p)\,\phi(p)\,, \tag{3.35}$$

where the derivative is taken at fixed φ. For ghosts the natural definition is $\hat{\gamma}_{\bar{c}} = \hat{\gamma}_c$. Further, eq. (3.35) implies

$$\hat{\gamma}_\phi(p) = \frac{1}{2}\partial_t \log \hat{Z}_\phi(p)\,, \quad \text{and} \quad R = \hat{Z}\cdot\hat{R}\,. \tag{3.36}$$

The field reparametrisation in eq. (3.35) does not change the effective action, in particular the regulator term ΔS_k does not change. It simply amounts to rewriting the effective action in terms of the new fields,

$$\hat{\Gamma}_k[\phi] = \Gamma_k[\varphi]\,. \tag{3.37}$$

Then, ϕ-derivatives $\hat{\Gamma}^{(n)}_k$ of the effective action $\Gamma_k = \hat{\Gamma}_k$ are given by eq. (3.16) with $\varphi \to \phi$,

$$\hat{\Gamma}^{(n)}_k(p_1,...,p_n) = \frac{\delta\hat{\Gamma}_k}{\delta\phi(p_1)\cdots\delta\phi(p_n)}\,. \tag{3.38}$$

As the fields ϕ and φ only differ by a momentum-dependent rescaling with $\hat{Z}^{1/2}$ the correlation functions are related by a simple rescaling with powers of $\hat{Z}^{1/2}$,

$$\Gamma^{(n)}(p_1,...,p_n) = \prod_{i=1}^n \hat{Z}^{1/2}_{\phi_i}(p_i)\,\hat{\Gamma}^{(n)}(p_1,\ldots,p_n)\,. \tag{3.39}$$

The rescaling with $\hat{Z}$ is free to choose. Thus it can be used to minimise the momentum transfer in the flow equation of the two-point function by eliminating the subleading terms in the flow exemplified in eq. (3.33). Note that this does not remove the related contributions, the momentum transfer is still present but does not feed-back directly in the flow, see [278]. This is also elucidated below.

The flow equation for the effective action now receives further contributions from the k-dependence of the fields ϕ. Finally, this leads to the following flow for $\hat{\Gamma}_{k,T}[\phi] = \Gamma_k[\varphi]$, see [278],

$$\begin{aligned}\left(\partial_t + \sum_i \fint_p \hat{\gamma}_{\phi_i}(p)\phi_i(p)\frac{\delta}{\delta\phi_i(p)}\right)\hat{\Gamma}_{T,k}[\phi] = \\ \frac{1}{2}\fint_p \hat{G}^{ab}_{\mu\nu}[\phi](p,p)\,(\partial_t + 2\hat{\gamma}_A(p))\hat{R}^{ba}_{\nu\mu}(p) \\ - \fint_p \hat{G}^{ab}[\phi](p,p)\,(\partial_t + 2\hat{\gamma}_C(p))\hat{R}^{ba}(p)\,,\end{aligned} \tag{3.40}$$

where $\hat{G}[\phi](p,q) = \left(\hat{\Gamma}^{(2)}_k[\phi] + \hat{R}\right)^{-1}(p,q)$ denotes the full regularised propagator for the propagation of ϕ, see eq. (3.24) with $\varphi \to \phi$ and $\Gamma^{(2)}_k \to \hat{\Gamma}^{(2)}_k$. The functional flow in eq. (3.40) looks rather complicated but it is simply a reparameterisation of the standard flow in eq. (3.28), or fig. (3.6). In the condensed notation introduced in section 3.2.3 this is more apparent. The flow equation eq. (3.40) then reads

$$\left(\partial_t + \phi\cdot\hat{\gamma}_\phi\cdot\frac{\delta}{\delta\phi}\right)\hat{\Gamma}_{T,k}[\phi] = \frac{1}{2}\mathrm{STr}\,\hat{G}[\phi]\cdot\,(\partial_t + 2\hat{\gamma}_\phi)\cdot\hat{R}_k\,. \tag{3.41}$$

Eq. (3.41) illustrates that it is only a reparametrisation the fields in a scale-dependent way.

Taking two derivatives with respect to $\phi_1(p)$ and $\phi_2(q)$ of eq. (3.40) at vanishing ghost fields and constant gauge field schematically yields the flow

$$\left(\partial_t + \hat{\eta}_{\phi_1}(p)\right)\hat{\Gamma}^{(2)}_{\phi_1\phi_2}(p) = \mathrm{Flow}^{(2)}_{\phi_1\phi_2}(p)\,, \tag{3.42}$$

where the right hand side of eq. (3.42) stands for the $\phi_1(-p)$ and $\phi_2(p)$ derivative of the right hand side of eq. (3.40),

$$\mathrm{Flow}^{(2)}_{\phi_1\phi_2} = \frac{\delta^2}{\delta\phi_1\delta\phi_2}\left(\frac{1}{2}\mathrm{Tr}\,\hat{G}[\phi]\cdot\,(\partial_t + \hat{\eta}_\phi)\cdot\hat{R}_k\right), \tag{3.43}$$

and

$$\hat{\eta}_\phi(p) = 2\hat{\gamma}_\phi(p) = \partial_t \log\hat{Z}_k(p)\,, \tag{3.44}$$

is the 'anomalous' dimension of the propagator related to the rescaling of the fields with $\hat{Z}$. The two-point functions for vanishing ghosts are diagonal/symplectic in field space. This enters eq. (3.42). The only non-vanishing components are $\hat{\Gamma}^{(2)}_{k,AA}$ and $\hat{\Gamma}^{(2)}_{k,c\bar{c}} = -\hat{\Gamma}^{(2)}_{k,\bar{c}c}$. The two-point functions for constant gauge fields are also diagonal in momentum space,

that is

$$\begin{aligned}\hat{\Gamma}_k^{(2)}(p,q) &= \hat{\Gamma}_k^{(2)}(p)(2\pi)^4\delta(p-q)\,,\\ \mathrm{Flow}^{(2)}(p,q) &= \mathrm{Flow}^{(2)}(p)(2\pi)^4\delta(p-q)\,,\end{aligned} \tag{3.45}$$

and the relation eq. (3.39) for the two-point functions reads

$$\Gamma^{(2)}(p) = \hat{Z}(p)\,\hat{\Gamma}^{(2)}(p)\,. \tag{3.46}$$

In order to restore locality in the flow the large momentum tail in eq. (3.33) must be removed in order to guarantee locality in momentum space, i.e. to minimise the momentum transfer. This is achieved by demanding

$$\partial_t\hat{\Gamma}_k^{(2)}(p)\Big|_{p^2>(\lambda k)^2} \equiv 0\,, \tag{3.47}$$

which implies

$$\hat{\eta}_\phi(p) = \frac{\mathrm{Flow}^{(2)}(p)}{\hat{\Gamma}_k^{(2)}(p)}\theta(p^2-(\lambda k)^2)\,. \tag{3.48}$$

Eq. (3.47) entails that the momentum transfer is switched off for momenta larger than the cutoff scale. The factor λ controls this scale and can be used for an error estimate.

After the computation of the localised correlation functions $\hat{\Gamma}^{(n)}$ the correlation functions $\Gamma^{(n)}$ are derived via rescaling with powers of $\hat{Z}$, see eq. (3.38) and eq. (3.46). The scaling factor is computed by integrating $\hat{\eta}_k$ defined in eq. (3.44),

$$\hat{Z}_k(p;T) = \hat{Z}_{k=0}(p;T)\,\exp\left\{\int_0^k dt'\;\hat{\eta}_{k'}(p;T)\right\}\,. \tag{3.49}$$

This determines $\hat{Z}_k$ up to a k-independent function and can be fixed as

$$\hat{Z}_{\phi,k=0}(p;T=0) = 1\,. \tag{3.50}$$

For the choice eq. (3.50) the two sets of correlation functions agree in the vacuum at $k=0$.

As the flow of general correlation functions can be written down solely in terms of $\hat{\Gamma}^{(n)}$ the relation eq. (3.47) with eq. (3.48) eliminates the momentum transfer in $\hat{\Gamma}^{(2)}$ from the flow. Note however, that a remnant of it is still present via the factor $2\hat{\gamma}_\phi = \hat{\eta}_\phi$ on the right hand side of the flow eq. (3.41). For regulators that decay sufficiently fast for momenta $p^2 \gg k^2$ this is quantitatively negligible. Indeed, for regulators which vanish identically for momenta bigger than λk the momentum transfer now is described solely by $\hat{\eta}_\phi(p)$ and decouples completely. In principle, the above construction and the definition eq. (3.50) leading to eq. (3.47) with $\lambda = 1$ can be deduced by evoking functional optimisation for momentum-dependent approximations, see [278]. The above heuristic arguments

entail that optimisation restores the locality of the flow also in general momentum- and frequency-dependent approximations.

Note that this technique of field reparametrisations is not restricted to storing the scale-dependence in the field. In section 4.1.3, a similar reparametrisation is done for thermal fluctuations in the ghost propagator.

3.2.6. Thermal Fluctuations

In section 3.2.1 the flow equation, eq. (3.15), is introduced for zero temperature. In general, the flow equation can also be applied at finite temperature. It is still an exact method that includes now both, thermal as well as quantum fluctuations. In this section the focus is on the signatures of temperature. In the FRG approach it turns out that these fluctuations can be treated independently from the quantum fluctuations by the help of purely thermal flows [277, 407]. These flows are simply the difference between flows at finite and zero temperature. Thus, to determine the quantum theory at finite temperature it is enough to add the thermal flow to the quantum flow, i.e. the full system can be studied in two separate steps. At first sight, this may seem to be redundant which would be true, if the flow equation could be solved exactly, i.e. without any truncation. But for approximate solutions this partitioning of flows facilitates calculations.

Furthermore, it is generally not necessary to obtain both results in a functional approach as only the full quantum theory, i.e. the theory at $k = 0$ is used as input for the thermal flow. One can even take lattice data, i.e. data from a method that does not suffer from approximations. Therefore, the insensitivity of the computation of thermal effects from the input can be investigated easily.

Thermal flows [277, 407] are constructed by

$$\Delta\Gamma_{T,k}[\varphi] = \Gamma_k[\varphi]|_T - \Gamma_k[\varphi]|_{T=0} , \tag{3.51}$$

$$\partial_t \Delta\Gamma_{T,k}[\varphi] = \frac{1}{2}\mathrm{Tr}\, G[\varphi]\cdot\partial_t R\Big|_T - \frac{1}{2}\mathrm{Tr}\, G[\varphi]\cdot\partial_t R\Big|_{T=0} , \tag{3.52}$$

thus, the thermal flow $\partial_t\Delta\Gamma_{T,k}[\varphi]$ accounts for the difference between the effective action at vanishing and finite temperature. Due to the thermal exponential suppression the flow eq. (3.51) should have locality properties with respect to the scale $k = T$, because temperature is an infrared phenomenon. As discussed in section 3.2.5 locality of the flow is important for the quantitative reliability of a given approximation.

Previous studies of infrared Yang–Mills correlation functions with functional methods, see section 2.3.2, have shown that sophisticated truncations are inevitable to quantitatively match lattice results. In addition, for ensuring gauge-invariance a fine-tuning procedure must be done in order to find the correct ultraviolet action that does not render a per-

turbative gluon mass along the flow. The benefit of the thermal flow is that it offers the possibility to take a different truncation for the thermal behaviour. Therefore, the two truncations can be optimised such that the relevant aspects of the individual fluctuations are covered. This facilitates the implementation on a technical level and a fine-tuning can be avoided, since gauge-invariance is ensured for the quantum theory and thermal masses are permitted.

The truncation for thermal effects may actually be easier. This conjecture is based on the following considerations: Firstly, only the difference of the flows at non-zero and zero temperature, $\partial_t \Delta\Gamma_{T,k}[\varphi]$, is sensitive to truncational errors. Secondly, which is actually connected to the first point, temperature is an infrared phenomenon, i.e. it should only modify the quantum theory below scales $k \lesssim 2\pi T$. Consequently, the truncation error is restrained to the infrared. In any truncation the difference is guaranteed to vanish above the temperature scale, i.e. it is ensured that no numerical error from higher scales can build up and affect the infrared. Thirdly, low temperatures account for a correction to the quantum theory, so it is supposed to be a small effect. Therefore, numerical inaccuracies deteriorate the correction only, i.e. the primary properties of the quantum theory are not altered.

In the study presented here this two-step procedure is applied. The implementation of the thermal flow eq. (3.51) is done as follows. The vacuum physics at vanishing temperature is the input for the thermal flow. A given set of correlation functions $\Gamma^{(n)}_{k=0}$ at $T = 0$ and $k = 0$ can be integrated with the flow eq. (3.15) at vanishing temperature in a given approximation up to a large momentum scale $k = \Lambda \gg 2\pi T$, viz.

$$\Gamma^{(n)}_{k=0}(p_1, ..., p_n)\Big|_{T=0} \xrightarrow{\text{flow}} \Gamma^{(n)}_{k=\Lambda}(p_1, ..., p_n)\Big|_{T=0} . \tag{3.53}$$

Thus, starting from the quantum theory at $k = 0$ (and $T = 0$), the correlation functions at all $k \leq \Lambda$ are known.

Two important comments are in order here. Firstly, in the reasoning of the FRG the theory is integrated from a scale Λ, at which the classical action serves as a starting point in the flow, to $k = \Lambda \to 0$. The integration from $k = 0 \to \Lambda$ with a different truncation does not reproduce this classical initial condition but instead some other action. In the picture of the theory space this corresponds to another point in fig. (3.4). But after all, this does not pose a problem as this does not need to reproduce the classical action but rather some action for which it is guaranteed that running down again at $T = 0$ in the given truncation yields the correct quantum theory again. In fact, if one obtained the classical action again, the purely thermal flow eq. (3.51) would be obsolete. In this case the inversion of the flow at $T = 0$ would have integrated in again all quantum effects. The flow at $T > 0$ would account for both types of fluctuations again. I want to emphasise that in going up to Λ some quantum fluctuations are actually integrated in, but only exactly those that are integrated out again in the flow down at finite temperature.

Secondly, although the name suggests so, the FRG is not a group in the mathematical sense but rather only a semi-group. This implies that there is no inverse, so it is generally not possible to reverse the flow. In fact, going from small k to higher values is an instable direction in Yang–Mills theory. However, for reasonable Λ, i.e. for the case here where only small temperatures are studied, this potential problem does not occur. This saves the procedure above for the case of infrared Yang–Mills theory, but in general this may pose an insurmountable problem.

Coming back to the line of thoughts for thermal flows, eq. (3.53) defines in the approximation at hand the initial conditions $\Gamma^{(n)}_{k=\Lambda}\Big|_{T=0}$ which give the correct vacuum correlation functions if integrated to $k = 0$. The ultraviolet scale Λ is chosen such that all thermal fluctuations are suppressed given the maximal temperature to be considered, $T_{\max}$. This implies

$$\frac{T_{\max}}{\Lambda} \ll 1\,. \tag{3.54}$$

Next, the flow is reversed, but at non-vanishing temperature $T \leq T_{\max}$. As the initial scale is far above temperature effects, switching on T does not change the initial conditions at leading order, i.e.

$$\frac{1}{\Lambda^{d_n}} \Delta\Gamma^{(n)}_{T,\Lambda}(p_1, ..., p_n) = 0 + O\left(\frac{T}{\Lambda}\right). \tag{3.55}$$

where d_n is the canonical dimension of $\Gamma^{(n)}$ and all momenta are of order Λ or bigger, $p_i^2 \gtrsim \Lambda^2$. This suggests to flow $\Delta\Gamma_{k,T}$ from the trivial initial condition eq. (3.55) to vanishing cutoff.
The idea of the computation is sketched in fig. (3.12), again by the help of the theory space which served to illustrate the flow equation at $T = 0$ in section 3.2.2. The sketch illustrates that the two flows in different truncations deviate from each other, thus, the reversed flow does not reproduce the classical action. The temperature has an effect in the infrared, where the scale is set by the temperature itself. The contributions above that scale cancel in the thermal flow, i.e. in the difference of the flow at finite and zero temperature.

The arguments above are partly based on the fact that the scale at which thermal fluctuations become important is about $2\pi T$. For the bosonic case this is exactly the first Matsubara frequency. This may seem very early for the discretisation effects to vanish. However, that this is actually the case for discretisations can be seen by the hand of trivial cases already. Here, it is employed that the finiteness of the temperature is equivalent to a finite extent in temporal direction. Thus, in some sense the study of finite temperature is related to finite volume investigation.

The first example is simple the investigation how fast the sum over discrete Matsubara frequencies n approaches the integral over temporal momentum p_0. In order to mimic a typical form of an integral the loop-integration over a propagator is carried out, where the

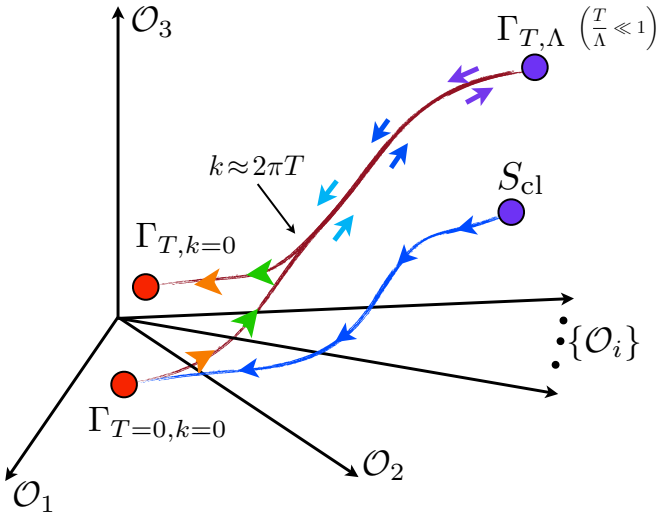

Figure 3.12.: This figure illustrates the setting for the computation of the temperature behaviour of correlation functions by the help of the theory space. The axes label (orthogonal) couplings $\mathcal{O}_i$ which serve as expansion coefficients of the effective action. First, starting at the classical action $S_{\rm cl}$ the flow for the pure quantum theory (blue line) yields the full quantum theory, i.e. at $k = 0$, for vanishing temperature. In a different truncation, optimised for the thermal behaviour, the flow is reversed back to a scale Λ where temperature effects are suppressed. This is not the classical action but an action that gives the correct vacuum physics if integrated down to $k = 0$ again with the truncation at hand. However, at the scale Λ temperature is switched on, $T \neq 0$, and flow integrates back to the infrared. Below the temperature scale $k \approx 2\pi T$ the flow and therefore the theory feels the temperature. Arriving at a different point in theory space at $k = 0$, $T \neq 0$ the theory includes both, quantum as well as thermal fluctuations.

integration over spatial momentum is approximated. This leaves the form

$$f(p_0, p) = \frac{p}{p_0^2 + p^2}\,, \tag{3.56}$$

where p is the absolute value of the spatial momentum. The integral over p_0 of this expression is finite,

$$F_{\rm T=0} = \frac{1}{2\pi}\int_{-\infty}^{\infty} dp_0\, f(p_0, p) \;=\; \frac{1}{2}\,. \tag{3.57}$$

Transforming this expression to the case of finite temperature, see section 3.1, yields the Matsubara sum

$$F_{\rm T>0}(p) = T\sum_{n=-\infty}^{\infty} f(2\pi T n, p) \;=\; \frac{1}{2}\coth\left(\frac{p}{2T}\right). \tag{3.58}$$

Thus, for large values of the ratio $\frac{p}{2T} \gg 1$ the $\coth\left(\frac{p}{2T}\right)$ approaches 1 and the sum ap-

proaches the integral. Herein, actually the decay is exponential due to the form of the $\coth(x) = (e^{2x}-1)/e^{2x}+1$. The velocity of this decay at $T = 1$ (in arbitrary units) is given in fig. (3.13(a)) and that the exponential decay $\exp\left(-2\frac{p}{2T}\right)$ is (trivially) realised can be seen by the help of fig. (3.13(b)). In this example it is obvious that the discretisation effect vanishes rather quickly above the temperature scale, even on a quantitative level.

But the above example, fig. (3.13), per se is not what enters flow equations. In the FRG the situation is more intricate, first of all because there are additional (spatial) integrals in the loop, but also because the regulator term complicates the expressions. But, even in the framework of the FRG it can be seen by the help of a simple example how temperature changes the system. As already detailed in section 3.1 the time direction is compactified at finite temperature, i.e. $\mathbb{R} \to [-\frac{1}{T}, \frac{1}{T}]$. This is equivalent to a finite size in time direction, thus, investigations at finite temperature are closely related to studies at finite volume. This is the next example, namely the flow of the tadpole t of a real massless scalar particle, i.e. for an interaction term $\frac{\lambda}{4!}\phi^4$ in a finite volume. The full flow equation is given in fig. (3.2.6). To keep things as simple as possible the truncation is chosen such that the three-point vertex vanishes, which is indicated by the dotted cross in fig. (3.2.6), the four-point vertex is momentum-independent with a coupling strength $\lambda = 1$, i.e. $\Gamma^{(4)} = 1$, and so is the wave-function renormalisation for the boson, i.e. $\Gamma^{(2)} = p^2$, and the propagator is regulated by an exponential regulator, cf. eq. (3.12), with $m = 1$, viz. $G_k(p) = p^2\left(1 + r^1(p^2/k^2)\right)$. That yields the expression for the flow of the tadpole

$$\dot{\mathrm{t}} = -\frac{1}{2}\int_p \left(G\,\dot{R}\,G\right)_k = -\frac{1}{8\,\pi^2}\int_0^\infty dp\; p^3 \frac{e^{-\frac{p^2}{k^2}}}{k^2} = -\frac{1}{16\pi^2}k^2\,, \tag{3.59}$$

where the dependence of $\dot{\mathrm{t}}$ on k is omitted. The (flow of the) tadpole is actually independent of the momentum p. Note that this expression has been transformed to spherical coordinates already, see also appendix D.1. The radial integral is now considered in a finite volume in radial direction. Of course, this discretisation procedure is not equivalent to a hypercubic discretisation, but at least for large momenta this is a good approximation. Anyway, here it is a further simplification for clarity. So the radial integral is transformed to a finite interval of length L which again has the effect that the spectrum is spanned by discrete modes $p \to \frac{2\pi n}{L}$, so written explicitly

$$\dot{\mathrm{t}}(L) = \frac{1}{8\pi}\frac{1}{L}\sum_{n=0}^{\infty}\left(\frac{2\pi n}{L}\right)^3 \frac{e^{-\frac{\left(\frac{2\pi n}{L}\right)^2}{k^2}}}{k^2}. \tag{3.60}$$

Note that in the infinite volume limit $L \to \infty$, eq. (3.60) turns into the four-dimensional integral given in eq. (3.59) again.

The dependence of the flow on the length of the box is plotted in fig. (3.15). In this figure two remarkable aspects that are particularly important for thermal flow equations are confirmed for this simple case. Firstly, finite volume effects are indeed restricted to

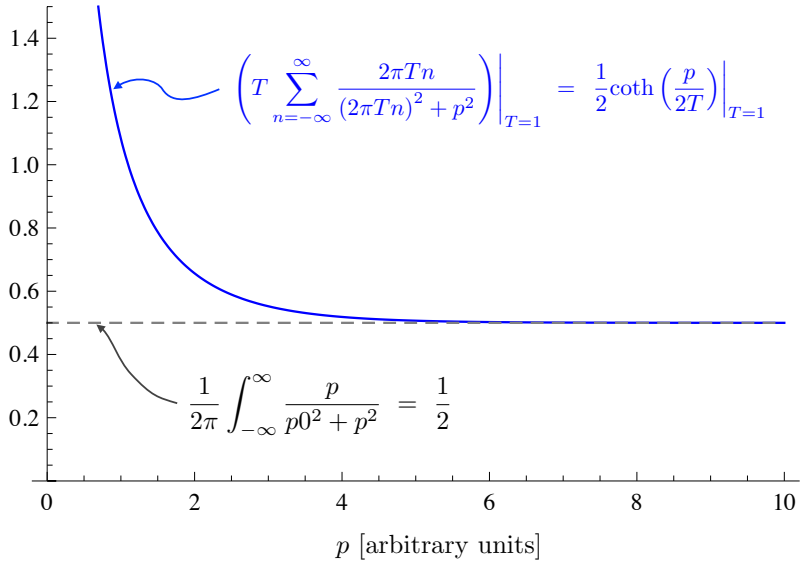

(a) Comparison of the Matsubara sum at finite temperature with the integration at vanishing temperature.

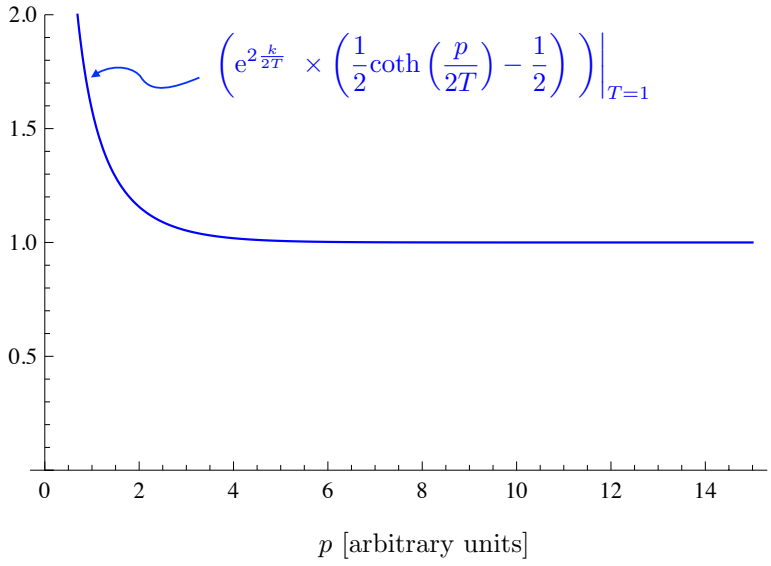

(b) Exponential approach of the Matsubara sum to the integral.

Figure 3.13.: Trivial example for the convergence of the Matsubara sum to the integral for scales that are far above the temperature.

the infrared, i.e. modes with a momentum much larger than the inverse length of the box do not feel the altered boundary conditions and behave as if temperature would be zero.

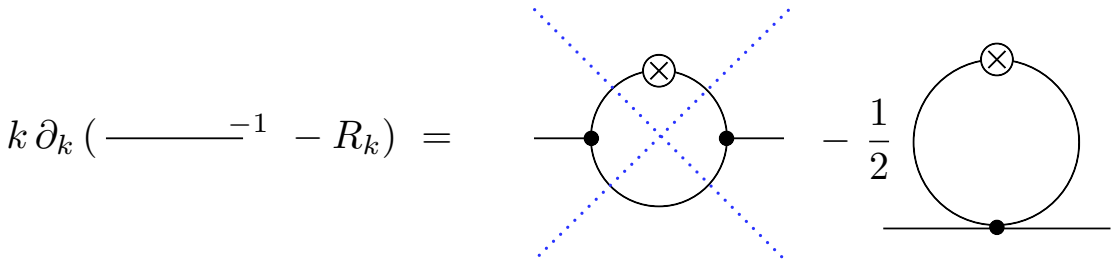

Figure 3.14.: Flow equation for the propagator in ϕ^4 theory. For the simplest investigation of finite volume effects only the tadpole is considered.

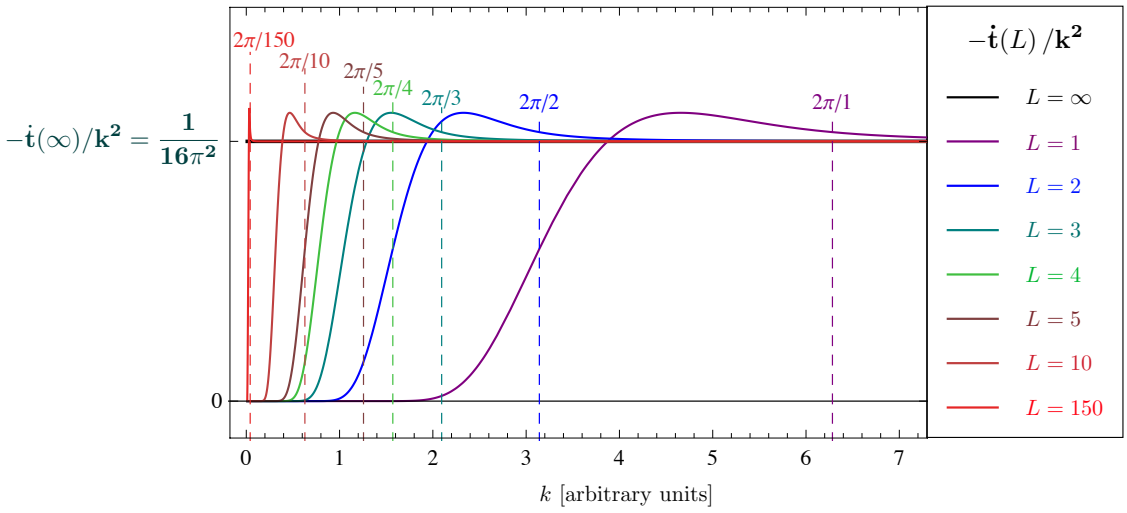

Figure 3.15.: The flow of the tadpole diagram in a massless ϕ^4 theory as a function of the renormalisation group scale k in a finite volume of length L. The effect of the discretisation of the spectrum due to the finiteness of the volume is crucial at scales smaller than the size of the box in momentum space, i.e. $k/(2\pi/L) \ll 1$. Above this scale set by the first mode the impact of the discretisation vanishes quickly as the modes are larger than the box and do not feel the altered boundary. The Matsubara formalism compactifies the time direction, therefore, it can be compared to a finite volume effect. It is found that thermal fluctuations are suppressed above the very same scale, i.e. above the first Matsubara mode, which is supported by this figure.

Secondly, also in the flow equation the scale at which the temperature effects (quantita-

tively) matter is actually quite low: Already for momenta larger than roughly the first mode $2\pi/L$ the theory starts to approach the zero temperature limit rapidly. The first mode in the case of finite temperature is $2\pi T$.

There is another interesting aspect in the example of the scalar tadpole which is the absence of additional scales. The only scale in the system is L, so everything is measured in this scale L. Therefore, the different curves in fig. (3.15) are similar if measured in L, i.e. if the curves are rescaled to the dimensionless momentum $k \to \hat{k} = kL$. This is shown in fig. (3.16), where the curves of all lengths lie on top of each other if plotted over $\hat{k}$.

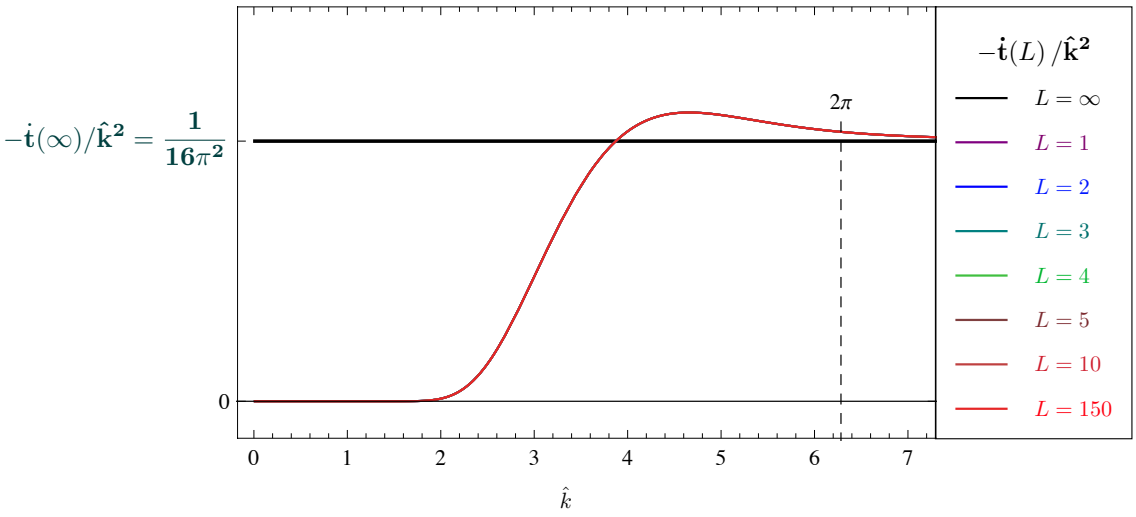

Figure 3.16.: In the tadpole for a massless scalar in a finite volume the only scale that enters is the length L. Therefore, if the system for different volumes is rescaled such that it is measured in units of this scale the effect is independent of the scale. In this plot the curves for the finite volume tadpole are given in the dimensionless variable $\hat{k} = k\,L$. Thus, the curves lie on top of each other.

So actually, the content of fig. (3.15) is highly redundant. But, this situation would be different if there were another scale in the system. This is the case for Yang–Mills theory as well as QCD, where the intrinsic scale Λ_{QCD} is generated[19]. In the presence of a mass there is a second scale and the system would not be trivially similar under a rescaling. This is illustrated by the same example of a scalar tadpole, however, this time the scalar has a mass of 1 (in arbitrary mass units), i.e. $\Gamma^{(2)} = p^2 + m^2$. That the scales are mixed in a multiscale system can be cleary seen in fig. (3.17). For inverse lengths much smaller than the mass the mass scale is dominating. In the opposite case the length sets the dominant scale. Therefore, in previously dimensionless units $\hat{k}$ the system shows the scale m.

[19]Note that although in Yang–Mills theory quarks are absent, nevertheless, the term Λ_{QCD} is used frequently in the literature. I stick to this definition.

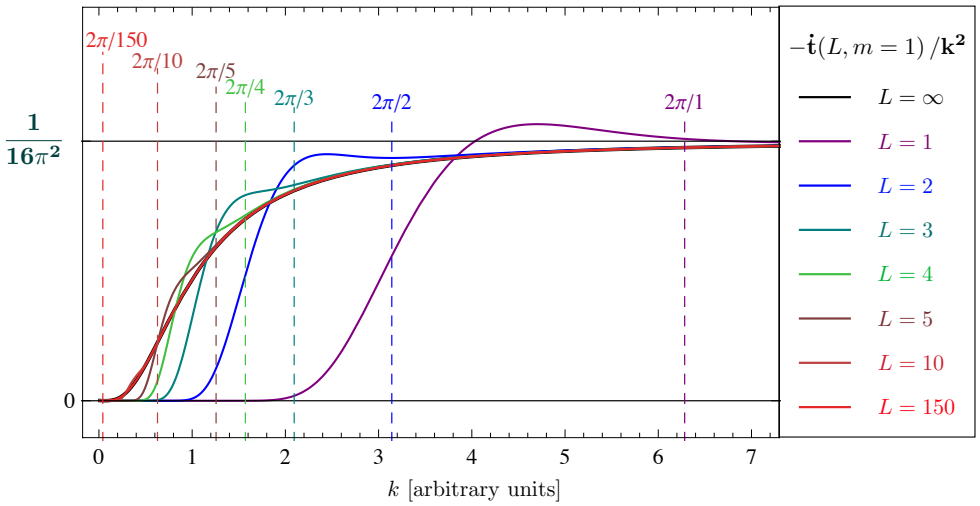

Figure 3.17.: In the flow of the tadpole of a massive scalar there are two scales, the size of the system as well as the mass of the particle. Put in different volumes and rescaled with respect to the volume, in contrast to the massless case in fig. (3.16), the situations are not equivalent due to the second scale set by the mass..

The above examples are simplified cases to outline what is to be approximately expected in systems at non-vanishing temperature. However, in thermal Yang–Mills theory it is more intricate. Therefore, the next step is to consider the rapidity of the decay of $\Delta\Gamma^{(n)}_{T,\Lambda} \to 0$ for large cutoff scales Λ for Yang–Mills theory. This is linked to the question of locality raised in the previous section 3.2.5. In fig. (3.12) it is indicated that $\Delta\Gamma^{(n)}_{T,k}$ starts to significantly deviate from zero at the thermal scale $k \approx 2\pi T$. However, at the example of the tadpole it is clear that the suppression for the flow $\dot{\Delta}\Gamma^{(n)}_{T,k}$ above that temperature scale is not stricly exponential but only polynomial. This implies that the longer $\Delta\Gamma^{(n)}_{T,k}$ survives at large scales $k \to \Lambda$ the more sensitive it is to the approximation at hand. Eventually, the polynomial contributions to the flow integrate-up to the standard thermal exponential suppression that relates to the thermal distribution functions as discussed in section 3.2.5.

To conclude there is only a polynomial decay in the flow which indeed plays a role for computing quantitatively reliable thermodynamical quantities. Additionally, in order to restore locality as much as possible one can utilise the field reparametrisation to guarantee that the flow is strictly confined to a range $p \leq \lambda k$, see eq. (3.47). This preserves the exponential decay that stabilises any approximation scheme. In the following this localised flow, eq. (3.47), is used for the calculation of infrared Yang–Mills correlators. As the local flow of $\hat{\Gamma}^{(2)}_k$ vanishes identically for momenta larger than λk for all temperatures T, this

yields

$$\Delta\hat{\Gamma}^{(2)}_{T,\Lambda}(p) = 0 + O(e^{-\Lambda/(T)}) \,, \tag{3.61}$$

neglecting the back-reaction of the polynomial decay of the thermal corrections of higher correlation functions. However, thermodynamic observables such as the pressure in section 4.3 are computated from the Wetterich equation, cf. eq. (3.28) and fig. (3.6) for Yang–Mills theory. Only the two-point functions enter here directly, all higher n-point functions only implicitly affect the thermodynamics as the propagators depend on them. Therefore, the corrections of higher Green functions are quantitatively small. Thus, in the thermodynamics the localisation procedure for the flow of the two-point functions pays-off in quantitative reliability.

Finally, the field reparametrisation must be undone in order to rearrange the k-dependence such that the parts that were put into the fields are fully shifted back to a k-dependence in the correlation functions $\Gamma^{(n)}$. This is done by a rescaling of the $\hat{\Gamma}^{(n)}$, that have been computed, with powers of $\hat{Z}_{k=0}$. At vanishing temperature the natural normalisation is simply $\hat{Z}_{k=0} = 1$, see eq. (3.49) and eq. (3.50), and the two sets of correlation functions agreed at $k = 0$. At finite temperature the flow is initialised at $k = \Lambda$ with $T/\Lambda \ll 1$. Here, the exponential suppression is valid for the difference of the localised correlation functions, eq. (3.61). Accordingly, it is safe to use the natural definition

$$\hat{Z}_\Lambda(p;T) := \hat{Z}_\Lambda(p;T=0) \,. \tag{3.62}$$

Eq. (3.62) implies that eq. (3.61) also applies to $\Delta\Gamma^{(2)}_{T,\Lambda}$: At the ultraviolet scale thermal fluctuations are exponentially suppressed for the two-point functions. Due to the immanent polynomial suppression due to the arguments leading to fig. (3.11), the use of the computational simple initial condition amounts to a temperature-dependent renormalisation of $\Gamma^{(n)}_k(T)$ at non-vanishing cutoff scale k. For the same reason eq. (3.62) also leads to $Z_{k=0}(p;T) \neq 1$, which needs to be determined from the flow of $\hat{\eta}_k$. Thus,

$$\begin{aligned} \hat{Z}_k(p;T) &= \hat{Z}_\Lambda(p;0) \exp\left\{\int_\Lambda^k dt' \, \hat{\eta}_k(p;T)\right\} \\ &= e^{\int_0^k dt' \, \hat{\eta}_k(p;0)} \, e^{\int_\Lambda^k dt' \, (\hat{\eta}_k(p;T) - \hat{\eta}_k(p;0))} \,, \end{aligned} \tag{3.63}$$

where eq. (3.49) was inserted in the second line. The relation eq. (3.63) entails that the rescaling factor $Z_{k=0}(p;T)$ contains the thermal part of the momentum transfer.

3.3. Dyson-Schwinger Equations

In this section I briefly summarise the idea, derivation and structure of DSEs. Especially, I emphasise Yang–Mills theory. Also DSEs allow for a study of the two main properties of low-energy QCD, i.e. confinement and dynamical chiral symmetry breaking, and even the full low-energy phase structure of QCD has been studied recently [88, 116, 117].

DSEs have been formulated in the mid of the last century separately by Freeman J. Dyson [424] and Julian S. Schwinger [425, 426]. They are an important tool to describe non-perturbative phenomena in quantum field theories, for reviews on DSEs in Yang–Mills theory and QCD see e.g. [239, 247, 253, 267]. DSEs provide equations for arbitrary n-point functions. The set of all n-point functions describes the quantum field theory exactly.

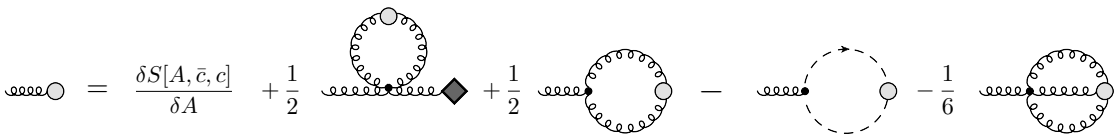

Figure 3.18.: Generating DSE for the gluon. The small dots denote bare vertices, the large blobs full vertices. The shaded diamond denotes an external gluon field A.

DSEs are the equations of motion for Green functions. Sticking to the path integral formulation of a quantum field theory, they derive from the observation that the path integral of a total derivative with respect to a quantum field vanishes. Taking Yang–Mills theory as an example, thus, having the interacting theory of gluon and ghost fields, this relation is given by

$$0 = \int \mathcal{D}\varphi \; \delta_{\varphi_a} \; e^{-S_{\mathrm{YM}}[\varphi]+J\cdot\varphi} = \left\langle -\delta_{\varphi_a} S_{\mathrm{YM}[\varphi]} + \eta_{ab} J_b \right\rangle_{J[\varphi]} , \tag{3.64}$$

where S_{YM} is the action of Yang–Mills theory with the particles subsumed in the field multiplet $\varphi = (A, c, \bar{c})$, whose sources are stored in J, and η accounts for the metric in field space given in eq. (3.22). The functional derivative is abbreviated as explained in section 3.2.3. Eq. (3.64)) holds under the assumption that the path integral is well defined and, further, that the integration measure is invariant under field translations[20]. Apart from that no approximations have been made, thus, under these mild assumptions the theory can be described exactly. Note that, albeit the presentation is done in Euclidean space here, DSEs equations can also be formulated in Minkowski space.

In eq. (3.64) the DSEs generate full Green functions, however, also expressions for the connected Green functions only as well as 1PI Green functions can be derived. In this work the latter one are of particular importance. The generating DSEs in this formulation are given by

$$\delta_{\varphi_a}\Gamma[\varphi] = \delta_{\phi_a} S_{\mathrm{YM}}[\phi]\Big|_{\phi\to\varphi_a + \frac{\delta^2 W}{\delta J_a \delta J_b}\delta_{\varphi_b}} . \tag{3.65}$$

There is one generating DSE for each field. Hence, for Yang–Mills theory there are two generating DSEs, one for the ghost[21] and one the gluon, respectively. These are diagram-

[20] There is an alternative way to derive DSEs following employing Heisenberg equations of motion and equal time commutation relations [427].

[21] Starting from the generating equation for the antighost yields the same (on-shell) Green functions as they are obtained from the generating DSE from the ghost.

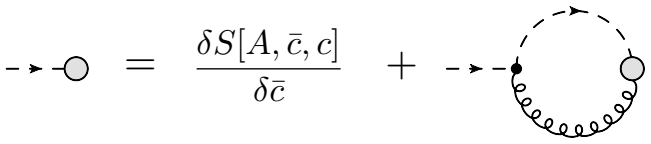

Figure 3.19.: Generating DSE for the ghost.

matically given in fig. (3.19) and fig. (3.19). From these generating equations all other n-point functions can be derived by taking functional derivatives with respect to fields and setting the sources to zero. The sources must only be taken to zero after having applied the functional derivatives as otherwise one would neglect some, if not all terms. To clarify this I use as an example an off-shell propagator, say G_{Ac}, on which another functional derivative with respect to the anti-ghost $\delta_{\bar{c}}$ acts. Setting the sources to zero before taking the derivative this off-shell contribution would vanish (e.g. the ghost-propagator DSE would be trivial), however, setting the sources to zero after the functional derivation the non-trivial structure is non-vanishing $\delta_{\bar{c}} G_{Ac}|_{J\to 0} = -G_{AA}\Gamma^{(3)}_{A\bar{c}c} G_{c\bar{c}}$.

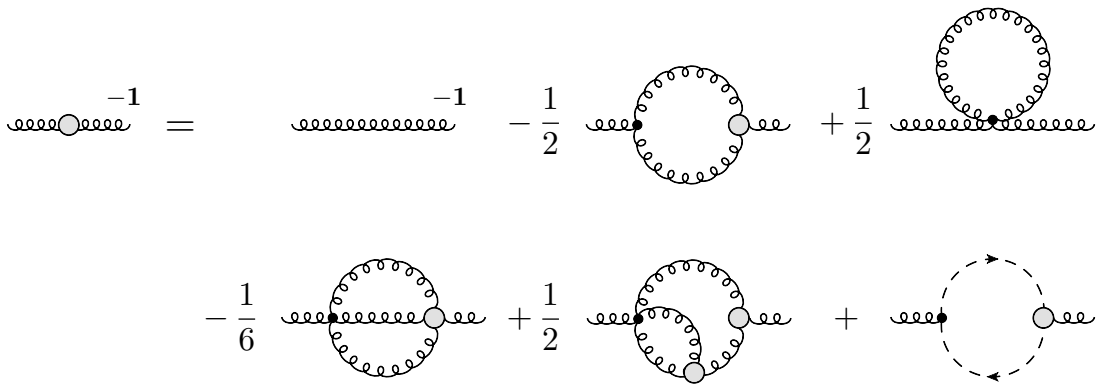

Figure 3.20.: DSE for the gluon propagator.

For later use as well as for comparison of the structures of flow equations and DSE I also give the DSEs for the two point functions of Yang–Mills theory, as well as the ghost-gluon vertex. The ghost propagator is given in fig. (3.21), the gluon propagator is given in fig. (3.20). These expressions have been checked with *DoDSE* [397, 398].

The structure of the DSEs fig. (3.21) and fig. (3.20) already shows that there is a drawback in the application of DSEs, just as it is encountered in the FRG. In general, the DSE for an n-point function depends itself on higher n-point functions, thus, also this set of equations

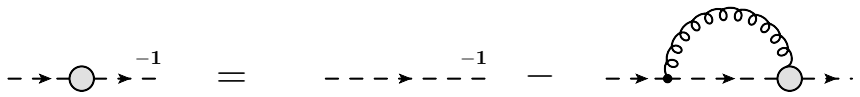

Figure 3.21.: DSE for the ghost propagator.

is infinite. In practice truncations must be done, following basically the same reasoning as in section 3.2.2.

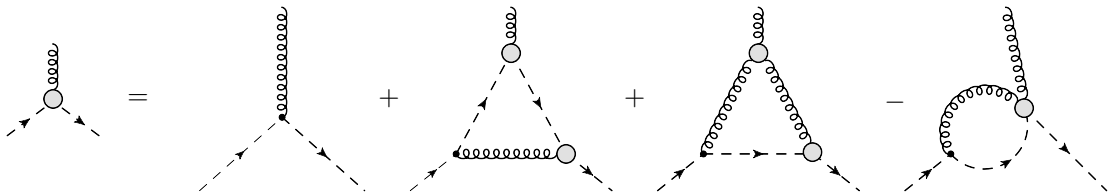

Figure 3.22.: DSE for the ghost-gluon vertex (having started from the generating DSE for the ghost).

3.4. Structural Aspects and Comparison of Functional Methods

The emphasis of this section is on the comparison of DSEs with flow equations. The idea of a flow equation follows the line of thought of Wilson, i.e. one aims at sequentially integrating quantum fluctuations of a momentum in a specific momentum range, which translates in the differential equation with respect to the renormalisation group scale. In contrast to this, solving the DSE means integrating all quantum fluctuations at once. The methods are related to each other as the flow can be seen as the differential form of a DSE with scale-dependent quantities and vice versa.

In the derivation of a flow equation the quadratic part of the action is modified such that a regulator term is added which suppresses fluctuations below an infrared scale. Via this trick the sequential integration of momentum shells is realised. This artificial scale is not introduced in the formalism of DSEs, which is a big advantage in resolving the n-point functions: Working with DSEs, Green functions generally depend on the momentum of the field as well as the the field expectation value. In the flow equation one has to resolve another dependency, namely the dependence on the renormalisation group scale k. This additional dependence on k in a flow equation is irrelevant in the full theory, however, in practical application, i.e. in truncated systems, this can hamper computations.

In the generating DSE, eq. (3.65)), there is always one functional derivative acting on the bare action, which translates into the fact that there is always the bare n-point function in the equation. Thus, each diagram in any DSEs contains a bare vertex. In comparison to a flow equation this means that a smaller number of different vertices contributes. E.g. the flow equation for the ghost-propagator, fig. (3.8), contains not only two diagrams where the loop contains two fully dressed ghost-gluon vertices but also two tadpole diagrams with a closed gluon or ghost loop, respectively. As the classical action does neither involve a bare two-ghost-two-gluon vertex, nor a ghost-ghost scattering kernel these tadpole diagrams are not present in the corresponding DSE, fig. (3.21). Furthermore, the two diagrams in the flow equation that contain the fully dressed ghost-gluon vertex, but the scale derivative of the regulator once in the internal gluon and once in the internal ghost propagator, merge to one single diagram in the DSE. This diagram has another simplification compared to the flow equation as one ghost-gluon vertex in it is bare.
However, the fact that there is always one bare vertex in each diagram of a DSE is not necessarily an advantage. It rather depends on the application of the equation. E.g. for critical phenomena this vertex does not carry the correct renormalisation group scaling, which hampers the access of critical physics within the DSE formalism, cf. appendix F.

Another interesting aspect of DSEs is that in some cases they can provide more than one equation for the same Green function, e.g. for the ghost-gluon vertex. Starting from the generating equation of the ghost guarantees that there is a bare ghost-gluon vertex in each diagram. This version is given in fig. (3.22). But starting from the gluon one-point function brings a bare three-gluon vertex about which would give another DSE involving twelve terms, some of them being of two-loop structure. Both equations are exact, but in practical computations one can decide according to the construction and validity of the truncation which form is more the appropriate one. Furthermore, by using the same truncation but the other equation one can get information about the total validity of the truncation.

Unfortunately, there are also disadvantages of DSEs. As the infrared is not regulated in the formalism of DSE also an important feature of the flow equation is absent, namely that if one starts with a finite (renormalised) theory it stays finite at all steps. This functional renormalisation is not implemented in a DSE. Therefore, a proper renormalisation procedure must be applied. Another disadvantage in contrast to flow equations is the appearance of two-loop diagrams[22], which can be seen already in the generating gluon DSE fig. (3.18) and also in the gluon propagator fig. (3.20). On the other hand, the flow equation has a one-loop form[23]. At this point it may be worth to mention again that these

[22] A non-Abelian gauge theory contains a four-point interaction in the classical action, which leads to two-loop diagrams. This is not a general feature for other theories as well, e.g. for a theory in which four-point interactions are absent two-loop diagrams would not emerge. In the same manner, if there are higher order interactions, e.g. in effective theories, there would even be higher loop-orders.

[23] As mentioned above the one-loop structure of the flow equation is immanent for quadratic regulators. In principle, it is possible to regulate also in higher orders of the fields. In this case the one-loop structure

loop-orders do not restrict the formalisms to the same-loop orders in perturbation theory as both, flow equations as well as DSEs, contain dressed vertices for which themselves loop-equations exist. Already inserting the equations for the three-point functions shows that the loop order increases, which would continue for all higher vertices. Note that this does not necessarily correspond to a perturbative resummation, i.e. summing up an infinite amount of perturbative diagrams. However, perturbative resummations can be accessed via choosing a perturbative truncation.

A flow equation can be seen as the differential form of a DSE. Thus, it is possible to derive a flow equation from a DSE by two steps. Firstly, a renormalisation group scale is introduced into the action in the same fashion as in the flow equation, namely by adding a regulator to the action. This renders all Green functions that appear in the DSE scale-dependent, not only the propagators, which receive a regulator term, but also the vertices as they depend on the propagators. Secondly, a total derivative with respect to this scale k is taken. This derivative acts on the vertices and the propagators. Further, in the propagators it hits the $\Gamma^{(2)}$, but also the regulator. It is this point where the typical term $\partial_t R$ arises,

$$-\partial_t G_k \;=\; G_k \left(\partial_t \left(R + \Gamma_k^{(2)}\right)\right) G_k \,, \tag{3.66}$$

where the scale derivative only acts onto the bracket.

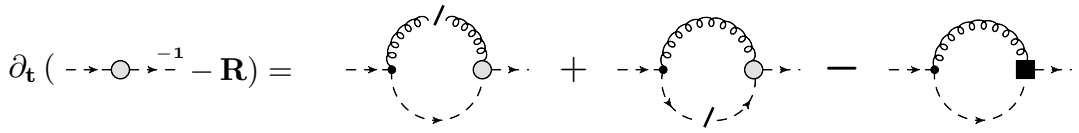

Figure 3.23.: By introducing a scale k in the DSE in the same way as in the FRG approach and then taking a total derivative of the DSE with respect to k one can derive a flow equation from the DSE. This figure shows the resulting flow equation for the ghost propagator. Compared with the FRG equation in fig. (3.8) the tadpole terms are missing. Their contributions are absorbed. The slashed lines denote the scale derivative of the full propagator (without the minus sign that arises in the derivative), i.e. the right hand side of eq. (3.66). The shaded blob denotes the full vertex, the square is the scale derivative acting on the vertex.

In the computations of correlation functions of Yang–Mills theory and QCD, that are presented in later chapters this procedure is employed for the ghost-propagator as well as the ghost-gluon vertex. For the ghost-propagator the resulting equation is given diagrammatically in fig. (3.23). Note that the derivative of the bare propagator vanishes. Both, fig. (3.23) and fig. (3.8) are exact equations for the ghost propagator, i.e. they describe

of a flow equation can be lost.

the same correlation function. But in the latter equation the four-point vertices have disappeared from the equation.

Alternatively, one can convince oneself that this procedure of taking a renormalisation group scale derivative of the scale-dependent DSE to produce a flow equation is equivalent to resumming the DSE with the flow. So inserting the flow equations for the $\Gamma^{(4)}_{\bar{c}c\bar{c}c}$ and $\Gamma^{(4)}_{\bar{c}A^2c}$ in the ghost DSE fig. (3.21) yields the very same equation as fig. (3.23). The actual computation is rather tedious, therefore I do not present it here.

This representation of flow equations may seem tempting at first sight, because in this form one recovers the feature that every diagram contains a bare vertex and, as a consequence, in some cases the number of vertices is reduced. However, the merits of this methods can be relativised. First of all, the equations depend not only on the n-point functions but also on the flows of them. As usual, this would be irrelevant in a full setting, but for truncated systems this is often disadvantageous. Secondly, and more importantly, the DSEs are not always of one-loop form, but can contain higher loop orders, e.g. DSE for the gluon propagator involves a two-loop diagram. As this structure would persist the scale derivative the corresponding flow equation is of two-loop order as well. Therefore, this alternative method is only promising in selected cases. In the computations for Yang–Mills theory presented below these cases are the ghost propagator and the ghost-gluon vertex.

4. Yang–Mills Theory at Non-Vanishing Temperature

In this chapter I present the results for Yang–Mills theory at non-vanishing temperature. In the approach followed here, which is explicated in chapter 3, the quantum theory given in terms of correlation functions serves as the starting point for the study of thermal effects. The first emphasis of this chapter is the truncation that is used to compute the flow of the quantum theory. Within the last decades it has turned out that sophisticated approximations are necessary to obtain quantitatively accurate correlation functions in the mid-momentum and infrared regime. The advancement of the truncation was part of this work. In order to find a proper truncation the flows of the vertices are studied in detail at vanishing temperature, in particular the ghost-gluon vertex and the purely gluonic vertices. The results are presented in section 4.1.
In section 4.2 I address to the computation of correlators at finite temperature following the line of thought of chapter 3. The study is optimised for low and intermediate temperatures, so for temperatures ranging from $0 \leq T \lesssim 5\,T_c$, where T_c is the phase transition temperature of the deconfinement-confinement phase transition. As lattice results for the chromoelectric and chromomagnetic gluon propagators as well as the ghost propagator are available, I compare the propagators obtained within the FRG setting with lattice gauge theory.
In section 4.2, I present results for Yang–Mills thermodynamics obtained in the FRG framework. Again, the focus lies on the range of temperatures around the deconfinement-confinement phase transition. As precise data for thermodynamic quantities from lattice gauge theory is given, I compare the results with the lattice.
In the last section of this chapter I summarise the main findings.

4.1. Approximation

In this section I detail the truncation that is applied in the following computation of correlation functions of Yang–Mills theory. The approximation allows for quantitative studies at vanishing as well as non-vanishing temperature.

In general, the structure of the flow of the effective action, see fig. (3.6), entails that flows of n-point functions depend explicitly on $(n+2)$-point functions. The relevant example

for the present work is the flow of the (inverse) Yang-Mills propagators $\Gamma_k^{(2)}$, displayed in fig. (3.7) and fig. (3.8). These flows depend on $\Gamma_k^{(n)}$ with $n \leq 4$. In other words, the functional flow in eq. (3.15), if broken up in the flows of n-point functions, constitutes an infinite hierarchy of coupled integro-differential equations. For computational purposes the system must be closed: The set of potentially contributing operators must be rendered finite such that the relevant physics is kept in the approximation, cf. section 3.2.2. Moreover, the approximation should be subject to self-consistency checks that give access to the systematic error.

At first, I describe the approximation put forward here for the flow of the propagators in fig. (3.7) and fig. (3.8). Then the explicit parameterisation/approximation in terms of $\Gamma_k^{(n)}$ with $n \leq 4$ is given: The propagators are not truncated but rather the full momentum dependence is taken into account. Further, the equations are closed with self-consistent approximations to the vertices which respect the renormalisation group properties of the vertices. For the ghost-gluon vertex the flow equation that is derived from the DSE of the vertex, see section 3.4, is studied at vanishing temperature. It turns out that the naive improvement of evaluating the vertex flow at the symmetric point and identifying the momentum argument with the renormalisation scale k is overestimating the change of the vertex with the scale. In particular in the propagator flows, this leads to a reweighting of diagrams with pure ghost content with respect to diagrams with purely gluonic content. Therefore, the resolution of the vertex in a momentum-dependent way is to be preferred. However, the full inclusion of the momentum-dependent vertex at finite temperature is beyond the scope of this work. Instead a constant vertex is taken, which is a relatively good truncation in view of the non-renormalisation of the ghost-gluon vertex. Further, it keeps the weights between the different diagrams as they have been established in the definition of the running coupling. This is explained further in section 4.1.3.

For the three-gluon and four-gluon vertices ansätze are used in this computation. They are constructed in such a way that the effects of the temperature in the vertices is mimicked. The effect is a suppression of the vertices for at least intermediate and high temperatures which is due to the suppression of the propagators in this temperature range. At vanishing temperature the ansätze are chosen such that they give the correct perturbative running for high scales k, but account for non-perturbative effects in the infrared. A posteriori, the validity of the ansatz at zero temperature for the three-gluon vertex is confirmed, especially in the infrared region. For this the flow equation for the three-gluon vertex as a function of the renormalisation group scale k is studied at the symmetric point with the momentum configuration $p^2 \gtrsim 0$. With this configuration the comparison with perturbation theory in the ultraviolet is valid and the perturbative running of the vertex is reproduced at ultraviolet scales. More details are given in section 4.1.4.
For the four-gluon vertex a similar ansatz is employed. On the one hand, this is supposed to be justified by the experience gained in the study of the validity of the three-point gluonic function. On the other hand, this vertex has been studied in the framework of its

DSE [428]. The reliability of the renormalisation group consistent four-gluon vertex can be compared with these DSE results.

4.1.1. Two-Point Functions and their Flows

Apart from the dependence on the field expectation value the two-point functions are fully taken into account, i.e. the dependence on (spatial) momentum p and renormalisation group scale k is kept[1]. In this computation the localised two-point functions $\hat{\Gamma}^{(2)}$ are employed, see section 3.2.5. In addition, the correlators in terms of cutoff-independent fields are obtained with eq. (3.39), eq. (3.49) and eq. (3.63).

In Landau gauge the gluon is a purely transversal particle with respect to spacetime, see eq. (2.28) and eq. (2.29). In contrast to this, the ghost is a Lorentz-scalar particle. Therefore, one (Lorentz-scalar) wave-functional renormalisation for each field is sufficient to describe the propagators at zero temperature, $Z_{A,k}(p)$ for the gluon[2] and $Z_{c,k}(p)$ for the ghost (and anti-ghost).
In section 3.2.6 it is argued that at non-vanishing temperature the heat bath breaks manifest Lorentz symmetry. This singles out the rest frame of the heat bath as a preferred frame. Consequently, in the three-dimensional spatial subspace there are two different tensor structures, which are obtained by projections on the longitudinal and transversal spatial direction with respect to the heat bath vector. The projection operators P_L and P_T are given by

$$\begin{aligned} P^T_{\mu\nu}(p_0,\vec{p}) &= (1-\delta_{\mu 0})\,(1-\delta_{\nu 0})\left(\delta_{\mu\nu} - p_\mu p_\nu/\vec{p}^{\,2}\right), \\ P^L_{\mu\nu}(p_0,\vec{p}) &= \Pi^{\mathrm{T}}_{\mu\nu}(p) - P^T_{\mu\nu}(p_0,\vec{p}), \end{aligned} \tag{4.1}$$

where $\Pi^{\mathrm{T}}_{\mu\nu}$ is the four-dimensional transversal projection operator, see eq. (2.28). These two tensors demand for a parametrisation of the gluon in terms of two different wave-function renormalisations $Z_{L,k}(p)$ and $Z_{T,k}(p)$. Both tensors are transversal in four dimensional space, thus, in the limit of $T \to 0$ these tensor structures reproduce exactly the four-dimensional projector and the two wave-function renormalisations agree $Z_{A,k}(p) = Z_{L,k}(p) = Z_{T,k}(p)$.
Trivially, the Lorentz-scalar structure of the ghost is independent of the heat bath vector, thus, the ghost can be parametrised with one function at vanishing as well as non-zero

[1] Note however, that the dependence on the field expectation value is dropped. The inclusion of this is subject of section 4.3 and chapter 5.

[2] At non-zero k the $O(4)$ symmetry is only realised, if the regulator is chosen to be symmetric. E.g. one possible non-symmetric definition is a three-dimensional regulator which only regulates the spatial momentum. In this case the differentiation between the longitudinal and transversal tensors in the three-dimensional subspace is inevitable for non-zero k, although the theory is $O(4)$ symmetric at $k = 0$, i.e. for vanishing temperature. Nonetheless, this regulator is applicable, yet it suffers from other hardships. As pointed out in section 3.2.5, locality of the flow is important. As three-dimensional regulators do not cut off the temporal direction the flow is rather non-local in this direction, as it only falls of polynomially. For quantitative numerical studies at non-vanishing temperature in the setup employed here, this regulator is therefore poorly suited.

temperature.

Finally, the parameterisation of the gluons and ghost is given by

$$\begin{aligned}\hat{\Gamma}^{(2)}_{A,L}(p_0,\vec{p}) &= Z_L(p_0,\vec{p})\,p^2\,P^L(p_0,\vec{p})\,,\\ \hat{\Gamma}^{(2)}_{A,T}(p_0,\vec{p}) &= Z_T(p_0,\vec{p})\,p^2\,P^T(p_0,\vec{p})\,,\\ \hat{\Gamma}^{(2)}_{c}(p_0,\vec{p}) &= Z_c(p_0,\vec{p})\,p^2\,,\end{aligned} \tag{4.2}$$

where the identity in colour space is suppressed and the Z's are functions of p_0 and $\vec{p}$ separately as the Euclidean $O(4)$ symmetry is broken by the temperature. In the following the abbreviation p^2 at non-vanishing temperature denotes $p^2 = p_0^2 + \vec{p}^2$.

In fact, the dependency on the Matsubara modes can be formulated in an easy approximation. The approximation is based on the fact that the effect of temperature vanishes quickly for momenta larger than the first Matsubara mode, see section 3.2.6. So higher Matsubara modes can be described well by shifting the spatial momentum of the zeroth Matsubara mode by the time component of the particular Matsubara mode, viz.

$$\Gamma^{(2)}_{\varphi}(p_0,\vec{p}) \approx \Gamma^{(2)}_{\varphi}\left(0,\sqrt{p_0^2+\vec{p}^2}\right). \tag{4.3}$$

This approximation turns out to be very good as it is known from the lattice and DSE [305, 429] and here it is confirmed a posteriori in fig. (4.18).

The parameterisation of $\Gamma^{(2)}$ follows from that of $\hat{\Gamma}^{(2)}$ in eq. (4.2), and is read off the definition of $\phi(\varphi)$ in eq. (3.35) and eq. (3.46),

$$\Gamma^{(2)}_{A,L/T} \simeq \hat{Z}_{L/T}(p)\,Z_{L/T}(p)\,p^2\,, \quad \Gamma^{(2)}_{c} \simeq \hat{Z}_{c}(p)\,Z_{c}(p)\,p^2\,. \tag{4.4}$$

These expressions can be inverted trivially, as the longitudinal tensor does not mix with the transversal one

$$\left(P^T_{\mu\nu}\mathscr{A} + P^L_{\mu\nu}\mathscr{B}\right)^{-1} = P^T_{\mu\nu}\mathscr{A}^{-1} + P^L_{\mu\nu}\mathscr{B}^{-1}\,. \tag{4.5}$$

Like in the case of vanishing temperature, the triviality of inversion is again due to the fact that Landau gauge does not allow for tensor structures that mix transverse and longitudinal directions. In arbitrary gauges this does not hold, see e.g. [430] for the general case and the inversion prescription.

The flow equations for the two-point functions are given diagrammatically in fig. (3.7) and fig. (3.8). Their right hand sides depend on the two-point functions as well as three- and four-point functions. In particular, there are tadpole diagrams which depend on the ghost-ghost and ghost-gluon scattering vertices $\Gamma^{(4)}_{\bar{c}c\bar{c}c}$ and $\Gamma^{(4)}_{\bar{c}A^2c}$, respectively. These vertices vanish classically and in a first approximation one is tempted to drop the related

diagrams. However, they can be considered in a rather simple way, which is detailed already in section 3.4, where an alternative flow equation for the ghost propagator was derived via taking a scale derivative of the ghost DSE. This provides a DSE-resummation of the vertices in a given approximation to the flow, given in fig. (3.23).

The DSE-flow is finite by construction, as it can be derived from the manifestly finite ghost flow in fig. (3.8) by inserting the DSEs for the ghost-ghost and ghost-gluon scattering vertices. These DSEs are also manifestly finite and require no renormalisation. This can be seen at the individual terms in fig. (3.21) and fig. (3.23), respectively. First of all, note that the total t-derivative of the propagators, $\partial_t G$, shown in eq. (3.66) acts as a ultraviolet-regularisation of the loops. They decay at least with G^2 as $\partial_t \Gamma_k^{(2)}$ tends towards a constant for large momenta. The total t-derivative $\partial_t \hat{G}$ decays even more rapidly with $\partial_t \hat{R}$ for large momenta due to eq. (3.47). This reflects again the locality implemented by eq. (3.47) and its practical importance. The last diagram is proportional to the flow of the ghost-gluon vertex. This is discussed in detail in the section 4.1.3, and is displayed schematically in fig. (4.5). Here, it suffices to say that the vertex itself is protected from renormalisation and its flow decays rapidly for large momenta.
Both flow equations given in fig. (3.8) and fig. (3.23) for the ghost are exact and are related via the above resummation procedure. In the present approximation scheme the DSE is more favorable, because the four-point functions do not appear explicitly in the total derivative of the DSE. But instead of dropping the related contributions, they are absorbed in the diagrams with cutted propagators. Notably, the ghost-ghost scattering vertex $\Gamma^{(4)}_{\bar{c}c\bar{c}c}$ disappeared completely from the set of flow equations of ghost and gluon propagators, whereas the ghost-gluon scattering vertex $\Gamma^{(4)}_{\bar{c}A^2c}$ is still present in the flow of the gluon two-point function.

The behaviour of the wave-function renormalisation of the ghost at non-vanishing temperature is such that it is suppressed with the temperature. The question arises whether it can turn negative. However, it can only be answered under consideration of the ghost-gluon vertex and the non-perturbative running coupling, both of which are introduced in section 4.1.3. Thus, the discussion of the behaviour of the Z_c is delayed to this section.

Forestalling the remaining details of the precise truncation at hand, fig. (4.1) shows the individual contributions to the full flows of the two-point functions. They are detailed already here, because they give valuable information about the structure of the truncation, in particular for gluonic vertices at zero and non-zero temperature, see section 4.1.4.

In fig. (4.1(a)), the purple, dashed–triple-dotted line shows the full flow of the gluon at zero temperature in the truncation at hand at a fixed renormalisation group scale $k = 5\,\mathrm{GeV}$. As the flow is not just a constant, it yields a non-trivial momentum-dependence of the gluon propagator along the flow.

In the truncation utilised here, the flow of the gluon receives three contributions stemming

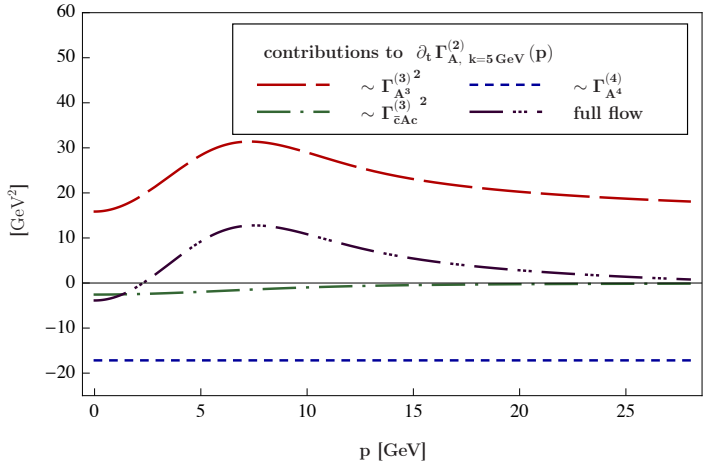

(a) Individual contributions to the flow of the gluon two-point function.

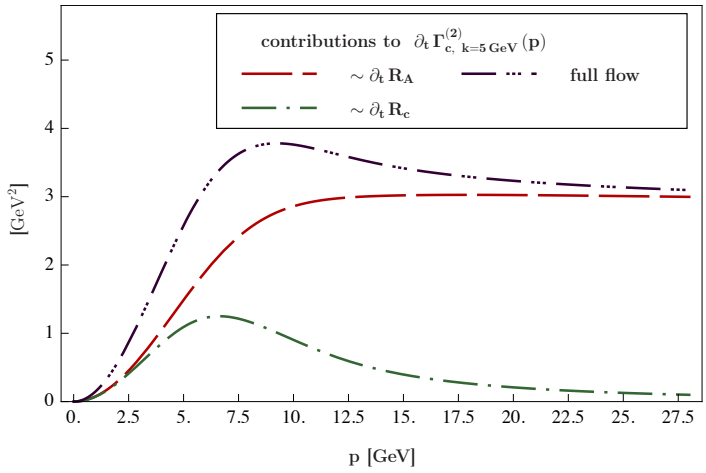

(b) Individual contributions to the flow of the ghost two-point function.

Figure 4.1.: Typical flows of the two-point functions of Yang–Mills at a fixed scale $k = 5\,\mathrm{GeV}$ in the truncation at hand, cf. fig. (4.12). Both flows are peaked around $p \gtrsim k$, where the location of the peak is determined by the choice of the shape function of the regulator. In the gluon flow, the contribution of the diagram involving two three-gluon vertices is largely cancelled by the tadpole.

from the first three loop diagrams in fig. (3.7). Naturally, the system is coupled in the sense that the two-point functions couple back into the diagrams, as the internal lines are full propagators. The red, long-dashed line denotes the contribution of the diagram involving two three-gluon vertices, i.e. the first diagram in fig. (3.7). It yields a positive contribution. In contrast to this, the other two diagrams yield negative partial flows. The third diagram in fig. (3.7) is called tadpole, shown by the blue, dashed line. It is constant here as it is independent of the external momentum due to the absence of momenta in

the classical tensor structure of the four-gluon vertex, cf. appendix E. As the classical tensor is the only one considered in the ansatz for the four-gluon correlator, the only momentum in the tadpole is the loop momentum itself, which is related to the scale k. The green, dashed-dotted line is the contribution of the ghost-loop, i.e. the second diagram in fig. (3.7).
At the scale considered here the ghost-contribution is the smallest one in absolute size. However, it is an interesting effect that most of the contributions of the tadpole cancel the flow of the diagram with two three-gluon vertices. As a result, the flow is diminished significantly in comparison with the individual gluonic contributions. This necessitates the balance between the individual diagrams which must not be spoiled by choosing a bad truncation. Furthermore, the flow changes its sign. This yields an even more complex change of the $\hat{\Gamma}^{(2)}_{A,k}(p)$ along the flow.

The full flow of the ghost two-point function is given as the purple, dashed–triple-dotted line in fig. (4.1(b)). It only has two different contributions in the truncation employed here. The green, dashed-dotted line shows the contribution of the diagram, where the scale derivative acts on the ghost regulator. The red, long-dashed curve shows the contribution from the diagram, where the scale derivative hits the gluon regulator. Interestingly, the contribution of the latter diagram approaches a constant at high momenta, because for the classical ghost-gluon vertex there is a tensor structure which is independent of the loop momentum, as at vanishing temperature the Lorentz-tensor structure is simply given by

$$\sim (p+q)_\mu \, p_\nu \Pi^{\mathrm{T}}_{\mu\nu}(q) = p^2 - \frac{(p_\mu q_\mu)^2}{q^2}\,, \tag{4.6}$$

where p is the external momentum, q the loop momentum, and the transversal projector is defined in eq. (2.28). As the second term in eq. (4.6) is subject to regularisation the term $\sim p^2$ dominates at large momentum.

In the flow of the ghost both diagrams give a positive contribution, however, note that the ghost-propagator is pushed to more negative values with increasing k due to the negative dispersion of the ghost, see eq. (2.32).

4.1.2. Vertices and their Flows

For the vertices it is convenient to take a paramerisation that separates the generic renormalisation group running of the vertices and split off the non-trivial rest. Herein, the natural running is determined by the external particles that enter the vertex. This generic running is therefore set by the wave-function renormalisations of the corresponding fields. As the two-point function is parametrised in Z_ϕ, there is the factor of $Z_\phi^{\frac{1}{2}}$ for each external field. This construction is motivated by one-loop perturbation theory, thus, it is clearly good for high values of k. For infrareddish scales below Λ_{QCD} this ansatz is not suited anymore. Therefore, in terms of $\bar{Z}$'s that are simply the perturbative ones in the far ultraviolet but mimic the correct infrared behaviour more accurately, the full vertex

ansätze are given. These modified factors $\bar{Z}$'s are proportional to the wave-function renormalisations Z, and hence carry the renormalisation group scaling of the vertex as well as the momentum dependence of the legs: They carry potential kinematical singularities, see e.g. [249].

Dropping the generic dependence on the renormalisation group scale for clarity, the $\bar{Z}$'s are defined by

$$\bar{Z}_{L/T}(p) = \frac{Z_{L/T}(p)\,p^2 - \left[Z_{L/T}(q)q^2\right]_{q\to 0}}{p^2}\,, \tag{4.7}$$

$$\bar{Z}_c(p) = Z_c(p)\,, \tag{4.8}$$

with $\bar{Z}_{L/T} = \bar{Z}_A$ at vanishing temperature. The subtraction prescription eq. (4.7) is well suited due to the use of decoupling type solution, i.e. $Z_{L/T}(q)q^2$ approaches a constant for $q \to 0$. The subtraction in the $\bar{Z}_{L/T,k}(p)$ guarantees that the infrared divergent function $Z_{L/T,k}(p)$ does not trigger an infrared-divergent vertex, which would yield divergent gluonic flow diagrams. That these divergences are not the physically realised correlation functions is confirmed later in section 4.1.4. This is also seen on the lattice [327]. Actually, for the ghost the usual wave-function renormalisation can remain as an ansatz in the vertices as the $Z_{c,k}(p)$ is regular.

In addition to that, the non-trivial part due to quantum and thermal fluctuations as well as the canonical momentum and tensor structure are added, i.e. tensors for Lorentz- or colour indices. In the following, this part is denoted by a general tensor $\mathcal{T}$. This gives the vertex construction for the vertices in the (localised) flows of the two-point functions of Yang–Mills theory

$$\hat{\Gamma}^{(n)}(p_1,...,p_n) = \prod_{i=1}^{n} \bar{Z}_{\phi_i}^{1/2}(p_i)\,\mathcal{T}(p_1,...,p_n)\,. \tag{4.9}$$

However, the shape of the wave-function renormalisation still does not reflect the expected properties of the gluonic vertices. Therefore, the $\bar{Z}_{L/T}(p)$ are frozen for $p \le p_{\text{peak}}$, where p_{peak} is the potential turning point of the inverse propagator $\Gamma^{(2)}_{L/T,k}$ in the infrared, defined by $\partial_p(p^2 Z_{L/T}(p))_{p=p_{\text{peak}}} = 0$. This turning point p_{peak} implies that the $\bar{Z}$ becomes negative below this scale and approaches its value in the $k \to 0$ limit from below 0. This is actually a sign of the bending over of the gluon propagator, thus, a sign of positivity violation, cf. section 2.3.1. By cutting off the $\bar{Z}_{L/T}$ at some scale above the turning point it is guaranteed to remain positive. Note that this is done simply for convenience in order to avoid the splitting of a positive vertex dressing into two negative factors. The $\bar{Z}$'s take into account the renormalisation group scaling of the fields and reflect the gaps present in the gluonic degrees of freedom.
At finite temperature the turning points depend on T and differ for Z_T and Z_L, the turning point of the latter tends towards *zero* for $T \to \infty$ due to the Debye screening.

This yields a renormalisation group invariant tensor $\mathcal{T}$. It is regular up to logarithms and carries the canonical momentum dimension as well as the tensor and colour structure. For the flow of the propagators, fig. (3.7) and fig. (3.8), $\mathcal{T}$ has to be computed for the three-gluon and four-gluon vertex, the ghost-gluon vertex and for the four-ghost as well as ghost-gluon scattering vertices. The latter two, which are absent on the classical level, are treated in terms of exact resummations in the ghost-propagator flow with the help of DSEs. The corresponding term in the gluon propagator involving the ghost-gluon scattering kernel is dropped.

For the other vertices, i.e. for the vertices that are present in the classical theory already, the locality of the flow equation is utilised in the following way: The flow only carries loop momenta $q^2 \lesssim k^2$ and is peaked at about $p^2 \approx k^2$. Hence, the vertices are well approximated by evaluating them at the symmetric point at $\vec{p}_i^{\,2} = k^2$, see also appendix B, and vanishing temporal components,

$$(p_i)_0^2 = 0 \qquad \text{and} \qquad \vec{p}_i^{\,2} = k^2 \,. \tag{4.10}$$

In this approximation the $\bar{Z}$-factors in eq. (4.7) and eq. (4.8) can be evaluated at the fixed momentum of the symmetric point with eq. (4.10), i.e. the momentum p in each $\bar{Z}$ is identified with the renormalisation group scale k in order to match it with the truncation for the vertices at the symmetric point. Therefore,

$$\begin{aligned} \bar{Z}_{A,k} &= \bar{Z}_A(k)\theta_6(k,k_s) + \bar{Z}_A(k_{\mathrm{IR}})\,(1-\theta_6(k,k_s))\,, \\ \bar{Z}_{c,k} &= \bar{Z}_c(k)\,, \end{aligned} \tag{4.11}$$

where the function $\theta_n(k,\mu)$ defines a function to freeze out the $\bar{Z}_A$ in the infrared in a smooth way, because not only the $\bar{Z}_{A,k}$ enters the computation. In addition, also its derivative with respect to k emerges due to the definition of the regulator of the gluon, see eq. (4.40). The regulator comprises the $\bar{Z}_{A,k}$ as a prefactor. In eq. (4.11) the parameter k_s regulates the point around which the $\bar{Z}_A$ is frozen and $\bar{Z}_A(k_{\mathrm{IR}})$ is the value it approaches in the deep infrared. The function $\theta_n(k,\mu)$ is smooth and approaches the Heaviside function in the limit $n \to \infty$. It is defined by

$$\theta_n(k,\mu) = 1 - \frac{\left(\frac{k}{\mu}\right)^n}{e^{\left(\frac{k}{\mu}\right)^n} - 1}\,. \tag{4.12}$$

The values of k_s and k_{IR} are chosen particularly for the properties of the gluonic two-point function, where the freezing scale $k_s \propto \Lambda_{\mathrm{QCD}}$ in eq. (4.11) is chosen such that it is of the order of p_{peak}, i.e. $k_s = .9\,\mathrm{GeV}$, the value of $k_{\mathrm{IR}} = 1.4\,\mathrm{GeV}$ and the function is chosen to be rather smooth $n = 6$. Actually, the freezing of the $\bar{Z}_{A,k}$ at k_s only defines the parameterisation of the ghost-gluon vertex. The soft step function $\theta_6(k,k_s)$ is given in fig. (4.2(a)) and the final expressions of the $\bar{Z}_{A,k}$ and $\bar{Z}_{c,k}$ at vanishing temperature are

given in fig. (4.2(b)) and fig. (4.2(c)).

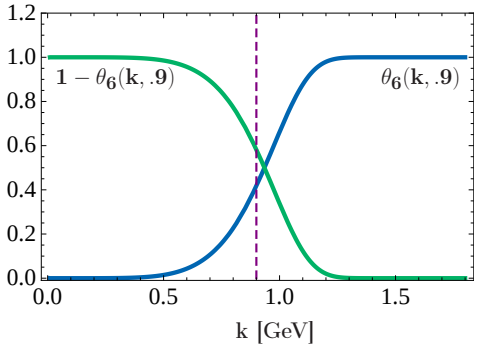

(a) Soft Heaviside function to freeze the $\bar{Z}_{A,k}$ in the infrared.

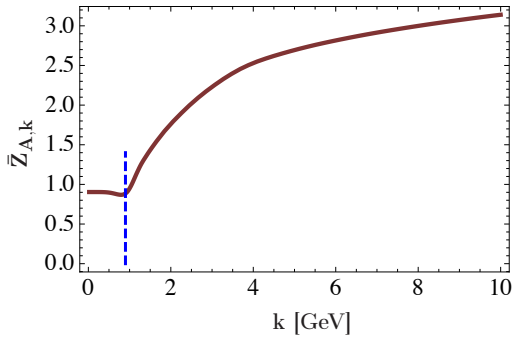

(b) $\bar{Z}_{A,k}$ as defined in eq. (4.11) at vanishing temperature.

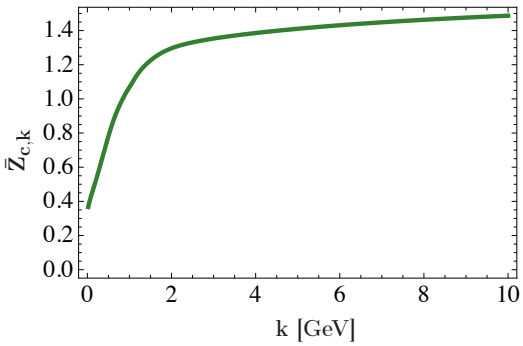

(c) $\bar{Z}_{c,k}$ as defined in eq. (4.11) at vanishing temperature.

Figure 4.2.: Definition of the $\bar{Z}_{A/c}(k)$ at vanishing temperature.

At non-vanishing temperature the $\bar{Z}_{A,k}$ is either $\bar{Z}_{L,k}$ or $\bar{Z}_{T,k}$, depending on the projection $P^{T/L}$ defined in eq. (4.1) on the respective leg of $\Gamma_k^{(n)}$.
In a slight abuse of notation this defines momentum-independent, but renormalisation group scale k-dependent factors $\bar{Z}(k)$: The $\bar{Z}$-factors in eq. (4.11) are functions of p_0^2 and $\vec{p}^2$, which are evaluated at eq. (4.10).

For the gluonic vertices at vanishing and non-zero temperature this gives a formally consistent definition. However, the effect of the temperature in the $\bar{Z}$'s does not necessarily render physically appropriate ansätze for the gluonic vertices at non-vanishing temperature. Further details on the truncation of the gluonic vertices at non-vanishing temperature are given in section 4.1.4.

4.1.3. Ghost-Gluon Vertex

In the truncated system three different vertices appear, the trigluon vertex $\Gamma^{(3)}_{A^3}$, the tetragluon vertex $\Gamma^{(4)}_{A^4}$ and the ghost-gluon vertex $\Gamma^{(3)}_{\bar{c}Ac}$. For these correlators the dressings $\mathcal{T}$ must be determined. Compared to other vertices, in these cases it is rather easy to find a reasonable ansatz. The reason for this is that these interaction terms have a classical counterpart, i.e. they are present in the classical action. All the other vertices emerge via quantum fluctuations. Though, for the classical vertices it is possible to determine the classical tensor structure by functional derivatives with respect to the external fields that enter the vertex. In the following only the classical tensor structures are kept, although in a full treatment the vertices would have to be spanned via all possible tensor basis obtained from a tensor decomposititon, wherein each tensor would carry a non-trivial dressing function. Spanning the full vertices is an intricate task, therefore, in most numerical Yang–Mills studies the classical tensor structures or at most subsets of the tensor basis have been considered. For the three remaining vertices in the truncation above only the classical tensor structure is taken into account.

In approximations in the framework of the FRG a reasonable ansatz for the non-perturbative vertices is the classical tensor structure, given in appendix E, with a k-dependent dressing function that encodes the quantum and thermal fluctuations. At the symmetric point the centre of mass momentum is identified with the renormalisation group scale k which yields that the vertices feel the scale in the most direct way, due to the locality of the flow. This strategy is followed for all three vertices that appear in the coupled system.

As a result, the ghost-gluon vertex is parametrised as

$$\mathcal{T}^{abc}_{\bar{c}Ac,\mu}(q,p) = z_{\bar{c}Ac,k}\,\frac{1}{g}[S^{(3)}_{\bar{c}Ac}(q,p)]^{abc}_{\mu} = z_{\bar{c}Ac,k}\,iq_\mu f^{abc}\,, \tag{4.13}$$

where g is the classical coupling, $S^{(3)}_{\bar{c}Ac}$ is the classical ghost-gluon vertex derived from eq. (2.18), carrying three colour indices and one Lorentz index, see appendix E. Further, p, q are the ghost and anti-ghost momenta, respectively, see fig. (4.3). Note that the non-perturbative running coupling is defined via the definition of the $z_{\bar{c}Ac,k}$. Due to momentum conservation in the vertex the dependence on the gluon momentum r is expressed as a dependence on the (anti-)ghost momentum.

The k-dependent factor $z_{\bar{c}Ac,k}$ is a renormalisation group invariant and defines a running coupling,

$$\bar{\alpha}_s(k) = \frac{z^2_{\bar{c}Ac,k}}{4\pi}\,, \tag{4.14}$$

with running momentum scale k. If expanded in powers of the coupling for large momenta, $\bar{\alpha}_s$ has the one and two-loop universal coefficients of the β-function of Yang–Mills theory. Note that this necessitates the fact that $\bar{Z}_{A,k} \to Z_{A,k}$ for large cutoff scales.

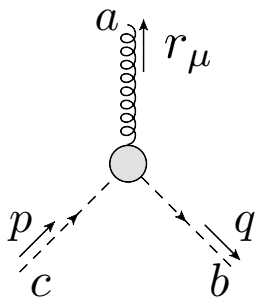

Figure 4.3.: Ghost-gluon vertex.

The flow of $z_{\bar{c}Ac,\,k}$ is extracted from that of the ghost-gluon vertex. The properties and the behaviour of this flow is studied next. Here, this flow is computed within a DSE-resummation similar to the derivation that is made for the ghost propagator. Again,

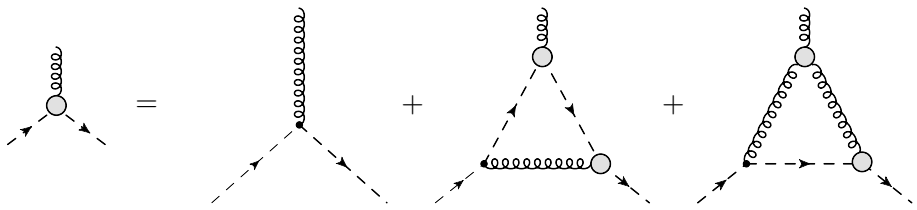

Figure 4.4.: DSE for the ghost-gluon vertex in the chosen truncation. The vertex without the shaded circle denotes the classical vertex.

the DSE-resummed flow is finite as it is derived from the standard flow equation for the ghost-gluon vertex which is finite by construction. Note however, that already the DSE in fig. (4.4) is finite without renormalisation procedure due to the non-renormalisation theorem for the ghost-gluon vertex. Due to simple kinematical reasons, it is also present in approximation schemes that respect the kinematical symmetries.

The above arguments allow to start straightaway with the simple ghost-gluon DSE, see fig. (4.4), which only contains one-loop terms. Similarly to the flow for the ghost propagator, the DSE in fig. (4.4) is turned into a flow equation by taking the t-derivative of fig. (4.5). The running of the vertex allows for a momentum- and temperature-dependent computation of the vertex which has an effect in the calculation of the propagators.

It remains to project the vertex flow onto that of the renormalisation group invariant dressing function $z_{\bar{c}Ac,\,k}$. Note that this is not the full vertex, as the $\bar{Z}$'s have been factorised, eq. (4.9). Omitting the k-argument, the projection on the classical vertex

structure is done by

$$\Gamma_{\bar{c}Ac}(P) = g \left(\frac{[\hat{\Gamma}^{(3)}_{\bar{c}Ac}]^{abc}_{\mu} [S^{(3)}_{\bar{c}Ac}]^{abc}_{\mu}}{[S^{(3)}_{\bar{c}Ac}]^{def}_{\nu} [S^{(3)}_{\bar{c}Ac}]^{def}_{\nu}} \bigg|_{g=1} \right)_{p^2=q^2=(p+q)^2=P^2} , \tag{4.15}$$

with an evaluation at the symmetric point at the momentum scale P. For the classical vertex $\Gamma^{(3)}_{\bar{c}Ac} = S^{(3)}_{\bar{c}Ac}$ derived from eq. (2.18) the dressing is simply unity, thus $\Gamma_{\bar{c}Ac,k}(P) = g$.

A first improvement compared to the classical vertex is to evaluate the vertex at the momentum scale k, as it is done in the vertex construction. What enters this approximation in particular is that the flow of the vertex receives the main contributions always from the momentum region around the renormalisation group scale. Thus the flow itself is only evaluated at $P = k$. So by construction, this ansatz neglects parts of the momentum-dependence of the vertex. At zero temperature, the effect of this reduction is studied next. In the course of this the non-perturbative running coupling is introduced.

At first, the ghost-gluon vertex is evaluated at $P = k$, motivated by the locality of the flow. The full ghost-gluon vertex does not renormalise in the ultraviolet, however, this feature is not seen in the flow as the relevant momentum scale is shifted with k. Thus, a logarithmic running remains in the scale-dependent vertex. This does not invalidate the ansatz for the vertex, as the physical point is by construction at $k = 0$ only, where the fixed point of the coupling of the ghost-gluon vertex remains unchanged.
The identification in the flow is done accordingly, viz.

$$\partial_t \Gamma_{\bar{c}Ac,k} = \partial_t \Gamma_{\bar{c}Ac,k}(P = k) . \tag{4.16}$$

Note that the left hand side depends on k via the evaluation at $P = k$ but also due to the implicit dependence of the vertex on the cutoff scale. The full vertex dressing in eq. (4.16) also includes the dressing of the legs as split off in eq. (4.9). Hence, the tensor component $z_{\bar{c}Ac,k}$ is given by

$$z_{\bar{c}Ac,k} = \frac{1}{\bar{Z}^{1/2}_{A,k} \bar{Z}_{c,k}} \Gamma_{\bar{c}Ac,k} . \tag{4.17}$$

The flow $\partial_t z_{\bar{c}Ac,k}$ is determined from eq. (4.17) and is directly related to that of the ghost-gluon vertex. Taking the t-derivative of eq. (4.17) leaves

$$\left(\partial_t + \frac{1}{2} \frac{\partial_t \bar{Z}_{A,k}}{\bar{Z}_{A,k}} + \frac{\partial_t \bar{Z}_{c,k}}{\bar{Z}_{c,k}} \right) z_{\bar{c}Ac,k} = \partial_t \Gamma_{\bar{c}Ac,k} \frac{1}{\bar{Z}^{1/2}_{A,k} \bar{Z}_{c,k}} .$$

Upon integration the flow, eq. (4.17), gives the vertex dressing of the ghost-gluon vertex at a given cutoff scale k,

$$z_{\bar{c}Ac,k} = z_{\bar{c}Ac,k=0} + \int_0^k \frac{dk'}{k'} \partial_{t'} z_{\bar{c}Ac,k'} . \tag{4.18}$$

The input into applications of thermal flows is the $T = 0$ theory. Therefore, the initial condition for $z_{k=0,\bar{c}Ac}\big|_{T=0}$ is required. The determination of the vertex is non-trivial. However, the insights that were gained during the last decades in functional approaches to the infrared sector of Yang–Mills theory (at vanishing temperature) allow to fix the value of the running coupling in the limit $k \to 0$. For a review see e.g. [276]. At vanishing temperature a one-parameter family of solutions with infrared enhanced ghost propagators and gapped gluon propagators in Landau gauge has been found. They are described in section 2.3.2. All solutions have a gluon propagator with a mass gap $m_{\text{gluon}} \propto \Lambda_{\text{QCD}}$. They only differ from each other in the deep infrared for momenta $p^2 \ll \Lambda_{\text{QCD}}$. There, the gluon propagator is described by

$$Z_A(p \ll \Lambda_{\text{QCD}}) \propto c(p) \frac{m_{\text{gluon}}^2}{p^2}\,, \tag{4.19}$$

where $c(p) \gtrsim 1$ is a momentum-dependent function which is bounded from below. For all solutions but one $c(p)$ it is also bounded from above. These solutions are called decoupling solutions, as the gluon decouples in that momentum regime. There is one distinguished member of this family where $c(p)$ diverges with $p^{2+2\kappa_A}$ with $\kappa_A < -1$, see section 2.3.2 or [276]. This solution is called scaling solution as the infrared propagators and vertices are uniquely determined by scaling laws up to constant prefactors, see e.g. [241, 244, 248, 249, 254, 276, 282].

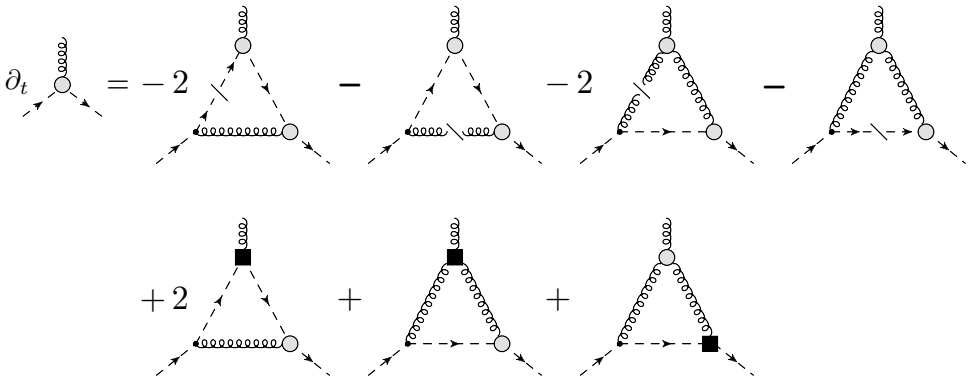

Figure 4.5.: Flow equation for the ghost-gluon vertex from the total t-derivative of the ghost-gluon vertex DSE in fig. (4.4). The cutted line stands for the scale derivative acting on the propagator of the corresponding field, see eq. (3.66). The shaded circles are the full vertices. The square denotes the scale derivative acting on the full vertex, the vertex indicated by a small black dot denotes the classical vertex.

Most importantly, the flow of the ghost-gluon vertex in fig. (4.5) is not sensitive to the infrared behaviour of the gluon propagator. Thus, it is insensitive to the choice of a scaling or decoupling solution as input for the thermal flow at vanishing temperature. All diagrams in fig. (4.5) vanish in the limit $k \to 0$ with powers of k^2/m_{gap}^2,

$$\lim_{k\to 0} \partial_t z_{\bar{c}Ac,\,k} \propto \frac{k^2}{m_{\mathrm{gap}}^2}\,. \tag{4.20}$$

This also entails that the vertex dressing tends toward a constant in the infrared. Therefore, the infrared value of the ghost-gluon vertex is the same for the whole class of solutions up to subleading terms in renormalisation group transformations. This can be used to compute $z_{\bar{c}Ac,\,k=0}\big|_{T=0}$ for the whole class of solutions. It has been shown that the scaling solution for constant ghost-gluon vertex dressings is determined in the FRG up to a renormalisation group constant, see [272],

$$z^2_{\bar{c}Ac,\,k=0}\big|_{T=0} \left(\frac{\bar{Z}_A(p)\bar{Z}_c^2(p)}{Z_{A,s}(p)Z_{c,s}^2(p)}\right)_{p=0} = 4\pi\alpha_{s,\mathrm{IR}}\,, \tag{4.21a}$$

with the scaling wave-function renormalisations $Z_{A/c,s}$ for ghost and gluon propagators, respectively. On the right hand side, the fixed point of the non-perturbative running coupling appears which is defined in terms of the ghost and gluon wave-function renormalisations [241],

$$\alpha_s(p) = \frac{g^2}{4\pi}\frac{1}{Z_A(p)\left(Z_c(p)\right)^2}. \tag{4.21b}$$

The fixed point of this coupling in the infrared $\alpha_{s,\mathrm{IR}}$ is analytically known [241]

$$\alpha_s(0) = -\frac{4\pi}{N_c}\frac{2}{3}\frac{\Gamma(-2\kappa)\Gamma(\kappa-1)\Gamma(\kappa+3)}{\left(\Gamma(-\kappa)\right)^2\Gamma(2\kappa-1)} \overset{N_c=3}{\approx} 2.97\,, \tag{4.21c}$$

where $\kappa \approx 0.595$, which also fixes the value of the unrenormalised coupling $g \approx 4.23071$ for the propagators at hand by eq. (4.21b).
For momenta $p \gg \Lambda_{\mathrm{QCD}}$ the $Z_{A/c,s}(p)$ tend towards the decoupling solutions up to renormalisation group scalings. Demanding equivalence for large momenta fixes the relative ultraviolet renormalisation condition. In summary, this allows to fix $z^2_{\bar{c}Ac,\,k}$ at vanishing temperature in terms of the ultraviolet renormalisation condition in a unique way for both, scaling and decoupling types of solutions. These couplings are shown in fig. (4.6), where the scaling solution shows the fixed point in the infrared. For the decoupling solution the same definition of the running coupling is used, thus, the coupling decreases in the infrared, as the wave-function renormalisation of the ghost tends to a constant and the wave-function renormalisation of the gluon diverges at $k \to 0$.

At non-vanishing temperature this coupling is employed as well. But there is a subtlety connected with the tensor structure of the gluon propagator. As mentioned above, the gluon propagator in Landau gauge has a purely transversal structure. However, at non-vanishing temperature this has to be projected with respect to the heat bath vector. These

two tensor structures allow for two different wave-function renormalisations for the gluon. As the coupling eq. (4.21b) is defined in terms of the gluonic wave-function, there are two separate couplings for the chromoelectric gluon $\alpha_{s,L}$ and the chromomagnetic gluon $\alpha_{s,T}$, both defined in analogy to eq. (4.21b), sc.

$$\alpha_{s,L/T}(p) = \frac{g^2}{4\pi} \frac{1}{Z_{L/T}(p) \left(Z_c(p)\right)^2} , \tag{4.22}$$

which also translates to similar expressions for the definition of the vertex $z^{L/T}_{\bar{c}Ac,\,k}$.

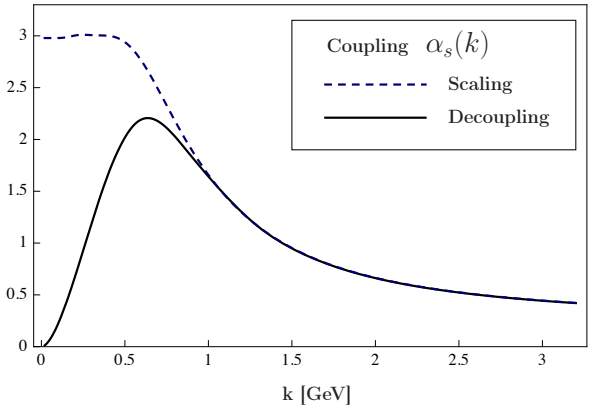

Figure 4.6.: The non-perturbative running coupling of Yang–Mills theory as defined in eq. (4.21b) for the scaling and decoupling solution. The coupling is constructed with the scaling propagators, it develops a renormalisation group fixed point in the deep infrared. Fixing the running coupling in the ultraviolet allows to use the same definition for the decoupling propagators as well. In the deep infrared this coupling vanishes. Thermal effects are insensitive to the choice of the type of solution of Yang–Mills correlation functions, because the deep infrared, i.e. the region where the two types differ, is suppressed.

In the light of the ongoing debate about the infrared behaviour of Landau gauge propagators in the vacuum it is important to stress the following: Firstly, the flow of the vertex function is not sensitive to the differences of the momentum behaviour of the propagators in the deep infrared, $p \ll \Lambda_{\mathrm{QCD}}$, as it is switched off for $k \to 0$ below Λ_{QCD}. Secondly, the above argument leading to eq. (4.21) only relies on the technical possibility of finding initial ultraviolet conditions for the flow in the given approximation which flow into the scaling solution in the infrared. This is trivially possible, see [272, 273, 276]. Then, the analytical values of the scaling solution fixes eq. (4.21) for both, scaling and decoupling solutions. This does neither resolve the infrared problem in Landau gauge Yang–Mills theory closely related to the picture of confinement, nor the Gribov problem in this gauge. However, above Λ_{QCD} there is no quantitative difference between the scaling or decoupling solution. For thermal effects only, which are the main concern of this work, these

two types of solutions show qualitatively the same behaviour also below the scale Λ_{QCD}, albeit they are qualitatively different in the deep infrared region.

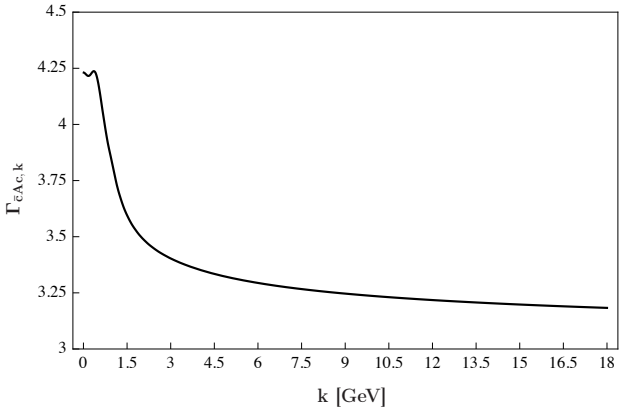

Figure 4.7.: Flow of the scale-dependent ghost-gluon vertex. The logarithic running is due to the identification of the centre-of-mass momentum with the renormalisation group scale k. Thus, the running of the vertex does not enter the ultraviolet regime in the unphysical scale k. The vertex is fixed at $k = 0$, where it is matched with the fixed point of the non-perturbative running coupling $\Gamma^{(3)}_{\bar{c}Ac,\,k=0} = g$. Note the absence of dimensions on the ordinate, as the $\Gamma^{(3)}_{\bar{c}Ac,\,k}$ relates to the dressing function, i.e. the canonical dimension is not comprised.

All in all, this leaves a relatively simple flow equation for the ghost-gluon vertex which can be solved self-consistently with the momentum-dependent propagators and the appropriate ansätze for the gluonic vertices to be detailed in the next section. The resulting vertex $\Gamma^{(3)}_{\bar{c}Ac,\,k}$ is given in fig. (4.7).

The vertex shows a relatively strong change in the running with the renormalisation group scale. In fact, the change of the vertex due to the running is much larger than change in momentum of the physical vertex, for a study in the framework of DSEs see [245, 431]. Futhermore, there are recent indications that a non-trivial vertex is not compatible with lattice results [432]. This yields an unphysical weighting of the different scales and effectively renders the infrared regime quantitatively more important than it actually is. This suggests that although the vertex has been improved in the sense that it entails a non-perturbative running, the ansatz is not an improvement of the physical result, if it is done in this naive way.

The truncation error due to latter intricacy is seen best in direct comparison with the momentum-dependent vertex, evaluated at the symmetric point P. Using the same truncation, the vertex is computed self-consistently in a coupled system with the propagators, so all changes are purely due to the dependence of the vertex on the external momentum

p. The initial condition for the vertex is chosen constant at vanishing scale $\Gamma^{(3)}_{\bar{c}Ac,\,k=0}(P) = g$ in order not to change the fixed point of the running coupling as described above[3]. Thus, the ghost-gluon vertex is given by

$$\Gamma_{\bar{c}Ac,\,k}(P) = \Gamma_{\bar{c}Ac,\,k=0} + \int_{k=0}^{k} \frac{dk'}{k'} \partial_t \Gamma_{\bar{c}Ac,\,k'}(P)\,. \tag{4.23}$$

The result for the running vertex at various p is given in fig. (4.8(b)), with the flow evaluated at various values of the external momentum $|p|$ given in fig. (4.8(a)). The short dashed curve is to be compared with the result from the momentum-independent vertex in fig. (4.7). By comparison the running in the scale-dependent vertex is significantly overestimated with respect to the momentum-dependent vertex.

Given the results for the various flows of the ghost-gluon vertex above, it is questionable whether the simple scale-dependent vertex is a real improvement with respect to the correct physical behaviour of the system. Unfortunately, a full inclusion of the momentum-dependent vertex at finite temperature is beyond the scope of this thesis. Thus, in the truncation of the results for the thermal behaviour of the Yang–Mills propagators presented below, the ghost-gluon vertex is chosen as bare.

In eq. (4.14), eq. (4.17) and eq. (4.21a) the coupling at vanishing temperature is defined. At non-vanishing temperature the coupling is suppressed below the temperature scale $k \sim T$, see e.g. [433]. Furthermore, in the vertex external transversal and longitudinal gluon legs have to be distinguished. However, for the case of the constant ghost-gluon vertex the temperature dependence is dropped. In addition, the differentiation of the longitudinal and transversal coupling affects the gluonic vertices only. This is detailed further in the next section 4.1.4.

At this point I come back to the question of the thermal behaviour of the wave-function renormalisation of the ghost, mentioned already in section 4.1.1. With increasing temperature the Z_c gets suppressed, as it will be seen in section 4.2. However, a vanishing wave-function renormalisation of the ghost would trigger a divergent flow in the ghost-gluon vertex. The signs of the contributions of the diagrams are such, that the vertex would vanish at this point. As the dressing function of the ghost-gluon vertex enters the equation for the ghost flow, this effectively stops the flow of the ghost at this point. There-

[3] Note that in principle the vertex must be fixed at ultraviolet scales. However, for the purpose of resolving the truncation error due to the neglection of the momentum-dependence in the vertex only, it is actually better to fix the vertex in the deep infrared to be momentum-independent in order to see a clear signal of the momentum-dependency in direct comparison with running vertex without explicit momentum-dependency. The change of the vertex indicates that initialising in the ultraviolet would give a constant vertex at large momenta and a rather mild change at intermediate and small momenta, as it would mimic the inverted short dashed curve in fig. (4.8(b)). This is constistent with results from studies with DSEs [245, 431]. Nevertheless, besides these arguments, the full computation has not been carried out here.

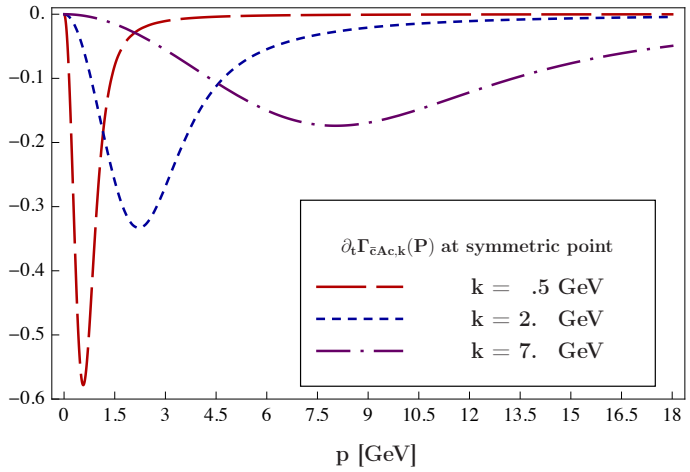

(a) Flow of the momentum-dependent ghost-gluon vertex at fixed renormalisation group scales k.

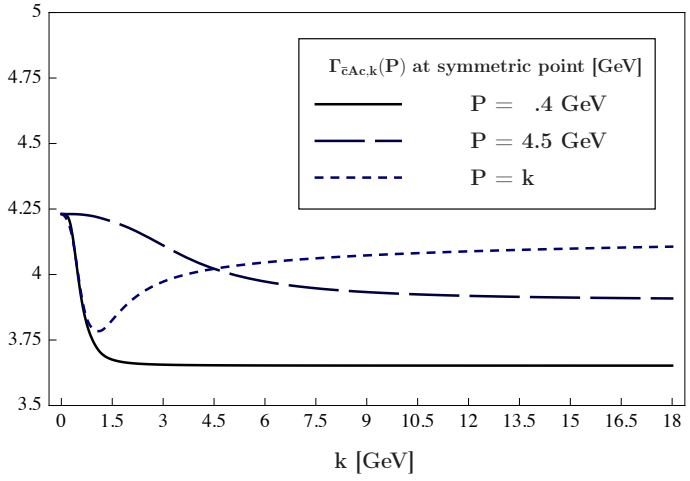

(b) Momentum-dependent ghost-gluon vertex at various external momenta p.

Figure 4.8.: Momentum-dependent ghost-gluon vertex coupled to the full propagators at vanishing temperature. The vertex in fig. (4.7) approximates the short dashed curve in fig. (4.8(b)) poorly, because its running overestimates the actual effect. This suggests, that the naive approximation in fig. (4.7) is not a good truncation, as it incorrectly weights the ultraviolet with respect to infrared scales. Note the absence of dimensions of the ordinate, as these curves relate to the dimensionless dressing function of the vertex.

fore, a negative wave-function renormalisation of the ghost is not realised in the case of the coupled system of the ghost-gluon vertex and the two-point functions. However, due to the reasons outlined above, the ghost-gluon vertex in the computation presented here

is taken to be scale independent, which induces this truncation error[4].
First and foremost, this would not represent the physical either, because it would yield a negative running coupling which gets more and more negative with the temperature. This unphysical effect due to a truncational shortcoming must be handled. For this purpose, the technique of field reparametrisations, which is already utilised to guarantee local flows, see section 3.2.5, is applied also here. However, this time it is not purely the scale-dependency which is put into the reparametrised ghost fields, but an additional dependence on the temperature.

The temperature-dependent ghost fields are defined by

$$\tilde{\hat{c}}_k = \tilde{Z}_k^{1/2}\hat{c}_k\,,\ \tilde{\bar{\hat{c}}}_k = \tilde{Z}_k^{1/2}\hat{\bar{c}}_k\,. \tag{4.24}$$

By definition the temperature dependence is put into the fields, that leaves the two-point functions of the corresponding fields to be independent of the temperature,

$$\tilde{\hat{\Gamma}}^{(2)}_{c,k,T} \coloneqq \hat{\Gamma}^{(2)}_{c,k,T=0}\,, \tag{4.25}$$

as long as the retransformation to the physical fields is not done. Note that this also affects the other correlation functions with ghost content and also the coupling $\bar{\alpha}_{s,k}$, but not the physical coupling, as it is detailed further below.
Similar to eq. (3.40) and eq. (3.43) the flow of the two-point function of the reparametrised ghosts is given by

$$\left(\partial_t + 2\tilde{\hat{\gamma}}\right)\tilde{\hat{\Gamma}}^{(2)}_{c,k,T} = \frac{\delta^2}{\delta\tilde{\bar{\hat{c}}}_k\delta\tilde{\hat{c}}_k}\left(\frac{1}{2}\mathrm{STr}\,\left(\tilde{\hat{G}}_{c,k}\left(\partial_t + 2\tilde{\hat{\gamma}}\right)\tilde{\hat{R}}_k\right) + \text{gluon loop}\right) = \tilde{\hat{\mathrm{Flow}}}^{(2)}_T\,, \tag{4.26}$$

where the index k on the ghost fields indicates that these fields are scale dependent already. In other words, they are parts of the field multiplet ϕ in eq. (3.35). Dropping the explicit but unmodified dependence on the purely gluon contributions, the definition of the anomalous dimension of the propagator is turned into

$$\tilde{\hat{\eta}}_{k,T} = 2\tilde{\hat{\gamma}} = \frac{\tilde{\hat{\mathrm{Flow}}}^{(2)}_T\left(\hat{\Gamma}^{(2)}_{c,k,T=0}, \tilde{\hat{\eta}}, \tilde{\hat{\Gamma}}^{(n\geq 3)}_{c,k,T}\right) - \hat{\mathrm{Flow}}^{(2)}_{T=0}\left(\hat{\Gamma}^{(2)}_{c,k,T=0}, \hat{\eta}, \hat{\Gamma}^{(n\geq 3)}_{c,k,T}\right)}{\hat{\Gamma}^{(2)}_{c,k,T=0}}\,, \tag{4.27}$$

with $\hat{\mathrm{Flow}}^{(2)}_{T=0}$ defined in eq. (3.43) and $\tilde{\hat{\mathrm{Flow}}}^{(2)}_T$ in eq. (4.26). The definition eq. (4.27) is well-defined, as the function $\hat{\Gamma}^{(2)}_{c,k,T=0}$ is strictly positive. This would not be the case for the gluonic two-point function.
This procedure guarantees that the ghost two-point function that enters the flow in terms

[4]Note that the exclusion of negative values of Z_c at finite temperature is not excluded via the inclusion of a running ghost-gluon vertex. Firstly, the truncation of the vertex plays a crucial role. But secondly, even if the vertex is formally capable of stabilising the system in combination with the ghost flow, the decrease of Z_c happens very fast. As a consequence, also in the latter case the system in numerically hard to resolve and the improvement of the truncation for the ghost flow as it is described for the constant ghost-gluon vertex remains to be a suitable implementation.

of the temperature-dependent ghosts is the one at vanishing temperature. In turn, the full non-trivial dependence on the temperature is not dropped but stored in the fields. Naturally, at the end of the computation this reparametrisation must be undone to express the results in terms of the physical fields, similar to eq. (3.49). This is done via integrating the $\tilde{\hat{Z}}_{c,k,T}$ via its definition, eq. (4.27),

$$\hat{\Gamma}^{(2)}_{c,k,T} = \tilde{\hat{Z}}_{c,k,T}\tilde{\hat{\Gamma}}^{(2)}_{c,k,T}\,, \tag{4.28}$$

$$= \tilde{\hat{Z}}_{c,\Lambda,T}\,\exp\left\{\int_\Lambda^k \frac{dk'}{k'}\tilde{\hat{\eta}}_{k,T}\right\}\,\tilde{\hat{\Gamma}}^{(2)}_{c,k,T}\,, \tag{4.29}$$

with $\tilde{\hat{Z}}_{c,\Lambda,T} = 1$. This yields the physical Green functions after having undone the reparametrisation of the k-dependent fields according to eq. (3.49).

Note that this puts parts of the temperature dependence also in the (tilded) vertices, cf. eq. (3.38), not only directly into the ghost-gluon vertex but also into gluonic vertices via the backcoupling. However, for the ghost-gluon vertex this redefinition directly affects the definition of the coupling via $z_{\bar{c}Ac,\,k}$, cf. eq. (4.17). In the latter definition the $\tilde{Z}_c$'s cancel exactly,

$$z_{\bar{c}Ac,\,k} = \frac{\tilde{\hat{\Gamma}}^{(3)}_{\bar{c}Ac,\,k}}{\sqrt{\bar{Z}_A}\tilde{\hat{Z}}_c} = \frac{\hat{\Gamma}^{(3)}_{\bar{c}Ac,\,k}}{\sqrt{\bar{Z}_A}\bar{Z}_c}\,. \tag{4.30}$$

Note that for the sake of clarity the hats are dropped in the definitions of the $\bar{Z}$'s as well as in the ghost-gluon vertex in eq. (4.17), but both relations refer to the hatted quantities. Therefore, the reparametrisation leaves the coupling $\bar{\alpha}_{s,k}$ unmodified. Naturally, the physical coupling is insensitive to reparametrisations of the fields too.
In conclusion, the thermal effects of the ghost two-point functions were put into the ghost fields. This does not neglect these fluctuations but is an exact rewriting of the flow equation. However, from the technical point of view, this betters the numerical stability, as problems due to unphysical negative values of the ghost wave-function renormalisation are removed.

4.1.4. Gluonic Vertices

To close the truncation it remains to determine the renormalisation group invariant tensors of the purely gluonic vertices, i.e. $\mathcal{T}_{A^3}$ of the three-gluon vertex and $\mathcal{T}_{A^4}$ of the four-gluon vertex. They are described within a parameterisation similar to eq. (4.13). So schematically they are given by

$$\mathcal{T}_{A^3} = z_{A^3,k}\,\frac{1}{g}S^{(3)}_{A^3}\,, \qquad \mathcal{T}_{A^4} = z_{A^4,k}\,\frac{1}{g^2}S^{(4)}_{A^4}\,, \tag{4.31}$$

where the vertex dressings $z_{A^3,k}$ and $z_{A^4,k}$ relate directly to the ghost-gluon dressing $z^2_{\bar{c}Ac,\,k} = 4\pi\bar{\alpha}_s(k)$, eq. (4.14), for large cutoff scales $k \gg \Lambda_{\mathrm{QCD}}$ or large momenta due to two loop universality. The tensor structure of the classical vertices $S^{(3)}_{A^3}$ and $S^{(4)}_{A^4}$ is given in appendix E.

Indeed, this reasoning has been validated in [428] with DSE-equations for the four-point coupling. Hence, there is $z_{A^4,k} \simeq z^2_{\bar{c}Ac,\,k}$ for most of the momentum regime with a potential deviation in the deep infrared for $k^2/\Lambda^2_{\mathrm{QCD}} \ll 1$. Again, the parametrisation is done accordingly,

$$z_{A^3,k} = z_{3,k}\, z_{\bar{c}Ac,\,k}\,, \quad z_{A^4,k} = z_{4,k}\, z^2_{\bar{c}Ac,\,k}\,, \tag{4.32}$$

where the $z_{i,k}, i = 3, 4$, are functions which are expected to approach unity for $k^2 \gtrsim \Lambda^2_{\mathrm{QCD}}$, that is

$$z_{i,k\gg\Lambda_{\mathrm{QCD}}} \to 1\,, \tag{4.33}$$

for $i = 3, 4$. Their infrared behaviour is determined by the only diagram in the flow that does not depend on the gapped gluon propagator, see fig. (4.9). The effect of these di-

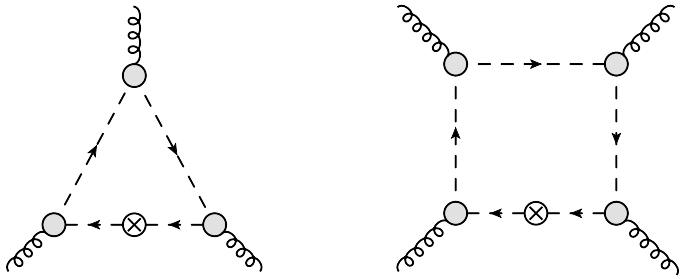

Figure 4.9.: Infrared dominating diagrams in the flow equations for the three-gluon vertex and the four-gluon vertex.

agrams on the vertices is determined by two competing effects: Firstly, these diagrams are suppressed relative to those that involve the ghost-gluon vertex due to their colour structures and the related vertex dressings. In the case of the four-gluon vertex this combinatorial suppression is of order $10^2 - 10^3$, which is nicely seen in the solution in [428]. For the three-gluon vertex the combinatorial suppression factor also turns out to be of order $10^2 - 10^3$, subject to the chosen momenta. This factor has been determined within a two-dimensional lattice study as 0.017, [434].
Secondly, these diagrams grow strong in the infrared in comparison to the respective diagram in the flow of the ghost-gluon vertex, which involves one gapped gluonic propagator. As already stressed above, for scales above Λ_{QCD}, the gluonic vertices are insensitive to the behaviour of the propagators in the deep infrared. Furthermore, their relative suppression to the diagrams given in fig. (4.9) is qualitatively similar for the scaling and decoupling solution for small scales. In the decoupling case the flow of the gluonic vertices for $k \to 0$ is proportional to k^0 up to logarithms. This leads to an effective suppression of diagrams with gluonic vertices, as such diagrams also involve gapped gluon propagators, and hence a suppression with k^2/m^2_{gap}. In the scaling case the diagrams with gluonic vertices decouple with powers of the scaling, which can be seen best in the DSE-hierarchy. However, quanti-

tatively the gluonic vertices may differ for small scales, but as they are suppressed in this regime, the impact of these quantitative differences on the behaviour of the propagators is subleading. Is it noteworthy that these differences do not affect the regime above Λ_{QCD}, which is directly visible in the approach of the FRG.

In summary, the above analysis entails that the related diagrams can be dropped for $k \leq \Lambda_{\mathrm{QCD}}$ and above this scale the vertices have a dressing similar to that of the ghost-gluon vertex. In the vertices the multiplicative dressing functions $\bar{Z}^{1/2}$ for the respective legs have been factorised.
The suppression at infrareddish scales can be mimicked in different ways Here, the diminishment of the gluonic vertices is satisfied via a polynomial decay with the same order of the coupling of the according vertex. This guarantees that the two diagrams with purely gluonic content in the flow of the gluon propagator, cf. fig. (3.7), are treated equally, as both diagrams are of order $z^2_{\bar{c}Ac,\,k} \sim \bar{\alpha}_{s,k} = \bar{\alpha}_s(k)$. The superposed function[5] is given by

$$z_{3,k} = \Theta(k - k_A) + k\ \Theta(k_A - k)\,,\ \ z_{4,k} = z^2_{3,k}\,, \tag{4.35}$$

which suppresses both diagrams quadratically in k for scales below $k_A = 1\,\mathrm{GeV}$.

The validity of the ansatz for the gluonic vertices can be measured by computing the flow of the vertices itself. Here, this has been done at vanishing temperature for the three-gluon vertex. The approximation is again such that only the classical tensor structure is taken into account and the symmetric point with centre of mass momentum P is chosen as a convenient kinematic configuration. In contrast to the ghost-gluon vertex, the centre of mass momentum is not identified with the renormalisation group scale k, as this would invalidate the comparison with perturbation theory, which necessitates a change between infrared and ultraviolet scales. This would not be the case if P were shifted with the scale. In other words, a mixing of scales would spoil the genuine perturbative signature[6]. Instead, the external momentum is chosen to be small but finite in order to guarantee that no diagrams vanish due to the external scale, but further that there is only one scale in the system, i.e. $P \geq 0$. In contradistinction to the non-renormalisation property of the ghost-gluon vertex, the three-gluon vertex carries a perturbative running. Therefore, the result for the vertex can be tested at ultraviolet scales. The perturbative running

[5] Note that the suppression of gluonic vertices in the infrared was varied with respect to the superposed function, e.g. by taking the ansatz

$$z_{3,k} = \frac{\left(\Gamma^{(2)}_{A,k}(k) - \Gamma^{(2)}_{A,k}(k)\right)}{\Gamma^{(2)}_{A,k}(k)}\,. \tag{4.34}$$

The results for the thermal behaviour of the Yang–Mills propagators turned out to be quantitatively insensitive for appropriate choices of $z_{i,k}$.

[6] Note that taking the external momentum $P = 0$ in the ghost-gluon vertex instead of $P = k$ would not ameliorate the approximation, it would even make it worse. In fig. (4.8(b)) this can be seen directly. Taking a large but fixed external momentum would yield a mixing of scales again. Thus, the reasoning that is employed for the gluonic vertices does not help to find a better but easy ansatz for the ghost-gluon vertex.

is guaranteed for the construction of the ansätze for the gluonic vertices as detailed in section 4.1.2. The result for the three-gluon vertex at vanishing temperature is given in fig. (4.1.4).

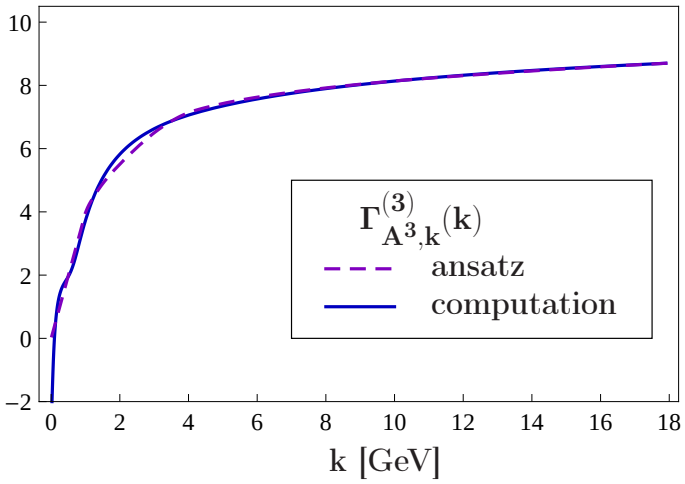

Figure 4.10.: Comparison of the ansatz for the three-gluon vertex with solution of the flow equation thereof. The vertex flow is evaluated at the symmetric point with vanishing centre of mass momentum to justify a comparison with the perturbative running that is employed to construct the ansatz.

The computation is directly compared with the ansatz for the three-gluon vertex defined in eq. (4.9), eq. (4.31) and eq. (4.35).

In order to solve the flow one needs to find the correct initial condition. Herefore, the situation for the three-gluon vertex is different than for the ghost-gluon vertex, which I shortly sketch here. For the ghost-gluon vertex the initial condition is determined from the non-perturbative running-coupling eq. (4.21b). As the physical coupling is strictly given only at $k = 0$, the infrared value of the dressing function of the vertex $z_{\bar{c}Ac,\,k=0}$ is determined such that the fixed point of the physical coupling $\alpha_s(p)$ at vanishing temperature is not changed. From the input data that has been used here this gives $z_{\bar{c}Ac,k} \approx 4.23071$, as detailed in section 4.1.3. Then the flow gives the initial conditions for arbitrary k, which allows to study the temperature-dependence of the vertex as well.
In contradistinction to this, for the three-gluon vertex it is not possible to fix the initial condition in the infrared directly, simply because its infrared value is not known. However, in the ultraviolet it matches perturbation theory whose running is recovered by the full vertex in this regime.

For the flow the perturbative running constitutes a solid test for the behaviour of the vertex (especially for the numerics), as the perturbative behaviour is well known and to

be found in textbooks, see e.g. [435]. However, a full treatment of the off-shell vertex is complicated due to the large set of twelve different Lorentz tensor structures, but can be done via a form factor decomposition [436] which is valid at any order in perturbation theory. In addtition, non-perturbative results for the three-gluon vertex are at hand, from continuum [437] as well as lattice studies [327].

Note that the behaviour of the three-gluon vertex given in fig. (4.1.4) at very small momenta is such, that the vertex becomes negative. Nevertheless, such a behaviour is valid, and in fact it is also seen in lattice simulations [327]. However, the scale at which the vertex passes the zero is higher than in the FRG result presented here.

A few additional comments regarding the solution given in fig. (4.1.4) are in order. The solution is obtained such that at first the flow equations for the momentum-dependent propagators are solved, using the truncation given in the sections above. For the full system, the perturbative ansatz of the three-gluon vertex fixes the initial condition for the vertex at the scale $k = \Lambda$. The flow equation is then evolved to the physical scale $k = 0$. In a strict sense, this is not a self-consistent computation, because firstly, the vertex in the ultraviolet is fixed with respect to the infrared value of the ansatz which in general differs from the computed vertex at $k = 0$ differ and secondly, the change of the vertex would have an effect on the propagators as well. In principle, this system would have to be iterated, i.e. the system should be evolved with the computed vertex from the infrared scale back to the ultraviolet value Λ, where the vertex is fixed again, and so on until the correlation functions are stable under this procedure. However, assuming that the iteration does not develop an instable direction, the full self-consistent result should not be very different from fig. (4.1.4), because the first iteration step is still quantitatively close to the ansatz.

To conclude, the ansatz that is used is accurate at least at vanishing temperature. The perturbative behaviour at ultraviolet scales $k \leq 5\,\mathrm{GeV}$ is reproduced by the running vertex. At intermediate and infrared scales the vertex clearly deviates from the perturbative result, which is seen in the computation. In the infrared regime the dominating diagrams are the ones with closed ghost loops, see fig. (4.9), as the ghost-propagator is enhanced, cf. section 2.3.2. Nevertheless, the ansatz for the gluonic vertex captures also this non-trivial behaviour within the expected accuracy. This agreement is crucially due to the switching off of the gluonic vertices in the infrared with the functions $z_{3,k}$ and $z_{4,k}$ defined in eq. (4.35).

At non-vanishing temperature the suppression of the non-perturbative running coupling at scales smaller than the temperature needs to be respected in the ansatz.
For the results presented in section 4.2 the thermal suppression is implemented via switching off the gluonic vertices below the temperature scale ξT. The latter scale is chosen such that the system is fully sensitive to the effects related to the first Matsubara mode, i.e. the suppression is chosen to occur only for scales $\xi < 2\pi$. In contrast to this, the suppression of the coupling increases quickly below the first Matsubara mode. This suggests

the choice $\xi = 3/2\,\pi$. Dropping the Lorentz- and colour- structure, the gluonic vertices are schematically given by

$$\begin{aligned}\Gamma^{(3)}_{A^3}(k) &= \bar{Z}^{3/2}_{A,\,k}\, z_{3,k}\, z_{\bar{c}Ac,\,k}\,\Theta(k-\xi T) + \frac{k}{\xi T}\,\bar{Z}^{3/2}_{A,\,\xi T}\, z_{3,\xi T}\, z_{\bar{c}Ac,\,\xi T}\Theta(\xi T - k)\,,\\ \Gamma^{(4)}_{A^4}(k) &= \bar{Z}^{2}_{A,\,k}\, z_{4,k}\, z^2_{\bar{c}Ac,\,k}\,\Theta(k-\xi T) + \frac{k^2}{(\xi T)^2}\,\bar{Z}^{2}_{A,\,\xi T} z_{4,\xi T}\, z^2_{\bar{c}Ac,\,\xi T}\,\Theta(\xi T - k)\,, \quad (4.36)\end{aligned}$$

which ensures that diagrams of the same order of the running coupling $\bar{\alpha}_{s,k}$ are suppressed below the temperature scale with the same polynomial order. Note that eq. (4.36) actually models the combined suppression of the full gluonic vertex, which is according to the vertex construction eq. (4.9) built up from the suppression of the non-perturbative running coupling defined from the ghost-gluon vertex and the thermal behaviour of the $\bar{Z}_{L/T,k}$'s. The sensitivity of the results with respect to the choice of the thermal scale $\xi\,T$ and the suppression are studied in detail in section 4.2.

Naively, the $\bar{Z}_{A,k}$ in eq. (4.36) stemming from the external legs are chosen accordingly to be $\bar{Z}_{T,\,k}$, if the attached leg is a transversal gluon, or $\bar{Z}_{L,\,k}$, if a longitudinal leg enters. A closer look on the thermal behaviour of the $\bar{Z}_{L/T,\,k}$'s shows that this is not a proper choice with regard to a suppression of the gluonic vertices with the temperature. Forestalling the results at finite temperature, the strength arising from the vertices in the diagrams with closed gluon loops in the gluon flow are shown in fig. (4.11). Note that below the scale $k = 1\,\mathrm{GeV}$ the gluonic vertices are switched off with $z_{i,k}$.

The comparison of the strength of vertices with only transversal and longitudinal external legs, respectively, shows that the definition of the thermal vertices with the transverse gluonic $\bar{Z}_{T,k}$ even enhances the gluonic contributions compared to vanishing temperature. Therefore, in view of the thermal suppression the vertices are defined to carry exclusively $\bar{Z}_{L,k}$ as prefactors. In order to give a correct weight between contributions of gluonic vertices with different legs also the coupling $\bar{\alpha}_{s,k}$ involves $\bar{Z}_{L,k}$ only. As explained in section 4.1.3 this does not affect the ghost-gluon vertex. Furthermore, I want to emphasise that this is not the physical coupling, which in turn differs with transversal and longitudinal gluons, see eq. (4.22).
The sensitivity of the results with respect to the definition of the gluonic vertices at non-vanishing temperature is studied in detail in section 4.2.

For a non-trivial ghost-gluon vertex the thermal behaviour of it would allow for refined treatments of the thermal behaviour of gluonic vertices as well. This is done by the help $z_{\bar{c}Ac,\,k,\,T}$.
The relative thermal suppression factor is safely encoded in the ratio of the full ghost-gluon vertex dressings at vanishing and finite temperature,

$$\frac{\Gamma_{\bar{c}Ac,\,k,\,T}}{\Gamma_{\bar{c}Ac,\,k,\,T=0}}\,. \quad (4.37)$$

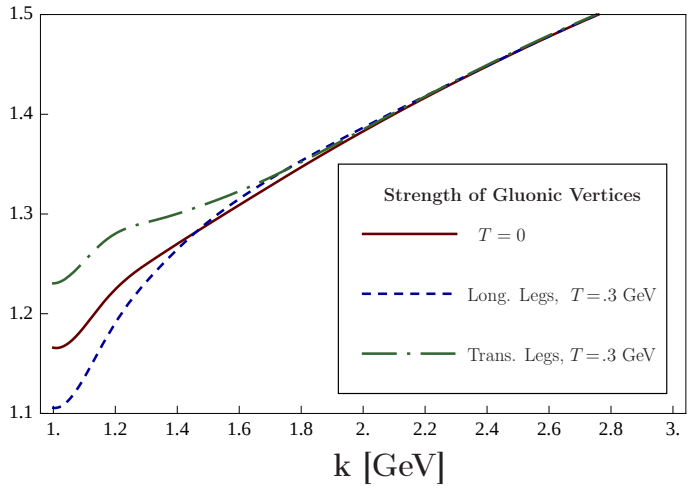

Figure 4.11.: Strength of the gluonic vertices in those diagrams of the gluon flow that contain closed gluon loops. At finite temperature the definition via the transversal gluon enhances the gluonic vertices with the temperature. As the gluonic couplings should be suppressed with the temperature, this ansatz is not a proper choice to approximate the gluonic vertices at non-vanishing temperature.

Since the temperature-dependent dressing factor $z_{\bar{c}Ac,\,k}$ is already included in the definition eq. (4.32), it is sufficient to deal with the reduced ratio of the wave function renormalisations,

$$r_{\bar{c}Ac}(k,T) = \frac{\bar{Z}_{A,k}^{1/2}\,\bar{Z}_{c,k}\Big|_{T}}{\bar{Z}_{A,k}^{1/2}\,\bar{Z}_{c,k}\Big|_{T=0}}\,, \tag{4.38}$$

leading to the final approximation of the gluonic vertex dressings by

$$z_i(k,T) = r_{\bar{c}Ac}(k,T)^{i-2}\,, \quad z_i^{\min}(k,T) = \frac{\bar{Z}_{k,A}}{Z_{k,A}} z_i(k,T)\,. \tag{4.39}$$

At non-vanishing temperature the structure functions z_{A^n} also have to carry the difference between the coupling to longitudinal and transversal gluons, which is relevant for the second choice in eq. (4.39). With increasing temperature the ratio $\bar{Z}_A/Z_A$ goes to $\bar{Z}_{L/T}/Z_{L/T}$.

However, the results presented in section 4.2 are obtained with the ansätze given in eq. (4.36).

4.1.5. Regulators

For a numerical treatment of finite temperature flow equations exponential regulators eq. (3.12) generally provide good numerical stability. As already pointed out in section 3.2.5 locality is a central issue. The importance of sufficiently local flows is also seen on the level of the regulator, where it turns out that the non-locality induced by the exponential regulator, eq. (3.12), with $m = 1$ spoils the stability of the flow. On the other hand, regulators with a steep descent lead to a slower convergence of the regularised thermal propagators and vertices towards the vacuum ones at $T = 0$. Indeed, for sharp cutoff functions or non-analytic ones thermal modifications are present for arbitrarily large cutoff scales Λ. This invalidates the use of the $T = 0$ initial conditions at the initial ultraviolet scale Λ. Accordingly, here an intermediate steepness of $m = 2$ is chosen for the computation, whose form is shown in fig. (3.1). The full regulators for the gluon and the ghost are given by

$$\begin{aligned} \hat{R}^{ab}_{L/T,\,k,\,\mu\nu}(p) &= \delta^{ab} P^{T/L}_{\mu\nu}\, \bar{Z}_{T/L,k}\, p^2\, r_2(p^2/k^2)\,, \\ \hat{R}^{ab}_{c,\,k}(p) &= \delta^{ab}\, \bar{Z}_{c,k}\, p^2\, r_2(p^2/k^2)\,, \end{aligned} \tag{4.40}$$

with the projection operators $P^{L/T}$ defined in eq. (4.1). Note that $Z_{c,k}(0)$ is chosen instead of $Z_{c,k}(k)$ for numerical convenience[7]. The ghost renormalisation function $Z_c(p;T)$ tends towards zero for small momenta and finite temperatures. The decrease of the Z_c is numerically hard to controll if done in a direct setting. Nevertheless, the numerics can be improved by applying the temperature-dependent field reparametrisation of the ghost as explained in section 4.1.2.

At vanishing temperature there is $\bar{Z}_{L,k} = \bar{Z}_{T,k}$ and the gluon regulator $R_{A,k} = R^T + R^L$ is proportional to the four-dimensional transversal projection operator Π^{T} defined in eq. (2.28).
As mentioned in section 2.3.2 and section 3.2.2, for the full propagator in the presence of a regulator the term schematically written as $\Gamma^{(2)} + R$ must be inverted. Therefore, choosing the regulator to carry the same Lorentz-tensor structure as the $\Gamma^{(2)}$ ensures that the inversion stays trivial. This is not only true for zero temperature, where only the purely transversal tensor has to be inverted, but even persists in the case of non-vanishing temperature, because in the inversion the purely $3d$-longitudinal and $3d$-transversal projectors do not mix and no further tensors are possible in Landau gauge. In other gauges this feature is not given.

[7] At this point I want to stress again that the regulator is in principle free to choose as long as it satisfies the contraints in section 3.2.2. Thus, taking $Z_{c,k}(0)$ is as valid as taken $Z_{c,k}(k)$, the only subtlety is that the absolute value of the prefactor must be such that the regulator term is of the same size as the term $\Gamma^{(2)}_{c,k}(p \lesssim k)$, which it is supposed to regulate for $p \lesssim k$ in the propagator $\left(\Gamma^{(2)}_{c,k}(p) + R_{c,k}(p)\right)^{-1}$. Note that this holds for the scaling as well as the decoupling solution, as the singularity in the ghost propagator occurs in the limit of vanishing renormalisation group scale, sc. $Z_{k,0}(0)$, where the regulator must vanish by construction, cf. section 3.2.2, so the vanishing prefactor does not spoil this choice.

4.1.6. Computational Details

The discussion of the approximation in section 4.1 yields a coupled set of partial integro-differential equation depicted in fig. (4.12). The initial condition is set in the vacuum, $T = 0$, at vanishing cutoff scale, $k = 0$. The vertices are determined by eq. (4.21c) and the relations in the section 4.1.3, section 4.1.4 and the input gluon and ghost propagators are taken from [276], see fig. (2.4), from which a decoupling solution is chosen.

In the numerical treatment the representation of the functions that are computed is important, as the function values are computed on grid points, but naturally not in the continuum. In the case of the propagators and vertices the grid is two-dimensional, one direction is the (spatial) momentum p, the other one the renormalisation group scale k. Taking trivial interpolations at each evaluation of a function is too slow, and also interpolations between the grid points may have disadvantages. The better approach is to expand the numerical function by the help of analytic functions over the full range at once, not only between the grid points individually.

Furthermore, the form of the function is decisive for the quality of the representation in terms of other basis functions, e.g. functions that are zero on a certain interval can not be resolved well by polynomials expansions. In the case of Yang–Mills theory two different quantities are expanded. For the gluonic contributions the two-point functions $\hat{\Gamma}^{(2)}_{L/T,k}(p)$ are taken. For the ghost its wave-function renormalisation turns out to be better suited for the expansion procedure which is described below. The reason is that $\hat{\Gamma}^{(2)}_{c,k}(p)$ vanishes at small momenta p for all k. This is hard to resolve along the direction of k with high quantitative accuracy. In contrast to this, for the decoupling solution the $\hat{Z}_{c,k}(p) = \hat{\Gamma}^{(2)}_{c,k}(p)/p^2$ is finite and more suited to the expansion.

A good set of basis functions are Chebyshev polynomials, see appendix C. In the code the functions were Chebyshev expanded in two dimensions, the renormalisation group scale k as well as the external momentum p, with the further grid refinement that the expansion in p direction was split into three regions. These regions were set by the points in the gluon propagator where generically the most change in the function happens: The first grid is $p \in [0, 1\,\mathrm{GeV}]$, as the peak in the dressing function of the gluon is at about 1 GeV, cf. fig. (2.4). The second grid is adjusted with respect to the largest cutoff scale $k = \Lambda$, therefore $p \in [1, \Lambda]$, as the presence of the scale derivative of the regulator in the loop integrals ensures that most change happens for $p \lesssim k$. The third grid is the grid above this scale $p \in [\Lambda, \zeta\Lambda]$, where $\zeta > 1$ is chosen such that above the scale $\zeta\Lambda$ nothing happens in the sense that fluctuations are suppressed. For the localised flow, cf. section 3.2.5, and the exponential regulator, eq. (3.12), with $m = 2$ the parameter can be chosen to be around $\zeta \approx 2$, without numerical error, see appendix D.3. The number of Chebyshev polynomials in the direction of k is chosen around 250, dependent on the choice of Λ. In the direction of p the numbers were chosen to be between 50 and 100, adapted to the grid volume. The two-dimensional grid is explaind further in appendix C in combination with

the Chebyshev expansion and the numerical integration routines.

The flow equations involve integrations over loops. These integrals need to be performed numerically here due to the complexity of the system. In this work, mainly two different approaches to numerical integration are employed. The first one is the Gauss–Legendre quadrature which is based on the idea of performing the Riemann sum in an improved way. The second idea is to expand the integrand in terms of Chebyshev polynomials and perform the integration for polynomials trivially. Both approaches are sketched further in appendix D, further details to Chebyshev polynomials are given in appendix C.

For the solution of the flow in the direction of k two methods have been used. Firstly, the integro-differential equations can be solved by an iteration procedure. Secondly, it can be performed by a direct evolution following the idea of a Runge–Kutta method. These two methods and their merits are described in more detail below.

The numerical integration routines as well as the Matsubara sum routines have been checked[8] in selected cases by changing the methods for the specific integration, further by applying the integration routines from [438] and with numerical integration in *Mathematica*. Also, the solution of the integro-differential equation itself has been checked with *Mathematica*.

The derivation of flow equations has been done with *Mathematica 7* [439, 440] by a self-written code, cf. section 3.2.3, that utilises open-source packages. For the contractions of colour as well as Lorentz indices the *Mathematica* package *FeynCalc* [402] has been used in this program. All results for the algebraic expressions in the flow equations (at vanishing and non-vanishing temperature) that are presented in this thesis were checked with the *FORM* [441] package *color* [442] for the contraction of colour indices and with the *Mathematica* package *tracer* [443] for the Lorentz contractions. The structural form of the equations themselves has been compared with the results obtained with the package *DoFun* [398] (that builds on *DoDSE* [397]) that derives flow equations as well as DSEs analytically.

The solution of the flow equations has been carried out with *C++*. The development of the full code was part of this thesis. However, for standard numerical applications some libraries could be used: For the Gauss–Legendre quadrature for the integration of loop diagrams, Chebyshev expansions the routines have been taken from the code in [444]. Modified routines for the multidimensional implementation of Chebyshev expansions are

[8] In this section I omit the trivial checks in the routines, such as e.g. varying the number of grid points in the Chebyshev expansion, integration ranges, number of Matsubara frequencies, number of nodes in the Gauss–Legendre quadrature etc. Note however, that the relevant integration ranges and number of Matsubara modes can be determined very easily in this case, as the regulator is four dimensional. After a shift in the loops each diagram contains a term $\sim \partial_t R_k(q_0^2 + \vec{q}^2)$ which vanishes quickly for $\left(q_0^2 + \vec{q}^2\right) \gg \zeta k$, therefore only the correct ζ has to be found once and for all for a chosen regulator shape function. This is explained further in appendix D.3.

partially constructed from these routines. Interpolations are done by the help of the *GNU Scientific Library* [438].

In principle, differential equations can be solved by iteration. In practice, this is only possible, if the iteration has a stable direction or at least a stable region in which it converges to the correct solution of the system. However, if the iteration is stable, the solution via this method is very efficient and high accuracy can be obtained easily. In order to solve the flow equation for the quantum theory at vanishing temperature, i.e. at $k = 0$ and $T = 0$, up to an ultraviolet scale $k = \Lambda$ an iteration procedure turns out to be well suited, because it is very stable for the direction $k \to \Lambda$.
Herein the iteration $(i+1)$ only depends on the given solution (i),

$$\Gamma^{(n)}_{k,(i+1)} = \Gamma^{(n)}_{k=0,(i)} + \int_0^k \frac{dk'}{k'} \mathrm{Flow}^{(n)}_{(i+1)} \left(\Gamma^{(n)}_{k,(i)}, \mathrm{Flow}^{(n)}_{(i)} \right) . \tag{4.41}$$

Incrementing the number of iterations until the solution is stable under further iteration, i.e. $\Gamma^{(n)}_{k,(m+1)} = \Gamma^{(n)}_{k,(m)}$ up to the desired accuracy, gives the solution of the flow equation. The starting point of the iteration is taken as $\Gamma^{(n)}_{k,(0)} = \Gamma^{(n)}_{T=0,k=0}$. The iteration converges rapidly to the initial condition $\Gamma^{(n)}_{\Lambda,T=0}(p^2)$ for the computations at finite temperature, the typical number of needed iterations is below 10 for all computations presented here.

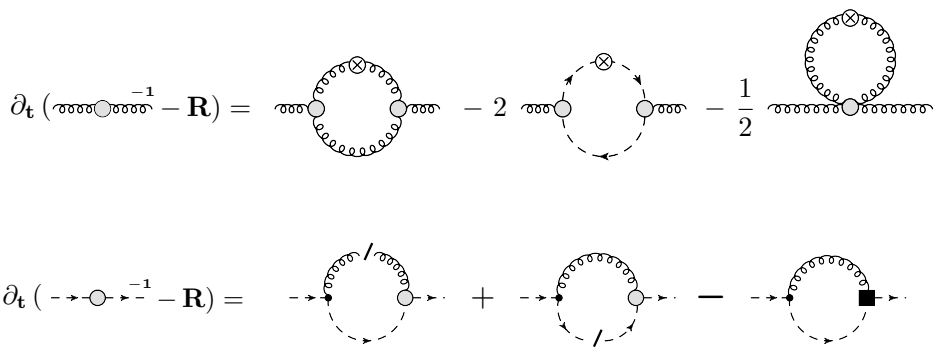

Figure 4.12.: Yang–Mills flows for propagators in the approximation discussed in section 4.1. All internal lines are full propagators, the shaded circles are dressed vertices, the small dots are classical vertices. The slashed propagators denote the scale derivative acting on the full propagator $\partial_t G_k$, cf. eq. (3.66). The black squares denote the scale-derivative acting on the full vertex $\partial_t \Gamma^{(n)}_k$. The flow of the ghost propagator are DSE-resummed and the ghost-tadpole in the gluon equation is neglected.

In contrast to the direction $k \to \Lambda$ in the zero temperature case, the flow from high to low scales at finite temperature involves instabilities if it is solved by iteration. This is due to the self-regulating nature of the equations for the wave-function renormalisation of the

ghost in combination with the ghost-gluon vertex dressing. Their structure is such that if one of the quantities becomes small it stops the flow of the other and in the following also its own flow. However, as soon as one of these quantities happens to be negative in an intermediate iteration step the iteration becomes unstable, i.e. each iteration step brings the iteration solution further away from the correct solution. The system is highly sensitive to this, as one has to resolve very small values numerically. This problem could be cured by modifying the iteration such that the functions are controlled to stay in the stable region, however, this control is intricate if the functions shall remain smooth, which they have to be for the next iteration. Furthermore, this "controlled" convergence to the correct solution is much slower than for the stable direction $k \to \Lambda$.
In addition, the iteration procedure is not necessarily stabilised via the temperature-dependent field reparametrisation of the ghost, see section 4.1.3.

Therefore, a more direct strategy is more appropriate to solve the flow, namely an evolution of the flow according to a Runge–Kutta solver

$$\Gamma^{(n)}_{k_{(i-1)}} = \Gamma^{(n)}_{k_{(i)}} + \frac{k_{(i-1)} - k_{(i)}}{k_{(i)}} \mathrm{Flow}^{(n)}_{k_{(i)}}, \tag{4.42}$$

from the initial condition $k_N = \Lambda \gg T$ to $k_0 = 0$. In the evolution the system reacts on the balancing effect between the ghost propagator and ghost-gluon vertex immediately. Thus, the purely numerical problem of possibly negative values of Z_c or $z_{\bar{c}Ac}$ in the iteration is avoided. It is important to note that the result is stable under iteration again, as it is the exact solution of the equation and further iterations just reproduce this solution. The sensitivity to the balancing is still present, but shows up in the form of a small evolution step size of $|k_{i-1} - k_i| \lesssim 10\mathrm{MeV}$.

The correctness of both implementations has been successfully tested via the interchanging of the two different method, i.e. the iteration procedure $k \to \Lambda$ for the initial condition was replaced with an evolution, and the solution from the evolution $k \to 0$ was tested with an iteration that reproduced this solution in two successive iteration steps.

4.2. Results

In this section I present the results for the Yang–Mills propagators at non-vanishing temperature in the truncation detailed in section 4.1. Furthermore, the validity of the approximations are tested. Finally, the thermal Yang–Mills correlators are directly compared with results from lattice gauge theory.

4.2.1. Results for the Propagators

In this section the results for the ghost and gluon propagators at non-vanishing temperature are presented. The temperature is given in lattice units. For the input propagators at vanishing temperature a decoupling solution is chosen in order to facilitate the comparison of thermal effects with lattice data. Above Λ_{QCD} the scaling and decoupling solutions are quantitatively equal, Even below that scale thermal effects are qualitatively similar for both types of solutions.

For physical applications these minor quantitative differences in the deep infrared are supposed to be irrelevant. Explicitly, this has been confirmed so far in various computations, such as the determination of the confinement-deconfinement phase transition temperature [11, 12, 112]. Thus, these results support the assumption that the deep infrared behaviour of Yang–Mills propagators is not of quantitative importance for the thermodynamics for temperatures in the range around the phase transition temperature either. Note however, that in principle the whole class of solutions is in reach by the method presented in this work.

As it is argued in section 3.2.6 the results for the ghost and gluon propagators show the typical thermal scale $2\pi T$. Below this scale there are significant temperature effects on the momentum dependence. In turn, above this scale the temperature fluctuations are suppressed and all propagators tend towards their vacuum counterparts. This supports the stability of the thermal flows as discussed in section 3.2.6.

A significant effect can be seen for the chromoelectric and chromomagnetic gluon propagators, which are the components of the propagator longitudinal and transversal to the heat bath. The zero mode of the longitudinal and transversal gluon propagator at various temperatures are given in fig. (4.13(a)) and fig. (4.14(a)) as a function of spatial momentum and compared to the propagator at vanishing temperature. The corresponding dressing functions are given in fig. (4.13(b)) and fig. (4.14(b)).

For low temperatures $T \lesssim 150$ MeV there is an enhancement of the longitudinal propagator. Such an enhancement is also seen on the lattice [115, 305, 323, 325, 327, 330, 445].

It has been emphasised on the basis of the FRG that specifically the propagator of the chromoelectric mode should show critical behaviour, if computed in the background fields that solve the non-perturbative equations of motion [323]. However, the significance of the lattice results so far as well as quantitative details are not settled yet.

For higher temperatures the longitudinal propagator is suppressed relative to the gluon propagator at vanishing temperature. This is the expected behaviour caused by the Debye screening mass due to the thermal screening of the chromoelectric gluon. For asymptotically high temperatures $T \gg T_c$ the chromoelectric gluon decouples from the interacting

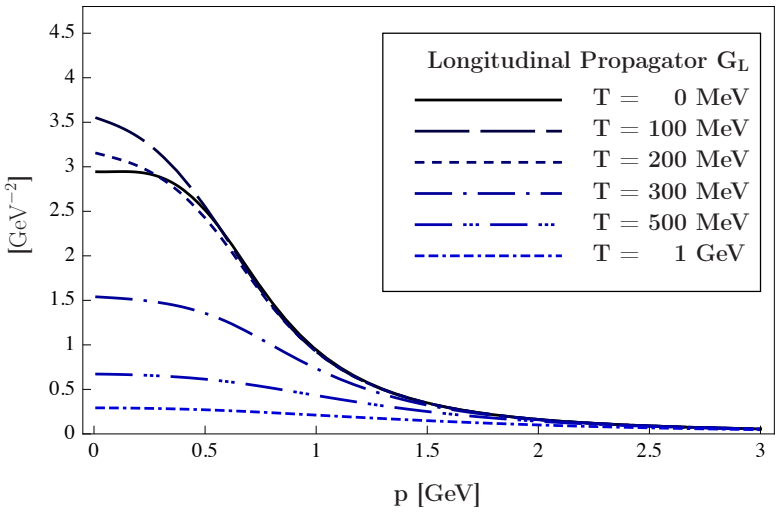

(a) Longitudinal gluon propagator G_L at different temperatures.

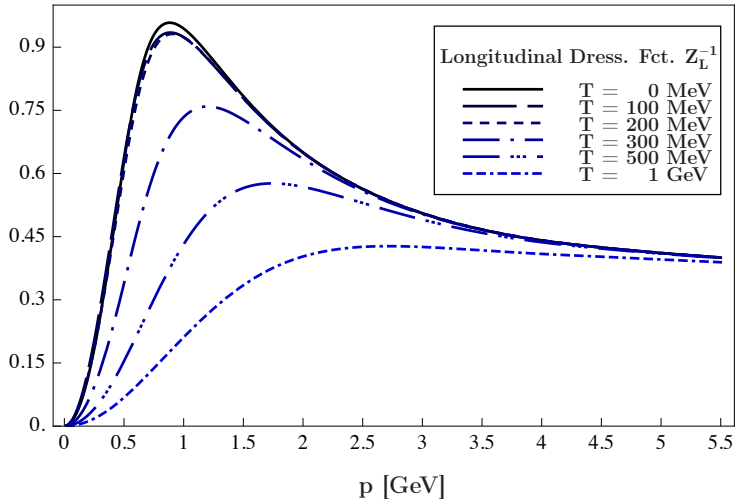

(b) Dressing function of the longitudinal gluon Z_L^{-1} at different temperatures as a function of spatial momentum.

Figure 4.13.: Yang–Mills two-point functions depend on temperature. As the heat bath singles out a preferred rest frame, there are two tensor structures in the remaining spatial subspace which yield two different gluonic propagators, the chromoelectric (longitudinal) and chromomagnetic (transversal) propagator. This figure shows the thermal behaviour of the zeroth Matsubara mode of the propagator and dressing function of the chromoelectric gluon as a function of the spatial momentum p. Higher modes can be approximated by shifting the spatial momentum of the zero mode by the time component.

theory which shows that the theory tends against the three-dimensional one in the high

temperature limit. The onset of this behaviour at about $T \approx 150$ MeV is earlier as in the respective lattice computations [115, 305, 323, 325, 327, 330, 445], where the thermal decoupling takes place for temperatures larger than the critical temperature.

In order to capture the behaviour of a steep descent of the chromoelectric gluon propagator around the deconfinement-confinement phase transition temperature, it is inevitable to extend the present truncation in such a way that the Polyakov loop potential is self-consistently included as a non-trivial background. The Polyakov loop potential is sensitive to the deconfinement-confinement phase transition and, therefore, it is indispensable to recover the critical phenomena. In addition to the background, the second derivative of the Polyakov loop appears in the denominator of the chromoelectric gluon propagator. It is non-zero for temperatures below the phase transition but vanishes quickly for increasing the temperature above T_c. Therefore, with the inclusion of the Polyakov loop potential the critical physics are seen also on the level of the propagators, however its manifestation is not clear. Thus, it is not sure so far, if its effect would actually bring the propagator closer to the lattice results.

Another upgrade of the truncation is to resolve the higher n-point functions, in particular the gluonic vertices, especially for momenta and frequencies below Λ_{QCD}. In contrast to this, for large temperature and momentum scales above Λ_{QCD}, the lack of quantitative precision of propagators as well as vertices at infrared scales is irrelevant. In this region of the temperature there is quantitative agreement with the lattice, see fig. (4.21(b)).
The resolution of gluonic vertices affects not only the deep infrared but also the mid-momentum region at both vanishing as well as non-vanishing temperature. Thus, it would also improve the thermodynamics that get their largest contributions from the mid-momentum regime.

The transversal mode is not enhanced for small temperatures, in clear distinction to the longitudinal mode. It is monotonously decreasing with temperature, see fig. (4.14(a)). Moreover, it develops a clear peak at about 500 MeV. This can be linked to positivity violation which has to be present for the transversal mode: In the high temperature limit it describes the remaining dynamical gluons of three-dimensional Yang–Mills theory in the Landau gauge. The infrared bending is more pronounced as that of respective lattice results. Its strength is subject to the lack of quantitative precision at these scales. The bending is clearly due to the truncation error in the gluonic vertices, whose suppression with the temperature is not resolved sufficiently. The strong dependence of the transversal gluons on the ansätze of the vertices is seen in detail in the truncation tests that are done at the end of this section, cf. fig. (4.19) and fig. (4.20).
In turn, for larger momenta the transversal propagator agrees well with the respective lattice propagator, see fig. (4.21(a)).

The ghost propagator is enhanced with the temperature, see fig. (4.15(a)). For its wave-function renormalisation this entails a suppression with the temperature, see fig. (4.15(b)).

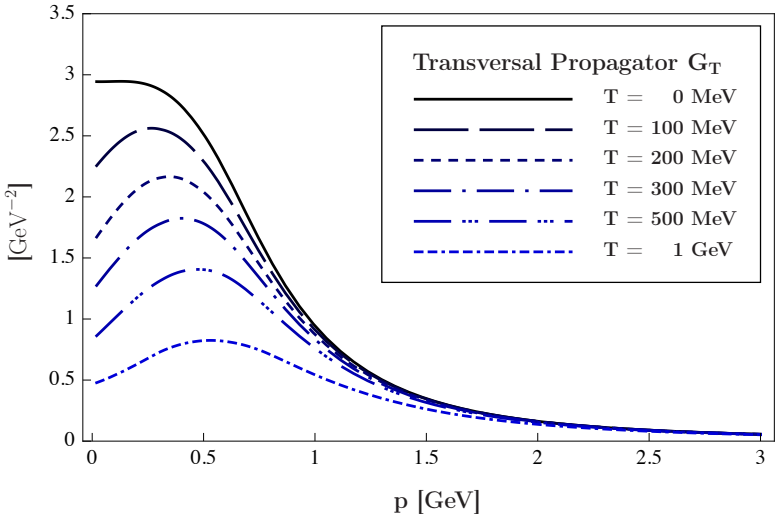

(a) Transversal gluon propagator G_T at different temperatures.

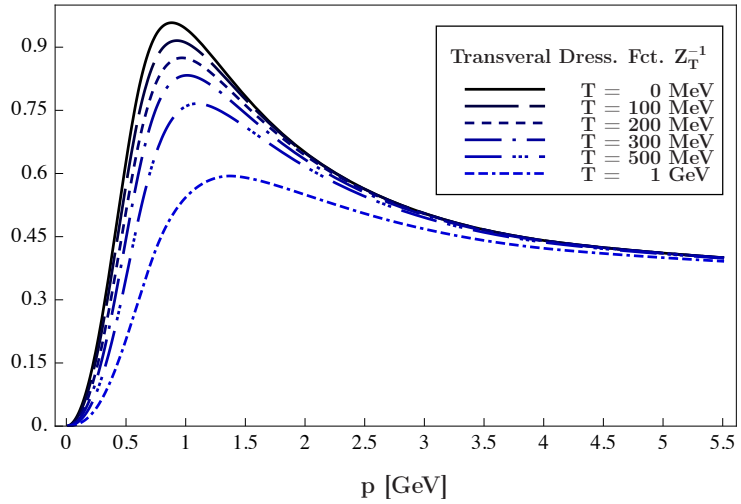

(b) Dressing function of the transversal gluon Z_T^{-1} at different temperatures.

Figure 4.14.: Thermal behaviour of the zeroth Matsubara mode of the propagator and dressing function of the chromomagnetic gluon as a function of the spatial momentum p.

This behaviour clearly deviates from lattice results, where the propagator seems to be unaffected by thermal fluctuations [115, 305, 323, 325, 327, 330]. This deviation is probably an artefact of the truncation employed here, where the constant ghost-gluon vertex is taken as bare at zero and non-zero temperature. However, the ghost-gluon vertex defines the running coupling in the formulation detailed in section 4.1.3, which is suppressed with the temperature in a full setup, as the physical coupling has to tend towards the

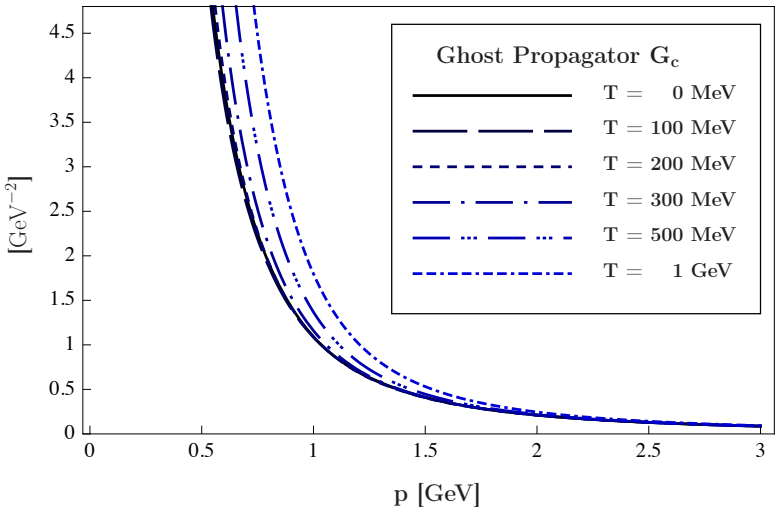

(a) Ghost propagator G_c at different temperatures.

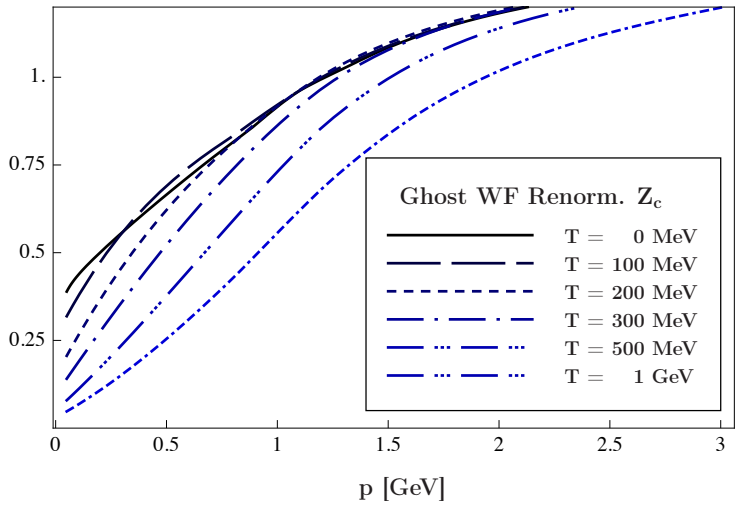

(b) Wave-function renormalisation of the ghost Z_c at different temperatures.

Figure 4.15.: In contrast to the gluons, the ghost is a Lorentz-scalar. Thus, it can be described with a single tensor structure. Here, the zeroth Matsubara modes of the ghost propagator and wave-function renormalisation are given as a function of the spatial momentum p. Higher modes can be approximated by shifting the spatial momentum of the zero mode by the time component.

three-dimensional coupling via the transmutation factor of p/T. In the FRG the latter suppression below the temperature scale translates into the suppression with k/T, which has not been considered here. However, the effect of the temperature in the ghost flow is unidirectional, i.e. the ghost propagator is enhanced. Most of the enhancement in the results in fig. (4.15(a)) builds up at scales, where k is well below T. Therefore, it is fair to

say that for a suppression of the coupling the enhancement of the ghost propagator would be attenuated in comparison with the results presented here. Thus, the improvement of the truncation with regard to a satisfactory inclusion of the running of the ghost-gluon vertex would bring the ghost propagator closer to the lattice result.

The enhancement of the ghost propagator appears to be potentially problematic, as one would assume that with increasing temperature the Z_c would become negative. This would yield an unphysical pole in the ghost propagator. Note however, that this can not happen due to the temperature-dependent field reparametrisation of the ghosts, see section 4.1.3, which stabilises the system. In fact, for the system without reparametrised ghost fields no solution could be obtained for temperatures $\lesssim 100\,\mathrm{MeV}$.
Though, the truncation error stemming from the constant ghost-gluon vertex is not absent. Rather, it is manifest in a different form which is the strong enhancement of the ghost propagator.

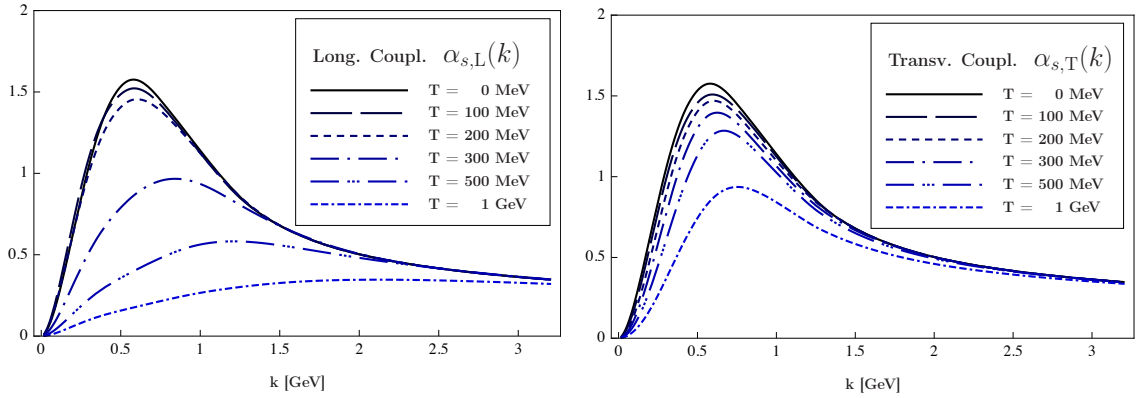

(a) The longitudinal coupling is increased for low temperatures and small scales, as the longitudinal gluon is enhanced in this temperature and momentum range. For higher temperatures the longitudinal gluon is suppressed, which is directly seen in the coupling.

(b) The transversal coupling bears the signature of the dressing function of the chromomagnetic gluon, it gets suppressed with increasing temperature.

Figure 4.16.: Following eq. (4.43) the non-perturbative running coupling depends on the temperature. The breaking of manifest Lorentz symmetry by the heat bath necessitates that there are two different couplings for the chromoelectric and chromomagnetic gluon, respectively. The dominating effect of these couplings is that both reflect the thermal behaviour of the gluonic wave-function renormalisation functions. With respect to the coupling at vanishing temperature, the chromoelectric coupling is enhanced for small temperatures and suppressed for intermediate and high temperatures. The chromomagnetic coupling is suppressed for all temperatures.

With the definition of the coupling in eq. (4.21b) and following the reasoning for the existence of two gluonic modes at non-vanishing temperature due to the breaking of manifest Lorentz symmetry by the heat bath as explained in section 4.1.1 there are two different

couplings for the chromoelectric and the chromomagnetic gluon, respectively. Note, that if used within the flow, the coupling is scale dependent [272,276] which leads to the definition

$$\alpha_{s,L/T}(k) = \frac{1}{4\pi} \frac{\left(\Gamma_{\bar{c}Ac,k}\right)^2 k^6}{\hat{\Gamma}^{(2)}_{L/T,k}(k) \left(\hat{\Gamma}^{(2)}_{c,k}(k)\right)^2} , \tag{4.43}$$

where $\Gamma_{\bar{c}Ac,k}$ depends on the localised correlation functions. It is the dressing of the full ghost-gluon vertex but not only of the renormalisation group invariant tensor $z_{\bar{c}Ac,\,k}$, see eq. (4.17). Naturally, both couplings are dependent on temperature. The enhancement or suppression of the gluons in combination with the ghost propagators is directly seen in the couplings. As the chromoelectric gluon is enhanced for small temperatures, the coupling becomes stronger in the infrared. In contrast, the suppression for higher temperatures downsizes the strength of the longitudinal coupling, see fig. (4.16(a)). The latter effect is also seen for the chromomagnetic gluon, however for all temperatures, as the propagators is suppressed for all temperatures with respect to the zero temperature propagator, see fig. (4.16(b)). Note that the expression of the coupling in terms of the physical fields and the corresponding vertex functions is crucial for the suppression of the coupling, as it compensates the overestimated suppression of the wave-function renormalisation of the ghost.

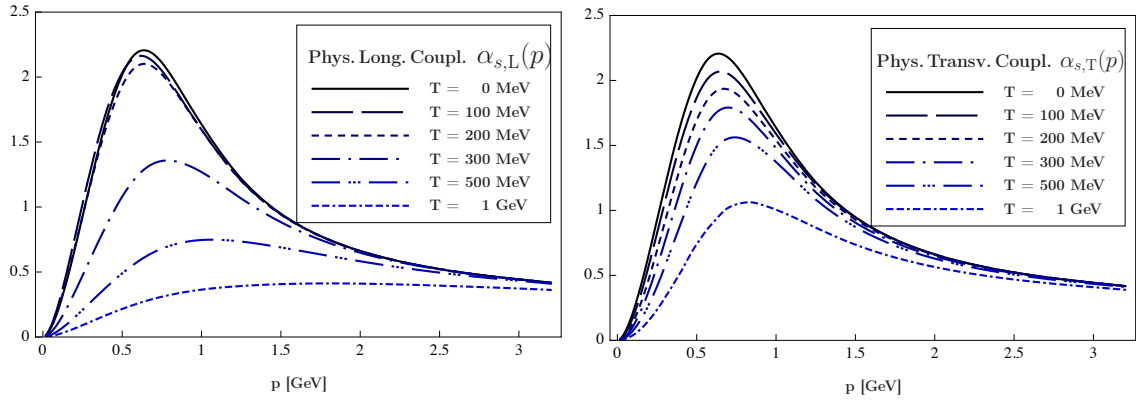

(a) The physical longitudinal coupling is increased for low temperatures and momenta. For higher temperatures the longitudinal gluon is suppressed, which is directly seen in the coupling.

(b) The physical transversal coupling is suppressed with increasing temperature.

Figure 4.17.: Physical couplings as defined in eq. (4.21b). The physical couplings feel the temperature via the wave-function renormalisation functions of the gluons and ghosts. With respect to the coupling at vanishing temperature, the chromoelectric coupling is enhanced for small temperatures, but suppressed for intermediate and high temperatures. The latter effect is seen for the transversal coupling at all temperatures.

The physical couplings eq. (4.22) look qualitatively similar to the running couplings. Both, the physical longitudinal coupling $\alpha_{s,L}(p)$, given in fig. (4.17(a)), as well as the physical

transversal coupling, given in fig. (4.17(b)), are suppressed with increasing temperature.

4.2.2. Truncation Tests

Naturally, the truncation at hand needs to be tested. In the following this is done by different definitions of the gluonic vertices and varying the strength of dressing functions. The necessity of this test is obvious already in view of fig. (4.11). Furthermore, the accuracy of the suppression of the gluonic couplings with the temperature needs to be quantified. In addition, the validity of the approximation for higher Matsubara modes is investigated.

The system was solved for the zeroth Matsubara mode only, as higher Matsubara modes can be approximated by shifting the spatial momentum of the zeroth Matsubara mode by the corresponding frequency, which is explained in section 4.1.1. This approximation is motivated by known results [305, 429]. At this point, the validity of this truncation is tested, the results for the zeroth, first and second Matsubara modes for the longitudinal gluon propagator, the transversal gluon propagator and the wave-function renormalisation of the ghost are given in fig. (4.18(a)), fig. (4.18(c)) and fig. (4.18(e)). The results were obtained by setting the temporal component of the external momentum as the corresponding Matsubara mode and solving the flow at finite temperature from the initial scale Λ. In this computation the effect of the backcoupling of higher modes is neglected. However, as the results deviate only little from the approximation, the change from the backcoupling would be small. In conclusion, this confirms that the approximation for the higher Matsubara modes is quantitatively reliable, as it is expected on the one hand side from the quick decay of thermal effects at scales above the first Matsubara mode and on the other hand side from known results [305, 429].

In section 4.1.4 it is detailed how the temperature dependence of the gluonic vertices is approximated by an ansatz that combined all necessary qualitative properties of the vertices. In order to check the sensitivity of the propagators at low temperatures to this choice the results with a strong suppression, eq. (4.36), are compared with a computation where the minimal suppression of the gluonic vertices is implemented, i.e. $\xi = 0$.

The result of the computation is given in fig. (4.19), again for the longitudinal gluon propagator and dressing function in fig. (4.19(a)) and fig. (4.19(b)), for the transversal gluon propagator and dressing function in fig. (4.19(c)) and fig. (4.19(d)), and for the ghost propagator and wave-function renormalisation in fig. (4.19(e)) and fig. (4.19(f)), respectively.

Fig. (4.19) shows clearly that the chromomagnetic gluon is sensitive to the choice of gluonic vertices. In particular, the bending of the propagator (and dressing function) is determined by the strength of the thermal behaviour of the gluonic interactions. The chromoelectric propagator feels the gluonic vertices, however only in a region where the

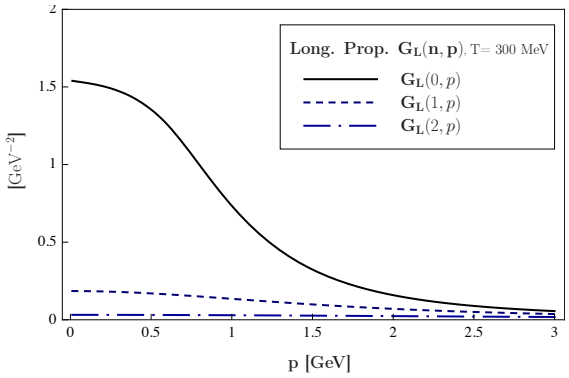

(a) Zeroth, first and second Matsubara mode of the longitudinal gluon propagator G_L.

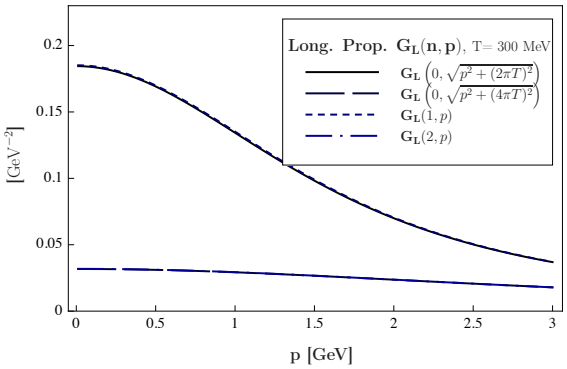

(b) Validity test of the "Zero-mode approximation" for the longitudinal gluon propagator.

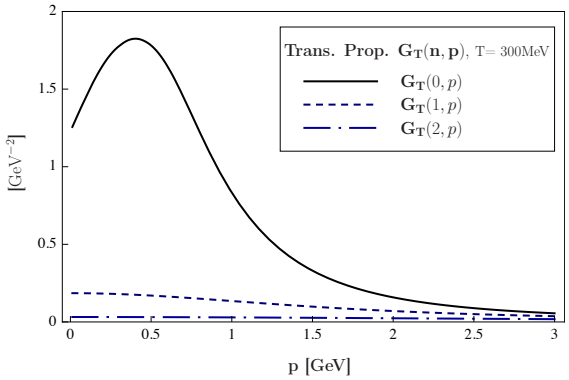

(c) Zeroth, first and second Matsubara mode of the transversal gluon propagator G_T.

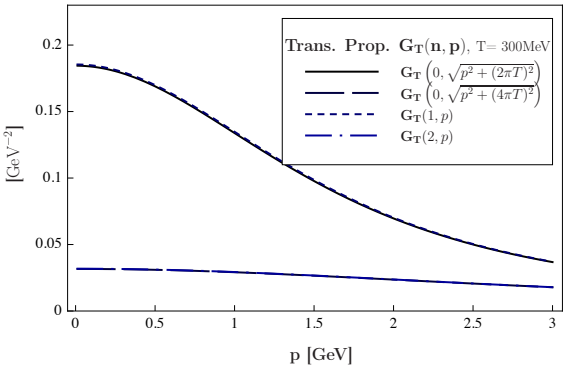

(d) Validity test of the "Zero-mode approximation" for the transversal gluon propagator.

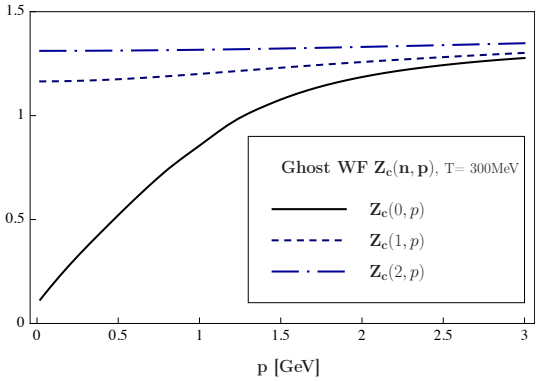

(e) Zeroth, first and second Matsubara mode of the ghost wave function renormalisation Z_c.

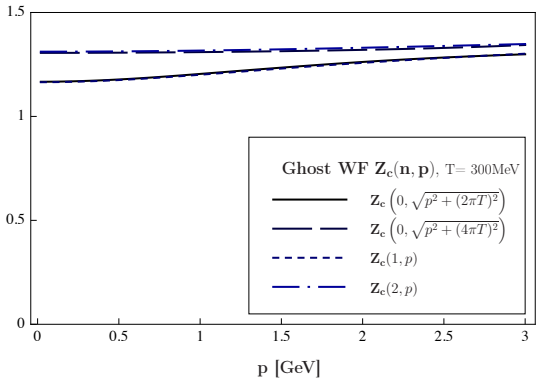

(f) Validity test of the "Zero-mode approximation" for the ghost wave function renormalisation.

Figure 4.18.: Higher Matsubara modes are well approximated by shifting the spatial momentum by the Matsubara mode, therefore resolving the zero mode only is already sufficient to achieve high accuracy. This is in agreement with DSE studies and lattice results [305, 429].

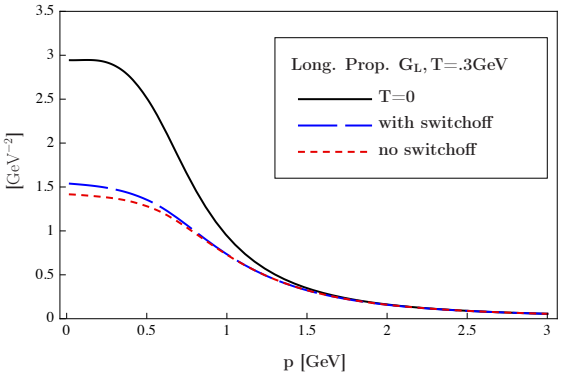

(a) Comparison of longitudinal propagator with minimal and maximal strength of the coupling of purely gluonic vertices according to eq. (4.36).

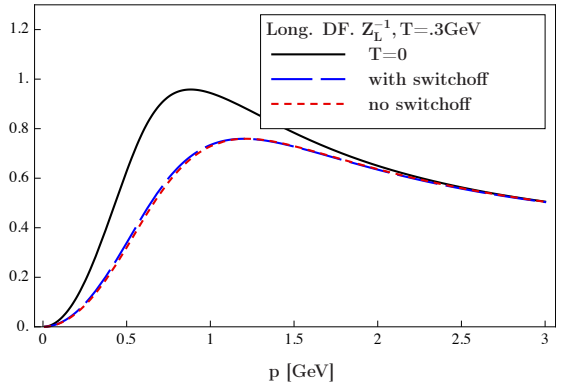

(b) Comparison of longitudinal dressing function with minimal and maximal strength of the coupling of purely gluonic vertices according to eq. (4.36).

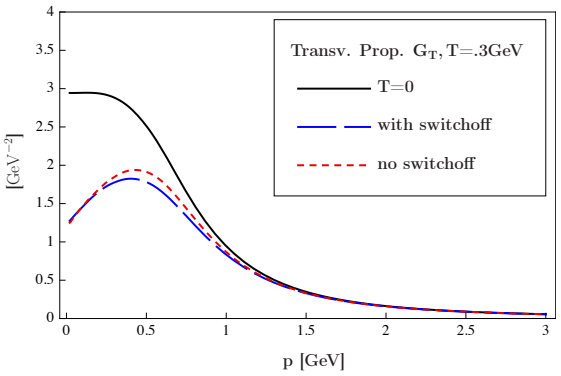

(c) Comparison of transversal propagator with minimal and maximal strength of the coupling of purely gluonic vertices according to eq. (4.36).

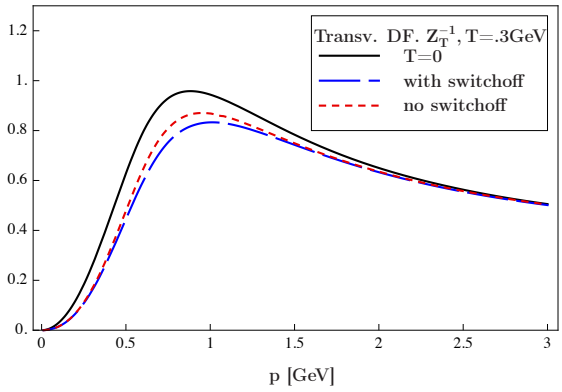

(d) Comparison of transversal dressing function with minimal and maximal strength of the coupling of purely gluonic vertices according to eq. (4.36).

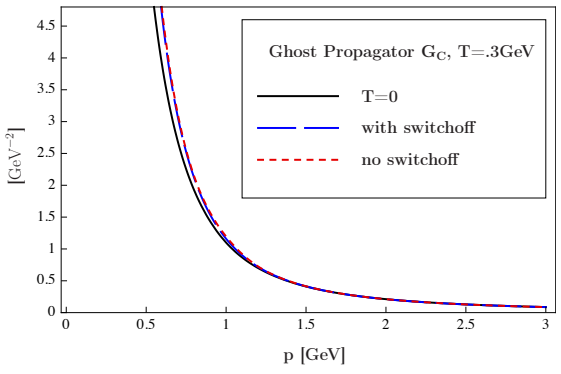

(e) Comparison of ghost propagator with minimal and maximal gluonic flow according to eq. (4.36).

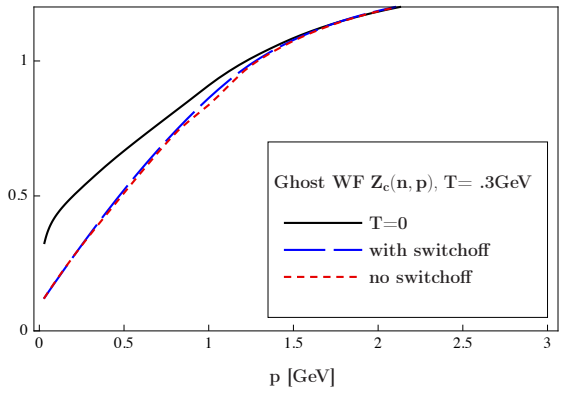

(f) Comparison of ghost dressing function with minimal and maximal gluonic flow according to eq. (4.36).

Figure 4.19.: Test for the truncation detailed in section 4.1 on the level of the two-point functions. The comparison shows results for the two-point functions that were obtained with and without switching off the gluonic vertices below the temperature scale $\xi T = 3/2\pi T$.

thermal mass dominates. The ghost hardly changes with the strength of the gluonic vertices, which is expected as those correlation functions only enter the ghost flow indirectly via the gluonic two-point functions. Thus, a moderate modification of the gluonic vertices should only give a small correction to the ghost flow, although it is a coupled system, see fig. (4.12). The main gluonic n-point functions that enter the ghost are the gluon propagators only, which themselves do not change significantly with the different strengths of the gluonic vertices. This is in agreement with the well-known fact that the infrared sector of Yang-Mills theory in Landau gauge has ghost dominance (for both scaling and decoupling solutions) for any dimension $d = 2, 3, 4$.
This truncation test gives an approximate error band for the propagators with respect to the ansatz of the gluonic vertices defined via reasonable $\bar{Z}_{L,k}$'s. The insufficiency of the naive ansätze is studied below.
As a result, the main impact of the truncation of the gluonic vertices is onto the longitudinal propagator below T_c, given in fig. (4.19(a)), The impact on the dressing functions thereof is given in fig. (4.19(b)).

A further investigation concerning the truncation described in section 4.1 is necessary, namely the choice of the longitudinal $\bar{Z}_{L,k}$ to appear in the gluonic vertices only. This truncation is compared with a computation in which the couplings are strictly related to the gluonic legs that enter the vertex, each of which contributing with a factor $\bar{Z}^{1/2}_{L/T,k}$. The result is given in fig. (4.20).

These result confirm the statement that the chromomagnetic gluon is very sensitive to the gluonic vertices. For larger temperatures the transversal propagator would even develop an unphysical pole which is purely due to the insufficient truncation. In contrast, the longitudinal and ghost quantities hardly feel the change in the gluonic vertices, as it is expected due to the reasoning above.

All in all, this confirms that the truncation has to improved with respect to a better resolution of vertices in order to quantitatively capture the deep infrared. It can be concluded that in particular the suppression of the coupling in the ghost-gluon vertex as well as the gluonic vertices is crucial for the correct description of the thermal correlation functions.

However, the dressing functions for the gluons show that at intermediate momenta, the qualitative effects are not changed, however, quantitatively there are deviations. In section 4.3 it is stressed that firstly, the quantitative accuracy of the Yang–Mills thermodynamics primarily depends on the chromoelectric as well as chromomagnetic propagator. Secondly, it is not the deep infrared which is relevant for the thermodynamic quantities[9], but it is the mid-momentum region which is the important region. Therefore, although first results for the thermodynamics agree already quite well with lattice data, see section 4.3, it is

[9]Besides, this is the reason why the thermodynamics is insensitive to the propagator input being of decoupling or scaling type. This has been explicitly checked in this work and is in agreement with previous findings [11].

expected that even better accuracy can be achieved by resolving the vertices also in a temperature-dependent way. In fact, this serves as the bigger motivation to resolve the gluonic vertices in the full momentum region, cf. section 4.1.4, than a better agreement in the deep infrared sector.

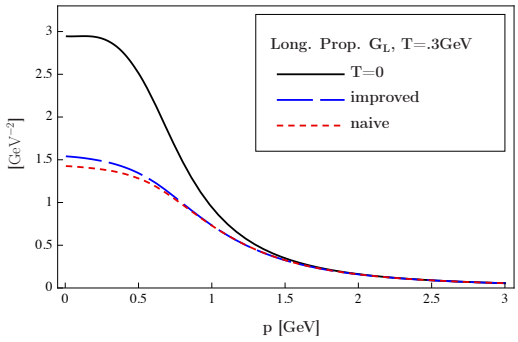

(a) Truncation test for the longitudinal propagator with respect to the ansätze of the gluonic vertices.

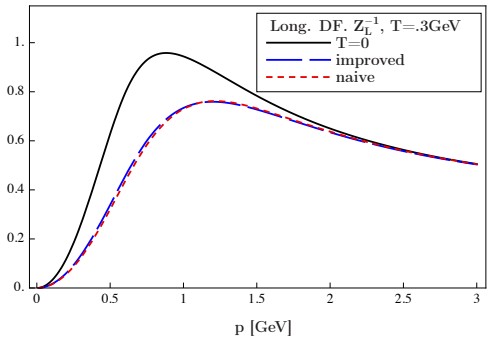

(b) Truncation test for the longitudinal dressing function with respect to the ansätze of the gluonic vertices.

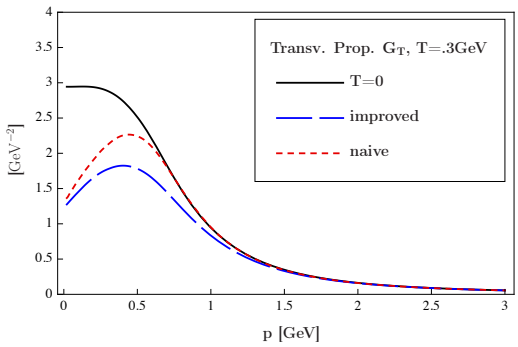

(c) Truncation test for the transversal propagator with respect to the ansätze of the gluonic vertices.

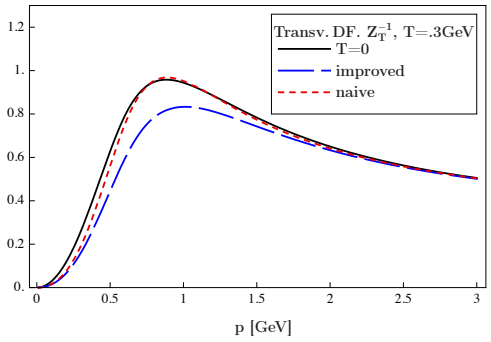

(d) Truncation test for the transversal dressing function with respect to the ansätze of the gluonic vertices.

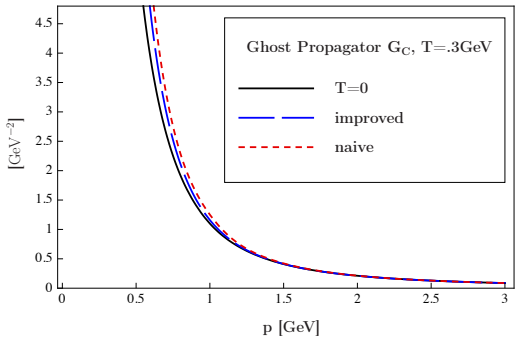

(e) Truncation test for the ghost propagator with respect to the ansätze of the gluonic vertices.

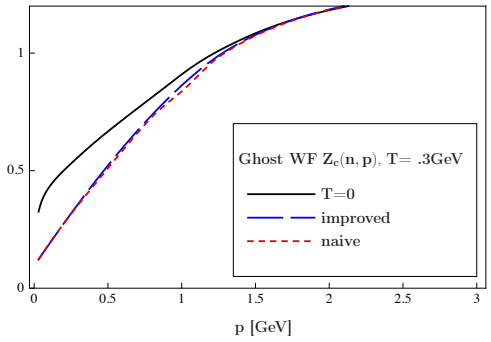

(f) Truncation test for the ghost wave-function renormalisation with respect to the ansätze of the gluonic vertices.

Figure 4.20.: Test for the truncation detailed in section 4.1.4 on the level of the two-point functions. The results were obtained with the naive and the improved ansätze for the purely gluonic vertices at non-vanishing temperature according to the analysis about fig. (4.11). The naive ansätze drive the system away from the physical situation, as the transverse gluon propagator is even enhanced and even develops an unphysical pole. Thus, the refined ansätze for the gluonic vertices are inevitable.

4.2.3. Comparison with Lattice Gauge Theory

As there is lattice data available for the Yang–Mills propagators at non-vanishing temperature [115,305,323,325,327,330], the results obtained in this work can be directly compared to lattice gauge theory. In the following data from [115, 323, 446] is used. However, the units and scales have to be matched. This is done in such a way that the lattice data is scaled to match the normalisation of section 4.2 at momenta $p \gtrsim 1\,\mathrm{GeV}$ at vanishing temperature. Take notice that the decoupling solution that was used here was not the one from the lattice to which the results are compared with. Thus, the deep infrared of the data deviates from the input propagators already at zero temperature, which persists also in the propagators at finite temperature. Apart from that there is quantitative agreement with the lattice data with respect to the (temperature-dependent) momentum region, where the thermal effects appear. In fig. (4.21(a)) the transversal propagators are compared. Note that the critical temperature in the lattice data is $T_c \approx 277\,\mathrm{MeV}$ (with $\sqrt{\sigma} = 440\,\mathrm{MeV}$).

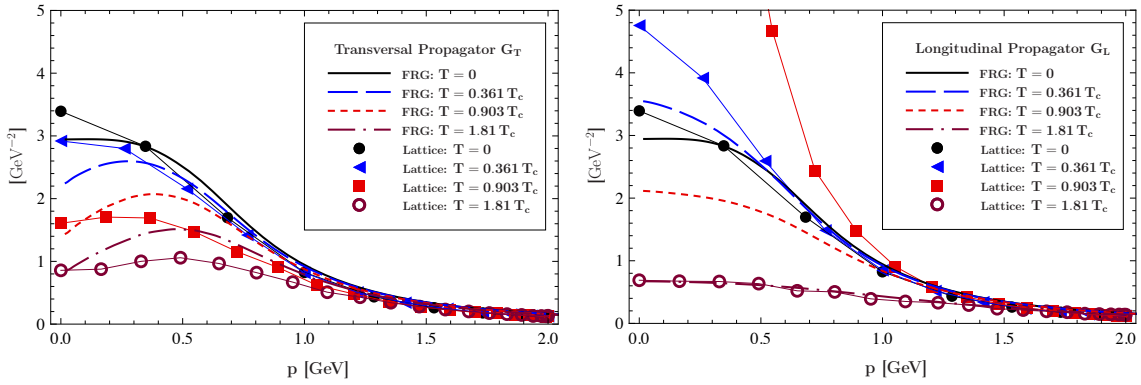

(a) Chromomagnetic gluon propagator in comparison with lattice data. The suppression of the chromomagnetic propagator for all temperatures is seen in both approaches. The FRG result shows a strong bending of the propagator at intermediate spatial momenta which is due to an insufficient truncation with respect to temperature-dependent three- and four-gluon vertices, see section 4.2.1. For small and large momenta there is quantitative agreement with lattice data.

(b) Chromoelectric gluon propagator in comparison with lattice data. On the lattice the chromoelectric propagator is enhanced for small temperatures. In contrast to this, above the deconfinement-confinement phase transition temperature $T \approx 277$ MeV the lattice shows suppression of the propagator. For the limits of small and high temperature, the FRG matches this behaviour quantitatively, i.e. for temperatures where the propagator is not directly affected by the critical physics the dominating effects are captured well, even the non-trivial enhancement. However, in particular at small temperatures the deviation of the propagators at vanishing temperature is most pronounced. However, for intermediate temperatures $150\,\mathrm{MeV} \lesssim T \lesssim 400\,\mathrm{MeV}$ the propagator from the functional method is smaller that on the lattice. In this temperature range there is a qualitative difference.

Figure 4.21.: Comparison of the gluon propagators with lattice results [115,323,446]. The lattice data is rescaled such that the $T = 0$ propagators match the gluon propagator at vanishing temperature, see section 4.2.1, at intermediate momenta $p \gtrsim 1\,\mathrm{GeV}$.

Clearly, the chromomagnetic gluon shows the same thermal behaviour as it is seen in the lattice simulations: At non-zero temperature the corresponding propagator is suppressed with respect to the vacuum. Without a doubt, the qualitative behaviour is seen in the FRG as well, however, even on a quantitative level the continuum results match in the region where the truncation is reliable. Therefore, the correlation functions quantitatively agree except for the strong bending of the continuum propagators at intermediate momenta. The difference at intermediate momenta is presumably due to the insufficiency of the truncation with respect to the thermal behaviour of purely gluonic vertices, which is corroborated by the truncation tests in fig. (4.19(c)) and fig. (4.20(c)). Nevertheless, the intervals of small and high momenta are largely unaffected by these truncation errors, which is reflected in a good quantitative agreement of the transversal gluon propagator in these momentum regions under disregard of the difference of the propagators at vanishing temperature in the deep infrared already which is still evident at small temperatures.

In contrast to this, the chromoelectric gluon on the lattice shows a qualitatively different behaviour for temperatures below and around the phase transition. Although the longitudinal propagators agree for $T = 0.361T_c \approx 100\text{MeV}$, it is exactly this region where the uncertainty due to the truncation for the gluonic vertices and the ghost-gluon vertex is large, as shown in fig. (4.19(a)) and fig. (4.20(a)) for $T = 300$ MeV.
Disregarding a potential truncation dependency in the deep infrared of the longitudinal propagator at low temperatures as shown in section 4.2.1, the present truncation the chromoelectric gluon shows the onset of the enhancement found on the lattice. Increasing the temperature this feature disappears and a qualitatively different effect for temperatures below T_c takes over. While the continuum result shows a strictly monotonic decreasing propagator, the counterpart on the lattice is enhanced in the confining regime, but reflects the phase transition in form of a rapid decrease at T_c.
Nevertheless, this deflection is expected to be missed in the present truncation, as the Polyakov loop potential $V(A_0)$ is pivotal for the critical behaviour around the phase transition. In a full calculation the inverse longitudinal gluon propagator is proportional to the second derivative of the Polyakov loop $\Gamma^{(2)}_{A,L} \sim V''(A_0)$, see [11,12,17,112]. This dependence introduces an additional screening of the vertex-approximations as well as vertex corrections, however, in the computations presented here it was dropped. This upgrade should also give access to the question of the signatures of criticality in the chromoelectric propagator discussed in [327]. Interestingly, such a term is absent in the magnetic modes. It is suggestive that the inclusion of A_0 stabilises the computation further. However, this analysis is beyond the scope of this thesis.

In all published lattice results the ghost propagator is insensitive to thermal fluctuations [115, 305, 323, 325, 327, 330]. In the data at hand, the propagators at different temperatures can not be distinguished within the error bars. Thus, the direct comparison for the ghost is not explicitly illustrated here, as it basically contains the information of fig. (4.15(a)). As it was detailed already, the ghost propagator is significantly enhanced

with increasing temperature. It is a reasonable hypothesis that the deviation of the propagator from the lattice result is due to the insufficient truncation of the ghost-gluon vertex whose thermal behaviour is neglected in the results presented in this thesis.

4.3. Yang–Mills Thermodynamics

The flow equation for the effective action allows to access the pressure and other thermodynamical observables in Yang–Mills theory by means of the full propagators only. This remarkable property has been already utilised and tested successfully in other theories, for results see [407, 422, 447].

In this thesis the focus is on the computation of the pressure $p(T)$, as a proper computation of it allows to determine the other thermodynamic quantities of the energy density $\epsilon(T)$ as well as trace anomaly $\Theta(T)$. The latter expression quantifies the deviation from the ideal gas result, so it is a measure for the interaction of the system. With Z being the partition function, there are relations for the thermodynamics quantities

$$p(T) = \frac{T}{V}\mathrm{Log}\{Z\}\,, \tag{4.44}$$

$$\epsilon(T) = T^2\partial_T\frac{p(T)}{T}\,, \tag{4.45}$$

$$\Theta(T) = \epsilon(T) - 3p(T)\,. \tag{4.46}$$

In the framework of the FRG the pressure is easily accessible, as it is nothing but the effective action evaluated on the equation of motion normalised to zero in the vacuum, i.e. at $T = 0$. Therefore, $p(T) = -\Delta\Gamma_{T,0}$, the latter being defined in eq. (3.52). More generally, if the theory is put in a background $\bar{A}$, the related thermal pressure reads

$$p(\bar{A}) = -\Delta\Gamma_{T,0}[\bar{A}]\,, \tag{4.47}$$

with a slight abuse of notation. It is understood that the ghost fields vanish, $c = \bar{c} = 0$. The pressure in eq. (4.47) can be accessed within a given approximation by evaluating the effective action on the equation of motion, or via a diagrammatic expression of the thermal fluctuations, e.g. the 2PI-expression for the effective action. In the flow equation approach the flow can be used directly for $\Gamma_{T,k}$ in the approximation at hand, with the definition for the regulator-dependent pressure,

$$p_k(\bar{A}, T) = -\Delta\Gamma_{T,k}[\bar{A}]\,, \tag{4.48}$$

and its flow

$$\partial_t p_k(\bar{A}, T) = -\partial_t\Delta\Gamma_{T,k}[\bar{A}]\,, \tag{4.49}$$

for regulator-independent backgrounds A_0, see also chapter 5. The flow in eq. (4.49) is

sensitive to thermal fluctuations, see eq. (3.51) and the discussion in section 3.2.6. Note that the definitions eq. (4.48) and eq. (4.49) have to be taken with precaution in gauge theories, as the theory is described by more than just the physical degrees of freedom as the flow necessitates a gauge-fixed approach. The pressure flow eq. (4.49) is sensitive to the normalisation of the path integral. Hence, it is potentially sensitive to regulator-dependent modifications of the auxiliary degrees of freedom, for discussions see [277, 278, 407].
A safe way to deal with such a situation is to project the path integral or the effective action only on the physical subspace before computing the pressure. If such a procedure can be formulated it avoids the potential necessity of non-trivial cancellations between contributions from the unphysical subspace. In the present case this concerns the ghost contribution, the gauge mode $A_{L,\mu}(p) = p_\mu/p^2 p_\nu A_\nu$ and one of the transversal modes, the one on the zero norm subspace. In turn, there are only the two physical transversal polarisations, the chromoelectric mode and one chromomagnetic mode, that enter the related flow of the pressure. This strategy is detailed further below.

The final expression for the thermal pressure is given in terms of the integrated flow,

$$\begin{aligned} p(\bar{A}) &= \frac{1}{2}\int_0^\Lambda \frac{dk}{k}\left(\operatorname{Tr} G[\bar{A}]\cdot\dot{R}_k\big|_T - \operatorname{Tr} G[\bar{A}]\cdot\dot{R}_k\big|_{T=0}\right) \\ &\quad + p_{\mathrm{ren}}(T)\,, \end{aligned} \tag{4.50}$$

where $\dot{R} = \partial_t R$ and $p_{\mathrm{ren}}(T) \neq \Delta\Gamma_{T,\Lambda}$ undoes the potential temperature-dependent renormalisation. $p_{\mathrm{ren}}(T)$ is Λ independent as the flow $\partial_t \Delta\Gamma_{T,k}$ vanishes quickly for $\Lambda/T \gg 1$. The precise position of the onset of the exponential decay and its slope are regulator dependent,

$$\exp\left(-c(R)\,\frac{k}{T}\right). \tag{4.51}$$

Sufficiently smooth and analytic regulators lead to suppression factors $c(R) \approx 1$. In turn, for regulators that are non-analytic in the Matsubara frequency, the thermal suppression factor disappears in general, that is $c(R) = 0$. Prominent examples for the latter are the four-dimensional exponential eq. (3.12), optimised eq. (3.13) or sharp regulator,

$$R_{\mathrm{sharp}}(q) = k^2\left(1/\theta(q^2-k^2)-1\right). \tag{4.52}$$

Within the exponentially decaying envelope the flow $\partial_t \Delta\Gamma_{T,k}$ oscillates. All the above properties can be studied already at one loop with classical propagators in the flow. This is displayed in fig. (4.22). Note however, that this is only the flow of the full pressure, where the term involving the Matsubara sum oscillates around the integral in the subtraction. In this flow the loop integrals have been carried out already. Naturally, the corresponding integrands of the individual loops at non-zero and zero temperature are regulated due to the term $\partial_t R_k(p)$ and are consequently free of oscillations.

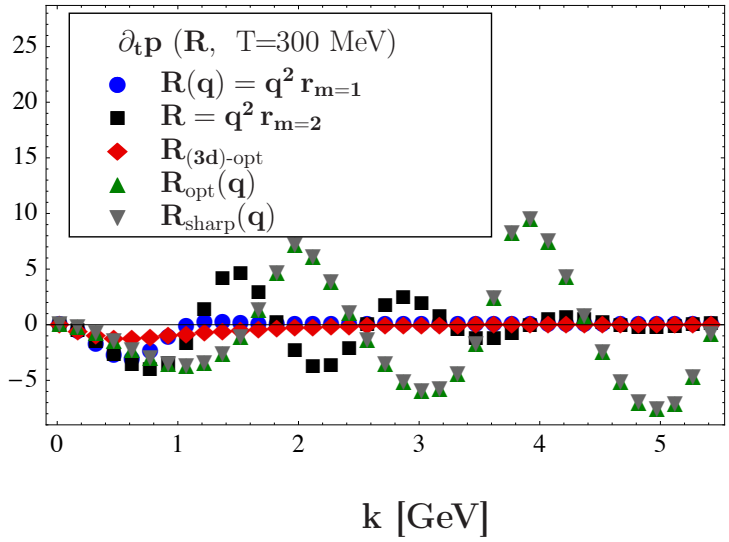

Figure 4.22.: The tree-level pressure flow $\partial_t p_k(T)$ at a fixed temperature $T = 300\,\text{MeV}$ and different regulators normalised to the canonical dimension. The pressure flow is a purely thermal flow as defined in eq. (4.50), i.e. it is constructed as a difference of the flow at finite temperature, hence involving a Matsubara sum and the flow at zero temperature, involving an integral over the temporal component of the loop momentum, q_0. Going to higher scales k this difference oscillates and in fact this oscillation can go to scales that are far above the typical temperature scale $2\pi T$. This effect is due to the shape of the regulator, in particular, it depends on the drop off of the regulator. The sharper the regulator falls off for $p \geq k$, the wider is the region of oscillations in k. In practical computations this effect rules out regulators that are too sharp.

In fig. (4.22) it is evident that the sharper a regulator gets the less does the thermal suppression work for the pressure. In turn, the smoother a regulator gets the harder it is to have control of the locality of the approximation scheme, see section 3.2.5. The latter can be cured by the use of the localised flow discussed in section 3.2.5. Here, the results are obtained with a relatively sharp regulator, see eq. (3.12) with $m = 2$.

The final expression in eq. (4.50) only depends on the scale-dependent ghost and gluon propagators in the background $\bar{A}$, see chapter 5. If the physics situation under discussion does not entail an external background field being present, the background field $\bar{A}$ should be the (minimal) solution of the equations of motion. For Yang–Mills theory at finite temperature and restricting to constant backgrounds yields

$$\bar{A}_\mu = \delta_{0\mu}\bar{A}_0\,, \quad \text{with} \quad \left.\frac{\partial V_{\text{eff}}(A_0)}{\partial A_0}\right|_{A_0=\bar{A}_0} = 0\,, \tag{4.53}$$

where $V_{\text{eff}}(A_0) = \Gamma_T[A_0]/\text{Volume}$ is the non-perturbative effective potential of a constant temporal gauge field A_0, see [11, 12, 17, 112]. V_{eff} takes the role of the Polyakov loop po-

tential in the present approach, cf. chapter 5. In the presence of an external background field these equations change accordingly. This is interesting in the context of early times in heavy-ion collisions which may inflict a physically relevant strong chromoelectric as well as chromomagnetic background.

The simple form of the flow equation eq. (4.50) defines the pressure flow for the two physical polarisations via a projection onto the related subspaces according to the projection operators defined in eq. (4.1).
This allows to split the gauge field regulator R_A as a block-diagonal matrix with the block entries

$$\begin{aligned} R^T &= P^T \cdot R_A \cdot P^T \,, \\ R^L &= P^L \cdot R_A \cdot P^L \,, \\ R^{\text{gauge}} &= (1 - \Pi^{\text{T}}) \cdot R_A \cdot (1 - \Pi^{\text{T}}) \,. \end{aligned} \tag{4.54}$$

The physical modes of the propagator are the chromoelectric and chromomagnetic one. The related pressure $p_\perp$ can be defined by projecting eq. (4.50) on these directions, that is

$$p_\perp(\bar{A}) = \frac{1}{2} \int_0^\infty \frac{dk}{k} \left(\operatorname{Tr} G[\bar{A}] \cdot \dot{R}_k^\perp\big|_T - \operatorname{Tr} G[\bar{A}] \cdot \dot{R}_k^\perp\big|_{T=0} \right) , \tag{4.55}$$

with

$$R^\perp = R^L + R^{T,(1)} \,. \tag{4.56}$$

In eq. (4.56) the second term $R^{T,(1)}$ is just the projection on a one-dimensional subspace of $P^T = (P^T)^{(1)} + (P^T)^{(2)}$. The ghost loop and the gauge mode loop are missing in eq. (4.55). Note however, that the ghost and the second transversal mode related to $(P^T)^{(2)}$ is contributing to the quantum and thermal fluctuations of the chromoelectric propagator $\sim P^L$ and the chromomagnetic propagator $\sim P^{T,(1)}$. In the following the latter, transversal definition eq. (4.55) is used.

One of the most interesting and most debated issues for the pressure of Yang–Mills theory and of QCD is its approach towards the Stefan–Boltzmann limit. It is very slow for large temperatures $T \gg T_c$, which can be understood within higher orders of HTL perturbation theory [347, 358–362] or 2PI-resummations [354–357], see section 2.3.3.
However, the temperature region

$$T_c \lesssim T \lesssim (3-5) T_c \tag{4.57}$$

has not been well-covered yet with continuum methods. The regime eq. (4.57) is truly non-perturbative and is sensitive to the confining physics. Precisely this temperature domain is the focus of this work, where quantitative agreement with the lattice is achieved.

The results are plotted in fractions of the Stefan–Boltzmann pressure in Yang–Mills theory,

which can be computed analytically for arbitrary regulators. Here, a convenient choice of the three-dimensional optimised regulator proportional to eq. (3.13) is taken to minimise the obstructions due to the choice of the regulator. For the cutoff function $R_k(q) = \vec{q}^2 r^{\text{opt}}(\vec{q}^2/k^2)$ the Stefan–Boltzmann pressure p_{SB_1} can be computed by taking classical (massless) propagators, so the pressure flow is given by

$$\begin{aligned} -\partial_t p_{\text{SB}_1,k}(T) &= \sum\!\!\!\!\!\!\int_q \frac{1}{2} G_k(q)\dot{R}_k(q) - \int_q \frac{1}{2} G_k(q)\dot{R}_k(q) \\ &= \frac{1}{2\pi^2}\left(T\sum_{n=-\infty}^{\infty} \int_0^k dq \frac{k^2 q^2}{k^2 + (2\pi T n)^2} - \frac{1}{2\pi}\int_{-\infty}^{\infty} dq_0 \int_0^k dq \frac{k^2 q^2}{k^2 + q_0^2}\right) \\ &= \frac{1}{12\pi^2} k^4 \left\{ \coth\left(\frac{k}{2T}\right) - 1 \right\} . \end{aligned} \tag{4.58}$$

Integration over k yields the Stefan–Boltzmann pressure,

$$p_{\text{SB}_1}(T) = -\int_\infty^0 \frac{dk}{k}\, \partial_t p_{\text{SB}_1,k}(T) = \frac{\pi^2 T^4}{90} , \tag{4.59}$$

where the trivial initial condition is justified, as thermal effects are suppressed at infinitely high scales. Furthermore, for dimensional reasons, the pressure of a free gas scales with T^4. Note again that naturally the result for p_{SB_1} in eq. (4.59) is independent of the choice of the regulator $R_k(p)$.

In the computation for eq. (4.59) the only scale is the temperature and the canonical scaling yields the T^4 behaviour. The situation is more complex in Yang–Mills theory. Even at vanishing temperature the gluon propagator develops an effective mass in the infrared due to quantum effects, cf. section 2.3.2. For temperatures around and below this additional scale, which is set from the peak in the dressing function at around 1 GeV, see fig. (2.4), there are deviations from the free gas result. The basic properties, e.g. the suppression at small temperatures as well as the slow convergence to the Stefan–Boltzmann limit, can be seen already in simple toy example. Similar to the investigations for finite volume in section 3.2.6, this toy is a real massive scalar in a "classical" truncation, i.e. $\Gamma^{(2)}_{\text{scalar}}(p) = p^2 + m^2$. Carrying out the same computation as in eq. (4.58) and eq. (4.59) reveals a few important aspects. Firstly, in comparison to the free gas the pressure is suppressed by the mass, but it is not an exponential suppression. Secondly, the temperature, at which the drop off of the suppression sharpens is not at the mass but significantly below this scale. Thirdly, the convergence to the classical limit is slow, even for temperatures much larger than the additional scale. The numerical result for the pressure normalised to p_{SB_1} is given in fig. (4.23). Note that there is effectively only one relevant parameter, which is the temperature measured in units of the mass.
Albeit this system is by no means comparable with the complexity of Yang–Mills theory as it is studied below, the thermal behaviour shows some relevant similiarities.

The Stefan–Boltzmann pressure eq. (4.59) is not yet the appropriate expression for Yang–Mills theory, because it is only for one colour-less mode. Consequently, the number of

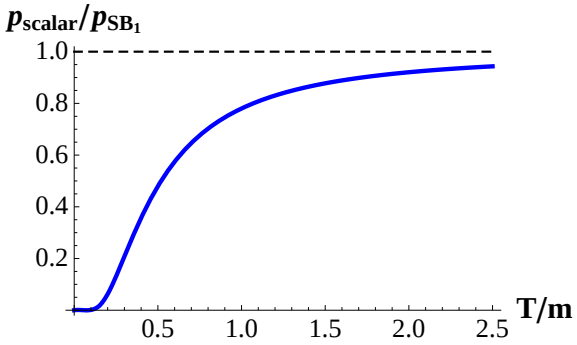

Figure 4.23.: Pressure for a massive scalar particle in a "classical" approximation normalised to the Stefan–Boltzmann value.

degrees of freedom must be adjusted. Thus, two[10] trivial corrections must be done to have the correct expression for Yang–Mills theory with its two physical polarisations and the underlying gauge group $SU(N_c)$. Firstly, the combinatorical factor of 2, as the chromoelectric as well as the chromomagnetic mode contribute to the physical pressure. Secondly, the trivial trace over colour indices must be done which gives for gluons (in the adjoint representation) a factor of $N_c^2 - 1$. In total, the Stefan–Boltzmann pressure for Yang–Mills theory p_{SB} is given by

$$p_{\mathrm{SB}} = \frac{\pi^2 T^4}{45}(N_c^2 - 1)\,. \tag{4.60}$$

Beyond perturbation theory the pressure in fractions of p_{SB} is given by

$$\frac{p(T)}{p_{\mathrm{SB}}} = \frac{1}{p_{\mathrm{SB}}} \int_0^\Lambda \frac{dk}{k} \frac{1}{2} \left[\sum\!\!\!\!\!\!\int_p \left(\dot{R}G\right)_T^{\varphi\varphi} - \int_p \left(\dot{R}G\right)_{T=0}^{\varphi\varphi} \right], \tag{4.61}$$

where a sum over species of fields and internal indices is implied and the factor $\frac{1}{2}$ is the generic factor in eq. (3.15). For the pressure definition eq. (4.50) the sum would run over all species of fields including ghosts, gauge mode and the second transversal mode related to $P^{T,(2)}$. The corresponding Stefan–Boltzmann pressure would be modified to account for the correct number of modes. For the transversal pressure to be considered here eq. (4.55) the sum runs over the chromoelectric mode and the first transversal mode related to $P^{T,(1)}$.

In the computation another approximation is made which concerns the manifestation of the temperature on different levels. The full form of the transversal pressure according to

[10] Note that in the case of fermions there is another factor of $\frac{7}{8}$ in the pressure. However both, gluons and ghosts obey bose statistics, albeit the ghosts are Grassmann fields.

eq. (4.61) can be split up to separate the two effects by adding a zero in the form

$$p(T) = \frac{1}{2}\int_0^\Lambda \frac{dk}{k}\left\{\underbrace{\sum\!\!\!\!\!\!\int_p \left(\dot{R}G\right)_T^{\varphi\varphi} - \int_p \left(\dot{R}G\right)_T^{\varphi\varphi}}_{\mathcal{A}} + \underbrace{\int_p \left(\dot{R}G\right)_T^{\varphi\varphi} - \int_p \left(\dot{R}G\right)_{T=0}^{\varphi\varphi}}_{\mathcal{B}}\right\}, \tag{4.62}$$

where the contribution coming from $\mathcal{A}$ is the main effect and the second term $\mathcal{B}$ brings a correction to it. In the results in fig. (4.24), fig. (4.25) and fig. (4.26) only the term coming from $\mathcal{A}$ is evaluated,

$$p_{\mathrm{YM}} \approx \frac{1}{2}\int_0^\Lambda \frac{dk}{k}\left\{\sum\!\!\!\!\!\!\int_p \left(\dot{R}G\right)_T^{\varphi\varphi} - \int_p \left(\dot{R}G\right)_T^{\varphi\varphi}\right\}. \tag{4.63}$$

Still, the correct thermal behaviour in eq. (4.63) is encoded in three dependencies. Firstly, there is the explicit dependence due to the spanning over Matsubara frequencies. Secondly, there is also the implicit temperature dependence of the propagators and regulators in $\left(\dot{R}G\right)_T$, which has been computed in this work in section 4.2.1. Thirdly, there is the effect of the Polyakov loop potential, which is sensitive to the critical physics at the phase transition.

At first, an interesting question is how important are these latter dependencies for the pressure. In fig. (4.24) this is studied by taking the temperature-independent propaga-

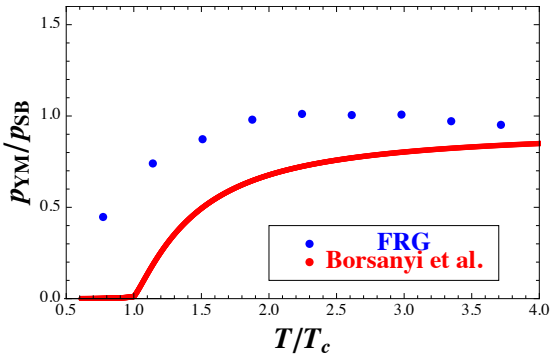

Figure 4.24.: Pressure of Yang–Mills theory from vacuum propagators on a vanishing Polyakov loop potential in comparison with lattice data [49]. For intermediate temperatures the pressure is even larger than the Stefan–Boltzmann result, which is expected from the known behaviour of a general Bose-gas. From this result it is evident that taking into account the implicit temperature dependence of the propagators is inevitable for accurate results of the thermodynamics.

tors from the pure quantum theory, but spanning them over the Matsubara modes in the loop in the flow equation. The pressure is computed on a vanishing background, and compared with lattice data from [49]. The result from the renormalisation group for $T = 0$-propagators clearly does not match the lattice data. Furthermore, it even overshoots the

Stefan–Boltzmann limit at intermediate temperatures and approaches the free gas limit for large temperatures slowly from above. Evidently, the behaviour of Yang–Mills theory is not captured correctly and the implicit temperature dependence of the propagators is important. Note that the effect of a non-trivial background does not correct this, as it only changes the behaviour of the pressure at temperature $T \lesssim T_c$, which is also seen in the comparison of fig. (4.25) with fig. (4.26).

The evaluation of eq. (4.61) with temperature-dependent propagators but on a trivial background is given in fig. (4.25). For temperatures above the phase transition the pressure of Yang–Mills theory obtained from eq. (4.61) matches the corresponding lattice data up to an accuracy of ≈ 12%. For temperatures in the confining domain the sharp drop of the temperature to almost[11] zero is not captured and, furthermore, no significance of the deconfinement-confinement phase transition is seen. This is not surprising, as the critical physics in continuum methods comes from the Polyakov loop potential, which has been neglected here. Therefore, in addition to the importance of the thermal behaviour, fig. (4.25) implies that the Polyakov loop potential is crucial as well. This agrees with findings in recently published works [448].

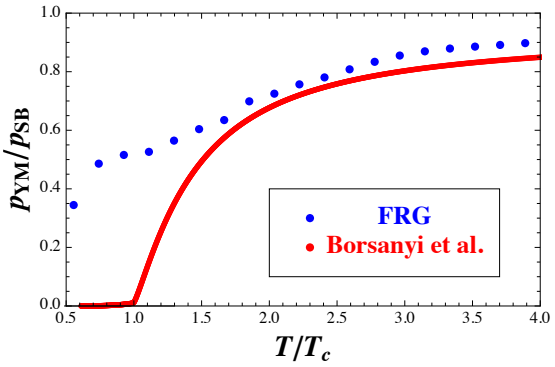

Figure 4.25.: Pressure of Yang–Mills theory with temperature-dependent propagators on a vanishing Polyakov loop potential. The pressure is not sensitive to the phase transition and the FRG does not reproduce the lattice data [49] for temperatures $T \lesssim T_c$. For temperatures above the deconfinement-confinement phase transition the Yang–Mills pressure obtained in FRG matches the corresponding lattice data within an accuracy of ≈12%.

The final result for the pressure is given in fig. (4.26). In fact, the result is very satisfying, as not only the qualitative features are recovered, but even on a quantitative level the agreement with lattice data is within a smaller error than it would have been expected a priori. At temperatures above T_c the pressure becomes perturbative. However, the approximation utilised here is optimised to capture the non-perturbative aspects, but not to yield high precision in the perturbative sector. In the domain where perturbative effects

[11] Note that the pressure does not exactly vanish, as the pressure of the gluonic bound states, the so called glueballs, gives a positive but small contribution.

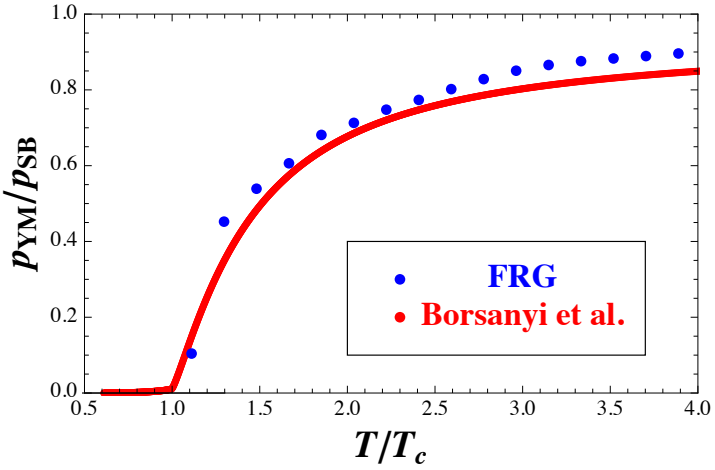

Figure 4.26.: Pressure of Yang–Mills theory from the functional renormalisation group in comparison with lattice gauge theory [49]. The thermal behaviour as well as the Polyakov loop potential are crucial to describe the pressure correctly. The suppression of the pressure at small temperatures is driven by the Polyakov loop potential. The quantitative accuracy of the behaviour at all temperatures is due to the thermal behaviour of the propagators.

are predominant the truncation at hand encodes full one-loop and parts of the two-loop contributions. Therefore, the deviation of the lattice at large temperatures is natural. But, as it is known from e.g. NNLO hard thermal loop perturbation theory [361], the accuracy in this temperature range could in principle be improved systematically to match the lattice very well.

Disregarding the last point, the results in this section suggest that the thermal behaviour of the propagators presented in section 4.2.1 is quite accurate, at least in the region above the phase transition, where they account for the high accuracy, which is also seen in the agreement of the propagators with lattice data, see section 4.2.3. Furthermore, it confirms that the inclusion of the non-trivial background, i.e. the approximation for evaluating the propagators to the Polyakov loop potential is satisfactory. To conclude, to the best of my knowledge, this is the first result within functional continuum methods for the pressure of Yang–Mills theory that captures the non-perturbative aspects and, furthermore, agrees with the lattice over a large temperature range around the deconfinement-confinement phase transition temperature.

I emphasise again that computing the pressure by integrating the pressure flow in eq. (4.49), eq. (4.61) is self-consistent and is making best use of the approximation at hand: In the flow equation approach all quantities derive from the flow equation of the effective action. This entails that $\partial_t \Gamma_k$ in a given approximation is by construction making maximal use of the approximation. Any quantity which can be expressed directly in terms of $\partial_t \Gamma_k$ is best computed in this representation. This strategy has been already used very successfully both in relativistic and non-relativistic field theories for the pressure, density and other

observables, see e.g. [111, 277, 376, 384, 407, 433, 447, 449–464].

4.4. Conclusion of Yang–Mills Theory at Non-Vanishing Temperature

As a summary of this chapter 4 Yang–Mills at non-vanishing temperature can be studied well by the help of the functional renormalisation group. The flow equation allows for a computation of the propagators in combination with vertices, for which approximations are inevitable, however, improvable in a systematic way. More importantly, the flow equation gives access to the rather straightforward computation of thermodynamic quantities over the full temperature range, i.e. in the confined as well as deconfined phase.

In the work presented in this thesis the propagators are studied in a momentum-dependent and also temperature-dependent way. It turns out that for quantitative accuracy not only in full QCD but already in pure gauge theory the implicit temperature dependence is crucial to obtain accurate results. This holds not even on a quantitative but already on the qualitative level.
At finite temperature there are two different (non-trivial) gluonic modes, the chromoelectric and the chromomagnetic mode. In this work it is found that for small temperatures the zero mode of the chromoelectric gluon is enhanced, which is in agreement with lattice data for small temperatures $T \lesssim 200\text{MeV}$. For higher temperatures the propagator is suppressed with respect to the zero temperature propagator. Also this suppression is in quantitative agreement with lattice data. However, the propagator starts to be suppressed at a different point in the FRG than in lattice gauge theory, so for temperatures $200\text{MeV} \lesssim T \lesssim 300\text{MeV}$ there is a qualitative deviation around the deconfinement-confinement phase transition temperature. A possible explanation for this is that the Polyakov loop potential has been neglected, i.e. the computation of the propagators is done in a vanishing potential. Thus, the possibility of a non-trivial potential to build up is eliminated.

On the lattice the chromoelectric propagator is the only quantity that directly reflects the deconfinement-confinement phase transition. The zero mode of chromomagnetic propagator is suppressed with respect to the zero temperature propagator for all temperatures and the behaviour is smooth. The results obtained in this thesis show this suppression in the functional continuum framework as well. Interestingly, the ghost propagator hardly feels the temperature in both approaches, the FRG and the lattice.
Higher modes of the propagators can be obtained within an error $< 3\,\%$ by shifting the momentum of the zero mode by the zero component of the higher Matsubara mode. This is consistent with studies with DSEs [429] and on the lattice [305].

The propagators are the important ingredient for the flow equation for the effective potential, which encodes the pressure. Having the propagators at hand, the pressure com-

putation shows that the qualitative features of the pressure of pure gauge theory can be obtained within this treatment. Herein, firstly the implicit temperature dependence of the propagators is crucial and secondly, the Polyakov potential is important, which is reasonable, as in the FRG approach this quantity encodes the critical physics that happens at the deconfinement-confinement phase transition.

Up to now, the consequences of the Polyakov loop potential were estimated in such a way that the main effect is captured. But strictly speaking, the pressure from the propagators in the non-trivial potential was not computed self-consistently. The fully self-consistent computation is very intricate and beyond the scope of this thesis, since in addition to the momentum dependence that was resolved here also the directions in colour space need to be treated individually.

5. Confinement from Correlation Functions

At the end of section 2.1.2 the notion of confinement is introduced. It denotes the absence of colour-charged states in the observed particle spectrum at low temperatures and densities. For high temperatures confinement ceases to exist, which necessitates a phase transition from the confined to a deconfined phase. For the pure gauge part of QCD there are scenarios that directly relate confinement of gluons to the infrared behaviour of the correlation functions of Yang–Mills theory, cf. section 2.3.1. Since the latter theory is supposed to trigger confinement also in full QCD, it stands to reason that criteria for quark confinement can be found in terms of Yang–Mills Green functions. Indeed, this connection could be established recently [11, 12, 465, 466]. For static quarks the expectation value of the Polyakov loop, eq. (2.1), is a true order parameter to distinguish the confined and the deconfined phase. In this chapter the Polyakov loop potential is numerically determined with non-perturbative functional continuum methods by the knowledge of low-order n-point functions.

5.1. Polyakov Loop Potential from Functional Methods

The expectation value of the Polyakov loop $\langle L[A_0]\rangle$, see eq. (2.1), contains the gauge field as the argument of the exponential function. Therefore, in a continuum description the computation of $\langle L[A_0]\rangle$ entails n-point functions up to infinite order. As a consequence, no direct computation is feasible, although there are signatures for a confining potential from correlation functions [467–469]. However, it can be shown [11, 465, 470] that in addition to $\langle L[A_0]\rangle$ also $L[\langle A_0\rangle]$ fulfills the requirements for an order parameter: In the deconfined phase it is an upper bound for $L[\langle A_0\rangle] \geq \langle L[A_0]\rangle > 0$ and it strictly vanishes in the confined phase.
In contradistinction, $L[\langle A_0\rangle]$ can be obtained from the functional continuum methods, as exclusively the expectation value of the temporal component of the gauge field is needed. The expectation value is simply the minimum of the effective potential[1] for $\langle A_0\rangle$, which can be computed in the background field formalism with A_0 being a constant background field with fluctuations about.

In this section different representations of the Polyakov loop potential are derived from the

[1] Note that the expectation value $\langle A_0\rangle$ is also of importance in other confinement description, since it is sensitive to topological defects [471].

FRG, DSEs and two-particle irreducible (2PI)-functionals. The Polyakov loop potential V is simply the free energy, i.e. one-particle irreducible (1PI) effective action Γ, evaluated on a constant background A_0.

Most functional approaches are based on closed expressions for the effective action or derivatives thereof in terms of full correlation functions. Hence, the knowledge of the latter in constant A_0-backgrounds allows to compute the Polyakov loop potential $V[A_0]$. In turn, confinement requires the Polyakov loop potential to have minima at the confining values for A_0. For the gauge group $SU(N_c)$ these are the center-symmetric points. This restricts the infrared behaviour of the correlation functions computed in the constant A_0-background.

Gauge covariance of the correlation functions and gauge invariance of the effective potential is achieved within the background field approach [472]. The idea relies on the separation of the gauge field into a non-dynamical background field and a fluctuating field. The background field is an auxiliary field. It is invariant under a gauge transformation which is independent of the gauge transformation of the full gauge field. The decisive point is to choose a gauge-fixing with respect to the background field which is constructed such that it singles out one configuration for the full field, but that the gauge-fixing and therefore the action itself is invariant under a combined gauge transformation of the full gauge field and the background field. Finally, the identification of the full gauge field with the background field after integration of fluctuations leaves a gauge invariant (effective) action, although the actual computation for the fluctuating field is done in a gauge-fixed setup. For introductions in the background field formalism see e.g. [279, 473].

In detail this entails that the gauge field A is split in a background $\bar{A}$ and fluctuations a about the background, viz.

$$A = \bar{A} + a\,. \tag{5.1}$$

By this separation, gauges can be constructed that transform covariantly under gauge transformations of both the background and the full gauge field,

$$D_\mu(\bar{A})(A-\bar{A})_\mu = 0\,, \qquad \text{with} \qquad D_\mu(A) = \partial_\mu - i\,g\,A_\mu\,. \tag{5.2}$$

Note that the ghost field does not need to be split and, therefore, it is not subject to the gauge transformation of the background field.
As a consequence, all correlation functions transform covariantly under combined gauge transformations of A and $\bar{A}$. Hence, the effective action Γ is invariant under combined gauge transformations. However, due to the gauge eq. (5.2) it now depends on the full gauge field A and $\bar{A}$ separately, $\Gamma = \Gamma[\bar{A}; a, c, \bar{c}]$, with the path intgegral representation

$$\exp^{-\Gamma[\bar{A};\phi]} = \int d\hat{\phi}\, \exp\left\{-S_A[\bar{A};\hat{\phi}] + \int_x \frac{\delta\Gamma}{\delta\phi}(\hat{\phi}-\phi)\right\}\,, \tag{5.3}$$

with the classical action

$$S_A[\bar{A};\phi] \;=\; \frac{1}{4}\int_x F^a_{\mu\nu}F^a_{\mu\nu} + \frac{1}{2\xi}\int_x \left(\bar{D}_\mu a^a_\mu\right)^2 + \int_x \bar{c}^a \bar{D}_\mu D^{ab}_\mu c^b \,.$$

Herein, the field multiplet is given by

$$\phi = (a, c, \bar{c}) \,, \qquad \text{and} \qquad \phi = \langle\hat{\phi}\rangle \,, \tag{5.4}$$

with the abbreviation $\int_x = \int_0^\beta dx_0 \int d^3x$ and $\beta = 1/T$. Note that the ghost term has changed. The Faddeev–Popov operator eq. (2.15) is the functional derivative of the gauge-fixing condition: In section 2.2 the gauge-fixing is done for the full gauge field $\partial_\mu A_\mu = 0$. This has been modified via the fixing with respect to the background $D_\mu(\bar{A})a_\mu = 0$, however, the covariant derivative of the background field does not depend on the gauge transformation parameter for the full gauge field, since the background is only an auxiliary field. As a consequence, it factorises from the functional derivative similar to ∂_μ in eq. (2.15) leaving the Faddeev–Popov operator $-\bar{D}_\mu D^{ab}_\mu$.
As a next step, the background $\bar{A}$ is identified with the physical background A, the expectation value of the field. This yields a gauge invariant effective action [472],

$$\Gamma[A, c, \bar{c}] = \Gamma[A; 0, c, \bar{c}] \,. \tag{5.5}$$

The Polyakov loop potential is given by eq. (5.5) evaluated on a constant A_0-background,

$$V[A_0] \coloneqq \frac{1}{\beta\mathcal{V}}\Gamma[A_0; 0] \,, \tag{5.6}$$

where $\mathcal{V}$ is the three-dimensional spatial volume. The Polyakov loop, eq. (2.1), is then evaluated at the minimum $\langle A_0\rangle \coloneqq A_{0,\min}$. As mentioned above, eq. (2.1) evaluated on the minimum of eq. (5.6) constitutes an order parameter such as $\langle L[A_0]\rangle \leq L[\langle A_0\rangle]$ [11, 465].

The functional equations for the effective action such as FRG, DSE and 2PI equations depend on the correlation functions $\Gamma^{(n)}$ of fluctuation fields a only. Schematically, they given by

$$\Gamma^{(n)}[\bar{A}](p_1, ..., p_n) = \left.\frac{\delta^n\Gamma[\bar{A}, a]}{\delta a(p_1)\cdots\delta a(p_n)}\right|_{a=0} \,, \tag{5.7}$$

where the unchanged ghosts and the internal and Lorentz indices are omitted. In [11] it is argued that the correlation functions in the background Landau gauge, $\Gamma^{(n)}[\bar{A}]$, are directly related to that in the Landau gauge, $\Gamma^{(2)}[0]$. This allows to use the latter correlation functions within the computation of the effective potential. The argument given in [11] for the two-point function, which straightforwardly extends to higher correlation functions, is that gauge covariance of the fluctuation field correlation functions constrains the difference between $\Gamma^{(2)}[0]$ and $\Gamma^{(2)}[\bar{A}]$.

At vanishing temperatures the gluon two-point function in the Landau gauge splits into a transversal part $\sim \Pi^{\mathrm{T}}_{\mu\nu}(p)$, given in eq. (2.28), and a longitudinal part with the projection

operator $\sim \Pi^{\mathrm{L}}_{\mu\nu}(p)$, given in eq. (3.32). Hence, the gluon propagator is transversal for all renormalisation group scales k, even though the longitudinal part receives finite corrections.
At non-vanishing temperatures one has to take into account chromoelectric and chromomagnetic modes, see section 4.1.1 for the projection operators and the parametrisations of the two-point functions.

In order to parametrise the background field correlation functions in terms of the Landau gauge the correlation functions in eq. (4.2) are evaluated at covariant momenta,

$$\begin{aligned}\left(\Gamma^{(2)}_{L/T}[a=0,A]\right)^{ab}_{\mu\nu} &= \sum_{L/T} P^{L/T}_{\mu\rho}(-D)\delta^{ab}(-D^2)\delta_{\rho\sigma}Z_{L/T}(-D_0,-\vec{D})P^{L/T}_{\sigma\nu}(-D) \\ &\quad + F^{cd}_{\rho\sigma}f^{abcd}_{\mu\nu\rho\sigma}(D) + \delta_{\mu\nu}\delta^{ab}\Delta m^2(D,A_0)\,. \end{aligned} \tag{5.8}$$

The f terms are proportional to the field strength tensor in the adjoint algebra $F^{cd}_{\rho\sigma}$. They can not be obtained from the correlation functions in Landau gauge. For a smooth limit to a vanishing background these terms satisfy that $f(\bar{A}=0)$ is non-singular. In fact, it depends on higher n-point functions in Landau gauge. Fortunately, it does not play a role here. Furthermore, since Landau–de-Witt gauge preserves the transversality of the correlation functions of the fluctuating fields, there can only be finite contributions to the longitudinal terms in the gauge field two-point functions. These contributions are irrelevant for the non-trivial transversal structure. Note that the projection operators $P^{L/T}$ do not commute with $Z_{L/T}(D_0,\vec{D})$ for general gauge fields. They do, however, for constant gauge fields A_0, which leaves a tensorial structure similar to eq. (4.2) but with generalised momenta.
On the other hand, $\Delta m^2(D,A_0)$ vanishes at $A_0=0$ or $T=0$: At finite temperature, the Polyakov loop L is a further invariant, i.e. the Polyakov line,

$$\mathcal{P}(\vec{x}) = \mathcal{P}\,\exp\left(ig\int_0^\beta dx_0\, A_0(x_0,x)\right), \tag{5.9}$$

transforms covariantly under gauge transformations. These terms are particularly important for the chromoelectric 00 component of the gluon two-point function, eq. (5.8). They are not covered by the Landau gauge term in eq. (5.8) for general A_0. This can be seen as follows: Consider $p=0$ for $\Gamma^{(2)}_{A,00}[A_0]$. This is directly related to $\partial^2_{A_0}V[A_0]$ even though it is not identical. In any case, it is periodic in

$$A^a_0\tau^a \to A^a_0\tau^a + \frac{1}{\beta g}\tau^a v^a\,, \tag{5.10}$$

with A_0 being in rotated in the a direction of the Cartan subalgebra of the $SU(N_c)$, which is spanned by its generators τ^a in the adjoint representation. The Cartan subalgebra is the maximal Abelian subgroup of the generators. For constant A_0 this rotation is always possible[2]. The periodicity comes from the Matsubara sum over all modes in loops, as they

[2]Note that the rotation into the Cartan direction is only done for convenience. In fact, the periodicity

are proportional to

$$2\pi T(n + g\beta A_0^a \tau^a)\,. \tag{5.11}$$

In view of the periodicity of the potential, the expectation value of the temporal gauge field A_0 can be mapped onto a set of compact variables φ^a,

$$\frac{\beta g}{2\pi} A_0 = \sum_{\tau^a} \tau^a \varphi^a = \sum_{\tau^a} \tau^a v^a \varphi\,, \tag{5.12}$$

where $\varphi = |\varphi^a|$ and the v^a are the unit vectors in the Cartan directions. They give the corresponding eigenvalues ν_l of the generators in the adjoint representation by

$$\nu_l = \mathrm{spec}\left\{ \left(\tau^a v^a\right)^{bc} \middle| \, v^2 = 1 \right\}\,. \tag{5.13}$$

Obviously, the $N_c^2 - 1$ eigenvalues depend on the direction. For $SU(2)$, however, the Cartan subalgebra is trivial as it is simply $\tau = \sigma_3/2$ in the adjoint representation. This matrix has the eigenvalues $\nu_l = 0, \pm 1$, thus, the potential only needs to be computed for $\varphi \in [0, 1)$, due to the symmetry for the eigenvalues ± 1. Note that this symmetry is generic, each non-vanishing eigenvalue occurs with both signs, which is obvious from the anti-symmetry of the generators in the adjoint representation.
In summary, this leaves a spectrum of the covariant momentum in the non-trivial background

$$p^2 \;\to\; \mathrm{spec}\left\{-D^2[\langle A_0 \rangle]\right\} = \vec{p}^2 + (2\pi T)^2 \left(n - \varphi\,\nu_l\right)^2\,, \tag{5.14}$$

with the continuous spatial momentum $\vec{p}$ and integer values for n. Again the periodicity of the potential is directly visible, as each value of φ can be mapped via a shift in the Matsubara sum to satisfy $|\varphi\,\nu_l| < 1$.

However, this periodicity is not present in the Landau gauge propagators as functions of momenta only. One could estimate it on the basis of the Polyakov loop potential as

$$Z_L(-D_0, \vec{D}) \to Z_L(-D_0, \vec{D}) + \left(\partial^2_{A_0} V[A_0] - \partial^2_{A_0} V[0]\right)\,. \tag{5.15}$$

Eq. (5.15) has the correct periodicity properties and the correct limits. In the second term it does not take into account the difference between $\bar{A}_0$ and a_0-derivatives. As this only affects the periodicity correction but not the dominating first term it should only cause minor errors.
The full propagators for Cartan fields A_0 and Matsubara modes $\omega_n(A_0)$ can be computed on the basis of flow results for the Landau gauge propagators by using the representation

$$G^{ab}_{A/c}[\omega_n(A_0)] \;=\; \sum_{l=1}^{N_c^2-1} G_{A/c}\big|_{\omega_n = 2\pi T(n+\varphi\,\nu_l)}\, \mathcal{P}_l\,, \tag{5.16}$$

where $\varphi\,\nu_l$ are the eigenvalues of $\beta g A_0$ and $\mathcal{P}_l$ the projection operators on the respective

persists in all directions and it is sufficient to restrict the computation to one of each distinct Weyl chambers.

eigenspaces.

5.1.1. Flow Equation for the Polyakov Loop Potential

The representation of the Polyakov loop potential has been introduced in [11, 12]. It is derived from the flow equation for the Yang-Mills effective action $\Gamma_k[\bar{A};\phi]$ at finite temperature T as

$$\partial_t \Gamma_k[\bar{A};\phi] \;=\; \frac{1}{2}\sum\!\!\!\!\!\!\int_p G^{ab}_{\mu\nu}[\bar{A};\phi](p,p)\,\partial_t R^{ba}_{\nu\mu}(p) - \sum\!\!\!\!\!\!\int_p G^{ab}[\bar{A};\phi](p,p)\,\partial_t R^{ba}(p)\,. \tag{5.17}$$

The full field-dependent propagator for a propagation from the fluctuation ϕ_1 to ϕ_2 is given by

$$G_{\phi_1\phi_2}[\bar{A};\phi](p,q) = \left(\frac{1}{\Gamma_k^{(2)}[\phi] + R_k}\right)_{\phi_1\phi_2}(p,q)\,. \tag{5.18}$$

This entails that eq. (5.17) only depends on the propagators of the fluctuations ϕ evaluated in a given background $\bar{A}$. This also holds for $\Gamma_k[A,c,\bar{c}]$. In eq. (5.18), the regulator function in field space, $R_{k,\phi_1\phi_2}$, is unchanged and given by

$$R_{k,A^a_\mu A^b_\nu} = R^{ab}_{\mu\nu}\,, \qquad R_{k,\bar{c}^a c^b} = -R_{k,c^b\bar{c}^a} = R^{ab}\,. \tag{5.19}$$

For more details see section 3.2.4. On the diagrammatic level the representation is equal to the flow equation given in fig. (3.6).

This yields the equation for the effective Polyakov loop potential $V[A_0]$,

$$V[A_0] = V_\Lambda[A_0] + \frac{1}{\beta g}\int_\Lambda^0 dt\,\partial_t\Gamma_k[A_0]\,, \tag{5.20}$$

where $V_\Lambda[A_0] = 0$ for sufficiently large $\Lambda/T \gg 1$ and sufficiently smooth regulators, see section 4.3. In conclusion, the computation of $V[A_0]$ with FRG-flows only requires the knowledge of the (scale-dependent) propagators $G_{A/c}$.

5.1.2. DSE-Representation for the Polyakov Loop Pxotential

Although DSEs have been applied for a great variety of physical systems and theories, they have hardly been employed for critical physics, in particular critical exponents. This is due to the fact that studies are hindered by the breaking of renormalisation group invariance in the DSEs. But since this method is exact, DSEs encode also the physics at phase transitions. In this section they serve to compute the Polyakov loop potential, thus, allow for a study of the phase transition. In principle, also critical exponents can be studied. For a related example I want to refer the reader to appendix F, where the Wilson–Fisher

fixed point of ϕ^4 theory in three dimensions is studied.

Since DSEs provide n-point functions with $n \geq 1$ only, cf. section 3.3, there is no direct representation for the effective potential. In spite of that, the derivative of the effective potential can be computed directly from the generating equation for the gluon given in fig. (3.18). In the background formalism with a static temporal non-vanishing background A_0, the functional derivative is taken with respect to the A_0. With a closer look on the generating DSE, eq. (3.65), this derivative acts on the effective action. This leaves the derivative of the Polyakov loop potential for the constant background considered here. On the right hand side of eq. (3.65), the derivative acts on the classical action, however, the loops genuinely contain the fluctuating fields. Written schematically, this yields the representation of $V'[A_0]$ according to

$$\frac{\delta(\Gamma[A_0;0]-S[A_0;0])}{\delta A_0(x)} = \frac{1}{2}S^{(3)}_{A_0aa}G_{aa} - S^{(3)}_{A_0c\bar{c}}G_{c\bar{c}} + \frac{1}{6}S^{(4)}_{A_0aaa}G^3_{aa}\Gamma^{(3)}_{aaa}\,,$$

with the classical vertices

$$S^{(3)}_{A_0aa} = \left.\frac{\delta^3 S_A}{\delta A_0 \delta a^2}\right|_{\phi=0}, \quad S^{(3)}_{A_0c\bar{c}} = \left.\frac{\delta^3 S_A}{\delta A_0 \delta c \delta \bar{c}}\right|_{\phi=0}, \quad S^{(4)}_{A_0aaa} = \frac{\delta^4 S_A}{\delta A_0 \delta a^3}\,. \tag{5.21}$$

The three-point vertices have one background leg and two fluctuation leg. They differ from the standard vertices. The gluonic vertex also has a piece from the gauge fixing term proportional to $1/\xi$. The ghost-gluon vertex also involves the gauge field derivative of $\bar{D}$ and not only D, see eq. (5.4). Naturally, in the vacuum all contributions would vanish, but due to the external background leg these contributions are non-zero.
The DSE has the same form as the standard DSE for the fluctuation fields, only the vertices differ. It is depicted in fig. (5.1). The external field is a background gluon field

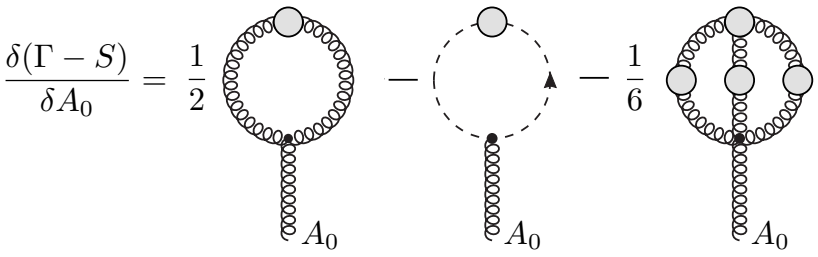

Figure 5.1.: DSE for the gluon one-point function.

with only a temporal component A_0. This is reflected in the projections. In conclusion, the computation of $V[A_0]$ only requires the knowledge of the propagators and of the full gluonic three-point function $\Gamma^{(3)}_{aaa}$.

5.1.3. 2PI-Representation for the Polyakov Loop Potential

Additionally, the functional DSE displayed in eq. (5.21) and fig. (5.1) also derives from the 2PI generating functional. For a review on 2PI effective action techniques see e.g. [474]. In general, NPI effective actions are another exact non-perturbative functional method. In particular, in physical situations where resummations, i.e. calculations of perturbative corrections up to infinite order are inevitable, they are very powerful since resummations are genuinely built in. In a consistent renormalisation scheme, 2PI expansions respect both the theory's symmetries and also the pattern for spontaneous symmetry breaking.

The generating equations for NPI effective actions are derived via the functional integral with source terms not only for the one-point function but for all n-point functions with $n \leq N$. As a consequence, the effective action is a functional not only of the field, but also of the n-point functions. Thus, for a theory with field content φ and the corresponding propagators $\mathcal{G}_{\varphi\varphi}$ the generating functional is $\Gamma_{2\mathrm{PI}}[\mathcal{G}_{\varphi\varphi}, \varphi]$.

For Yang–Mills theory in the background field formalism the 2PI generating functional is given by

$$\begin{aligned}\Gamma_{2\mathrm{PI}}[G, \bar{A}; \phi] &= S_A[\bar{A}, \phi] - \frac{1}{2}\mathrm{Tr}\log G_A + \mathrm{Tr}\log G_c \\ &\quad -\frac{1}{2}\mathrm{Tr}\,\Pi_A G_A + \mathrm{Tr}\,\Pi_c G_c + \Phi[G, \bar{A}; \phi]\,,\end{aligned}$$

where Φ contains only the two-particle-irreducible pieces and $\Pi_{A/c} = G^{-1}_{A/c} - S^{(2)}_{A/c}$ are the gluon vacuum polarisation and ghost self-energy respectively. The effective action is then given with

$$\Gamma[\bar{A}; \phi] = \Gamma_{2\mathrm{PI}}[G[\bar{A}; \phi], \bar{A}; \phi] \quad \text{with} \quad \left.\frac{\delta\Gamma_{2\mathrm{PI}}}{\delta G}\right|_{G=G[\bar{A};\phi]} = 0\,, \tag{5.22}$$

the effective action is the 2PI-effective action evaluated on the gap equation. The derivative with respect to $\bar{A}_0$ of $\Gamma[\bar{A}; \phi]$ in its 2PI-representation, eq. (5.22), hits the explicit $\bar{A}$-dependence in the classical vertices as well as the one in the propagators. The latter terms, however, vanish due to the gap equation displayed in eq. (5.22),

$$\begin{aligned}\frac{\delta(\Gamma[A_0; 0] - S[A_0; 0])}{\delta A_0(x)} &= \left(\mathrm{Tr}\,\frac{\delta\Gamma_{2\mathrm{PI}}}{G}\,\frac{\delta G[A_0; \phi]}{\delta \bar{A}_0} + \frac{\delta\Gamma_{2\mathrm{PI}}[G, \bar{A}; \phi]}{\delta \bar{A}_0}\right)_{G=G[\bar{A};\phi]} \\ &= \frac{1}{2}S_{A_0 aa}G_{aa} - S_{A_0 c\bar{c}}G_{c\bar{c}} + \left.\frac{\delta\Phi[G, \bar{A}; \phi]}{\delta \bar{A}_0}\right|_{G=G[\bar{A};\phi]}\,,\end{aligned} \tag{5.23}$$

where, by comparison, the last term simply is

$$\left.\frac{\delta\Phi[G, \bar{A}; \phi]}{\delta \bar{A}_0}\right|_{G=G[\bar{A};\phi]} = \frac{1}{6}S_{A_0 aaa}G^3_{aa}\Gamma^{(3)}_{aaa}\,. \tag{5.24}$$

Eq. (5.24) can be proven in any order of a given 2PI-expansion scheme such as 2PI pertur-

bation theory or the $1/N$-expansion. Therefore, for all practical purposes of the present task, the 2PI-computation is already covered by the DSE-computation, even though one may not respect the self-consistent 2PI approximation. Note that this is not the case for e.g. dynamics of a given system in which conservation laws such as energy and particle number conservation play a role.

5.2. Results for the Polyakov Loop Potential and T_c

In this section the results for the computation of the Polyakov loop potential are given. The main focus of the work presented here is to complement previous results obtained in the FRG framework [11, 12] with others methods. Therefore, the Polyakov loop potential obtained from the DSE is studied in detail. The equation for the potential in the 2PI formalism coincides for this purpose presented here with the corresponding DSE, thus, no separate calculation is necessary. The insensitivity of the transition temperatures of the difference between infrared scaling or decoupling solution is confirmed, which had been found in the FRG and is in agreement with general expectations. Furthermore, the effect of the implicit temperature-dependence of the propagators presented in chapter 4 is studied.
The phase transition temperatures and the nature of the phase transitions are compared with lattice gauge theory.

5.2.1. Results from the FRG

As discussed before the flow equation has the minimal representation for the Polyakov loop potential as it only requires the full propagators of Landau gauge Yang–Mills theory in a given background.

For the case of temperature-independent propagators this setup has been applied for the gauge groups $SU(2)$ and $SU(3)$ [11, 12] that are present in the Standard Model of particle physics. In addition, other Lie groups have been investigated, in particular general $SU(N_c)$, the symplectic $Sp(2)$ and the exceptional Lie group $E(7)$ [12], where the latter two have the center $Z(2)$.

In the subsequent section 5.2.2 the Polyakov loop potentials for $SU(2)$ and $SU(3)$ are computed from the DSE representation. The obtained results are compared to the corresponding FRG computations. The critical temperatures from the FRG [11] are $T^{\mathrm{FRG}}_{c,\mathrm{SU}(2)} \approx 266\,\mathrm{MeV}$ and $T^{\mathrm{FRG}}_{c,\mathrm{SU}(3)} \approx 289\,\mathrm{MeV}$ at a lattice string tension of $\sqrt{\sigma} = 440\,\mathrm{MeV}$. The potentials and order parameters are summarised in fig. (5.2), the individual figures are taken from [11].

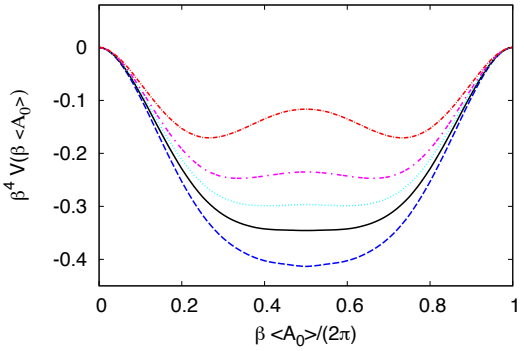

(a) Polyakov loop potential for $SU(2)$ for the temperatures T = 260, 266, 270, 275, and 285 MeV from bottom to top.

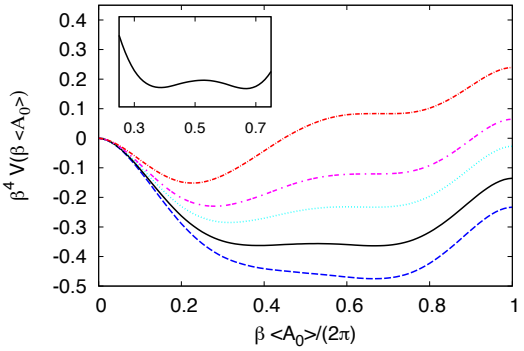

(b) Polyakov loop potential for $SU(3)$ for the temperatures T = 285, 289.5, 295, 300, and 310 MeV from bottom to top.

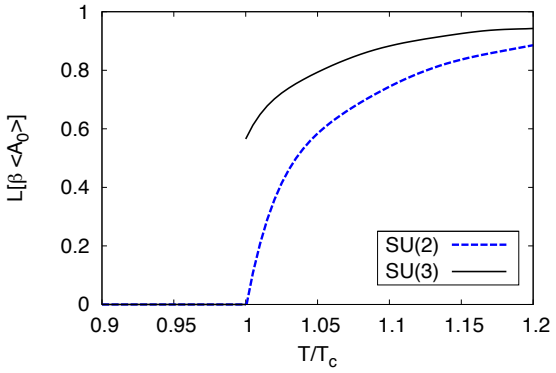

(c) Order parameters for the deconfinement-confinement phase transition in $SU(2)$ and $SU(3)$, showing second and first order phase transitions, respectively.

Figure 5.2.: Polyakov loop potential from its FRG representation with vacuum scaling propagators. The phase transition temperature of $SU(2)$ is $T^{\mathrm{FRG}}_{c,\mathrm{SU}(2)} \approx 266\,\mathrm{MeV}$, for $SU(3)$ it is $T^{\mathrm{FRG}}_{c,\mathrm{SU}(3)} \approx 289\,\mathrm{MeV}$. Results and figures are taken from reference [11] and printed with permission of Elsevier, license number 2958691101164.

5.2.2. Results from DSE & 2PI

The full computation of the Polyakov loop potential from DSE and 2PI methods contains the computation of the three diagrams given in fig. (5.1). This shows that indeed the two-point functions and the full three-gluon vertex are sufficient to fully compute this equation. However, the approximation employed here is such that the two-loop term is dropped. This discards the dependence on the three-point function. The remaining two one-loop diagrams depend on the gluon and ghost propagators only, whose full momentum- and temperature-dependencies are taken into account. The diagrammatic expression is given in fig. (5.3). In the following the contributions from the loops in the given background are derived.

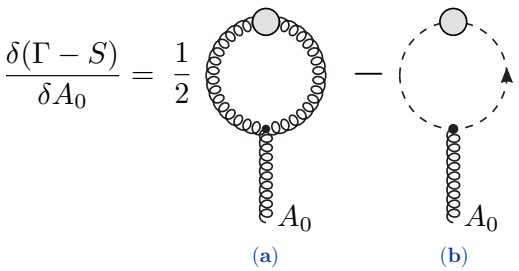

Figure 5.3.: DSE one-loop approximation for the derivative of the effective potential.

At first, a note on the value of the classical coupling is in order. The only relevant aspect for quark confinement is the shape of the Polyakov loop potential with respect to the minima, but not its absolute value. In other words, only the position of the minima decides about a confining or deconfining potential. Having dropped the two-loop diagram involving the full three-gluon vertex, the only coupling that enters the equation is the classical one. Being constant and of equal order in both one-loop diagrams it factorises completely, thus, its absolute value is irrelevant for the search of the minimum. For this reason it is safely fixed to unity.

At vanishing temperature the gluon propagator has a transversal and a longitudinal structure. In Landau gauge the longitudinal component remains tree-level, but the transversal one is modified by quantum effects,

$$G^{ab}_{\mu\nu}(p) = \delta^{ab}\Pi_{\mu\nu}(p)G_A(p)\,, \qquad G_A(p) \;=\; \frac{1}{Z_A(p)\,p^2}\,, \tag{5.25}$$

where $Z_A(p)$ is the wave-function renormalisation of the gluon introduced in eq. (2.29). Naturally, the DSE does not depend on the renormalisation group scale k but only on the physical Green functions. Thus, if the two-point functions are taken from the FRG computation, only the functions $\Gamma^{(n)}_{k=0}(p)$ are needed.
For vanishing fluctuation fields and a constant background the full gluonic propagator can be parametrised according to

$$G_A = G_{A,\perp} + G_{A,\text{gauge}} \quad \text{with} \quad G_{A,\text{gauge}_{\mu\nu}} = \xi \bar{D}_\mu \frac{1}{\bar{D}^2} \bar{D}_\nu\,, \tag{5.26}$$

where the longitudinal term from the gauge mode is modified compared to standard Landau gauge, because the gauge fixing is not done with respect to a trivial background but to the constant background field. However, the transversality relations persist, however, in terms of the covariant momentum,

$$\bar{D}_\mu G_{A,\perp\mu\nu} = 0 \quad \text{and} \quad \bar{D}_\mu G_{A,\text{gauge}_{\mu\nu}} = \xi \bar{D}_\mu \frac{1}{\bar{D}^2} \bar{D}_\nu\,. \tag{5.27}$$

This is a consequence of the corresponding Slavnov-Taylor identities: The quantum corrections to the propagator are transversal, hence the gauge sector is unchanged.

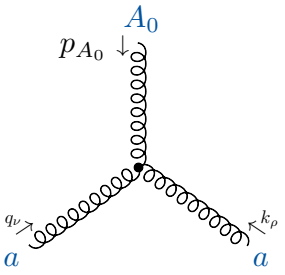

Figure 5.4.: Three-gluon vertex with a purely temporal background leg attached.

The three gluon vertex, fig. (5.4), in the background for all momenta ingoing is defined in eq. (5.21). At vanishing fluctuating fields it is schematically given by

$$S_{A_0 a a \rho\mu\nu} = S_{A_0 a a \rho\mu\nu} + \frac{1}{\xi}\frac{\delta(\bar{D}_\mu \bar{D}_\nu)}{\delta \bar{A}_\rho}\,, \tag{5.28}$$

where the first term simply carries the standard classical tensor structure given in appendix E. This tensor vanishes if two legs are closed with a longitudinal tensor. Thus, for the contribution to the gauge mode only the remaining term is relevant. The second term originates from the background field dependence of the gauge fixing term, see eq. (5.4). Together with the longitudinal structure of the gauge mode this leaves the contribution of the gauge sector as

$$\frac{1}{2}\mathrm{Tr}\frac{1}{\xi}\frac{\delta(\bar{D}_\mu \bar{D}_\nu)}{\delta \bar{A}_\rho} G_{A,\mathrm{gauge}\,\mu\nu} = \frac{\delta}{\delta \bar{A}_\rho}\frac{1}{2}\mathrm{Tr}\log(-\bar{D}^2)\,, \tag{5.29}$$

where the trace on the right hand side does not include a trace over Lorentz indices. This term is equal to 1-loop perturbation theory. Hence, it gives $1/2 V^{\mathrm{Weiss}}_{SU(N_c)}$, i.e. half of the Weiss potential [475, 476], which is analytically known

$$V^{\mathrm{Weiss}}_{SU(N_c)} = -\frac{d-2}{\pi^{d/2}}\Gamma(d/2)\,T^d \sum_{l}^{N_c^2-1}\sum_{n=1}^{\infty}\frac{\cos\left\{2\pi n \nu_l\,|\varphi|\right\}}{n^d}\,. \tag{5.30}$$

For $SU(2)$ the Weiss potential is given in fig. (5.5), where it is normalised to the canonical dimension T^4. Note that the only temperature dependence is the canonical one, thus, fig. (5.5) is independent of the temperature. Furthermore, the potential is periodic in φ and with the eigenvalues $\nu_l = \{\pm 1, 0\}$ for $SU(2)$ it has minima at integer values of φ. However, the Polyakov loop vanishes for values of $\varphi = 1/2$, since $L[\langle A_0\rangle] \sim \mathrm{Tr}\,\mathrm{Exp}\left\{2\pi\varphi\left(\tau\cdot v^1 + \tau\cdot v^2\right)\right\} = 0$ for $\varphi = 1/2$ and $\tau = \sigma_3/2$. This shows that the perturbative potential does not yield a vanishing expectation value of the Polyakov loop according to the line of thought in section 5.1. Consequently, perturbation theory does not shows

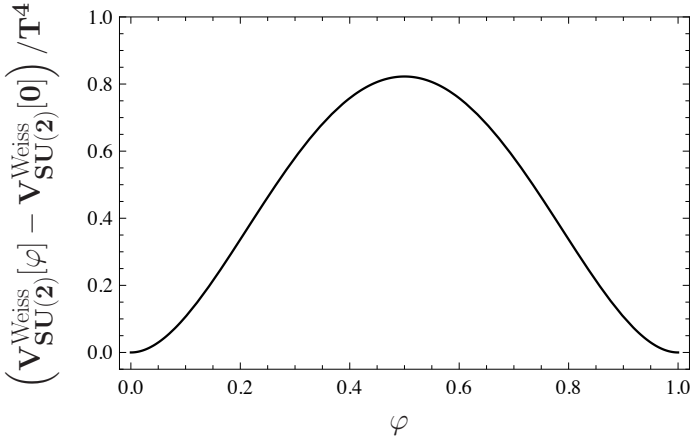

Figure 5.5.: (Perturbative) Weiss potential for $SU(2)$. The confining value is at $\varphi = 1/2$, however, the Weiss potential has minima at integer values of φ. Thus, this potential does not exhibit confinement.

confinement, as expected. This can be mapped onto the longitudinal mode: Since the gauge mode in Landau gauge is trivial it generates a deconfining potential.

The full ghost propagator is parametrised similarly as in Landau gauge, because the background is only of gluonic nature. Hence,

$$G^{ab}(p) = -\delta^{ab} G_c(p)\,, \text{ with } G_c(p) = \frac{1}{Z_c(p)\,p^2}\,, \tag{5.31}$$

where $Z_c(p)$ is the wave-function renormalisation of the ghost introduced in eq. (2.30).

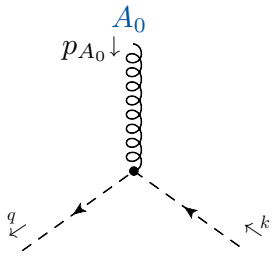

Figure 5.6.: Classical ghost-gluon vertex with attached background field.

Concerning the ghost-gluon vertex there is a subtlety arising from the Faddeev–Popov operator, which depends on the external background field as well. In Landau gauge, the derivative with respect to the gluon A only acts on the covariant derivative $\mathcal{D}(A)$, cf. eq. (2.16). In contrast to this, in the background field formalism the derivative with respect to the background A_0 acts on both covariant derivatives in the Faddeev–Popov

operator $-\bar{D}_\mu(\bar{A})D^{ab}_\mu(\bar{A}+a)$, see eq. (5.4). Thus, compared to the Landau gauge ghost-gluon vertex, $S^{(3)}_{Ac\bar{c}}$, an additional factor of 2 arises in the vertex $S^{(3)}_{A_0c\bar{c}}$ in the background fixed formalism, defined in eq. (5.21).

The first diagram that is to be computed is the gluon loop, given as the diagram labelled (a) in fig. (5.3). The non-trivial part of the computation concerns the transversal part $G_{A,\perp}$, which couples to the standard part of the three-gluon vertex, S_{aaa}, derived from $1/2\int \mathrm{tr}F^2$. It is similar to the three-gluon vertex given in appendix E.
Written out it translates for the purely temporal momentum $(p_{A_0})_0 = 2\pi T\varphi$ of the external gluon and without color and the global i to

$$\begin{aligned}\frac{1}{2}\sum\!\!\!\!\!\!\int_q G_{\mu\nu}(p_{A_0}+q)S^{(3)}_{A_0aa,\,0\mu\nu}(p_{A_0},p_{A_0}+q,-p_{A_0}-q)&\\ = g\frac{1}{2}\sum\!\!\!\!\!\!\int_q G_A(p_{A_0}+q)\left(2(p_{A_0}+q)_0\,(\delta_{\mu\mu}-1)\right)&\\ = 3\,g\sum\!\!\!\!\!\!\int_q 2\pi T(n_q+\varphi)\,G_A(p_{A_0}+q)\,,&\end{aligned} \tag{5.32}$$

where due to symmetry only the term $\propto p_{A_0}+q_0 = 2\pi T(\varphi+n_q)$ survives.

Also, the ghost loop given as diagram (b) in fig. (5.3) takes a simple form

$$\begin{aligned}-\sum\!\!\!\!\!\!\int_q G_c(p_{A_0}+q)S^{(3)}_{A_0c\bar{c},0}(p_{A_0}+q,p_{A_0},-p_{A_0}-q)&\\ = -2ig\sum\!\!\!\!\!\!\int_q G_c(p_{A_0}+q)\;2\pi T(\varphi+n_q).&\end{aligned}$$

Therefore, the final equation for the derivative of the Polyakov loop potential is just the sum of the longitudinal mode giving half of the derivative of the Weiss potential[3], the transversal gluon loop and the ghost loop,

$$\begin{aligned}V'(\varphi) &= \frac{1}{2}\left(V^{\mathrm{Weiss}}_{SU(N_c)}\right)' + \sum\!\!\!\!\!\!\int_q 2\pi T\,(n_q+\varphi)\\ &\quad\times\left[3\,G_A\,(q+p_{A_0}) - 2G_c\,(q+p_{A_0})\right]\,.\end{aligned} \tag{5.33}$$

The generating equation for the Polykov loop potential, eq. (5.33), depends on non-trivial propagators. As a consequence, it can only be solved numerically. The loop integrals are numerically simple because the loop integrations and Matsubara sums are finite.

[3]The fact that the longitudinal mode gives half of the Weiss potential can be checked by taking classical propagators in the loop. This has been done analytically but also numerically to test the numerics. Another valuable numerics check is the periodicity of the potential.

Results for $SU(2)$

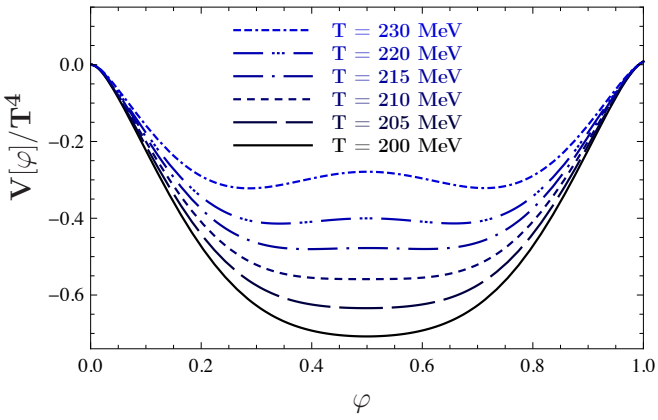

(a) Polyakov loop potential for $SU(2)$. For low temperatures the minimum is at the confining value $\varphi = 1/2$ for $SU(2)$. For higher temperatures the minimum moves to a different value which signals the deconfinement-confinement phase transition.

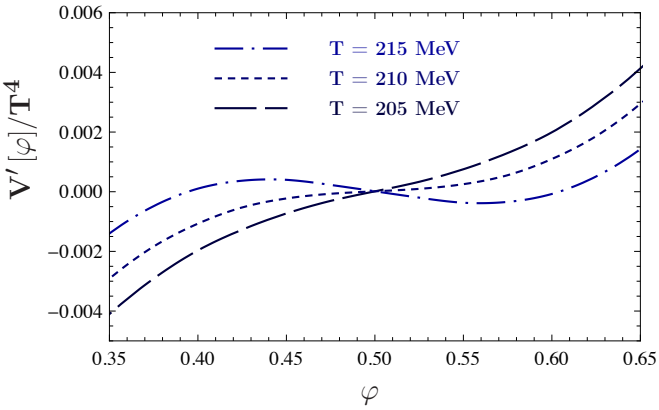

(b) At the phase transition temperature the derivative of the Polyakov potential for $SU(2)$ changes at the confining value from a positive to negative slope, turning the minimum of the potential into a local maximum.

Figure 5.7.: Polyakov loop potential for $SU(2)$ from its DSE representation with vacuum scaling propagators.

Eq. (5.33) only depends on the ghost and gluon propagators. In the following three different kinds of propagators are used. At first, the difference between the decoupling and the scaling solutions of Yang–Mills propagators at vanishing temperature, cf. section 2.3.2, is studied.

Similar to the pressure, cf. section 4.3, the finiteness of the temperature has a two-fold effect. On the one hand side, the Matsubara sum yields an explicit dependence and on the other hand side, the wave-function renormalisation are temperature dependent. Therefore, the third approximation for the Polyakov loop potential is obtained with the temperature-dependent propagators presented in chapter 4.

The Polyakov loop potential for $SU(2)$ from the scaling propagators at vanishing temperature is given in fig. (5.7(a)). As argued before the position of the minimum decides about a confining ($\varphi = 1/2$) or deconfining ($\varphi \neq 1/2$) potential. In fig. (5.7(a)) the Polyakov loop potential is given at different temperatures, the critical temperature T_c for the deconfinement-confinement phase transition is obtained best by the help of the derivative of the Polyakov loop potential, which is plotted in fig. (5.7(b)). The phase transition happens at the point at which the minimum in the potential moves away from $\varphi = 1/2$. As it is a smooth transition, the potential is flat around $\varphi = 1/2$ at this temperature. Thus, a vanishing derivative of the potential in this region signals the phase transition. Being computed from the scaling propagators the critical temperature is $T_c^{\text{scal}} \approx 210\,\text{MeV}$. In comparison to this, the FRG result gives a critical temperature of $T_c^{\text{FRG}} \approx 266\,\text{MeV}$ in [11], using the same input. However, note that the two-loop diagram has been omitted in the computation presented here which could potentially correct for this deviation.

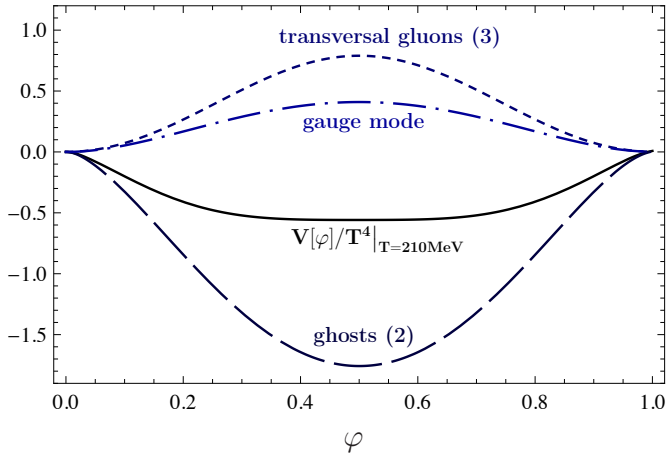

Figure 5.8.: Individual contributions from the gauge mode, the transversal gluons and the ghost loop with trivial implicit temperature dependence in the Polyakov loop potential obtained from its presentation in the framework DSEs.

Functional methods have the advantage that often the mechanisms and individual contributions can be resolved. In this case it is trivially possible due to the additive structure of the equation for the potential, eq. (5.33). As outlined above the gauge mode gives half of the perturbative one-loop potential. The factor of one-half stems from the fact that the perturbative potential is made up from the two physical modes: the transverse polarisations of the gluon. The Polyakov loop potential is gauge invariant, thus only the physical modes must contribute. Naturally, the perturbative result simply reproduces this feature. In fact, for trivial propagators all different modes contribute combinatorically with the same weight. So the cancellation of the unphysical modes can be understood easily. All of the four gluonic degrees of freedom contribute equally with $\frac{1}{2}V^{\text{Weiss}}_{SU(N_c)}$ each. The amplitude of the ghost potential is equal to this, however, these modes contribute with a negative sign. So a trivial summation cancels the two unphysical mode, leaving exactly $V^{\text{Weiss}}_{SU(N_c)}$.

For perturbative propagators this cancellation is directly seen in the DSE representation in eq. (5.33).

In addition, the different parts from the transversal gluon and the ghosts can be resolved also for the full propagators which exhibit a crucially different momentum dependence. The gauge mode is not affected by quantum effects.
The individual contributions for the scaling propagators at vanishing temperature are given in fig. (5.8) for the Polyakov loop potential at about the deconfinement-confinement phase transition temperature. As expected from perturbation theory, the pattern persists that the gluons contribute with a deconfining potential whereas the ghosts add a confining piece. However, the magnitude of the single contributions has changed, as the gluon propagators have a mass gap in the infrared whereas the ghost propagators are even enhanced. Note that the latter feature is significant in the scaling solution, however, the gluon suppression is seen in both infrared Yang–Mills solutions, the scaling and the decoupling one. In total, the interplay of these effects yields a confining potential for small temperatures, because the ghost loop dominates. For larger temperatures the infrared sector becomes less important, since the propagators are evaluated at higher momenta due to the spreading of the Matsubara modes. At high momenta the propagators become perturbative. At very high temperatures this yields the deconfining $V^{\text{Weiss}}_{SU(N_c)}$. This entails that in between there is a phase transition. This is clearly seen in the data.

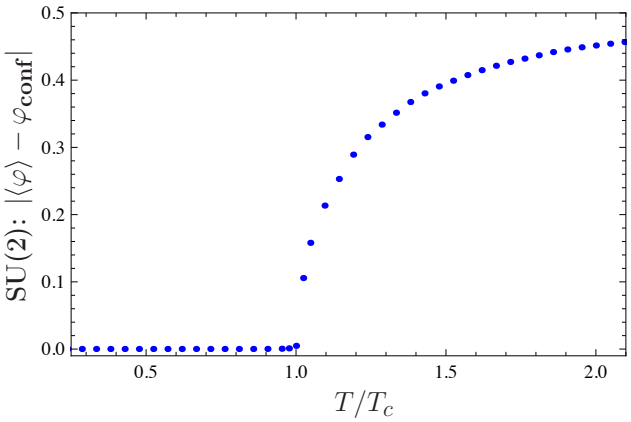

Figure 5.9.: The expectation value of the temporal gluon serves as an order parameter for the phase transition [11,465], the confining value for $SU(2)$ is $\varphi_{\mathbf{conf}} = 1/2$. The figure shows the expectation value obtained from temperature-independent scaling propagators. The continuous change of the minimum signals a second order phase transition for $SU(2)$. This is in agreement with lattice results, see e.g. [364, 365].

Furthermore, the order of the phase transition can be determined as well. From the lattice it is known that the the phase transition for $SU(2)$ is of second order. This means that the

order parameter does not jump at the critical temperature. In the Polyakov loop potential in fig. (5.7(a)) this is seen by the help of the change of its minimum. In addition to the expectation value of the Polyakov loop, the Polyakov loop evaluated on the minimum of the potential is an order parameter. The latter quantity only vanishes for distinct minima, thus, the position of the minimum also serves as an order parameter. In fig. (5.7(a)) the minimum moves continuously but is strictly at its confinig value in the confined phase. This implies that the phase transition is of second order. The expectation value of the minimum $\langle\varphi\rangle$ as a function of the temperature measured in the units critical temperature $T_c^{\text{scal}} \approx 210\,\text{MeV}$ is given in fig. (5.9), where the continuous transition is evident.

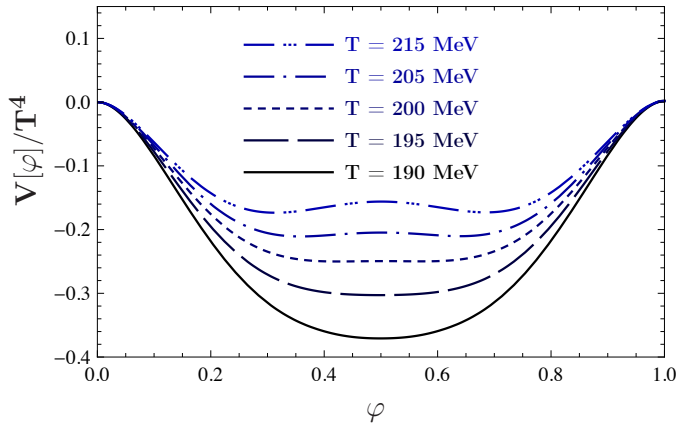

(a) Polyakov loop potential for $SU(2)$.

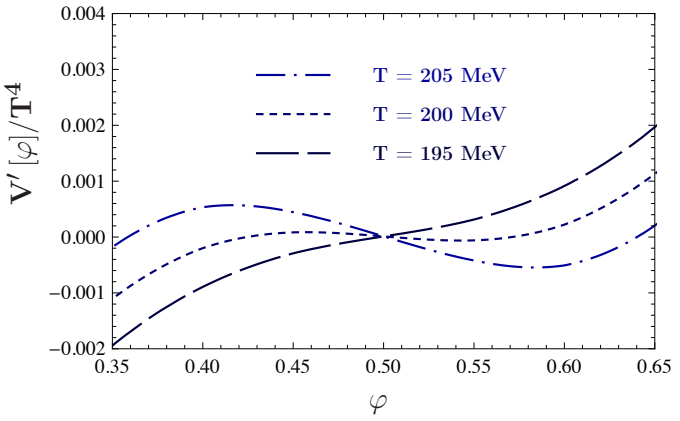

(b) Phase transition temperature for $SU(2)$.

Figure 5.10.: Polyakov loop potential for $SU(2)$ from the DSE with temperature-independent Yang–Mills propagators from a decoupling solution.

In the FRG studies [11, 12] it is argued that the Polyakov loop potential should be insensitive to the deep infrared regime. Thus, scaling and decoupling solutions should give approximately the same phase transition temperature. This is due to the fact that the phase transition is driven by the mid-momentum region, which is in between the infrared and the perturbative physics. In this domain both types of solutions are quantitatively

equal. Thus, the Polyakov loop potential is not sensitive to the type of Yang–Mills solution in the deep infrared.
In the computation presented here the dependence on the different inputs is given by comparison of the Polyakov loop potential obtained with decoupling propagators at vanishing temperature, given in fig. (5.10), with the potential from the scaling propagators studied above in fig. (5.7). Also, in the DSE representation the insensitivity with respect to the different infrared behaviour is clearly confirmed. This is seen on the level of the deconfinement-confinement phase transition temperature. For the decoupling solution it is $T_c^{\mathrm{dec}} \approx 200\mathrm{MeV}$.

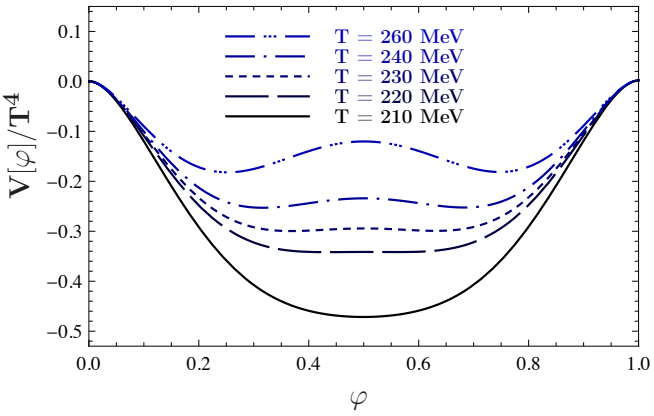

(a) Polyakov loop potential for $SU(2)$.

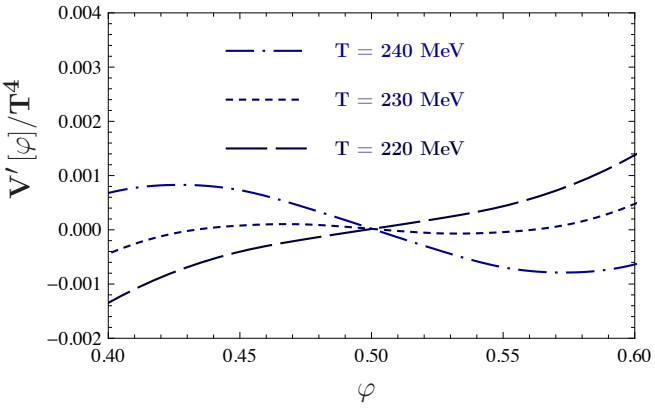

(b) Phase transition temperature for $SU(2)$.

Figure 5.11.: Polyakov loop potential for $SU(2)$ from the DSE with temperature-dependent Yang–Mills propagators from section 4.2.1.

These results can be improved such that the implicit temperature dependence of the two-point functions is taken into account. This dependence was studied in chapter 4 where the input was a decoupling solution to facilitate the comparison with lattice results. Note that the non-trivial modes in the gluon loop in the DSE for the Polyakov loop potential contribute with three degenerate transversal gluon wave-function renormalisation functions, which is a result of Euclidean $\mathcal{O}(4)$-symmetry and the transversality of the gluon

propagators in Landau gauge. At finite temperature these modes are generally different, see chapter 4. They split up in two chromomagnetic modes and one chromoelectric mode. The computation for the Polyakov loop potential with temperature-dependent propagators is done such that there are two individual diagrams that have the same structure of the one-loop gluon diagram of the equation at vanishing temperature, see fig. (5.3). Instead of the overall factor of three, one loop involves the chromoelectric gluon with the combinatorical factor of one and the other gluon loop depends on the chromomagnetic mode with a prefactor of two. Hence, the full equation is given by

$$\begin{aligned} V'(\varphi) &= \frac{1}{2}\left(V_{SU(2)}^{\text{Weiss}}\right)' + \not\int_q 2\pi T\,(n_q+\varphi) \\ &\quad \times\left[\,G_L\,(q+p_{A_0}) + 2\,G_T\,(q+p_{A_0}) - 2G_c\,(q+p_{A_0})\right]. \end{aligned} \tag{5.34}$$

Of course, in the perturbative limit the Weiss potential is satisfied also for this split, since the perturbative mode counting has not changed.

The results for the effective potential of the Polyakov loop from temperature-dependent Yang–Mills propagators is given in fig. (5.11). The effect of the implicit temperature dependence is such that in comparison with the vacuum decoupling solution $T_c^{\text{dec}} \approx 200\,\text{MeV}$ the critical temperature of the deconfinement-confinement phase transition is raised to $T_c^{\text{fin.T}} \approx 230\,\text{MeV}$.

Also for the case of thermal propagator input, the individual contributions can be resolved according to the loops in eq. (5.34), the compilation is given in fig. (5.12). By the help of the individual contributions it is evident that the potential is confining for low temperatures, due to the suppression of the gluons. The gauge mode gives half of the Weiss potential. In addition, both the chromomagnetic as well as the chromoelectric mode are suppressed due to their effective masses, which is seen in comparison with the gauge mode. Note that the curve of the contribution of the chromomagnetic gluon is the sum of two modes. The suppression is now a two-fold effect from the gap the gluons exhibit at vanishing temperature already, see section 2.3.2, but also of the thermal suppression. Due to the latter manifestation of temperature, the gluonic modes yield a smaller contribution than in the zero temperature computation in fig. (5.7(a)). In contrast, the ghost propagator has hardly changed at the temperature where the deconfinement-confinement phase transition happens. As a direct consequence, the confining contribution of the ghosts is equal but the deconfining one is diminished. In total, this yields a higher phase transition temperature.

Note that in chapter 4 the results for the ghost propagator differ from the corresponding lattice findings, however, only at larger temperatures. At the temperatures around the deconfinement-confinement phase transition of quarks the only quantitative difference is the absent enhancement of the longitudinal gluon in the FRG formulation. Nevertheless, it remains as an open question, if the evaluation of the chromoelectric mode on the non-trivial background in the computation above corrects for this quantitative difference. The

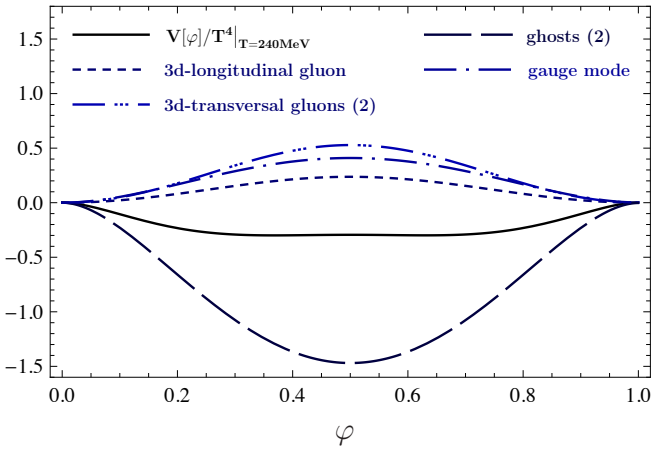

Figure 5.12.: Individual contributions from the gauge mode, the chromoelectric and chromomagnetic gluons and the ghost with non-trivial implicit temperature dependence to the Polyakov loop potential in its DSE representation. The numbers in the brackets denote the number of degenerate modes that are summed in the corresponding curve. The gluonic modes are suppressed due to the effective mass scale which arises from the quantum mass gap and the thermal mass. At low temperatures the confining ghost potential dominates which yields a confining potential. At higher temperatures the ratio of absolute ghost to gluon contribution decreases which renders a deconfining potential.

inclusion of the Polyakov loop in the propagator would be an appealing explanation for the deviation at low temperatures, because the FRG formulation of the thermal propagators according to chapter 4 is not sensitive to the phase transition. In turn, the critical physics in the continuum formulation is encoded in the Polyakov loop.

The results can be compared to lattice gauge theory, which finds [47, 48]

$$T^{\text{lattice}}_{c,\,\mathrm{SU(N_c)}}/\sqrt{\sigma} \;=\; 0.596(4) + \frac{0.453(30)}{N_c^2}\,, \tag{5.35}$$

for $2 \leq N_c \leq 8$. This formula is obtained in [47], where improved gluonic operators on the lattice [48] were used and the blocking and smearing techniques were refined in comparison to earlier studies. This actually changed the values found in early studies of $T_c^{\text{lattice}}/\sqrt{\sigma}$ significantly for $SU(2)$ and $SU(3)$.
For the case of $SU(2)$ eq. (5.35) gives $T^{\text{lattice}}_{c,\,\mathrm{SU(2)}}/\sqrt{\sigma} \approx 0.709$. Thus, with a lattice string tension $\sqrt{\sigma} = 440\,\mathrm{MeV}$ the phase transition temperature found in the DSE representation of the Polyakov loop potential is too low, $T_c^{\text{fin.T}}/\sqrt{\sigma} \approx 0.523$, which is possibly due to the missing contribution from the two-loop diagram.

Results for $SU(3)$

In fact, for fixed directions of A_0 in the Cartan subalgebra, the Polyakov loop potential for arbitrary $SU(N_c)$ can be obtained by the pure knowledge of the $SU(2)$ potential[4],

$$V_{\mathrm{SU(N_c)}}(\varphi^a) = \sum_{l=1}^{N_c^2-1} \frac{1}{2} V_{\mathrm{SU(2)}}(\nu_l\,\varphi)\,. \tag{5.36}$$

The Cartan subalgebra of the gauge group of QCD, $SU(3)$, is two-dimensional, i.e. maximally two generators commute with each other. In the standard notation, see e.g. [477], these are the Gell-Mann matrices τ^3 and τ^8. The direction can be parametrised by the help of them. Thus, the Polyakov loop potential is given as a function of the magnitude φ^3, φ^8 of the background field in these directions. In general, this gives

$$V(\varphi^3,\varphi^8) = V_{\mathrm{SU(2)}}\left(\varphi^3\right) + V_{\mathrm{SU(2)}}\left(\frac{\varphi^3+\sqrt{3}\varphi^8}{2}\right) + V_{\mathrm{SU(2)}}\left(\frac{\varphi^3-\sqrt{3}\varphi^8}{2}\right). \tag{5.37}$$

The $SU(3)$ Polyakov loop potential for the two different inputs of temperature-independent scaling propagators and the temperature-dependent decoupling ones are given in fig. (5.13). Fig. (5.13(a)) is computed from the $SU(2)$ potential from temperature-independent propagators. Fig. (5.13(b)) shows the same quantity derived from thermal propators, which are given in chapter 4.
The deconfinement-confinement phase transition temperature of these results is higher compared to $SU(2)$, for the scaling vacuum propagators it is $T^{\mathrm{scal}}_{c,\mathrm{SU(3)}} \approx 240\mathrm{MeV}$, for the case of the thermal propagators $T^{\mathrm{fin.T}}_{c,\mathrm{SU(3)}} \approx 280\,\mathrm{MeV}$. The quantitative importance of the implicit temperature dependence of the wave-function renormalisation is also seen in the $SU(3)$ potential, which is a direct consequence of the quantitative difference of the $SU(2)$ potentials, fig. (5.7(a)) and fig. (5.11(a)).
In lattice gauge theory the critical temperature is found as $T^{\mathrm{lattice}}_{c,\mathrm{SU(3)}}/\sqrt{\sigma} \approx .646\,\mathrm{MeV}$ [47,48], cf. eq. (5.35). The input propagators in chapter 4 were matched with the lattice string tension $\sqrt{\sigma} = 440\,\mathrm{MeV}$ which gives a ratio $T^{\mathrm{fin.T}}_{c,\mathrm{SU(3)}}/\sqrt{\sigma} \approx 0.637$, in good agreement with lattice data.

As explained above the position of the minimum of the effective potential is an order parameter, which reflects order of the phase transition. The position of the minimum for the $SU(3)$ potential is given in fig. (5.14). In contrast to the second order phase transition in $SU(2)$, the minimum of the potential of $SU(3)$ jumps from the confining value $\langle\varphi\rangle = 2/3$ to a different value, see also fig. (5.13). This abrupt change signals a first order phase transition, which is consistent with lattice gauge theory [44].

Before I end this chapter I want to emphasise again that, although the critical tempera-

[4]Note that the non-trivial dependence of the input propagators on the value of N_c is neglected in this, as it has been in chapter 4.

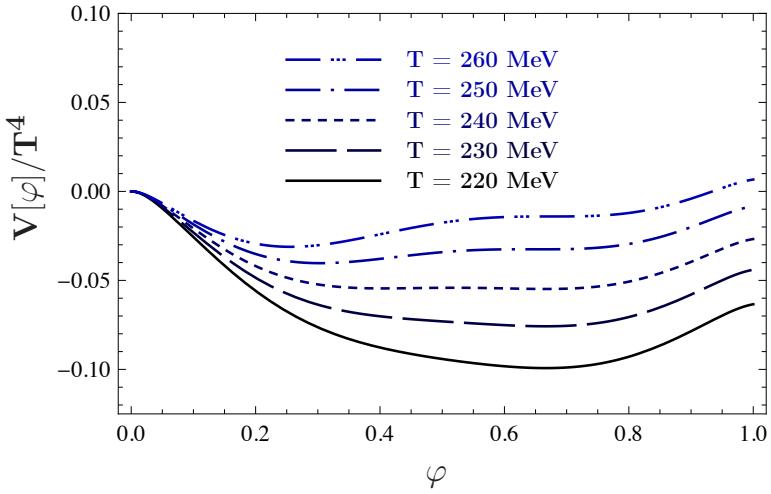

(a) Polyakov loop potential for $SU(3)$ obtained from temperature-independent scaling propagators from [276].

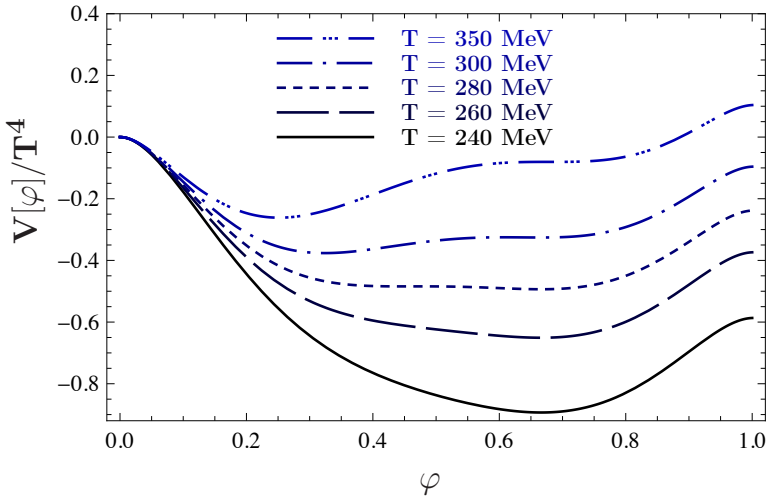

(b) Polyakov loop potential for $SU(3)$ obtained from temperature-dependent propagators from chapter 4.

Figure 5.13.: The Polyakov loop potential for $SU(3)$ can be obtained from the $SU(2)$ potential according to eq. (5.37). This figure shows the $SU(3)$ potential in the $\varphi = \varphi^3$ direction. The confining value is $\varphi = 2/3$. The position of the minimum serves as an order parameter for the deconfinement-confinement phase transition. At the critical temperature it jumps from its confining value to a non-confining value. This signals a first order phase transition for $SU(3)$, which is in agreement with lattice results, see e.g. [20].

tures for the deconfinement-confinement phase transition in $SU(2)$ and $SU(3)$ obtained from the best truncation within functional methods agree well with lattice gauge theory, there are caveats arising from truncations. Thus, the high accuracy may be a lucky coincidence. Nevertheless, it is fair to infer from the previous results that the occurence of the phase transition at the correct order of magnitude is definitely not affected by these approximations. In the following I summarise the potential problems and arguments why

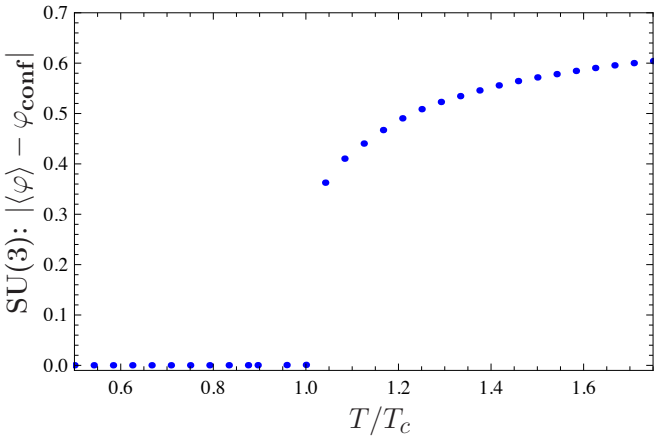

Figure 5.14.: First order phase transition for $SU(3)$ obtained from temperature-independent scaling propagators. The expectation value of the temporal gluon serves as an order parameter for the deconfinement-confinement phase-transition. The confining value for $SU(3)$ is $\varphi_{\mathbf{conf}} = 2/3$.

these deviations from the lattice in the corresponding parts could be subleading in the computation of the Polyakov loop potential.

Firstly, the main ingredients for the DSE representation of the Polyakov loop potential are the propagators. The good agreement is achieved with the temperature-dependent propagators given in chapter 4. For the temperatures of the phase transitions the results for the chromomagnetic gluon and the ghost are in satisfactory agreement with the lattice. In contrast to this, the chromoelectric propagator is significantly enhanced on the lattice. This is not seen in the FRG. However, the FRG propagator is evaluated on a non-trivial background. The background is identified with the Polyakov loop potential which is directly sensitive to the critical physics, in contradistinction to the computations of the thermal propagators presented in section 4.2.1. Therefore, although there is a clear deviation in the propagators, the way in which they occur in the subsequent computations may correct for this. This conjecture is supported by the quantitative agreement of the pressure given in fig. (4.3).

Secondly, another benchmark for the DSE Polyakov loop potential are the FRG results, which give higher critical temperatures for the same input. Since in the one-loop truncation of the DSE only the propagators enter, this may be due to the missing two-loop contribution. However, the two-loop contribution can be approximated by a diagram which has the same structure as the one-loop gluon term but with a three-gluon vertex correction. This vertex correction is supposedly a small correction. The latter statement is based on the results for the two-point functions at vanishing temperature in the DSE framework [276] given in section 2.3.2 in fig. (2.4), in which the two-loop diagrams have been dropped. Nevertheless, these results show that the main contributions arise from the one-loop diagrams and the two-loop terms give a small correction. This suggests that the two-loop diagram in the DSE representation of the Polyakov loop potential gives only a small correction as well.

5.3. Conclusions

The standard order parameter for quark confinement is the expectation value of the Polyakov loop potential. In addition to that, it could be shown that also the Polyakov loop evaluated on the expectation value of a purely temporal gauge field and, therefore, the latter expectation value itself serves as an order parameter as well [11,465]. This quantity is the minimum of the effective potential of the Polyakov loop, which is studied in this chapter within the framework of functional continuum methods. In these approaches quark confinement can be directly related to the behaviour of the propagators of Yang–Mills theory [11, 12].

In the FRG approach this has been pioneered in [11, 465]. In turn, the focus of the work presented here is on other functional methods, in particular DSEs and 2PI-effective actions. It turns out that the determining equation in the 2PI representation is equal to the one derived in the DSE. In this chapter this equation is solved numerically. The computation of the Polyakov loop potential gives the critical temperatures of the deconfinement-confinement phase transition of the gauge groups $SU(2)$ and $SU(3)$ which are of second and first order, respectively, as it is generally expected [11,12,44,47,48,364,365,478]. The critical temperatures are $T_c^{\mathrm{SU}(2)} \approx 230\,\mathrm{MeV}$ and $T_c^{\mathrm{SU}(3)} \approx 280\,\mathrm{MeV}$, measured in units of a lattice string tension $\sqrt{\sigma} = 440\,\mathrm{MeV}$. Thus, $T_c^{\mathrm{SU}(2)}/\sqrt{\sigma} \approx 0.523$ and $T_c^{\mathrm{SU}(3)}/\sqrt{\sigma} \approx 0.637$. These are compared with results from lattice gauge theory which yield $T_{c,\,\mathrm{latt}}^{\mathrm{SU}(2)}/\sqrt{\sigma} \approx 0.709$ and $T_{c,\,\mathrm{latt}}^{\mathrm{SU}(3)}/\sqrt{\sigma} \approx 0.646$ [47, 48].

6. On the QCD Phase Diagram from Functional Methods

The phase diagram of QCD can be studied within functional approaches from first principles [17,111–117]. The promising advantage of these methods is that they are not restricted to small values of the chemical potential. These approaches describe the theory in terms of correlation functions, wherein n-point functions of low order have an outstanding role. In this chapter I present results from an FRG approach for the two-point functions of QCD in the vacuum. An extension to correlation functions at non-zero temperature and/or quark chemical potential is possible and conceptually straighforward.
The results in this chapter are preliminary and, therefore, merely a status report of the work in progress. Thus, the exposition here is kept very compact as it only serves to impart the idea that is employed in this approach.

6.1. Unquenched Yang–Mills Propagators from the FRG

6.1.1. Method

After having studied QCD Green functions in the unphysical limit of infinitely heavy quarks, a natural advancement is to consider dynamical quarks, i.e. full QCD. The study of the fully coupled self-constistent system of infrared propagators of QCD has been pioneered in the framework of DSEs in [247, 479–481]. Afterwards, the study of Green functions of non-perturbative QCD from DSEs has been continued and it has developed as an active field of research [88, 116, 117, 260, 482–485], which can be directly compared with lattice simulations [486–493].
In this section Yang–Mills propagators in the presence of dynamical quarks are studied in the framework of the FRG. At first, I outline the strategy that is employed to consider quark fluctuations. This relies on the general properties of the FRG that are also utilised in the computation of the temperature-dependent propagators and thermodynamics of Yang–Mills theory in chapter 4.

As detailed in section 3.2.2 the FRG allows to look at a physical system at different scales. Therefore, the knowledge of the theory at one particular scale allows to compute the theory at all other scales. At large scales the running coupling of Yang–Mills theory becomes weak, thus, the theory can be desribed with perturbation theory. This gives access for

computing Yang–Mills theory also in the non-perturbative regime, e.g. for the full quantum theory.
However, this transition can be reversed[1]. In the case of thermal fluctuations, cf. chapter 4, this is utilised such that the full quantum theory is evolved to a scale $\Lambda/T \gg 1$ where thermal fluctuations of a fixed temperature are suppressed. Therefore, at this point the pure quantum theory is the appropriate initial condition for the thermal theory, which can be obtained by solving the flow equation of the thermal field theory down to the physical limit of vanishing renormalisation group scale.
The method to include quark fluctuations is based on the same considerations. Again, the full quantum effective action of Yang–Mills theory is taken as an input. The reversed flow can be done up to a high scale where the contributions of the quark loops in the equations are known from perturbation theory. They can be added to the effective action of Yang–Mills theory at this perturbative scale. In this way the initial condition can be obtained and full QCD can be studied by solving the flow to vanishing scale.

Note that this construction can be combined for unquenching and thermal effects. Furthermore, it can be extended even to the case of non-vanishing quark chemical potential μ. Similarly to the thermal fluctuations the signatures of the chemical potential vanish at large scales $\mu/\Lambda \ll 1$.

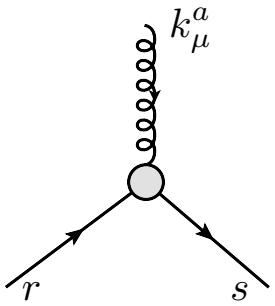

Figure 6.1.: Quark-gluon vertex.

The evolution of the full quantum Yang–Mills theory to the renormalisation group scale Λ is equal for both applications of thermal field theory and QCD. As the same truncation for the gauge part is employed here, the details for the first step of the computation are given in section 4.1. However, the second step differs for the two applications. For thermal fluctuations the initial condition at Λ is unchanged from the zero temperature case. In turn, for the quark fluctuations the perturbative contributions have to be taken into account. Note that as a simple approximation, the quark propagator and quark-gluon vertex are taken as classical at all scales. This is done in view of the way the results will be used in the study of the phase diagram, where at low chiral symmetry is

[1] Note that the inversion is not generally possible, cf. section 3.2.6, but for the purpose and scales presented here it is feasible.

dynamically broken and quarks and gluons are confined. At high and intermediate scales it is known from DSE studies that the quark sector is quantitatively close to the perturbative behaviour, for a review see e.g. [247]. In turn, it deviates for low scales. But, for the low energy regime the FRG formulation can be refined via dynamical hadronisation, i.e. the information of the bound states are not solely subsumed in the quark propagator and quark-gluon vertex any more but predominantly absorbed in other effective couplings. Thus, the approximation of the quark propagator and its coupling to the gluon is not the decisive part in this region. Note however, that the approximation for the vertex could be improved easily by exploiting its STI, see e.g. [339]. For a detailed study of the quark-gluon vertex in DSEs see [483]. In addition to that, in the FRG ansätze derived from this entity can be improved further by equipping the vertex with a renormalisation group scale-dependent dressing. This would also be an easy improvement for the wave-function renormalisation of the quark.
The quark propagator G_{q} and the quark-gluon vertex used in the computation presented in this chapter are schematically given by

$$G_{\mathrm{q}}(r, m_{\mathrm{q}}) = \frac{1}{-i\not{r} + m_{\mathrm{q}}}\,, \quad \left(\Gamma^{(3)}_{\mathrm{Aq\bar{q}}}\right)^{a}_{\mu}(k; r, s) \;=\; -ig\tau^{a}\gamma_{\mu}\,, \tag{6.1}$$

where r, s and k are the momenta of the quark, anti-quark and gluon, respectively, m_{q} is the mass of the considered quark flavour, the colour-structure is given by the Gell-Mann matrices τ^{a} and the Lorentz structure is given in terms of the Dirac matrices γ_{μ}. In the diagrammatic form the quark-gluon vertex is given in fig. (6.1), the quark propagator is illustrated by an arrowed solid line.

In the discussion of flow equations for two-point functions the generic diagrams that emerge contain three- and four-point interactions. For the quark fluctuations in the flow equation for the gluon propagator this yields two different types of diagrams, one involving two quark-gluon vertices and a closed quark loop and a tadpole contribution with the quark-gluon scattering kernel with a closed quark loop. The latter tadpole structure arises in the ghost propagator as well but, naturally, involving a quark-ghost scattering kernel. In contradistinction, the diagrams with two three-point vertices are forbidden due to the conservation of either ghost-number of fermion-number in the vertices. In the following the scattering-kernels are dropped in the approximation, since they do not have a classical analogue. As a result, the only modification on the level of Yang–Mills propagators is the quark-loop diagram, which is given in fig. (6.2).
Note that in the truncation at hand the quark propagator is classical and, therefore, no flow equation for the corresponding two-point function is solved. However, the propagator is regularised by the help of a cutoff function. In section 3.2.2 it is argued that the tensor structure of the regulating term should be equal to the tensor structure of the two-point function. Thus, in the case of the fermionic field the regulating term is $\sim \not{p}\, r(p^2/k^2)$.

As outlined before the initial condition of Yang–Mills theory is not the appropriate one for full QCD. It has to be corrected with the perturbative quark contribution, which is a

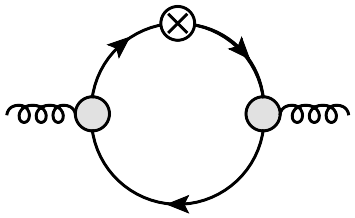

Figure 6.2.: The fluctuations of dynamical quarks give a contribution to the flow of the gluon propagator.

momentum-dependent quantity. In the truncation at hand, only the initial condition for the gluonic two-point function has to be adjusted. Schematically, the procedure is given by

$$\Gamma^{(2),\,\mathrm{YM}}_{A,\,k=\Lambda}(p) \to \Gamma^{(2),\,\mathrm{YM}}_{A,\,k=\Lambda}(p) + \Delta\Gamma^{(2)}_{A,\,k=\Lambda}(p)\,, \tag{6.2}$$

where $\Gamma^{(2),\,\mathrm{YM}}_{A,\,k=\Lambda}(p)$ is the gluonic two-point function of pure gauge theory at the renormalisation group scale $k = \Lambda$. The second term on the right hand side of eq. (6.2), $\Delta\Gamma^{(2)}_{A,\,k=\Lambda}(p)$, accounts for the quark contribution and is proportional to the canonical behaviour $\sim p^2$ with an additional logarithmic running with the renormalisation group scale Λ, viz.

$$\Delta\Gamma^{(2)}_{A,\,k=\Lambda}(p) = \Delta Z_{\mathrm{q}}\, p^2 \,\ln\left\{\frac{\Lambda^2 + m_{\mathrm{q}}^2}{m_{\mathrm{q}}^2}\right\}. \tag{6.3}$$

Note that for large scales $\Lambda \gg m_{\mathrm{q}}$ the logarithm approaches $\ln\left\{\Lambda^2\right\}$. The term ΔZ_{q} is taken as a constant and it could be set by the analytical result from perturbation theory, however only at the appropriate scale. For an arbitrary but large scale Λ the running of the quark-loop in this approximation can also be extracted from the flow of the diagram by

$$\Delta Z_{\mathrm{q}} = \partial_{p^2}\partial_t \Delta\Gamma^{(2)}_{A,\,k=\Lambda}(p)\Big|_{p\to 0}\,. \tag{6.4}$$

Note that this causes a different normalisation in the ultraviolet that has to be considered in the interpretation of the results.

Additionally, the adjustment according to the procedure in eq. (6.2) needs to be refined in view of gauge invariance. The naive addition of the flow of the quark loop would excite a perturbative mass term for the gluon which is forbidden by gauge invariance. The appearence of this mass term is a signature of the wrong initial condition. In principle, this would have to be cured by fine-tuning the initial condition to find the appropriate starting values for the full quantum theory. In spite of that, the emergence of a mass can be considered on an approximate level[2] in a far simpler way, namely by subtracting the mass directly along the flow. This is done in two steps. First of all, by subtracting the

[2]The approximation has been checked via the comparison of the mass subtraction given here with the mass that emerges along the full flow. For the results presented below the accuracy is $\lesssim 5\%$.

emerging mass directly in the flow, hence, in the transition from pure Yang–Mills theory to QCD the flow is corrected with

$$\partial_t \Gamma^{(2),\,\mathrm{YM}}_{A,\,k}(p) \to \partial_t \left(\Gamma^{(2),\,\mathrm{YM}}_{A,\,k}(p) + \Delta\Gamma^{(2)}_{A,\,k}(p) - \Delta\Gamma^{(2)}_{A,\,k}(p=0) \right) . \tag{6.5}$$

Second of all, the two-point functions of the ghost and the gluon now deviate from the corresponding quantities in pure gauge theory due to the quark fluctuations. Naturally, they couple back to the flow. As a consequence, the fine-tuning that has been done to cancel the perturbative mass in Yang–Mills theory is not the proper one for this case. However, it is still approximately correct since the subtraction of the flow, see eq. (6.5), cancels the main contributions. The development of the mass is forbidden by gauge-invariance, however, strictly only in the perturbative domain. Forestalling the results for quarks with constituent quark masses, the emerging masses $(\delta m)^2$ for the subtraction procedure in eq. (6.5) in the perturbative region is shown in fig. (6.3). Evidently, the

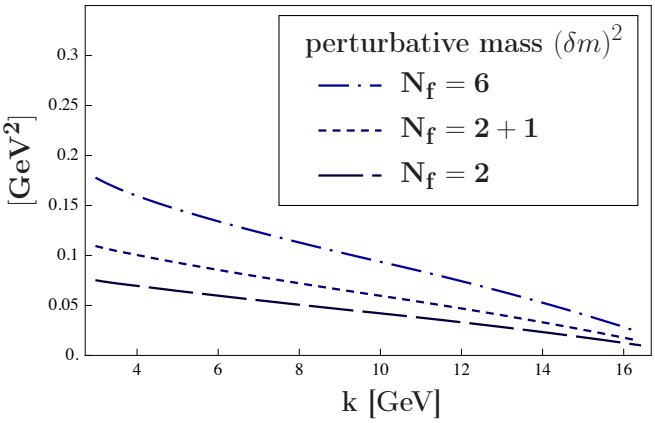

Figure 6.3.: A perturbative mass $(\delta m)^2$ in the unquenched gluon propagator builds up due to the approximative nature of the method eq. (6.5). This mass term breaks gauge-invariance, thus, it is extracted from the results.

effect grows with the number of flavours. Therefore, the study of QCD in the limit of large N_f is supposedly not feasible with this method. I comment on this further at the end of this section. Anyhow, these masses can be read off and subtracted from the gluonic two-point functions,

$$\Gamma^{(2)}_A(p) \to \Gamma^{(2)}_A(p) - (\delta m)^2 . \tag{6.6}$$

Of course, this method is not exact but is the best approximation that can be applied which does not require additional fine-tuning.

Of course, the way how quark fluctuations are considered, eq. (6.5), is an approximation not only regarding the truncation of Green functions. In fact, the procedure above constitutes a scale-dependent normalisation which is generally different from the one used in Yang–Mills theory. In section 6.1.2 this is seen directly in the wave-function renormalisations of both the gluon and the ghost fields.

The quarks have a physical mass. For high energies these masses are the bare masses, however, at scales where chiral symmetry is dynamically broken the light quarks acquire far higher masses. In the following the dependence of the constituent quark mass is tested on the level of the two-point functions. The solution with bare quark masses only is compared to the computation which comprises the changing masses at the chiral phase transtion. For reference the bare quark masses are given in tab. (2.1). The constituent quark mass is taken from an FRG computation of the QCD phase diagram which I sketch in section 6.2. The additional mass $\tilde{m}$ due to the breaking of chiral symmetry is used as pure input in the flow of the gluon and ghost propagators, it is given in fig. (6.4). The data is taken from a computation in progress which advances previous FRG results [112, 494]. This mass is non-zero only at relatively small scales k where the gluon flow is subject to ghost dominance. Thus, the effect of dynamical chiral symmetry breaking is qualitatively irrelevant for the unquenched Yang–Mills propagators.

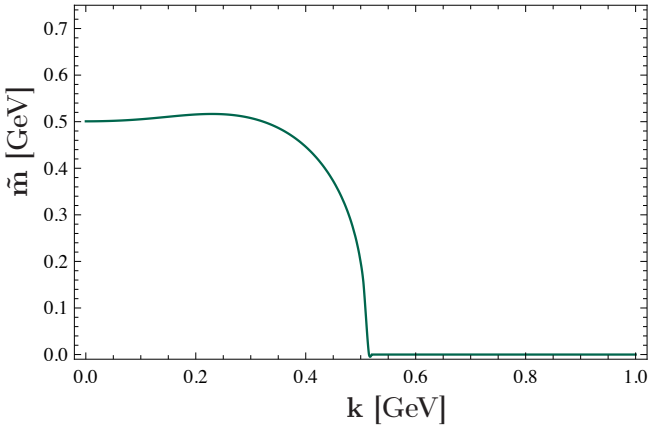

Figure 6.4.: Emerging quark mass contribution due to chiral symmetry breaking along the renormalisation group scale k.

There are six different quark flavours in the Standard Model of elementary particle physics. Each quark flavour contributes to the flow of the gluon propagator separately. Thus, the dependence of the two-point functions on the number of quark flavours N_f can be studied easily by considering the quark fluctuations arising from the diagram in fig. (6.2) for each flavour individually. However, note that the method described by eq. (6.5) and eq. (6.6) is an approximation which gets worse the further one goes away from the limit of pure gauge theory. Theoretically, the study concerning the dependence on N_f is possible for values larger than the physical value. This has also already been studied with the FRG, see e.g. [495, 496] and references therein. However, the limit of large N_f is inaccessible within the method presented here. Even for investigations of multi-flavour QCD the capabilities of this approach may be limited. Nevertheless, the value of N_f is varied in the computations presented below as the method is supposed to be reliable for realistic values

of N_f.

6.1.2. Results

In this section three different cases of mass input are investigated. The first choice are constituent quark masses with respect to the constituent quark mass given in fig. (6.4). The second computation is done with current quark masses only. At the end the comparison with the chiral limit is done. The results are compared with data from DSE studies [479] and lattice QCD [486].

At first, the most realistic case of consitutent quark masses, see fig. (6.4) and additionally tab. (2.1), are taken into account. For quarks depending on constituent quark masses, the gluon propagator,

$$\left(\Gamma_A^{(2)}\right)^{-1} = \left(Z_A(p)\, p^2\right)^{-1} , \tag{6.7}$$

in given in fig. (6.5(a)), its corresponding dressing function Z_A^{-1} is shown in fig. (6.5(b)). Note that the notation is adjusted to the significant differences in the quark masses, cf. tab. (2.1), with respect to the scale $\Lambda_{\mathrm{QCD}} \approx 200\,\mathrm{MeV}$. $N_f = 2$ stands for taking into account the up and down flavour, whose masses are negligible with respect to Λ_{QCD}. The notation $N_f = 2+1$ denotes the case of fluctuations of the two light flavours and the strange quark, whose mass is of the order of the intrinsic scale. The last results for $N_f = 6$ include all physical quarks. Note that the heavy quarks are hardly affected by the mass that emerges due to dynamical chiral symmetry breaking.
In fig. (6.5) the results for two, two plus one and six quark flavours, respectively, are compared with the propagator of pure gauge theory, $N_f = 0$. The gluon is directly sensitive to the quark contribution. Fig. (6.5(b)) shows that this leads to a suppression of the dressing function in the mid-momentum region. With increasing N_f it is suppressed further, which is in agreement with DSE results [88, 116, 117, 247, 260, 479–482, 484, 485].

An interesting aspect in fig. (6.5(b)) is the comparatively small change between the transition from $N_f = 2+1$ to $N_f = 6$ with respect to $N_f = 2$ to $N_f = 2+1$. This effect is due to the large quark masses of the heavy flavours. For large quark masses the loop propagators in the diagram given in fig. (6.2) are suppressed. Thus, their contributions are diminished. Naturally, the relevance of this effect depends on the relative scales in the system, here it is $\Lambda_{\mathrm{QCD}} \approx 200\,\mathrm{MeV}$. Thus, only the masses of the light flavours allow for significant fluctuations. The direct consequence is the small deviation of the $N_f = 6$ results to the $N_f = 2{+}1$ results. In the following also the chiral limit, i.e. $m_f \to 0$, is studied.

With regard to the full two-point function the dressing function does not resolve the infrared very well, since it vanishes for all non-singular values of the propagator. But the infrared shows a very interesting effect, namely, that the effective mass does not increase but stays of the same order. In fact, the propagator for $2+1$ flavours is enhanced. Note that an enhancement of the propagator is actually necessary for large values of N_f since

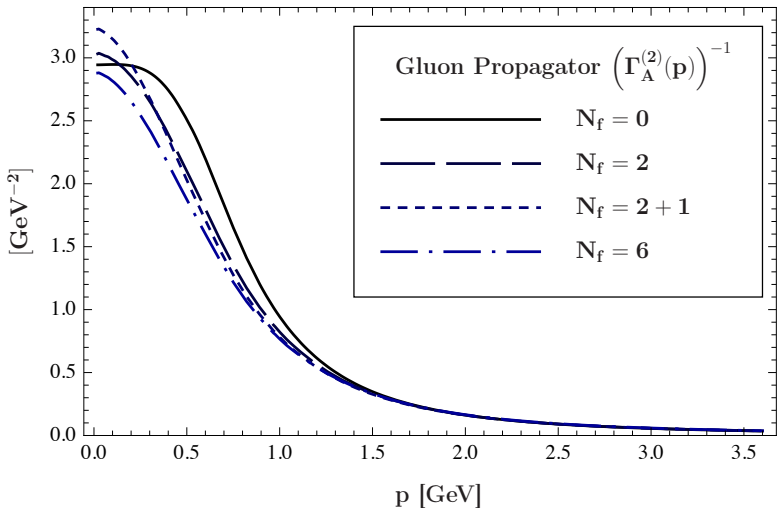

(a) Gluon propagator for pure gauge theory, $N_f = 2$, $N_f = 2+1$ and $N_f = 6$.

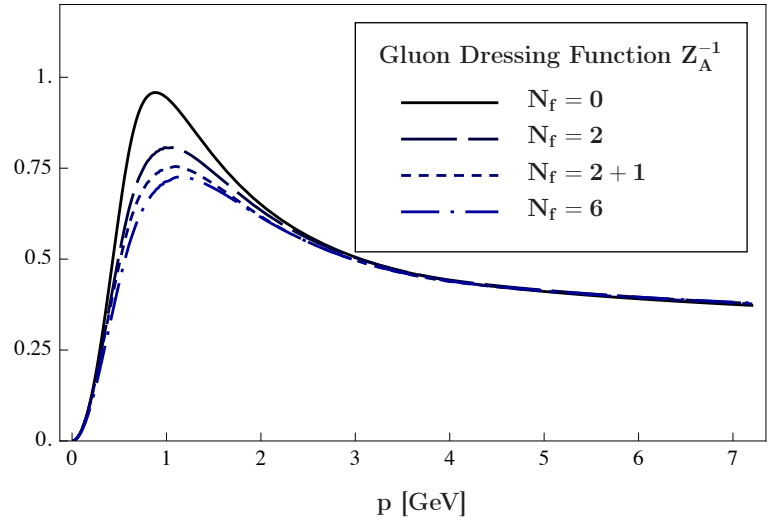

(b) Dressing function of the gluon for pure gauge theory, $N_f = 2$, $N_f = 2+1$ and $N_f = 6$.

Figure 6.5.: Gluon propagator and dressing function from the FRG as a function of the number of quark flavours. In the results in this figure constituent quark masses, see fig. (6.4) and tab. (2.1), have been considered.

the finiteness is related to confinement. For QCD, however, the quarks yield a deconfining contribution. Therefore, for large numbers of N_f the gluon propagator should diverge which necessitates a decrease of the effective mass. Under these considerations it is plausible that the propagators are not significantly suppressed in the deep infrared. Note that for $N_f = 6$ the propagator is in fact suppressed, however, it is only a small effect which may be due to the decreasing level of accuracy of the approximation for large N_f. I want to emphasise that in other studies in functional methods the propagator is in fact suppressed significantly, see e.g. [485] for a recent study, the FRG shows a clear deviation at this point.

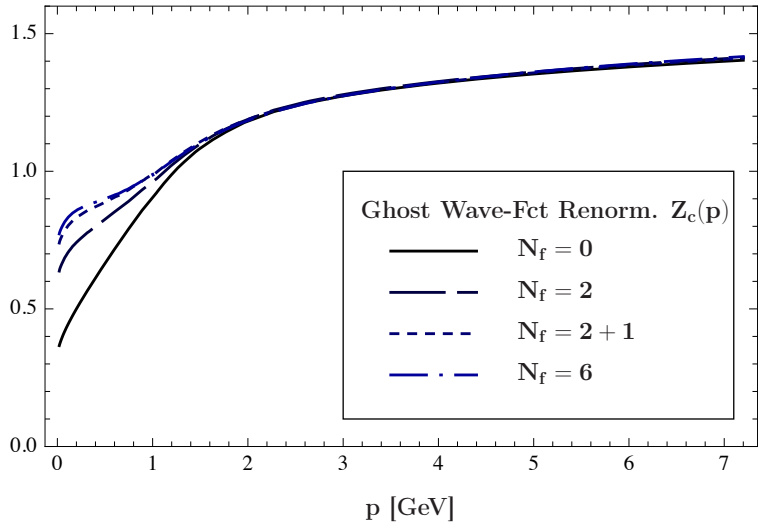

Figure 6.6.: The ghost is sensitive to the quark fluctutations via the coupling to the gluon. This figure shows the wave-function renormalisation of the ghost $Z_c(p)$ as a function of momentum and the number of quarks, N_f, with constituent quark masses, cf. fig. (6.4) and tab. (2.1).

In contradistinction to the gluon propagator, the ghost propagator feels the quark only via its coupling to the gluon propagator. As a consequence, the effect of unquenching is expected to be less pronounced. This conjecture is confirmed in the results presented here. The wave-function renormalisation of the ghost is given in fig. (6.6). Naturally, the suppression of quark fluctuations from the heavy flavours according to the discussion above is also seen here, since the $N_f = 6$ curve is close to the $N_f = 2 + 1$ one.

The results can be compared to other methods. The case of $N_f = 2 + 1$ is given in fig. (6.7(a)). The figure is taken from [247], it shows results from DSEs [479] as well as lattice QCD [486]. Note that for a better comparison of data the corresponding FRG data in fig. (6.7(b)) is rescaled with a factor $\mathcal{C}_{\text{norm}} = 2.35$ such that the gluon dressing function of pure Yang–Mills theory is of the same height as the one of the lattice data. The $N_f = 2+1$ result is rescaled with the same factor leaving the relative suppression with respect to the pure gauge part unchanged.

The constituent quark mass is non-zero at low energy scales only. In this regime, however, the gluon and ghost propagators are dominated by the ghost content which is only sensitive to the quark fluctuations via its coupling to the gauge field. Therefore, the effect of dynamical chiral symmetry breaking is expected to be subleading. Note, however, that this only holds for the two-point functions presented here. Of course, the matter sector of QCD is highly sensitive to the chiral phase transition.
In view of these aspects of the constituent quark mass, the small deviation of the results for the gluon dressing function in fig. (6.8), that is obtained without the consideration of chiral symmetry breaking, is reasonable. Since the wave-function renormalisations of the

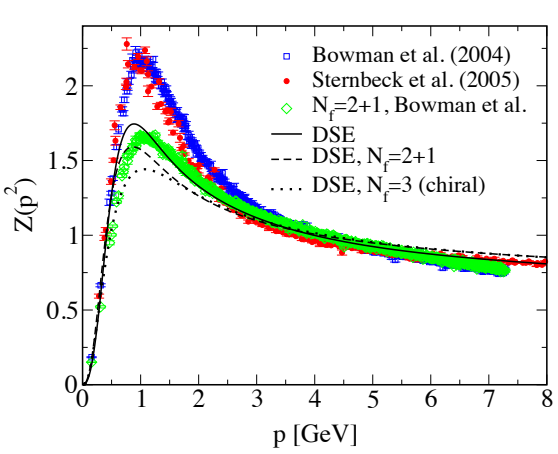

(a) DSE and lattice results for the unquenched gluon dressing function $Z(p^2) = Z_A(p)^{-1}$ for $N_f = 2+1$ in comparison to pure gauge theory. The figure is taken from [247] and printed with permission of IOP Publishing Ltd, it contains data from [479] and [486].

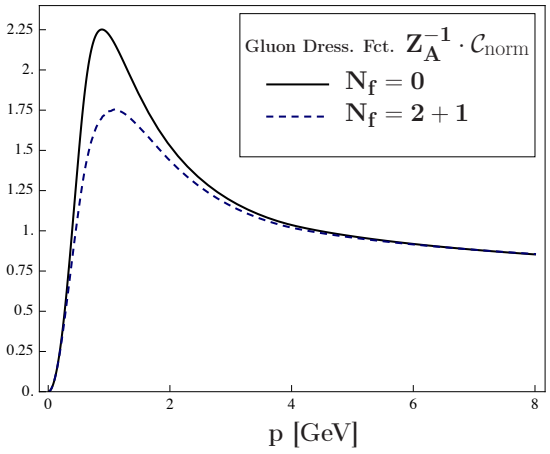

(b) Rescaled FRG result for the unquenched gluon dressing function for N_f = 2+1 in comparison to pure gauge theory.

Figure 6.7.: Comparison of results of different methods for the unquenched gluon dressing function.

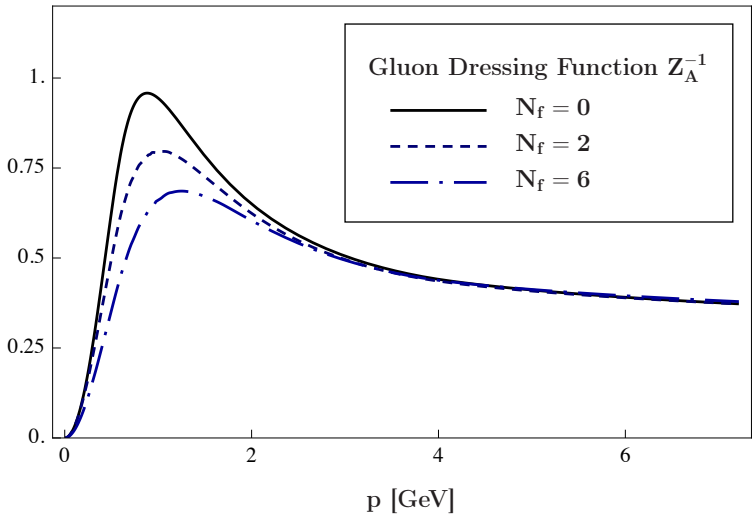

Figure 6.8.: Unquenched gluon dressing function of matter fluctuations with current quark masses.

ghost in the results with constituent and current quark masses are not distinguishable by eye, they are not explicitly illustrated here.

Another situation that is often studied theoretically is the chiral limit, i.e. all quarks are massless. For the results presented here dynamical chiral symmetry breaking is neglected in this case. This is the more interesting because chiral symmetry is exact at all scales for these configurations. The results for the gluon dressing function with two and six massless flavours is given in fig. (6.9). As expected the case of two light flavours is not

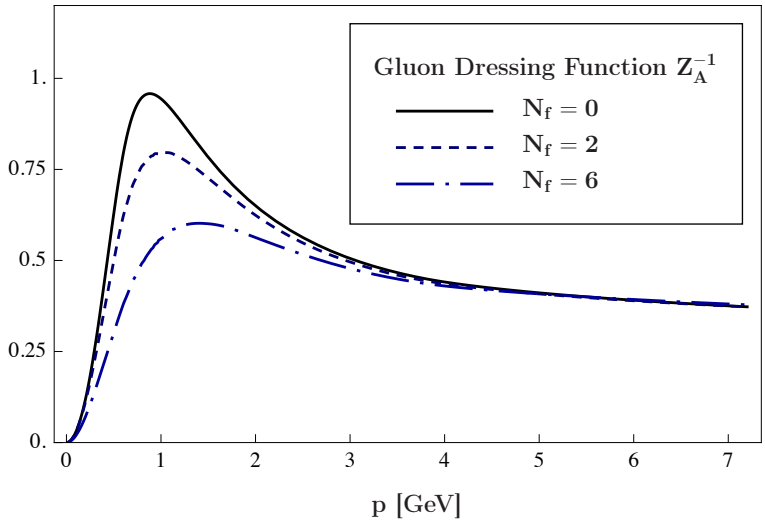

Figure 6.9.: Unquenched gluon dressing function in the chiral limit.

significantly changed, because the masses of the light quark are of the order of 1 – 2% of the relevant scale. Hence, they are quantitatively irrelevant. In contrast to this, the fluctuations of heavy quarks are heavily affected, since in this limit they are dynamical. Thus, they enhance the effect that is observed in the two-flavour case.

6.2. Conclusions and Outlook

In the FRG approach it is possible to compute non-perturbative Green functions of full QCD. The method which is presented in this chapter is constructed such that the full quantum Yang–Mills theory is taken as the starting point. It is evolved to a renormalisation group scale Λ at which quark fluctuations are perturbative and well known. Solving the flow equation for this system gives the non-perturbative two-point functions with dynamical quarks. This method is not limited to vacuum physics. Furthermore, non-zero temperature T and/or chemical potential μ can be studied as long as the scale Λ is chosen such that at this energy the fluctuations of (fixed equilibrium) T and μ are under control.

In this chapter preliminary results for the Yang–Mills propagators in the presence of dynamical quarks in the vacuum are presented. The two-point functions are computed as momentum-dependent functions of the quark masses and the number of quark flavours. The results agree qualitatively well with studies in the DSE approach [88, 116, 117, 247, 260, 479–485] and lattice gauge theory [486–493].
The main motivation for the computation of Green functions is their importance for studies of the QCD phase diagram from first principles with continuum methods[3], which is the

[3]Note that the correlation functions are also relevant in model studies, since they close the gap from perturbative physics to the scale at which the model serves to be a good approximation. In other words, the model parameters can be set from correlation functions that are obtained from a perturbative or

future field of application of the results presented in this chapter. In the formulation of the FRG it is possible to link the hadronic phase to the genuinely different phase in which quarks and gluons are the prevailing degrees of freedom. This is done via well-established rebosonisation techniques [111, 278, 494, 497–501], to which in this context is also referred to as dynamical hadronisation. The latter methods work such, that in addition to the quark-gluon vertex effective couplings of fermions are introduced which absorb the contributions from the fermion scattering kernels. The link to the hadronic, i.e. bound state description, is established via a Hubbard–Stratonovich transformation [502, 503] for these effective fermion couplings. In the dynamical hadronisation formalism the chiral condensate emerges. It is an order parameter for dynamical chiral symmetry breaking. This condensate also triggers a mass term for the bound states. Hence, it gives access to the constituent quark mass. It is a crucial aspect of this technique that the transition to the hadronic phase is not preset in this construction. In fact, one starts in the phase dominated by quark-gluon dynamics. The rebosonisation technique only allows the system itself to choose which degrees of freedom are active but it does not constrain the dynamics at all. In contrast, the chiral phase transition is only sensitive to the running coupling α_s, which is defined from the low-order correlation functions, see eq. (4.21b). Having said that, it is obvious that high precision in the computations of full QCD can only be obtained from quantitatively accurate correlation functions. So in the near future the insights that have been gained in this chapter and chapter 4 are going to be combined in order to study the full correlation functions at non-vanishing temperature and quark chemical potential, giving direct access to the full phase diagram of QCD.

even classical action.

7. Conclusions

The main motivation for the work presented in this thesis is the phase diagram of QCD. So far, the different states of hadronic matter can only be conjectured, since both, experimental and theoretical approaches, suffer from technical limitations. In this thesis functional continuum methods are employed. They are non-perturbative tools and applicable also in the strong coupling regime, where QCD is governed by the two characteristic effects of confinement and dynamical chiral symmetry breaking.

In the theoretical limit of infinitely heavy quarks the gauge bosons remain as the only dynamical particles. This system is called Yang–Mills theory, and due to the non-Abelian nature of the underlying gauge group it is an interacting system on its own. In fact, this pure gauge part of QCD is believed to be decisive for confinement, which denotes the absence of coloured states in the observed particle spectrum. Although great effort has been invested, the precise mechanism of confinement is not known yet, neither in Yang–Mills theory, nor in full QCD.

The study of Yang–Mills theory with non-perturbative functional methods is one of the main topics in this thesis. These continuum approaches provide a description of the theory in terms of correlation functions. However, due to the complexity of the system, most studies did not take into account the temperature dependence of Green functions. Chapter 4 is dedicated to the inclusion of thermal effects in the framework of the FRG. In particular, the propagators of the two physical polarisations of the gluon, the chromoelectric and the chromomagnetic mode are computed in the presence of non-zero temperature. The study is done in Landau gauge, which necessitates the incorporation of Faddeev–Popov ghosts.
At non-vanishing temperature the chromomagnetic propagator is suppressed with respect to its vacuum behaviour. But even in the infinite temperature limit it remains dynamical. In contrast to this, the chromoelectric mode develops a thermal mass, hence, it decouples from the interacting system. Interestingly, the chromoelectric propagator shows a highly non-trivial behaviour. At low temperatures $T \lesssim 200\,\mathrm{MeV}$ it is enhanced with respect to the vacuum. For temperatures above this value it shows a clear suppression. With increasing temperature the suppression is more distinct. It turns out that the thermal effects in the vertices must not be neglected in reliable truncations. The results presented in this thesis are in quantitative agreement with lattice data except for the chromoelectric mode at temperatures close to the critical temperature of the deconfinement-confinement phase

transition $T_c \approx 280\,\mathrm{MeV}$. The strong enhancement of the chromoelectric propagator at temperatures $150\,\mathrm{MeV} < T < T_c$ is missed in the FRG. Note that the thermal behaviour is not sensitive to the choice of a scaling or decoupling solution, which are the two mathematically possible but qualitatively different solutions of Yang–Mills theory in the deep infrared. On the lattice, however, only the decoupling solution is found. Therefore, for the study presented in this thesis, a decoupling solution was chosen. The results of chapter chapter 4 are published in [13, 14].

By definition, correlation functions of Yang–Mills theory are gauge-dependent, but nevertheless they encode gauge-invariant physics. For example, thermodynamic observables can be studied in terms of n-point functions. Note that the term observable in this case refers to lattice simulations, since pure gauge theory is not accessible in experiment. The FRG provides direct access to the thermodynamics, since it provides an equation for the free energy. In this work the pressure of Yang–Mills theory is computed from the temperature-dependent propagators. For the first time within continuum methods the behaviour of the pressure is correctly described over the full temperature range, in particular for temperatures around the deconfinement-confinement phase transition. Two effects are crucial for the quantitative agreement: the temperature dependence of the propagators and the Polyakov loop potential, which encodes the critical physics at the phase transition. The results are very promising, however, still preliminary.

The interactions of gluons are responsible for the confinement of quarks as well. An order parameter for the confinement of static quarks is the expectation value of the Polyakov loop potential, which can be computed from low-order correlation functions of Yang–Mills theory. As a consequence, pure gauge theory yields direct information for the phase diagram of QCD.
In this work the Polyakov loop potential is studied within functional methods. Complementing previous works in the FRG approach [11, 12], mainly DSEs and 2PI effective actions are employed in this work to study the critical physics that happen at temperatures of the deconfinement-confinement phase transition.
In chapter 5, the Polyakov loop potential is computed from the temperature-dependent gluon and ghost propagators of pure gauge theory, giving a first order phase transition for $SU(3)$ and a second order phase transition for $SU(2)$. The critical temperatures $T_c^{SU(3)} \approx 280\,\mathrm{MeV}$ and $T_c^{SU(2)} \approx 230\,\mathrm{MeV}$, respectively, are found. With a lattice string tension of $\sqrt{\sigma} \approx 440\,\mathrm{MeV}$, this yields $T_c^{SU(3)}/\sqrt{\sigma} \approx .636$ and $T_c^{SU(2)}/\sqrt{\sigma} \approx .523$. The corresponding results from lattice gauge theory are $T_{c,\,\mathrm{lattice}}^{SU(3)}/\sqrt{\sigma} \approx .646$ and $T_{c,\,\mathrm{lattice}}^{SU(2)}/\sqrt{\sigma} \approx .709$ [47, 48].

Chapter 6 deals with the inclusion of dynamical quarks. Naturally, their fluctuations also affect the correlators without external quark content. This unquenching is studied for different numbers of quark flavours and for the different cases of constituent, current and vanishing quark masses. The quark fluctuations suppress the gluon propagator at intermediate momenta significantly. At low momenta, however, the gluon propagator is

almost unchanged. This may be a signature of the fact that for large numbers of quark flavours the gluon propagator diverges at vanishing momentum. However, the results in chapter 6 are preliminary, thus, this question is not conclusively answered in this thesis. In the near future the correlation functions are going to be used in investigations of the phase diagram of QCD from first principles within functional methods, advancing previous works [112, 494].

A. Flow Equations

In this appendix the information from fig. (3.7), fig. (3.8), fig. (3.9) and fig. (3.10) are given in terms of actual formulae. As mentioned in section 3.2.3 a *Mathematica* program was written to derive flow equations algorithmically. The formulae here are the full flow equations and no truncations have been done so far.The output was generated by *Mathematica* as well.

For applications, note that the loop momentum can be shifted such that the similarity of some terms in the formulae below is manifest, e.g. the four terms with ghost-loops in the gluon propagator yield the same contribution to the flow, so the diagram has only be computed once with a combinatorical factor of four. These simplifications due to momentum shifts have not been employed in the equations below, but have been done in the diagrammatic illustrations in fig. (3.7), fig. (3.8), fig. (3.9) and fig. (3.10).

The corresponding figures for the DSEs can be translated in a similar fashion from the diagrammatic illustration.

The flow for the gluon propagator, fig. (3.7), is given by

$$
\begin{aligned}
&\partial_t \left\{ \left(\Gamma^{(2)}_{A,k} \right)^{ba}_{\nu\mu} (p,-p) \right\} = \\
&-\frac{1}{2} \int_q (R_c)^{\mathrm{cd}}(q)\,(G_c)^{\mathrm{de}}(q)\,(G_c)^{\mathrm{fc}}(q)\,(\Gamma_{AA\bar{c}c})^{baef}_{\nu\mu}(-p,p,q,-q) \\
&+\frac{1}{2} \int_q (R_c)^{\mathrm{cd}}(q)\,(G_c)^{\mathrm{de}}(q)\,(G_c)^{\mathrm{fc}}(q)\,(\Gamma_{AAc\bar{c}})^{baef}_{\nu\mu}(-p,p,q,-q) \\
&-\frac{1}{2} \int_q (R_A)^{\mathrm{cd}}_{\rho\sigma}(q)\,(G_A)^{\mathrm{de}}_{\sigma\tau}(q)\,(G_A)^{\mathrm{fc}}_{\upsilon\rho}(q)\,(\Gamma_{A4})^{\mathrm{baef}}_{\nu\mu\tau\upsilon}(-p,p,q,-q) \\
&+\frac{1}{2} \int_q (R_A)^{\mathrm{cd}}_{\rho\sigma}(q)\,(G_A)^{\mathrm{de}}_{\sigma\tau}(q)\,(G_A)^{\mathrm{hc}}_{\xi\rho}(q)\,(G_A)^{\mathrm{fg}}_{\upsilon\omega}(p+q)\,(\Gamma_{A3})^{\mathrm{aef}}_{\mu\tau\upsilon}(p,q,-p-q)\,(\Gamma_{A3})^{\mathrm{bgh}}_{\nu\omega\xi}(-p,p+q,-q) \\
&+\frac{1}{2} \int_q (R_A)^{\mathrm{cd}}_{\rho\sigma}(q)\,(G_A)^{\mathrm{de}}_{\sigma\tau}(q)\,(G_A)^{\mathrm{hc}}_{\xi\rho}(q)\,(G_A)^{\mathrm{fg}}_{\upsilon\omega}(q-p)\,(\Gamma_{A3})^{\mathrm{agh}}_{\mu\omega\xi}(p,q-p,-q)\,(\Gamma_{A3})^{\mathrm{bef}}_{\nu\tau\upsilon}(-p,q,p-q) \\
&-\frac{1}{2} \int_q (R_c)^{\mathrm{cd}}(q)\,(G_c)^{\mathrm{de}}(q)\,(G_c)^{\mathrm{hc}}(q)\,(G_c)^{\mathrm{fg}}(p+q)\,(\Gamma_{cA\bar{c}})^{\mathrm{caf}}_{\mu}(q,p,-p-q)\,(\Gamma_{cA\bar{c}})^{\mathrm{gbh}}_{\nu}(p+q,-p,-q) \\
&-\frac{1}{2} \int_q (R_c)^{\mathrm{cd}}(q)\,(G_c)^{\mathrm{de}}(q)\,(G_c)^{\mathrm{hc}}(q)\,(G_c)^{\mathrm{fg}}(q-p)\,(\Gamma_{cA\bar{c}})^{\mathrm{ebf}}_{\nu}(q,-p,p-q)\,(\Gamma_{cA\bar{c}})^{\mathrm{gah}}_{\mu}(q-p,p,-q) \\
&-\frac{1}{2} \int_q (R_c)^{\mathrm{cd}}(q)\,(G_c)^{\mathrm{de}}(q)\,(G_c)^{\mathrm{hc}}(q)\,(G_c)^{\mathrm{fg}}(p+q)\,(\Gamma_{cA\bar{c}})^{\mathrm{fae}}_{\mu}(-p-q,p,q)\,(\Gamma_{cA\bar{c}})^{\mathrm{hbg}}_{\nu}(-q,-p,p+q) \\
&-\frac{1}{2} \int_q (R_c)^{\mathrm{cd}}(q)\,(G_c)^{\mathrm{de}}(q)\,(G_c)^{\mathrm{hc}}(q)\,(G_c)^{\mathrm{fg}}(q-p)\,(\Gamma_{cA\bar{c}})^{\mathrm{fbe}}_{\nu}(p-q,-p,q)\,(\Gamma_{cA\bar{c}})^{\mathrm{hag}}_{\mu}(-q,p,q-p)\,. \qquad \text{(A.1)}
\end{aligned}
$$

The flow for the ghost propagator, fig. (3.8), is given by

$$
\begin{aligned}
&\partial_t \left\{ \left(\Gamma^{(2)}_{c,k} \right)^{ba} (p,-p) \right\} = \\
&-\frac{1}{2} \int_q (R_A)^{\mathrm{cd}}_{\rho\sigma}(q)\,(G_A)^{\mathrm{de}}_{\sigma\tau}(q)\,(G_A)^{\mathrm{fc}}_{\upsilon\rho}(q)\,(\Gamma_{c\bar{c}AA})^{baef}_{\tau\upsilon}(-p,p,q,-q) \\
&-\frac{1}{2} \int_q (R_c)^{\mathrm{cd}}(q)\,(G_c)^{\mathrm{de}}(q)\,(G_c)^{\mathrm{fc}}(q)\,(\Gamma_{c\bar{c}\bar{c}c})^{baef}(-p,p,q,-q) \\
&+\frac{1}{2} \int_q (R_c)^{\mathrm{cd}}(q)\,(G_c)^{\mathrm{de}}(q)\,(G_c)^{\mathrm{fc}}(q)\,(\Gamma_{c\bar{c}c\bar{c}})^{baef}(-p,p,q,-q) \\
&+\frac{1}{2} \int_q (R_A)^{\mathrm{cd}}_{\rho\sigma}(q)\,(G_A)^{\mathrm{de}}_{\sigma\tau}(q)\,(G_A)^{\mathrm{hc}}_{\xi\rho}(q)\,(G_c)^{\mathrm{fg}}(q-p\,(\Gamma_{cA\bar{c}})^{\mathrm{bef}}_{\tau}(-p,q,p-q)\,(\Gamma_{cA\bar{c}})^{\mathrm{gha}}_{\xi}(q-p,-q,p) \\
&+\frac{1}{2} \int_q (R_c)^{\mathrm{cd}}(q)\,(G_c)^{\mathrm{de}}(q)\,(G_c)^{\mathrm{hc}}(q)\,(G_A)^{\mathrm{fg}}_{\upsilon\omega}(q-p)\,(\Gamma_{cA\bar{c}})^{\mathrm{bfe}}_{\upsilon}(-p,p-q,q)\,(\Gamma_{cA\bar{c}})^{\mathrm{hga}}_{\omega}(-q,q-p,p) \\
&+\frac{1}{2} \int_q (R_c)^{\mathrm{cd}}(q)\,(G_c)^{\mathrm{de}}(q)\,(G_c)^{\mathrm{hc}}(q)\,(G_A)^{\mathrm{fg}}_{\upsilon\omega}(p+q)\,(\Gamma_{cA\bar{c}})^{\mathrm{bgh}}_{\omega}(-p,p+q,-q)\,(\Gamma_{cA\bar{c}})^{\mathrm{efa}}_{\upsilon}(q,-p-q,p) \\
&+\frac{1}{2} \int_q (R_A)^{\mathrm{cd}}_{\rho\sigma}(q)\,(G_A)^{\mathrm{de}}_{\sigma\tau}(q)\,(G_A)^{\mathrm{hc}}_{\xi\rho}(q)\,(G_c)^{\mathrm{fg}}(p+q)\,(\Gamma_{cA\bar{c}})^{\mathrm{bhg}}_{\xi}(-p,-q,p+q)\,(\Gamma_{cA\bar{c}})^{\mathrm{fea}}_{\tau}(-p-q,q,p)\,. \qquad \text{(A.2)}
\end{aligned}
$$

The flow for the ghost-gluon vertex, fig. (3.9), is given by

$$
\partial_t \left(\Gamma^{(3)}_{c\bar{c}A} \right)^{cba}_{\mu}(t,s,r) \quad = \quad A^{cba}_{\mu}(t,s,r) + B^{cba}_{\mu}(t,s,r) + C^{cba}_{\mu}(t,s,r) + D^{cba}_{\mu}(t,s,r) + E^{cba}_{\mu}(t,s,r)\,, \qquad \text{(A.3)}
$$

with

$$
\begin{aligned}
&A^{cba}_{\mu}(t,s,r) = \\
&-\frac{1}{2} \int_q (G_A)^{\mathrm{jk}}_{\zeta\gamma}(q+r+s)\,(G_c)^{\mathrm{ef}}(q)\,(G_c)^{\mathrm{gh}}(q+r)\,(G_c)^{\mathrm{ld}}(q+r+s+t)\,(R_c)^{\mathrm{de}}(q) \\
&\qquad (\Gamma_{cA\bar{c}})^{\mathrm{ckl}}_{\gamma}(t,q+r+s,-q-r-s-t)\,(\Gamma_{cA\bar{c}})^{\mathrm{hjb}}_{\zeta}(q+r,-q-r-s,s)\,(\Gamma_{cA\bar{c}})^{\mathrm{fag}}_{\mu}(q,r,-q-r) \\
&-\frac{1}{2} \int_q (G_A)^{\mathrm{jk}}_{\zeta\gamma}(q+r+t)\,(G_c)^{\mathrm{ef}}(q)\,(G_c)^{\mathrm{gh}}(q+r)\,(G_c)^{\mathrm{ld}}(q+r+s+t)\,(R_c)^{\mathrm{de}}(q) \\
&\qquad (\Gam_{cA\bar{c}})^{\mathrm{lkb}}_{\gamma}(-q-r-s-t,q+r+t,s)\,(\Gamma_{cA\bar{c}})^{\mathrm{cjh}}_{\zeta}(t,-q-r-t,q+r)\,(\Gamma_{cA\bar{c}})^{\mathrm{gaf}}_{\mu}(-q-r,r,q) \\
&-\frac{1}{2} \int_q (G_A)^{\mathrm{ld}}_{\delta\sigma}(q+r+s+t)\,(G_A)^{\mathrm{ef}}_{\tau\upsilon}(q)\,(G_A)^{\mathrm{gh}}_{\omega\xi}(q+r)\,(G_c)^{\mathrm{jk}}(q+r+t)\,(R_A)^{\mathrm{de}}_{\sigma\tau}(q) \\
&\qquad (\Gamma_{A3})^{\mathrm{afg}}_{\mu\upsilon\omega}(r,q,-q-r)\,(\Gamma_{cA\bar{c}})^{\mathrm{klb}}_{\delta}(q+r+t,-q-r-s-t,s)\,(\Gamma_{cA\bar{c}})^{\mathrm{chj}}_{\xi}(t,q+r,-q-r-t) \\
&-\frac{1}{2} \int_q (G_A)^{\mathrm{gh}}_{\omega\xi}(q+r+s)\,(G_c)^{\mathrm{ef}}(q)\,(G_c)^{\mathrm{jd}}(q+r+s+t)\,(R_c)^{\mathrm{de}}(q) \\
&\qquad (\Gamma_{cAA\bar{c}})^{bafg}_{\mu\omega}(s,r,q,-q-r-s)\,(\Gamma_{cA\bar{c}})^{\mathrm{chj}}_{\xi}(t,q+r+s,-q-r-s-t) \\
&-\frac{1}{2} \int_q (G_A)^{\mathrm{ld}}_{\delta\sigma}(q+r+s+t)\,(G_A)^{\mathrm{ef}}_{\tau\upsilon}(q)\,(G_A)^{\mathrm{gh}}_{\omega\xi}(q+r)\,(G_c)^{\mathrm{jk}}(q+r+s)\,(R_A)^{\mathrm{de}}_{\sigma\tau}(q) \\
&\qquad (\Gamma_{A3})^{\mathrm{afg}}_{\mu\upsilon\omega}(r,q,-q-r)\,(\Gamma_{cA\bar{c}})^{\mathrm{clk}}_{\delta}(t,-q-r-s-t,q+r+s)\,(\Gamma_{cA\bar{c}})^{\mathrm{jhb}}_{\xi}(-q-r-s,q+r,s) \\
&-\frac{1}{2} \int_q (G_A)^{\mathrm{jd}}_{\zeta\sigma}(q+r+s+t)\,(G_A)^{\mathrm{ef}}_{\tau\upsilon}(q)\,(G_c)^{\mathrm{gh}}(q+t)\,(R_A)^{\mathrm{de}}_{\sigma\tau}(q) \\
&\qquad (\Gamma_{cAA\bar{c}})^{bahj}_{\mu\zeta}(s,r,q+t,-q-r-s-t)\,(\Gamma_{cA\bar{c}})^{\mathrm{cfg}}_{\upsilon}(t,q,-q-t) \\
&-\frac{1}{2} \int_q (G_A)^{\mathrm{ld}}_{\delta\sigma}(q+r+s+t)\,(G_A)^{\mathrm{jk}}_{\zeta\gamma}(q+s+t)\,(G_A)^{\mathrm{ef}}_{\tau\upsilon}(q)\,(G_c)^{\mathrm{gh}}(q+t)\,(R_A)^{\mathrm{de}}_{\sigma\tau}(q) \\
&\qquad (\Gamma_{A3})^{\mathrm{akl}}_{\mu\gamma\delta}(r,q+s+t,-q-r-s-t)\,(\Gamma_{cA\bar{c}})^{\mathrm{hjb}}_{\zeta}(q+t,-q-s-t,s)\,(\Gamma_{cA\bar{c}})^{\mathrm{cfg}}_{\upsilon}(t,q,-q-t) \\
&-\frac{1}{2} \int_q (G_A)^{\mathrm{ld}}_{\delta\sigma}(q+r+s+t)\,(G_A)^{\mathrm{ef}}_{\tau\upsilon}(q)\,(G_c)^{\mathrm{gh}}(q+t)\,(G_c)^{\mathrm{jk}}(q+r+t)\,(R_A)^{\mathrm{de}}_{\sigma\tau}(q) \\
&\qquad (\Gamma_{cA\bar{c}})^{\mathrm{klb}}_{\delta}(q+r+t,-q-r-s-t,s)\,(\Gamma_{cA\bar{c}})^{\mathrm{haj}}_{\mu}(q+t,r,-q-r-t)\,(\Gamma_{cA\bar{c}})^{\mathrm{cfg}}_{\upsilon}(t,q,-q-t) \\
&-\frac{1}{2} \int_q (G_A)^{\mathrm{ld}}_{\delta\sigma}(q+r+s+t)\,(G_A)^{\mathrm{jk}}_{\zeta\gamma}(q+s+t)\,(G_A)^{\mathrm{ef}}_{\tau\upsilon}(q)\,(G_c)^{\mathrm{gh}}(q+s)\,(R_A)^{\mathrm{de}}_{\sigma\tau}(q) \\
&\qquad (\Gamma_{A3})^{\mathrm{akl}}_{\mu\gamma\delta}(r,q+s+t,-q-r-s-t)\,(\Gamma_{cA\bar{c}})^{\mathrm{cjh}}_{\zeta}(t,-q-s-t,q+s)\,(\Gamma_{cA\bar{c}})^{\mathrm{gfb}}_{\upsilon}(-q-s,q,s)\,, \qquad \text{(A.4)}
\end{aligned}
$$

$$
\begin{aligned}
&B_{\mu}^{cba}(t,s,r) = \\
&-\frac{1}{2}\int_q (G_A)^{\mathrm{ld}}_{\delta\sigma}(q+r+s+t)\,(G_A)^{\mathrm{ef}}_{\tau\upsilon}(q)\,(G_c)^{\mathrm{gh}}(q+s)\,(G_c)^{\mathrm{jk}}(q+r+s)\,(R_A)^{\mathrm{de}}_{\sigma\tau}(q)\,(\Gamma_{cA\bar{c}})^{\mathrm{clk}}_{\delta}(t,-q-r-s-t,q+r+s) \\
&\qquad (\Gamma_{cA\bar{c}})^{\mathrm{jah}}_{\mu}(-q-r-s,r,q+s)\,(\Gamma_{cA\bar{c}})^{\mathrm{gfb}}_{\upsilon}(-q-s,q,s) \\
&-\frac{1}{2}\int_q (G_A)^{\mathrm{jk}}_{\zeta\gamma}(q+r+t)\,(G_A)^{\mathrm{gh}}_{\omega\xi}(q+t)\,(G_c)^{\mathrm{ef}}(q)\,(G_c)^{\mathrm{ld}}(q+r+s+t\,(R_c)^{\mathrm{de}}(q)\,(\Gamma_{A3})^{\mathrm{ahj}}_{\mu\xi\zeta}(r,q+t,-q-r-t) \\
&\qquad (\Gamma_{cA\bar{c}})^{\mathrm{lkb}}_{\gamma}(-q-r-s-t,q+r+t,s)\,(\Gamma_{cA\bar{c}})^{\mathrm{cgf}}_{\omega}(t,-q-t,q) \\
&-\frac{1}{2}\int_q (G_A)^{\mathrm{gh}}_{\omega\xi}(q+t)\,(G_c)^{\mathrm{ef}}(q)\,(G_c)^{\mathrm{jk}}(q+s+t)\,(G_c)^{\mathrm{ld}}(q+r+s+t)\,(R_c)^{\mathrm{de}}(q)\,(\Gamma_{cA\bar{c}})^{\mathrm{lak}}_{\mu}(-q-r-s-t,r,q+s+t) \\
&\qquad (\Gamma_{cA\bar{c}})^{\mathrm{jhb}}_{\xi}(-q-s-t,q+t,s)\,(\Gamma_{cA\bar{c}})^{\mathrm{cgf}}_{\omega}(t,-q-t,q) \\
&-\frac{1}{2}\int_q (G_A)^{\mathrm{jk}}_{\zeta\gamma}(q+r+s)\,(G_A)^{\mathrm{gh}}_{\omega\xi}(q+s)\,(G_c)^{\mathrm{ef}}(q)\,(G_c)^{\mathrm{ld}}(q+r+s+t)\,(R_c)^{\mathrm{de}}(q)\,(\Gamma_{A3})^{\mathrm{ahj}}_{\mu\xi\zeta}(r,q+s,-q-r-s) \\
&\qquad (\Gamma_{cA\bar{c}})^{\mathrm{ckl}}_{\gamma}(t,q+r+s,-q-r-s-t)\,(\Gamma_{cA\bar{c}})^{\mathrm{fgb}}_{\omega}(q,-q-s,s) \\
&-\frac{1}{2}\int_q (G_A)^{\mathrm{gh}}_{\omega\xi}(q+s)\,(G_c)^{\mathrm{ef}}(q)\,(G_c)^{\mathrm{jk}}(q+s+t)\,(G_c)^{\mathrm{ld}}(q+r+s+t)\,(R_c)^{\mathrm{de}}(q)\,(\Gamma_{cA\bar{c}})^{\mathrm{kal}}_{\mu}(q+s+t,r,-q-r-s-t) \\
&\qquad (\Gamma_{cA\bar{c}})^{\mathrm{chj}}_{\xi}(t,q+s,-q-s-t)\,(\Gamma_{cA\bar{c}})^{\mathrm{fgb}}_{\omega}(q,-q-s,s)\,,
\end{aligned}
\tag{A.5}
$$

$$
\begin{aligned}
&C_{\mu}^{cba}(t,s,r) = \\
&-\frac{1}{2}\int_q (G_A)^{\mathrm{jd}}_{\zeta\sigma}(q+r+s+t)\,(G_A)^{\mathrm{ef}}_{\tau\upsilon}(q)\,(G_c)^{\mathrm{gh}}(q+r+t)\,(R_A)^{\mathrm{de}}_{\sigma\tau}(q)\,(\Gamma_{cAA\bar{c}})^{cafg}_{\mu\upsilon}(t,r,q,-q-r-t) \\
&\qquad (\Gamma_{cA\bar{c}})^{\mathrm{hjb}}_{\zeta}(q+r+t,-q-r-s-t,s) \\
&+\frac{1}{2}\int_q (G_A)^{\mathrm{gh}}_{\omega\xi}(q+s)\,(G_c)^{\mathrm{ef}}(q)\,(G_c)^{\mathrm{jd}}(q+r+s+t)\,(R_c)^{\mathrm{de}}(q)\,(\Gamma_{cAA\bar{c}})^{cahj}_{\mu\xi}(t,r,q+s,-q-r-s-t) \\
&\qquad (\Gamma_{cA\bar{c}})^{\mathrm{fgb}}_{\omega}(q,-q-s,s) \\
&+\frac{1}{2}\int_q (G_A)^{\mathrm{jd}}_{\zeta\sigma}(q+r+s+t)\,(G_A)^{\mathrm{ef}}_{\tau\upsilon}(q)\,(G_c)^{\mathrm{gh}}(q+s)\,(R_A)^{\mathrm{de}}_{\sigma\tau}(q)\,(\Gamma_{cA\bar{c}})^{\mathrm{gfb}}_{\upsilon}(-q-s,q,s) \\
&\qquad (\Gamma_{cA\bar{c}A})^{cahj}_{\mu\zeta}(t,r,q+s,-q-r-s-t) \\
&-\frac{1}{2}\int_q (G_A)^{\mathrm{gh}}_{\omega\xi}(q+r+t)\,(G_c)^{\mathrm{ef}}(q)\,(G_c)^{\mathrm{jd}}(q+r+s+t)\,(R_c)^{\mathrm{de}}(q)\,(\Gamma_{cA\bar{c}})^{\mathrm{jhb}}_{\xi}(-q-r-s-t,q+r+t,s) \\
&\qquad (\Gamma_{cA\bar{c}A})^{cafg}_{\mu\omega}(t,r,q,-q-r-t) \\
&-\frac{1}{2}\int_q (G_A)^{\mathrm{gh}}_{\omega\xi}(q+t)\,(G_c)^{\mathrm{ef}}(q)\,(G_c)^{\mathrm{jd}}(q+r+s+t)\,(R_c)^{\mathrm{de}}(q)\,(\Gamma_{cA\bar{c}})^{\mathrm{cgf}}_{\omega}(t,-q-t,q) \\
&\qquad (\Gamma_{\bar{c}AAc})^{bahj}_{\mu\xi}(s,r,q+t,-q-r-s-t) \\
&-\frac{1}{2}\int_q (G_A)^{\mathrm{jd}}_{\zeta\sigma}(q+r+s+t)\,(G_A)^{\mathrm{ef}}_{\tau\upsilon}(q)\,(G_c)^{\mathrm{gh}}(q+r+s)\,(R_A)^{\mathrm{de}}_{\sigma\tau}(q)\,(\Gamma_{cA\bar{c}})^{\mathrm{cjh}}_{\zeta}(t,-q-r-s-t,q+r+s) \\
&\qquad (\Gamma_{\bar{c}AAc})^{bafg}_{\mu\upsilon}(s,r,q,-q-r-s) \\
&+\frac{1}{2}\int_q (G_A)^{\mathrm{jd}}_{\zeta\sigma}(q+r+s+t)\,(G_A)^{\mathrm{ef}}_{\tau\upsilon}(q)\,(G_A)^{\mathrm{gh}}_{\omega\xi}(q+r)\,(R_A)^{\mathrm{de}}_{\sigma\tau}(q)\,(\Gamma_{A3})^{\mathrm{afg}}_{\mu\upsilon\omega}(r,q,-q-r) \\
&\qquad (\Gamma_{c\bar{c}AA})^{cbhj}_{\xi\zeta}(t,s,q+r,-q-r-s-t) \\
&+\frac{1}{2}\int_q (G_A)^{\mathrm{jd}}_{\zeta\sigma}(q+r+s+t)\,(G_A)^{\mathrm{ef}}_{\tau\upsilon}(q)\,(G_A)^{\mathrm{gh}}_{\omega\xi}(q+s+t)\,(R_A)^{\mathrm{de}}_{\sigma\tau}(q)\,(\Gamma_{A3})^{\mathrm{ahj}}_{\mu\xi\zeta}(r,q+s+t,-q-r-s-t) \\
&\qquad (\Gamma_{c\bar{c}AA})^{cbfg}_{\upsilon\omega}(t,s,q,-q-s-t)\,,
\end{aligned}
\tag{A.6}
$$

$$
\begin{aligned}
&D_{\mu}^{cba}(t,s,r) = \\
&+\frac{1}{2}\int_q (G_c)^{\mathrm{ef}}(q)\,(G_c)^{\mathrm{gh}}(q+s+t)\,(G_c)^{\mathrm{jd}}(q+r+s+t)\,(R_c)^{\mathrm{de}}\left(q\,(\Gamma_{cA\bar{c}})_{\mu}^{\mathrm{jah}}(-q-r-s-t,r,q+s+t)\right) \\
&\qquad (\Gamma_{c\bar{c}\bar{c}c})^{cbfg}(t,s,q,-q-s-t) \\
&+\frac{1}{2}\int_q (G_c)^{\mathrm{ef}}(q)\,(G_c)^{\mathrm{gh}}(q+r)\,(G_c)^{\mathrm{jd}}(q+r+s+t)\,(R_c)^{\mathrm{de}}(q)\,(\Gamma_{cA\bar{c}})_{\mu}^{\mathrm{gaf}}(-q-r,r,q) \\
&\qquad (\Gamma_{c\bar{c}\bar{c}c})^{cbhj}(t,s,q+r,-q-r-s-t) \\
&-\frac{1}{2}\int_q (G_c)^{\mathrm{ef}}(q)\,(G_c)^{\mathrm{gh}}(q+s+t)\,(G_c)^{\mathrm{jd}}(q+r+s+t)\,(R_c)^{\mathrm{de}}(q)\,(\Gamma_{cA\bar{c}})_{\mu}^{\mathrm{haj}}(q+s+t,r,-q-r-s-t) \\
&\qquad (\Gamma_{c\bar{c}c\bar{c}})^{cbfg}(t,s,q,-q-s-t) \\
&-\frac{1}{2}\int_q (G_c)^{\mathrm{ef}}(q)\,(G_c)^{\mathrm{gh}}(q+r)\,(G_c)^{\mathrm{jd}}(q+r+s+t)\,(R_c)^{\mathrm{de}}(q)\,(\Gamma_{cA\bar{c}})_{\mu}^{\mathrm{fag}}(q,r,-q-r) \\
&\qquad (\Gamma_{c\bar{c}c\bar{c}})^{cbhj}(t,s,q+r,-q-r-s-t)\,,
\end{aligned}
\tag{A.7}
$$

$$
\begin{aligned}
&E_{\mu}^{cba}(t,s,r) = \\
&-\frac{1}{2}\int_q (G_c)^{\mathrm{ef}}(q)\,(G_c)^{\mathrm{gd}}(q+r+s+t)\,(R_c)^{\mathrm{de}}(q)\,(\Gamma_{c\bar{c}A\bar{c}c})_{\mu}^{cbafg}(t,s,r,q,-q-r-s-t) \\
&+\frac{1}{2}\int_q (G_c)^{\mathrm{ef}}(q)\,(G_c)^{\mathrm{gd}}(q+r+s+t)\,(R_c)^{\mathrm{de}}(q)\,(\Gamma_{c\bar{c}Ac\bar{c}})_{\mu}^{cbafg}(t,s,r,q,-q-r-s-t) \\
&-\frac{1}{2}\int_q (R_A)_{\sigma\tau}^{\mathrm{de}}(q)\,(G_A)_{\tau\upsilon}^{\mathrm{ef}}(q)\,(G_A)_{\omega\sigma}^{\mathrm{gd}}(q+r+s+t)\left(\Gamma_{c\bar{c}A3}\right)_{\mu\upsilon\omega}^{\mathrm{cbafg}}(t,s,r,q,-q-r-s-t)\,.
\end{aligned}
\tag{A.8}
$$

The flow of the three-gluon vertex, fig. (3.10), is given by

$$
\partial_t \left(\Gamma^{(3)}_{A^3}\right)_{\rho\nu\mu}^{cba}(t,s,r) \quad = \quad a_{\rho\nu\mu}^{cba}(t,s,r) + b_{\rho\nu\mu}^{cba}(t,s,r) + c_{\rho\nu\mu}^{cba}(t,s,r) + d_{\rho\nu\mu}^{cba}(t,s,r) + e_{\rho\nu\mu}^{cba}(t,s,r)\,,
\tag{A.9}
$$

with

$$
\begin{aligned}
&a_{\rho\nu\mu}^{cba}(t,s,r) = \\
&-\frac{1}{2}\int_q (R_A)_{\sigma\tau}^{\mathrm{de}}(q)\,(G_A)_{\tau\upsilon}^{\mathrm{ef}}(q)\,(G_A)_{\omega\xi}^{\mathrm{gh}}(q+r)\left(\Gamma_{A3}\right)_{\mu\upsilon\omega}^{\mathrm{afg}}(r,q,-q-r)\,(G_A)_{\zeta\gamma}^{\mathrm{jk}}(q+r+s)\left(\Gamma_{A3}\right)_{\nu\xi\zeta}^{\mathrm{bhj}}(s,q+r,-q-r-s) \\
&\qquad (G_A)_{\delta\sigma}^{\mathrm{ld}}(q+r+s+t)\left(\Gamma_{A3}\right)_{\rho\gamma\delta}^{\mathrm{ckl}}(t,q+r+s,-q-r-s-t) \\
&-\frac{1}{2}\int_q (R_A)_{\sigma\tau}^{\mathrm{de}}(q)\,(G_A)_{\tau\upsilon}^{\mathrm{ef}}(q)\,(G_A)_{\omega\xi}^{\mathrm{gh}}(q+r)\left(\Gamma_{A3}\right)_{\mu\upsilon\omega}^{\mathrm{afg}}(r,q,-q-r)\,(G_A)_{\zeta\gamma}^{\mathrm{jk}}(q+r+t)\left(\Gamma_{A3}\right)_{\rho\xi\zeta}^{\mathrm{chj}}(t,q+r,-q-r-t) \\
&\qquad (G_A)_{\delta\sigma}^{\mathrm{ld}}(q+r+s+t)\left(\Gamma_{A3}\right)_{\nu\gamma\delta}^{\mathrm{bkl}}(s,q+r+t,-q-r-s-t) \\
&-\frac{1}{2}\int_q (R_A)_{\sigma\tau}^{\mathrm{de}}(q)\,(G_A)_{\tau\upsilon}^{\mathrm{ef}}(q)\,(G_A)_{\omega\xi}^{\mathrm{gh}}(q+s)\left(\Gamma_{A3}\right)_{\nu\upsilon\omega}^{\mathrm{bfg}}(s,q,-q-s)\,(G_A)_{\zeta\gamma}^{\mathrm{jk}}(q+r+s)\left(\Gamma_{A3}\right)_{\mu\xi\zeta}^{\mathrm{ahj}}(r,q+s,-q-r-s) \\
&\qquad (G_A)_{\delta\sigma}^{\mathrm{ld}}(q+r+s+t)\left(\Gamma_{A3}\right)_{\rho\gamma\delta}^{\mathrm{ckl}}(t,q+r+s,-q-r-s-t) \\
&-\frac{1}{2}\int_q (R_A)_{\sigma\tau}^{\mathrm{de}}(q)\,(G_A)_{\tau\upsilon}^{\mathrm{ef}}(q)\,(G_A)_{\omega\xi}^{\mathrm{gh}}(q+t)\left(\Gamma_{A3}\right)_{\rho\upsilon\omega}^{\mathrm{cfg}}(t,q,-q-t)\,(G_A)_{\zeta\gamma}^{\mathrm{jk}}(q+r+t)\left(\Gamma_{A3}\right)_{\mu\xi\zeta}^{\mathrm{ahj}}(r,q+t,-q-r-t) \\
&\qquad (G_A)_{\delta\sigma}^{\mathrm{ld}}(q+r+s+t)\left(\Gamma_{A3}\right)_{\nu\gamma\delta}^{\mathrm{bkl}}(s,q+r+t,-q-r-s-t) \\
&-\frac{1}{2}\int_q (R_A)_{\sigma\tau}^{\mathrm{de}}(q)\,(G_A)_{\tau\upsilon}^{\mathrm{ef}}(q)\,(G_A)_{\omega\xi}^{\mathrm{gh}}(q+s)\left(\Gamma_{A3}\right)_{\nu\upsilon\omega}^{\mathrm{bfg}}(s,q,-q-s)\,(G_A)_{\zeta\gamma}^{\mathrm{jk}}(q+s+t)\left(\Gamma_{A3}\right)_{\rho\xi\zeta}^{\mathrm{chj}}(t,q+s,-q-s-t) \\
&\qquad (G_A)_{\delta\sigma}^{\mathrm{ld}}(q+r+s+t)\left(\Gamma_{A3}\right)_{\mu\gamma\delta}^{\mathrm{akl}}(r,q+s+t,-q-r-s-t) \\
&-\frac{1}{2}\int_q (R_A)_{\sigma\tau}^{\mathrm{de}}(q)\,(G_A)_{\tau\upsilon}^{\mathrm{ef}}(q)\,(G_A)_{\omega\xi}^{\mathrm{gh}}(q+t)\left(\Gamma_{A3}\right)_{\rho\upsilon\omega}^{\mathrm{cfg}}(t,q,-q-t)\,(G_A)_{\zeta\gamma}^{\mathrm{jk}}(q+s+t)\left(\Gamma_{A3}\right)_{\nu\xi\zeta}^{\mathrm{bhj}}(s,q+t,-q-s-t) \\
&\qquad (G_A)_{\delta\sigma}^{\mathrm{ld}}(q+r+s+t)\left(\Gamma_{A3}\right)_{\mu\gamma\delta}^{\mathrm{akl}}(r,q+s+t,-q-r-s-t)\,,
\end{aligned}
\tag{A.10}
$$

$$
\begin{aligned}
&b^{cba}_{\rho\nu\mu}(t,s,r) = \\
&-\frac{1}{2}\int_q (R_A)^{\mathrm{de}}_{\sigma\tau}(q)\,(G_A)^{\mathrm{ef}}_{\tau\upsilon}(q)\,(G_A)^{\mathrm{gd}}_{\omega\sigma}(q+r+s+t)\left(\Gamma_{A^5}\right)^{\mathrm{cbafg}}_{\rho\nu\mu\upsilon\omega}(t,s,r,q,-q-r-s-t) \\
&-\frac{1}{2}\int_q (R_c)^{\mathrm{de}}(q)\,(G_c)^{\mathrm{ef}}(q)\,(G_c)^{\mathrm{gd}}(q+r+s+t)\left(\Gamma_{A^3\bar{c}c}\right)^{\mathrm{cbafg}}_{\rho\nu\mu}(t,s,r,q,-q-r-s-t) \\
&+\frac{1}{2}\int_q (R_c)^{\mathrm{de}}(q)\,(G_c)^{\mathrm{ef}}(q)\,(G_c)^{\mathrm{gd}}(q+r+s+t)\left(\Gamma_{A^3c\bar{c}}\right)^{\mathrm{cbafg}}_{\rho\nu\mu}(t,s,r,q,-q-r-s-t)\,,
\end{aligned}
\tag{A.11}
$$

$$
\begin{aligned}
&c^{cba}_{\rho\nu\mu}(t,s,r) = \\
&\frac{1}{2}\int_q (G_c)^{\mathrm{ef}}(q)\,(G_c)^{\mathrm{gh}}(q+t)\,(G_c)^{\mathrm{jk}}(q+s+t)\,(G_c)^{\mathrm{ld}}(q+r+s+t)\,(R_c)^{\mathrm{de}}(q) \\
&\quad (\Gamma_{cA\bar{c}})^{\mathrm{kal}}_{\mu}(q+s+t,r,-q-r-s-t)\,(\Gamma_{cA\bar{c}})^{\mathrm{hbj}}_{\nu}(q+t,s,-q-s-t)\,(\Gamma_{cA\bar{c}})^{\mathrm{fcg}}_{\rho}(q,t,-q-t) \\
&+\frac{1}{2}\int_q (G_c)^{\mathrm{ef}}(q)\,(G_c)^{\mathrm{gh}}(q+t)\,(G_c)^{\mathrm{jk}}(q+r+t)\,(G_c)^{\mathrm{ld}}(q+r+s+t)\,(R_c)^{\mathrm{de}}(q) \\
&\quad (\Gamma_{cA\bar{c}})^{\mathrm{haj}}_{\mu}(q+t,r,-q-r-t)\,(\Gamma_{cA\bar{c}})^{\mathrm{kbl}}_{\nu}(q+r+t,s,-q-r-s-t)\,(\Gamma_{cA\bar{c}})^{\mathrm{fcg}}_{\rho}(q,t,-q-t) \\
&+\frac{1}{2}\int_q (G_c)^{\mathrm{ef}}(q)\,(G_c)^{\mathrm{gh}}(q+t)\,(G_c)^{\mathrm{jk}}(q+s+t)\,(G_c)^{\mathrm{ld}}(q+r+s+t)\,(R_c)^{\mathrm{de}}(q) \\
&\quad (\Gamma_{cA\bar{c}})^{\mathrm{lak}}_{\mu}(-q-r-s-t,r,q+s+t)\,(\Gamma_{cA\bar{c}})^{\mathrm{jbh}}_{\nu}(-q-s-t,s,q+t)\,(\Gamma_{cA\bar{c}})^{\mathrm{gcf}}_{\rho}(-q-t,t,q) \\
&+\frac{1}{2}\int_q (G_c)^{\mathrm{ef}}(q)\,(G_c)^{\mathrm{gh}}(q+t)\,(G_c)^{\mathrm{jk}}(q+r+t)\,(G_c)^{\mathrm{ld}}(q+r+s+t)\,(R_c)^{\mathrm{de}}(q) \\
&\quad (\Gamma_{cA\bar{c}})^{\mathrm{jah}}_{\mu}(-q-r-t,r,q+t)\,(\Gamma_{cA\bar{c}})^{\mathrm{lbk}}_{\nu}(-q-r-s-t,s,q+r+t)\,(\Gamma_{cA\bar{c}})^{\mathrm{gcf}}_{\rho}(-q-t,t,q) \\
&+\frac{1}{2}\int_q (G_c)^{\mathrm{ef}}(q)\,(G_c)^{\mathrm{gh}}(q+r)\,(G_c)^{\mathrm{jk}}(q+r+t)\,(G_c)^{\mathrm{ld}}(q+r+s+t)\,(R_c)^{\mathrm{de}}(q) \\
&\quad (\Gamma_{cA\bar{c}})^{\mathrm{fag}}_{\mu}(q,r,-q-r)\,(\Gamma_{cA\bar{c}})^{\mathrm{kbl}}_{\nu}(q+r+t,s,-q-r-s-t)\,(\Gamma_{cA\bar{c}})^{\mathrm{hcj}}_{\rho}(q+r,t,-q-r-t) \\
&+\frac{1}{2}\int_q (G_c)^{\mathrm{ef}}(q)\,(G_c)^{\mathrm{gh}}(q+s)\,(G_c)^{\mathrm{jk}}(q+s+t)\,(G_c)^{\mathrm{ld}}(q+r+s+t)\,(R_c)^{\mathrm{de}}(q) \\
&\quad (\Gamma_{cA\bar{c}})^{\mathrm{kal}}_{\mu}(q+s+t,r,-q-r-s-t)\,(\Gamma_{cA\bar{c}})^{\mathrm{fbg}}_{\nu}(q,s,-q-s)\,(\Gamma_{cA\bar{c}})^{\mathrm{hcj}}_{\rho}(q+s,t,-q-s-t) \\
&+\frac{1}{2}\int_q (G_c)^{\mathrm{ef}}(q)\,(G_c)^{\mathrm{gh}}(q+r)\,(G_c)^{\mathrm{jk}}(q+r+t)\,(G_c)^{\mathrm{ld}}(q+r+s+t)\,(R_c)^{\mathrm{de}}(q) \\
&\quad (\Gamma_{cA\bar{c}})^{\mathrm{gaf}}_{\mu}(-q-r,r,q)\,(\Gamma_{cA\bar{c}})^{\mathrm{lbk}}_{\nu}(-q-r-s-t,s,q+r+t)\,(\Gamma_{cA\bar{c}})^{\mathrm{jch}}_{\rho}(-q-r-t,t,q+r)\,,
\end{aligned}
\tag{A.12}
$$

$$
\begin{aligned}
&d^{cba}_{\rho\nu\mu}(t,s,r) = \\
&+\frac{1}{2}\int_q (G_c)^{\mathrm{ef}}(q)\,(G_c)^{\mathrm{gh}}(q+s)\,(G_c)^{\mathrm{jk}}(q+s+t)\,(G_c)^{\mathrm{ld}}(q+r+s+t)\,(R_c)^{\mathrm{de}}(q)\,(\Gamma_{cA\bar{c}})^{\mathrm{lak}}_{\mu}(-q-r-s-t,r,q+s+t) \\
&\quad (\Gamma_{cA\bar{c}})^{\mathrm{gbf}}_{\nu}(-q-s,s,q)\,(\Gamma_{cA\bar{c}})^{\mathrm{jch}}_{\rho}(-q-s-t,t,q+s) \\
&+\frac{1}{2}\int_q (G_c)^{\mathrm{ef}}(q)\,(G_c)^{\mathrm{gh}}(q+s)\,(G_c)^{\mathrm{jk}}(q+r+s)\,(G_c)^{\mathrm{ld}}(q+r+s+t)\,(R_c)^{\mathrm{de}}(q)\,(\Gamma_{cA\bar{c}})^{\mathrm{haj}}_{\mu}(q+s,r,-q-r-s) \\
&\quad (\Gamma_{cA\bar{c}})^{\mathrm{fbg}}_{\nu}(q,s,-q-s)\,(\Gamma_{cA\bar{c}})^{\mathrm{kcl}}_{\rho}(q+r+s,t,-q-r-s-t) \\
&+\frac{1}{2}\int_q (G_c)^{\mathrm{ef}}(q)\,(G_c)^{\mathrm{gh}}(q+r)\,(G_c)^{\mathrm{jk}}(q+r+s)\,(G_c)^{\mathrm{ld}}(q+r+s+t)\,(R_c)^{\mathrm{de}}(q)\,(\Gamma_{cA\bar{c}})^{\mathrm{fag}}_{\mu}(q,r,-q-r) \\
&\quad (\Gamma_{cA\bar{c}})^{\mathrm{hbj}}_{\nu}(q+r,s,-q-r-s)\,(\Gamma_{cA\bar{c}})^{\mathrm{kcl}}_{\rho}(q+r+s,t,-q-r-s-t) \\
&+\frac{1}{2}\int_q (G_c)^{\mathrm{ef}}(q)\,(G_c)^{\mathrm{gh}}(q+s)\,(G_c)^{\mathrm{jk}}(q+r+s)\,(G_c)^{\mathrm{ld}}(q+r+s+t)\,(R_c)^{\mathrm{de}}(q)\,(\Gamma_{cA\bar{c}})^{\mathrm{jah}}_{\mu}(-q-r-s,r,q+s) \\
&\quad (\Gamma_{cA\bar{c}})^{\mathrm{gbf}}_{\nu}(-q-s,s,q)\,(\Gamma_{cA\bar{c}})^{\mathrm{lck}}_{\rho}(-q-r-s-t,t,q+r+s) \\
&+\frac{1}{2}\int_q (G_c)^{\mathrm{ef}}(q)\,(G_c)^{\mathrm{gh}}(q+r)\,(G_c)^{\mathrm{jk}}(q+r+s)\,(G_c)^{\mathrm{ld}}(q+r+s+t)\,(R_c)^{\mathrm{de}}(q)\,(\Gamma_{cA\bar{c}})^{\mathrm{gaf}}_{\mu}(-q-r,r,q) \\
&\quad (\Gamma_{cA\bar{c}})^{\mathrm{jbh}}_{\nu}(-q-r-s,s,q+r)\,(\Gamma_{cA\bar{c}})^{\mathrm{lck}}_{\rho}(-q-r-s-t,t,q+r+s)\,,
\end{aligned}
\tag{A.13}
$$

$$
\begin{aligned}
&e^{cba}_{\rho\nu\mu}(t,s,r) = \\
&-\frac{1}{2}\int_q (G_c)^{\mathrm{ef}}(q)\,(G_c)^{\mathrm{gh}}(q+r)\,(G_c)^{\mathrm{jd}}(q+r+s+t)\,(R_c)^{\mathrm{de}}(q)\,(\Gamma_{AAc\bar{c}})^{\mathrm{cbhj}}_{\rho\nu}(t,s,q+r,-q-r-s-t) \\
&\quad (\Gamma_{cA\bar{c}})^{\mathrm{fag}}_{\mu}(q,r,-q-r) \\
&+\frac{1}{2}\int_q (G_c)^{\mathrm{ef}}(q)\,(G_c)^{\mathrm{gh}}(q+r)\,(G_c)^{\mathrm{jd}}(q+r+s+t)\,(R_c)^{\mathrm{de}}(q)\,(\Gamma_{AA\bar{c}c})^{\mathrm{cbhj}}_{\rho\nu}(t,s,q+r,-q-r-s-t) \\
&\quad (\Gamma_{cA\bar{c}})^{\mathrm{gaf}}_{\mu}(-q-r,r,q) \\
&-\frac{1}{2}\int_q (G_c)^{\mathrm{ef}}(q)\,(G_c)^{\mathrm{gh}}(q+s+t)\,(G_c)^{\mathrm{jd}}(q+r+s+t)\,(R_c)^{\mathrm{de}}(q)\,(\Gamma_{AAc\bar{c}})^{\mathrm{cbfg}}_{\rho\nu}(t,s,q,-q-s-t) \\
&\quad (\Gamma_{cA\bar{c}})^{\mathrm{haj}}_{\mu}(q+s+t,r,-q-r-s-t) \\
&+\frac{1}{2}\int_q (G_c)^{\mathrm{ef}}(q)\,(G_c)^{\mathrm{gh}}(q+s+t)\,(G_c)^{\mathrm{jd}}(q+r+s+t)\,(R_c)^{\mathrm{de}}(q)\,(\Gamma_{AA\bar{c}c})^{\mathrm{cbfg}}_{\rho\nu}(t,s,q,-q-s-t) \\
&\quad (\Gamma_{cA\bar{c}})^{\mathrm{jah}}_{\mu}(-q-r-s-t,r,q+s+t) \\
&-\frac{1}{2}\int_q (G_c)^{\mathrm{ef}}(q)\,(G_c)^{\mathrm{gh}}(q+s)\,(G_c)^{\mathrm{jd}}(q+r+s+t)\,(R_c)^{\mathrm{de}}(q)\,(\Gamma_{AAc\bar{c}})^{\mathrm{cahj}}_{\rho\mu}(t,r,q+s,-q-r-s-t) \\
&\quad (\Gamma_{cA\bar{c}})^{\mathrm{fbg}}_{\nu}(q,s,-q-s) \\
&+\frac{1}{2}\int_q (G_c)^{\mathrm{ef}}(q)\,(G_c)^{\mathrm{gh}}(q+s)\,(G_c)^{\mathrm{jd}}(q+r+s+t)\,(R_c)^{\mathrm{de}}(q)\,(\Gamma_{AA\bar{c}c})^{\mathrm{cahj}}_{\rho\mu}(t,r,q+s,-q-r-s-t) \\
&\quad (\Gamma_{cA\bar{c}})^{\mathrm{gbf}}_{\nu}(-q-s,s,q) \\
&-\frac{1}{2}\int_q (G_c)^{\mathrm{ef}}(q)\,(G_c)^{\mathrm{gh}}(q+r+t)\,(G_c)^{\mathrm{jd}}(q+r+s+t)\,(R_c)^{\mathrm{de}}(q)\,(\Gamma_{AAc\bar{c}})^{\mathrm{cafg}}_{\rho\mu}(t,r,q,-q-r-t) \\
&\quad (\Gamma_{cA\bar{c}})^{\mathrm{hbj}}_{\nu}(q+r+t,s,-q-r-s-t) \\
&+\frac{1}{2}\int_q (G_c)^{\mathrm{ef}}(q)\,(G_c)^{\mathrm{gh}}(q+r+t)\,(G_c)^{\mathrm{jd}}(q+r+s+t)\,(R_c)^{\mathrm{de}}(q)\,(\Gamma_{AA\bar{c}c})^{\mathrm{cafg}}_{\rho\mu}(t,r,q,-q-r-t) \\
&\quad (\Gamma_{cA\bar{c}})^{\mathrm{jbh}}_{\nu}(-q-r-s-t,s,q+r+t) \\
&-\frac{1}{2}\int_q (G_c)^{\mathrm{ef}}(q)\,(G_c)^{\mathrm{gh}}(q+t)\,(G_c)^{\mathrm{jd}}(q+r+s+t)\,(R_c)^{\mathrm{de}}(q)\,(\Gamma_{AAc\bar{c}})^{\mathrm{bahj}}_{\nu\mu}(s,r,q+t,-q-r-s-t) \\
&\quad (\Gamma_{cA\bar{c}})^{\mathrm{fcg}}_{\rho}(q,t,-q-t) \\
&+\frac{1}{2}\int_q (G_c)^{\mathrm{ef}}(q)\,(G_c)^{\mathrm{gh}}(q+t)\,(G_c)^{\mathrm{jd}}(q+r+s+t)\,(R_c)^{\mathrm{de}}(q)\,(\Gamma_{AA\bar{c}c})^{\mathrm{bahj}}_{\nu\mu}(s,r,q+t,-q-r-s-t) \\
&\quad (\Gamma_{cA\bar{c}})^{\mathrm{gcf}}_{\rho}(-q-t,t,q) \\
&-\frac{1}{2}\int_q (G_c)^{\mathrm{ef}}(q)\,(G_c)^{\mathrm{gh}}(q+r+s)\,(G_c)^{\mathrm{jd}}(q+r+s+t)\,(R_c)^{\mathrm{de}}(q)\,(\Gamma_{AAc\bar{c}})^{\mathrm{bafg}}_{\nu\mu}(s,r,q,-q-r-s) \\
&\quad (\Gamma_{cA\bar{c}})^{\mathrm{hcj}}_{\rho}(q+r+s,t,-q-r-s-t) \\
&+\frac{1}{2}\int_q (G_c)^{\mathrm{ef}}(q)\,(G_c)^{\mathrm{gh}}(q+r+s)\,(G_c)^{\mathrm{jd}}(q+r+s+t)\,(R_c)^{\mathrm{de}}(q)\,(\Gamma_{AA\bar{c}c})^{\mathrm{bafg}}_{\nu\mu}(s,r,q,-q-r-s) \\
&\quad (\Gamma_{cA\bar{c}})^{\mathrm{jch}}_{\rho}(-q-r-s-t,t,q+r+s)\,.
\end{aligned}
\tag{A.14}
$$

B. Kinematic Configurations for Vertices

In Yang–Mills theory the full computation of vertex functions is a tedious task, due to the complicated tensor structures that arise in the vertices. In principle, the vertex has to be spanned via all possible tensors in the corresponding tensor basis, each of which is modified by quantum and thermal fluctuations. Therefore, for each tensor structure a scalar dressing function would be necessary to describe the full vertex. In addition to that, in the case of non-vanishing temperature the dressing functions would depend on the temporal and spatial components separately.

As a first step, vertices can be approximated in the way that only the classical tensor structure or a subset of tensors is taken into account. Another simplification is to consider special kinematic configurations for the momenta that enter the vertex.

In the thesis the symmetric point is frequently used as a particular kinematic configuration of the vertex with the classical tensor structure. In this appendix the properties of the symmetric point are summarised and the basis that is used is given.

All flow equations in this thesis, also the ones for the vertices, have been generated with the computer algebra tool described in section 3.2.3. By definition in the code all momenta are counted as ingoing. Therefore, also below all momenta are counted as coming into the vertex.

The properties of the symmetric point of three-point functions are

$$p_1^2 = p_2^2 = p_3^2 = P^2 \,, \tag{B.1}$$

$$p_1 \cdot p_2 = p_2 \cdot p_3 = p_3 \cdot p_1 = -\frac{P^2}{2} \,, \tag{B.2}$$

where p_i, $i = 1, 2, 3$ are the external momenta entering the vertex and P is the centre of mass momentum. The first relation expresses that all momenta have the same absolute value. The second relation allows for the first one to be satisfied in a plane by setting an angle of $22\pi/3$ between the momenta.

In this thesis the symmetric point is employed in three dimensions as well as four dimen-

sions. In spherical coordinates an arbitrary vector is given by

$$l^{(3d)} = l \begin{pmatrix} \sin\varphi_1 \cos\varphi_2 \\ \sin\varphi_1 \sin\varphi_2 \\ \cos\varphi_1 \end{pmatrix}, \; l^{(4d)} = l \begin{pmatrix} \sin\phi_1 \sin\phi_2 \cos\phi_3 \\ \sin\phi_1 \sin\phi_2 \sin\phi_3 \\ \sin\phi_1 \cos\phi_2 \\ \cos\phi_1 \end{pmatrix}, \tag{B.3}$$

cf. appendix D.
A possible basis for the external momenta is found by choosing the coordinate system such that $\varphi_2 = \pi/2$ and $\phi_2 = 0$, respectively, which leaves the angles $\pm 2\pi/3$ between the external momenta to be a rotation in φ_1 and ϕ_1 only.
The basis in three dimensions is explicitly given by

$$p_1^{(3d)} = P \begin{pmatrix} 0 \\ 0 \\ 1 \end{pmatrix}, \; p_2^{(3d)} = P \begin{pmatrix} 0 \\ \sqrt{(3)}/2 \\ -1/2 \end{pmatrix}, \; p_3^{(3d)} = P \begin{pmatrix} 0 \\ -\sqrt{(3)}/2 \\ -1/2 \end{pmatrix}, \tag{B.4}$$

and the extension to four dimensions is trivially given by

$$p_1^{(4d)} = P \begin{pmatrix} 0 \\ 0 \\ 0 \\ 1 \end{pmatrix}, \; p_2^{(4d)} = P \begin{pmatrix} 0 \\ 0 \\ \sqrt{(3)}/2 \\ -1/2 \end{pmatrix}, \; p_3^{(4d)} = P \begin{pmatrix} 0 \\ 0 \\ -\sqrt{(3)}/2 \\ -1/2 \end{pmatrix}. \tag{B.5}$$

Due to momentum conservation in the vertex, the relations in eq. (B.2) reduce to constraints for two external momenta only, say p_1 and p_2. Therefore, for contractions with an arbitrary momentum the relations of two basis vectors are sufficient to give the general case.
A loop momentum q in three and four dimensions can be parametrised according to eq. (B.3). As a result, the contractions of an external momentum with the loop momentum are given by

$$\begin{aligned} p_1^{(3d/4d)} \cdot q^{(3d/4d)} &= P\,|q|\,A\,, \\ p_2^{(3d/4d)} \cdot q^{(3d/4d)} &= P\,|q|\,B^{(3d/4d)}\,, \end{aligned} \tag{B.6}$$

with the abbreviations

$$\begin{aligned} A &= \cos\phi_1\,, \\ B^{(3d)} &= \frac{\sqrt{(3)}}{2}\sin\phi_1 \sin\phi_2 - \frac{1}{2}\cos\phi_1\,, \\ B^{(4d)} &= \frac{\sqrt{(3)}}{2}\sin\phi_1 \cos\phi_2 - \frac{1}{2}\cos\phi_1\,. \end{aligned}$$

For the four-point vertices the symmetric point can be chosen in different ways. Reason-

able configurations are either the flat symmetric point, i.e. all momenta have the same absolute value and lie in the same plane with an angle of $\pi/2$, or the real symmetric configuration where the momenta of equal absolute value start in the four corners of a tetraeder. However, this shall not be detailed further as no results for four-point functions are incorporated in this thesis.

C. Chebyshev Polynomials

In numerical calculations for Green functions one has to find a way how to efficiently determine and evaluate dressing functions. These functions are analytic and are thus qualified for a polynomial expansion. In practice a simple power series is often not the optimal choice, as the error is smallest at the expansion point but increases going away from it. Furthermore, the error is not bounded. For a Chebyshev expansion up to order N and decreasing coefficients the error is largest at order $N+1$, where the Chebyshev polynomial is bounded to be $T_{N+1} \leq 1$ and its extrema are distributed over the full expansion interval. That is why Chebyshev polynomials are a good choice for practical purposes, with the drawback that it is a polynomial expansion with the usual problem, e.g. instabilities at the interval boarders may be instable, especially derivatives thereof. For a very extensive discussion of Chebyshev polynomials in non-perturbative functional methods see e.g. the highly recommendable reference [504], a detailed general discussion in numerical applications see [444]. There are two common formulae how to generate the polynomials $T_n(x)$. One is given by the relation

$$T_n(x) = \cos\left(n \arccos x\right), \tag{C.1}$$

whereas the other one is given by the recursion

$$\begin{aligned} T_n(x) &= 2xT_{n-1}(x) - T_{n-2}(x), \quad \text{for } n \geq 2 \\ &\text{with } T_0 = 1,\ T_1 = x\,. \end{aligned} \tag{C.2}$$

The Chebyshev polynomials fulfill both a continuous and a discrete orthogonality relation in the interval $[-1,1]$. The continuous orthogonality relation is given by

$$\int_{-1}^{1} dx \frac{T_i(x)T_j(x)}{\sqrt{1-x^2}} = \begin{cases} 0 & \text{for } i \neq j \\ \frac{\pi}{2} & \text{for } i = i \neq 0 \\ \pi & \text{for } i = i = 0 \end{cases}. \tag{C.3}$$

For the discrete version this boils down to

$$\sum_{k=1}^{N} T_i(x_k)T_j(x_k) = \begin{cases} 0 & \text{for } i \neq j \\ \frac{N}{2} & \text{for } i = i \neq 0 \\ N & \text{for } i = i = 0 \end{cases}. \tag{C.4}$$

The expansion interval is $x \in [-1,1]$, as only there the Chebyshev functions are orthogonal. For expansion in another interval $s \in [a,b]$ one has to map the independent variable s to the interval $[-1,1]$ by

$$x = \frac{1}{2}\left(s\left(b-a\right) + \left(b+a\right)\right). \tag{C.5}$$

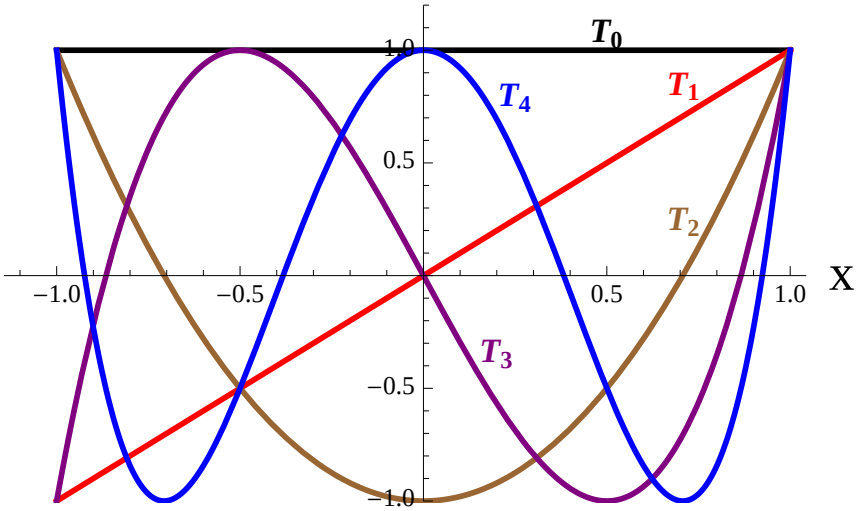

Figure C.1.: Chebyshev polynomials up to order 4.

Naturally, the coefficients c_n of the Chebyshev series contain the information of the fitted function. From eq. (C.1) it is immediately evident that the N zeros of T_n are at

$$x_i = \cos\left(\frac{\pi\,(i-1/2)}{N}\right),\ i = 1,\ldots,N\,. \tag{C.6}$$

Applying the discrete orthogonality relation in eq. (C.4) one can derive a formula for the coeffcients. The expansion shall be exact at the zeros of the Chebyshev polynomials, so expanding a function $f(x)$ up to order N one has at each zero

$$\begin{aligned} f(x_i) &= \sum_{j=0}^{N-1} c_j T_j(x_i) - \frac{c_0}{2} \equiv \sum_{j=0}^{N-1}{}' c_j T_j(x_i) \\ \Rightarrow \sum_{i=1}^{N} T_n(x_i) f(x_i) &= \sum_{j=0}^{N-1}{}' c_j \sum_{i=1}^{N} T_n(x_i) T_j(x_i) = \frac{N}{2} \sum_{j=0}^{N-1}{}' c_j \delta_{nj} = \frac{N}{2} c_n \end{aligned} \tag{C.7}$$

So the coefficients can be easily calculated by

$$c_n = \frac{2}{N} \sum_{i=1}^{N} f(x_i) T_n(x_i). \tag{C.8}$$

Therefore, it is sufficient to know the function value at the positions of the Chebyshev zeros in order to fully expand the function up to order N. As an important remark for technical reasons, note again that the expansion is exact at the zeros of the expansion, therefore, by a sophisticated choice of the expansion interval numerical stability can be maximised. Note, herefore, especially that the density of zeros, i.e. gridpoints is lowest around the middle of the expansion interval and increases going to each end of the interval, as it can already be anticipated from fig. (C.1).
Having the coefficients at hand a fast way to evaluate the function is not to compute the

sum by brute force but to use Clenshaw's recurrence formula [505] instead

$$\begin{aligned} d_{m+1} &= d_m = 0 \\ d_j &= 2xd_{j+1} - d_{j+2} + c_j, \ j = m-1, m-2, \ldots, 1 \\ f(x) &= d_0 = xd_1 - d_2 + \tfrac{1}{2}c_0. \end{aligned} \tag{C.9}$$

As (even indefinite) integrations (differentiations) of polynomials are trivial, Chebyshev expanded functions can be integrated (differentiated) easily, even on the level of the coefficients. The integrated (differentiated) function is then given by Chebyshev coefficients C_n (c'_n) itself, calculable from the N Chebyshev coefficients c_n

$$\begin{aligned} C_n &= \tfrac{c_{n-1}-c_{n+1}}{2n}, \ i > 0 \\ c'_n &= c'_{n+2} + 2nc_{n+1}, \ n = N-2, \ldots, 1 \end{aligned} \tag{C.10}$$

The coefficient C_0 is an integration constant to be determined otherwise, whereas the starting coefficients in the recurrence formula for differentiation are $c'_{N+2} = c'_{N+1} = 0$.
Of course for all standard operations with Chebyshev polynomials numerical functions are available, e.g. in [444].
For applications in the renormalisation group framework the expanded function often does not depend on only one but rather two momentum arguments. For instance the wave-function renormalisation function $Z(p, k, \phi)$ depends in general on the external momentum p, the renormalisation scale k and the field ϕ. Neglecting the field dependence one still has to make an expansion for two variables. For the same reasons as in one dimension Chebyshev polynomials are also a good choice here.
Given a function $f = f(x, y)$ one first expands in x-direction at the Chebyshev zeros in y direction, so at each zero y_j one gets the Chebyshev coefficients c_i in x-direction

$$c_i = \frac{2}{N_x} \sum_{k=1}^{N_x} f(x_k, y_j) T_i(x_k). \tag{C.11}$$

Evaluating the function at the zeros y_j one can determine the (x-dependent) Chebyshev coefficients in y-direction by

$$d_j(x) = \frac{2}{N_y} \sum_{k=1}^{N_y} f(x, y_k) T_j(y_k), \tag{C.12}$$

where one evaluates $f(x, y_k)$ in the usual fashion

$$\begin{aligned} f(x, y_k) &= \sum_{i=1}^{N_x} c_i(y_k) T_i(x), \\ c_i(y_k) &= \frac{2}{N_x} \sum_{l=1}^{N_x} f(x_l, y_k) T_i(x_l). \end{aligned} \tag{C.13}$$

Therefore, there is for each $d_j(x)$

$$d_j(x) = \frac{4}{N_x N_y} \sum_{k=1}^{N_y} \sum_{i,l=1}^{N_x} f(x_l, y_k) T_i(x_l) T_i(x) T_j(y_k). \tag{C.14}$$

And the function evaluation of $f(x, y)$ is thus

$$f(x, y) = \frac{4}{N_x N_y} \sum_{j,k=1}^{N_y} \sum_{i,l=1}^{N_x} f(x_l, y_k) T_i(x_l) T_i(x) T_j(y_k) T_j(y)\,. \tag{C.15}$$

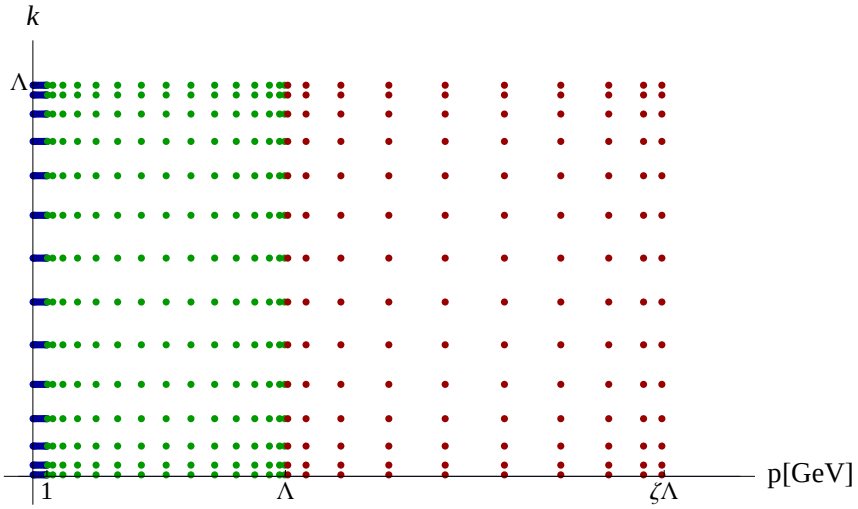

Figure C.2.: Grid for the Chebyshev expansion of the functions in the directions of the external momentum p and the renormalisation group scale k. In the direction of p the grid is divided in three regions, that are shown in the different colours. The regions are adapted such that the behaviour of the functions along the flow is captured in a most efficient way, with the focus on the change in the gluon wave-function renormalisation which changes the most around 1GeV.

For the computation of the propagators and vertices in Yang–Mills theory with the functional renormalisation group there are two variables in the function, the external field momentum p and the renormalisation group scale k. In section 4.1.6 the computational details are sketched, the expansion is done by the help of Chebyshev polynomials in these two dimensions. However, the functions in the direction of p are not very well suited for an expansion over the full momentum interval up to large values, so either a large number of grid points is necessary, or the grid must be divided again. This latter strategy is used for the work presented here, as already shortly sketched in section 4.1.6. The partitioning of the grid that is used (with different numbers of nodes) is given in fig. (C.2), where Λ is the largest renormalisation group scale, see section 3.2. The choice of the value of ζ is detailed in appendix D.3.

D. Numerical Integrations

D.1. Integration Measure

In Euclidean space of dimension d it is convenient to work in hyperspherical coordinates

$$\begin{aligned} q_1 &= q\cos\phi_1 \\ q_2 &= q\sin\phi_1\cos\phi_2 \\ q_3 &= q\sin\phi_1\sin\phi_2\cos\phi_3 \\ &\vdots \\ q_{d-1} &= q\sin\phi_1\sin\phi_2\ldots\sin\phi_{d-2}\cos\phi_{d-1} \\ q_d &= q\sin\phi_1\sin\phi_2\ldots\sin\phi_{d-2}\sin\phi_{d-1}\,. \end{aligned} \tag{D.1}$$

For the integration over the d-dimensional space one has to compute the Jacobian. Abbreviating with

$$\begin{aligned} s_\phi &:= \sin\phi \\ c_\phi &:= \cos\phi \\ s_{\phi_1,\phi_2,\ldots,\phi_n} &:= \sin\phi_1\sin\phi_2\ldots\sin\phi_n \end{aligned}$$

the Jacobian gives

$$\begin{aligned} J &= \frac{\partial(q_1,q_2,\ldots,q_d)}{\partial(q,\phi_1,\phi_2,\ldots,\phi_{d-1})} \\ &= \begin{vmatrix} c_{\phi_1} & -q\,s_{\phi_1} & 0 & 0 & \ldots \\ s_{\phi_1}c_{\phi_2} & q\,c_{\phi_1}c_{\phi_2} & -q\,s_{\phi_1,\phi_2} & 0 & \ldots \\ \vdots & & & & \\ & & & \ddots & \\ & & & & -q\,s_{\phi_1,\ldots,\phi_{d-1}} \\ s_{\phi_1,\ldots,\phi_{d-1}} & q\,c_{\phi_1}s_{\phi_2,\ldots,\phi_4} & q\,c_{\phi_2}s_{\phi_1,\phi_3,\ldots,\phi_{d-1}} & \ldots & q\,s_{\phi_1,\ldots,\phi_{d-2}}c_{\phi_{d-1}} \end{vmatrix} \\ &= q^{d-1}\prod_{i=1}^{d-2}(\sin\phi_i)^{d-1-i}\,. \end{aligned} \tag{D.2}$$

Thus, a d-dimensional momentum integral can be transformed to spherical coordinates as

$$\int_{\mathbb{R}^d}\frac{d^dq}{(2\pi)^d} = \frac{1}{(2\pi)^d}\int_0^\infty dq\int_0^{2\pi}d\phi_{d-1}\int_0^\pi d\phi_{d-2}\int_0^\pi d\phi_{d-3}\ldots\int_0^\pi d\phi_1\;\; q^{d-1}\prod_{i=1}^{d-2}(\sin\phi_i)^{d-1-i} \tag{D.3}$$

Here, mainly integrations in four dimensions are used for applications at zero temperature.

In addition, at non-vanishing temperature for integrations of the spatial subspace the three-dimensional case was employed. Often the integrands are independent of a certain number of angles, as the integration is over the whole space. Then one can choose the coordinate system such that one vector is aligned with one axis. In this case one can perform the trivial angular integral(s) which gives volume factor(s). Some typical relations are

$$\Omega(1) = \int_0^{2\pi} d\phi = 2\pi \tag{D.4}$$

$$\Omega(3) = \int_0^{2\pi} d\phi_2 \int_0^{\pi} d\phi_1 \ \sin\phi_1 = 4\pi \tag{D.5}$$

$$\Omega(4) = \int_0^{2\pi} d\phi_3 \int_0^{\pi} d\phi_2 \int_0^{\pi} d\phi_1 \ \sin^2\phi_1 \sin\phi_2 = 2\pi^2 \tag{D.6}$$

$$\Omega(d) = \frac{2\sqrt{\pi}^{d-1}}{\Gamma\left(\frac{d}{2} - \frac{1}{2}\right)}, \tag{D.7}$$

thus

$$\int \frac{d^3q}{(2\pi)^3} \ f(q) = \frac{1}{2\pi^2} \int_0^{\infty} dq\, q^2 f(q) \tag{D.8}$$

$$\int \frac{d^3q}{(2\pi)^3} \ f(q,\phi_1) = \frac{1}{(2\pi)^2} \int_0^{\infty} dq\, q^2 \int_0^{\pi} d\phi_1 \ \sin\phi_2 f(q,\phi_1) \tag{D.9}$$

$$\int \frac{d^4q}{(2\pi)^4} \ f(q) = \frac{1}{8\pi^2} \int_0^{\infty} dq\, q^3 f(q) \tag{D.10}$$

$$\int \frac{d^4q}{(2\pi)^4} \ f(q,\phi_1) = \frac{1}{4\pi^3} \int_0^{\infty} dq\, q^3 \int_0^{\pi} d\phi_1 \sin^2\phi_1 f(q,\phi_1) \tag{D.11}$$

$$\int \frac{d^4q}{(2\pi)^4} \ f(q,\phi_1,\phi_2) = \frac{1}{(2\pi)^3} \int_0^{\infty} dq\, q^3 \int_0^{\pi} d\phi_1 \int_0^{\pi} d\phi_2 \sin^2\phi_1 \sin\phi_2 f(q,\phi_1,\phi_2) \tag{D.12}$$

Numerical procedures may be instable when the angles in the integrals taken as they are above. In particular, as the angles mainly appear in sine or cosine functions, the integration over the cosine of the angle, $x := \cos\phi$, is potentially superior to the integration over the variable ϕ itself. The transformation yields the relation

$$\begin{aligned} \int_0^{\pi} d\phi \ \sin\phi\, f(\cos\phi) &= \int_{\cos 0}^{\cos\pi} d(\cos\phi) \frac{\partial\cos\phi}{\partial\phi} \sin\phi\, f(\cos\phi) \\ &= \int_1^{-1} dx \ (-f(x)) \\ &= \int_{-1}^{1} dx\, f(x), \end{aligned} \tag{D.13}$$

and similarly with $\sin\phi = \sqrt{1-\cos^2\phi}$

$$\int_0^{\pi} d\phi \ \sin^2\phi\, f(\cos\phi) = \int_{-1}^{1} dx \sqrt{1-x^2}\, f(x). \tag{D.14}$$

However, which procedure is practically better depends on the individual case and can

not be decided generally.

The effects of the temperature T in this thesis are considered via a projection onto purely thermal flows. So schemetically one deals with subtractions of the form $\Delta\partial_t\Gamma = \partial_t\Gamma_T - \partial_t\Gamma_0$. The flows $\partial_t\Gamma_T$, $\partial_t\Gamma_T$ involve loop integrals, however, in the zero temperature case it is a four-dimensional integral whereas at non-vanishing temperature (and in the imaginary time formalism) one deals with the Matsubara sum and the three-dimensional spatial integral. In the numerics it turns out that the numerical cancellation of the flows at scales $k \gg T$ is more accurately implemented if also the $4d$-integral at $T = 0$ is split up into the temporal and spatial integral, respectively, $\int \frac{d^4q}{(2\pi)^4} \to \int \frac{dq_0}{2\pi} \int \frac{d\vec{q}}{(2\pi)^3}$. For the propagators the only Lorentz vectors that appear in the flows are the external momentum p, and the loop momentum q. Their relative relation can be parametrised via one angle ϕ, thus, the loop is written in the form

$$\int_{\mathbb{R}^4} \frac{d^4q}{(2\pi)^4}\, f(p^2, q^2, \cos\phi) \to \frac{1}{(2\pi)^3} \int_{-\infty}^{\infty} dq_0 \int_0^{\infty} d\vec{q}\; \vec{q}^{\,2} \int_{-1}^{1} dx\, \sqrt{1-x^2}\, f(p_0^2, q_0^2, \vec{p}^{\,2}, \vec{q}^{\,2}, x). \tag{D.15}$$

Obviously, the integration takes much longer in this procedure, but the accuracy compensates for this disadvantage.

D.2. Gauss–Legendre Quadrature

There are different methods how to perform the integral of a function numerically. I only discuss the two general ideas that are exploited in this thesis. This section closely follows [444], which is a good reference for a more extensive treatment of numerical integration and numerical methods in general.

The first method is the straightforward way of performing the Riemann sum, see fig. (D.2), i.e. undoing the continuum-limit in the integral formulation and summing up the products of the function values $f(x_i)$ at given nodes x_i times the distance Δx to the next point, therefore, with $N + 1$ being the number of nodes and $x_1 = a$ and $x_{N+1} = b$,

$$\int_a^b f(x)dx \approx \sum_{i=1}^{N} f(x_i)\Delta x\,. \tag{D.16}$$

This is why the methods based on this idea are often referred to as quadratures. However, this can be done in more sophisticated ways that enhance stability and accuracy. For instance, instead of taking the function $f(x_i)$ just at one of the end-points x_i of the small interval of length Δx and approximating the contribution to the integral by a rectangle, the function can be taken at both end-points x_i and x_{i+1} and then averaged over the upper sum and lower sum, see fig. (D.2), thus

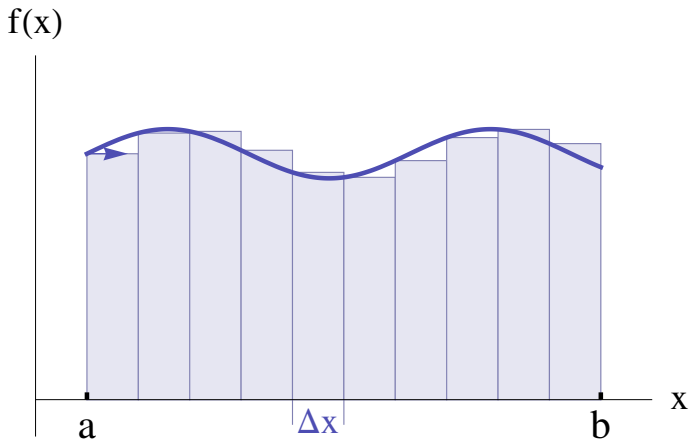

Figure D.1.: Riemann sum to perform the numerical integration.

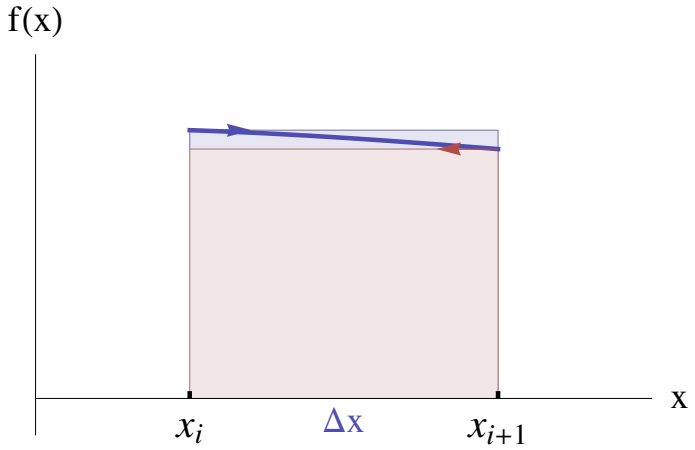

Figure D.2.: Averaged Riemann sum to perform the numerical integration.

$$F_{i,i+1} = \int_{x_i}^{x_{i+1}} f(x)dx \approx \frac{1}{2}\left(f(x_i) + f(x_{i+1})\right)\Delta x\,, \tag{D.17}$$

where $F_{i,i+1}$ is the contribution to the intregral coming from the function $f(x)$ in the interval $x \in [x_i, x_{i+1}]$. In this case, the weighting factor of the two contributions is simply $\frac{1}{2}$. This can be improved further by the help of more general weights.
Another improvement is not to take the grid points equally distanced, but to choose a refined grid which can be chosen such that is particularly suited to the shape of the function $f(x)$ in the integration interval.
Both improvements are employed in the Gauss–Legendre quadrature, which is used in this thesis. The integral of a function $f(x)$ is approximated by

$$\int_a^b dx\, f(x) \approx \sum_{i=1}^{N} \omega_i f(x_i)\,, \tag{D.18}$$

where $f(x_i)$ are the values of the function $f(x)$ at the integration nodes x_i, with $i =$

$1, \ldots, N$ which are the zeros of the Legendre polynomials in the integration interval $[a, b]$, with the weights involving the Legendre polynomials $P_i(x)$

$$\omega_i = \frac{2}{(1 - x_i^2)(P_N'(x_i))^2}. \tag{D.19}$$

Routines for the determination of the abscissas and weights are available as coded functions directly, see e.g. [438, 444].

Another conceptual way that is utilised here is linked to the Chebyshev expansion, see appendix C. The Chebyshev polynomials can be integrated trivially. Therefore, it is often advantageous to expand the integrand itself in terms of Chebyshev polynomials and then apply the general integration prescription for polynomials. Usually, in the loop integrations in Yang–Mills theory this is a good idea because the functions are smooth.

D.3. Integration Range for $4d$-Regulators

Flow equations generically involve the scale derivative of the regulator $\partial_t R_k(q)$, where q is the loop momentum and k is the renormalisation group scale. Over the loop momentum the integral is taken which extends to infinity, in principle. In practical computations, however, it is advantageous to resolve only a smaller grid, that is adapted to the properties of the integrand, i.e. not to integrate in a region in which the integrand is zero within numerical accuracy.
This procedure is particularly easy for $4d$-regulators. At vanishing temperature this is a trivial statement as the integrand simply falls of and is zero for $q^2 > (\zeta k)^2$. For an exponential regulator, which is mainly used in this thesis, the damping of the regulator is proportional to $\sim \exp\left\{-(q/k)^4\right\}$. So for the value of $\zeta = 2.5$ machine precision is reached. Thus, the integration can be cut off at this point.
Fortunately, also for non-vanishing temperature this can be used, however, the damping is then $\sim \exp\left\{-\left(\left(q_0^2 + q_V^2\right)/k^2\right)^2\right\}$, where q_0 is the temporal component and q_V is the absolute value of the spatial momentum. So the different possibilities of the reaching of the region where the integrand falls off must be respected.
Moreover, due to the shape of the derivative of the regulator, the integrand is always peaked around $q_0^2 + q_V^2 \approx k$. So the idea is to split the grid again to resolve the region below and above this peak separately, which brings most accuracy by the same amount of grid points, in particular, if the integrand is expanded in Chebyshev polynomials. It simply guarantees that the peak itself is realised, which is not necessarily satisfied if the regulators are too sharp for the integration grid.

These two ideas result in a integration that is performed in four regions A, B, C_1 and C_2 separately, given in fig. (D.3). These regions are the four integrals on the right hand side

of the transformation

$$\int_{-\infty}^{\infty} dq_0 \int_0^{\infty} dq_V f(q_0, q_V) \rightarrow \mathbf{A} + \mathbf{B} + \mathbf{C_1} + \mathbf{C_2} =$$
$$= \int_{-k}^{k} dq_0 \int_0^{\sqrt{k^2-q_0^2}} dq_V\, f(q_0, q_V) + \int_{-k}^{k} dq_0 \int_{\sqrt{k^2-q_0^2}}^{\sqrt{(\zeta k)^2-q_0^2}} dq_V\, f(q_0, q_V) +$$
$$+ \int_{k}^{\zeta k} dq_0 \int_0^{\sqrt{(\zeta k)^2-q_0^2}} dq_V\, f(q_0, q_V) + \int_{-k}^{-\zeta k} dq_0 \int_0^{\sqrt{(\zeta k)^2-q_0^2}} dq_V\, f(q_0, q_V) \tag{D.20}$$

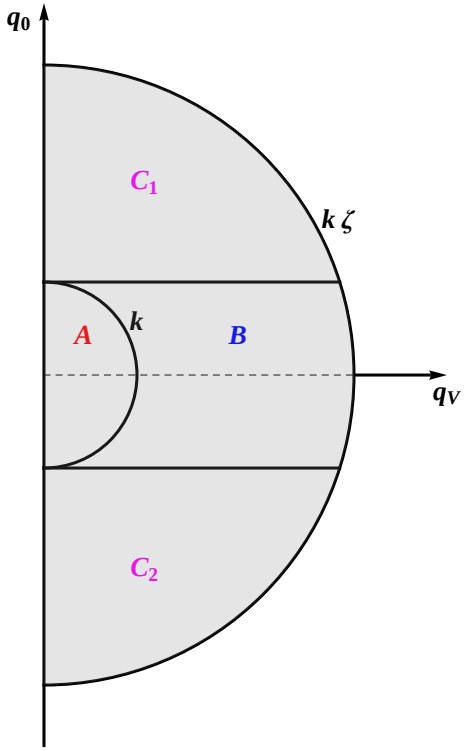

Figure D.3.: Optimised integration ranges at non-vanishing temperature for $4d$-regulators. q_V is the absolute value of the momentum in the spatial subspace, q_0 is the temporal component, which is discretised in the case of non-vanishing temperature.

I want to emphasise that these transformations are exact up to machine precision in the formal way. But on the technical side this transformation constitutes a big improvement by little effort. In the integration of a large but naive region, either the number of nodes in the integration must be increased[1], or the computing time is significantly longer. Note that the number of needed grid point in two dimensions goes quadratically, so already a

[1] In case of a Chebyshev expansion it is even another problem, as polynomial expansions are not well suited for resolving the zero.

doubling of the area would demand four times the computing time.
Furthermore, and this is actually the bigger numerical problem, the form of the integrand is such that it is peaked around $p \approx k$. So performing the integration over the full region at once, the peak structure is hard to resolve by the trivial integration grid, especially in two dimensions.
The gain of the improved grid was tested in some selected cases. Dependent on the number of grid points that is needed to get the same accuracy as in the improved grid, the computing time in the trivial case is higher by a factor of $10^2 - 10^3$ for values $4\text{GeV} < k < 10\text{GeV}$, and rises further for higher k.
To conclude, dividing the integration regions below and above $p = k$ is inevitable for numerical accuracy.

At finite temperature the integration over q_0 becomes a sum. The number of Matsubara modes that are summed are also given by the cut-off, so with $q_0 = 2\pi T n$ the highest mode $N_{\max}$ that numerically contributes is given by

$$N_{\max} = \lfloor \frac{\zeta k}{2\pi T} \rfloor . \tag{D.21}$$

E. Classical Vertices

In this appendix I give the classical Green functions for Yang–Mills theory in the definitions that are used in this thesis. In Landau gauge there are five classical n-point functions, the gluon propagator, the ghost propagator, the three- and four-gluon vertex and the ghost-gluon vertex.
The gluon propagator in Landau gauge is purely transversal, it is given by

$$\left(S^{(2)}_{A^2}\right)^{ab}_{\mu\nu}(p) \;=\; \delta^{ab}\Pi_{\mu\nu}(p)\frac{1}{p^2}\,, \tag{E.1}$$

with the transversal projector $\Pi_{\mu\nu}$ defined in eq. (2.28).
The ghost propagator is given by

$$\left(S^{(2)}_{c\bar{c}}\right)^{ab}_{\mu\nu}(p) \;=\; -\,\delta^{ab}\frac{1}{p^2}\,. \tag{E.2}$$

The three-gluon vertex is given by

$$(S_{A^3})^{abc}_{\mu\nu\rho}(p,q,r) \;=\; igf^{abc}\left[(p-q)_\rho\delta_{\mu\nu}+(q-r)_\mu\delta_{\rho\nu}+(r-p)_\nu\delta_{\mu\rho}\right]\,, \tag{E.3}$$

where all momenta are counted as ingoing.

The four-gluon vertex is given by

$$\begin{aligned}(S_{A^4})^{abcd}_{\mu\nu\rho\sigma}(p,q,r,s) \;=\; & g^2\left\{f^{eab}f^{ecd}\left[\delta_{\mu\rho}\delta_{\nu\sigma}-\delta_{\mu\nu}\delta_{\rho\sigma}\right]+\right.\\ & f^{ebc}f^{ead}\left[\delta_{\mu\nu}\delta_{\rho\sigma}-\delta_{\mu\rho}\delta_{\nu\sigma}\right]+\\ & \left.f^{ebd}f^{eac}\left[\delta_{\mu\nu}\delta_{\rho\sigma}-\delta_{\mu\sigma}\delta_{\nu\rho}\right]\right\}\,.\end{aligned} \tag{E.4}$$

The ghost-gluon vertex is given by

$$(\Gamma_{cA\bar{c}})^{abc}_{\mu}(p;q,r) \;=\; -igf^{abc}r_\mu\,, \tag{E.5}$$

where p is the gluon, q the ghost and r the anti-ghost momentum and all momenta are ingoing.

F. Critical Exponents of Three-Dimensional ϕ^4-Theory from DSEs

In this appendix I present a toy example that shows a method to extract critical exponents from the DSE. This system was partly studied in [470]. These results are not put in the main text as the results are puzzling and not fully understood yet. To get straight to the point: The truncation that is used in this study is supposed to be able to resolve a behaviour that is beyond mean-field, but, nevertheless, the results obtained here show mean-field exponents. The system is numerically intricate and hard to stabilise, but could be controlled in the end in a way that is described below. Albeit numerous tests on the numerics have been made no numerical errors have been found so far. In summary, these results are obtained in the way presented below, nevertheless, from the physics point of view they are to be taken with a grain of salt.

A central issue in the analysis of phase transitions and critical phenomena is the concept of universality. It describes the fact that for continuous phase transitions microscopic details do not have an impact on the critical behaviour of the system at macroscopic scales. Thus, two microscopically different systems can show the same critical behaviour. Therefore, in the vicinity of the phase transition they can be described by the same scaling exponents. By the help of these scaling exponents systems can be grouped into universality classes. One universality class contains all systems that share the same scaling exponent. As a consequence of universality, it suffices to study one representative of each class to learn about the behaviour of all the systems within this class.
In this context $O(N)$-models have turned out to be a very powerful tool to study a plethora of microscopically different physical systems, e.g. polymers, liquid-vapour transition, superfluidity of He^4 as well as ferromagnets and also the QCD phase transition with two massless quark flavors.

The most extensively applied method to study universal properties is the renormalisation group. The renormalisation group has provided illuminating insight into the concept of universality itself and, furthermore, has allowed for calculations of critical universal properties.
The Dyson–Schwinger formalism is an approach that is closely connected to the functional form of the renormalisation group. DSEs are based on the translational invariance of the functional integral. Therefore both, DSEs and FRG equations can directly be derived from it. Both methods are purely non-perturbative approaches. To put it bluntly, DSEs can be seen as integrated FRG equations. Practically, this means that one does not treat

quantum fluctuations sequencially as the FRG does but rather integrates over all of them at once. Due to the connection between these two methods one expects that critical phenomena can be studied within both methods. This serves as the motivation for the study presented here, where critical exponents of ν of ϕ^4-theory in three dimensions are investigated on the level of the DSE.

F.1. $O(N)$ Model

$O(N)$-models are important for the study of phase transitions because within these systems it is convenient to study vaious aspects of spontaneous symmetry breaking. This section is pure textbook knowledge and follows the lines of [477].
For an N-component real massive scalar field the Lagrangian is made up by kinematic and interaction terms for an N-dimensional real vector. The Lagrangian is symmetric under orthogonal transformations in N-dimensions.
In the case of spontaneously broken symmetry, the vacuum expectation value is not invariant under a symmetry which is obeyed by the initial Lagrangian. For the $O(N)$-model this means that the expectation value of the norm of the field no longer vanishes but rather acquires a value proportional to the ratio of the mass and the coupling. Note that only the norm of the N-dimensional vector is constrained, i.e. $(\phi^i)^2 > 0$. So this state is still symmetric under rotations in the $(N-1)$-dimensional subspace. An expansion around the new, true vacuum involves one massive field which describes the radial fluctuation around the vacuum and $N-1$ (massless) Golstone modes.
Here the easiest $O(N)$-model is studied, which is simply the standard ϕ^4-theory. The number of dimensions is three. From renormalisation group studies it is known that ϕ^4-theory in three dimensions, or in general in $d < 4$ dimensions, has another fix point besides the free-field fix point. This non-trivial fix point is called Wilson-Fisher fix point. The critical behaviour is related to that fix point.
For the $O(1)$-model the Lagrangian is symmetric under a sign-flip of the field-value $\phi \to -\phi$. The Lagrangian is given by

$$\mathcal{L}[\phi] = \frac{1}{2}(\partial_\mu \phi)^2 - \frac{1}{2}m^2\phi^2 - \frac{\lambda}{4!}\phi^4. \tag{F.1}$$

Decreasing the mass parameter to negative values $m^2 \to -m^2 \equiv \mu^2$ this symmetry is spontaneously broken, and the vacuum expectation value of the field becomes

$$\langle\phi\rangle = \pm\sqrt{\frac{6}{\lambda}}\mu. \tag{F.2}$$

Around this new minimum in the potential one can make an expansion in a new field. One finds that the Lagrangian for the new field with mass μ^2 contains also cubic and quadratic interactions among itself. The initial symmetry is no longer apparent, it is rather hidden in the new parameters, the effective mass and the coupling constants of the new field, respectively.

F.2. Method

The method itself is based on the generating DSE for the effective action. For the moment, a possible momentum-dependence of the potential is neglected. Approximating the ϕ-propagator and higher n-point functions via their bare expressions, the generating DSE in three (Euclidean) dimensions can be written as

$$\frac{\delta\Gamma}{\delta\Phi} = \frac{\delta S}{\delta\Phi} + \frac{\lambda}{2}\int_p^{3\mathrm{d}} G_p^{(0)}\phi - \frac{\lambda}{3!}\int_{p,q}^{3\mathrm{d}} G_p^{(0)}G_q^{(0)}G_{p+q}^{(0)}V^{(3)}\,, \tag{F.3}$$

having made the abbreviation for the bare propagator $G_p^{(0)} = G^{(0)}(p^2) = \frac{1}{p^2+V''}$ and the loop integrations

$$\int_p^{3\mathrm{d}} = \int_{\mathbb{R}^3}\frac{d^3p}{(2\pi)^3}\,, \quad \text{and} \quad \int_{p,q}^{3\mathrm{d}} = \int_{\mathbb{R}^3}\frac{d^3p}{(2\pi)^3}\int_{\mathbb{R}^3}\frac{d^3q}{(2\pi)^3}\,. \tag{F.4}$$

Furthermore, $\Gamma[\phi]$ is the effective action, $S[\phi]$ the classical action an $V[\phi]$ the effective potential. Note that the second derivative of the potential, $V''[\phi]$, and the fourth derivative $V^{(4)}[\phi]$ with respect to the field ϕ give the effective mass and the effective coupling, respectively, at the given field value. In the following I refer to the first integral expression as the *tadpole*-integral and to the second integral as the *sunset*-integral. The interesting observation in this equation is that the two integral expressions can be solved analytically, as it is evident below. This provides an ordinary differential equation for the effective potential.

The regularisation of the integrals in eq. (F.3) contains two "tricks". Firstly, for the tadpole-integral the mass of the scalar field is split into $\bar{m}^2 = m^2 + \Delta m^2$, with m being the renormalised mass and the counterterm

$$\Delta m^2 = -\frac{\lambda}{2}\int_p^{3\mathrm{d}}\frac{1}{p^2}\,. \tag{F.5}$$

Combining the derivative of the classical action with the tadpole gives

$$\frac{\delta S}{\delta\Phi} + \phi\frac{\lambda}{2}\int_p^{3\mathrm{d}}\frac{1}{p^2+V''} = \frac{1}{2}(p^2+m^2)\phi + \phi\frac{\lambda}{2}\int_p^{3\mathrm{d}}\left(\frac{1}{p^2+V''} - \frac{1}{p^2}\right). \tag{F.6}$$

The latter integral is finite and the evaluation of it gives

$$\phi\frac{\lambda}{2}\int_p^{3\mathrm{d}}\frac{-V''}{p^2(p^2+V'')} = -\phi\frac{\lambda}{8\pi}\sqrt{V''}. \tag{F.7}$$

Secondly, it is also necessary to regularise the other divergent integral in eq. (F.3). The procedure for the sunset-integral involves another trick. Herefore the full expression is divided by $V^{(3)}$ and afterwards a derivative with respect to the field is taken. This acts on each propagator as

$$\frac{\delta}{\delta\phi}G_p^{(0)} = -G_p^{(0)}V^{(3)}G_p^{(0)}. \tag{F.8}$$

With appropriate shifts in the loop momentam, the resulting three expressions are actually identical can sum up trivially to give a combinatorical factor. So speaking casually, taking the derivative w.r.t. ϕ gives a fourth propagator and a factor. Already counting the powers in this integral suggests, that it is finite for non-zero values of V'', and the evaluation of it yields

$$\begin{aligned} -\frac{\lambda}{3!}\frac{\delta}{\delta\phi}\left(\int_{p,q}^{3\mathrm{d}} G_p^{(0)}G_q^{(0)}G_{p+q}^{(0)}\right) &= \frac{\lambda V^{(3)}}{2}\int_{p,q}^{3\mathrm{d}} G_p^{(0)}G_q^{(0)}(G_{p+q}^{(0)})^2 \\ &= \frac{\lambda V^{(3)}}{192\pi V''}. \end{aligned} \tag{F.9}$$

At this point the equation for the effective potential has been rendered finite. It is convenient to rewrite the remaining equation into a total derivative and to carry out one integration over ϕ analytically. This yields an ordinary differential equation for the effective potential

$$-\frac{V'}{V^{(3)}} + \frac{S'}{V^{(3)}} - \frac{\lambda}{8\pi}\phi\frac{\sqrt{V''}}{V^{(3)}} + \lambda\frac{\ln(V'')}{192\pi^2} = c. \tag{F.10}$$

Herein c is the integration constant fixed at a large field value $\Phi_{\text{classical}}$, where quantum fluctuations are suppressed so much that the effective action descends into the classical action. Therefore, the term proportional to $V'(\Phi_{\text{classical}})$ is cancelled by $S'(\Phi_{\text{classical}})$, and c is fixed by the values for the renormalised tadpole and sunset integrals, thus

$$c = -\frac{1}{8\pi}\sqrt{m^2+\frac{\lambda}{2}\Phi_{cl}^2} + \frac{\lambda}{192\pi^2}\ln\left(m^2+\frac{\lambda}{2}\Phi^2_{\text{classical}}\right). \tag{F.11}$$

Solving eq. (F.3) this way is only possible under the assumption of a bare scalar propagator. In contrast to this, for a renormalised propagator these integrals must be solved numerically.

F.3. Numerics

Although eq. (F.10) is an ordinary differential equation, finding a numerical solution is non-trivial. This is mainly due to the sunset term, which involves a product of the third derivative of the effective potential $V^{(3)} \sim \lambda\phi$ with the logarithm of the second derivative $ln(V'') \sim ln(m^2+\lambda\phi^2)$. In the symmetric phase the vacuum expectation value of the field $\langle\phi\rangle$ vanishes, and so does $V^{(3)}$. Directly at the phase transition also the effective mass μ is zero.

Within the region of interest here, i.e. around the phase transition, $V^{(3)}$ and the effective mass of ϕ vanish. So at the phase transition and at the value $\phi = 0$ the solver has to deal with the limit of a vanishing quantity $V^{(3)}(0)$ times a logarithmically divergent term $ln(0)$. Analytically this limit is well-defined and yields zero. But numerically the system becomes very unstable at the phase transition. Thus approaching the point where the symmetry breaking or symmetry restoration sets in (no matter from what phase one approaches) standard solving methods for differential equations fail in integrating the equation over the full range of $\phi\in[0,\Phi_{cl}]$. This interval is chosen such that one starts at $\Phi_{\text{classical}}$, which

is a value of the field chosen such that quantum fluctuations are suppressed. Here the theory is described by the classical action, thus $S[\Phi_{\text{classical}}]$ serves as the initial condition for the differential equation, as described above.
In order to stabilise the system it is possible to choose a matching point ϕ_m in the interval and match a solution that is valid in the upper half of the interval with another one, that is valid in the lower half. This matching point must be chosen such that at ϕ_m both solutions still suffice eq. (F.10) up to a chosen accuracy.
For the solution in the lower half, $V_{ode}[\phi]$, eq. (F.10) is solved, but not starting at the upper bound of the interval, but fix the equation at $\phi = 0$, thus, one imposes the effective values instead of the bare ones. Here a note to the validity of this approach is in order. As a final step, the bare parameters must be mapped onto the effective ones, i.e. in the used here nomenclature $\{m, \lambda\} \to \{\mu, \bar{\lambda}\}$. The differential equation does not depend on the "direction" in which it is solved. Thus it is also a valid approach to assume the evolved parameters and integrate them over the interval to see, which input values would have given these values. For given values of the effective mass μ boundary conditions can be imposed based on the physical properties of the solution: at $\phi = 0$ the first derivative must vanish, since the effective potential has an extremum at this point. Furthermore the second derivative of the effective potential at $\phi = 0$ is the effective mass μ^2. Thus the other boundary conditions is $V'_{ode}[\phi = 0] = 0$ and $V''_{ode}[\phi = 0] = \mu^2$ and eq. (F.10) can be integrated from $\phi = 0$ upwards to ϕ_m. Note that this solution also becomes unstable for too large values of ϕ. Actually, solvers break down at field values, where the system is not described by the classical action yet. Thus this method is not capable of solving eq. (F.10) for the full range $[0, \Phi_{\text{classical}}]$ either. Due to this the point of ϕ_m must be chosen carefully, as the differential equation must be fulfilled up to a high accuracy. In principle this accuracy can be chosen freely, but the result for the critical exponent crucially depends on it, so a high accuracy is inevitable to reasonably extract critical exponent ν.
The upper solution, $V_{it}[\phi]$ is obtained from the non-integrated form of the generating eq. (F.10) via iteration, starting with the classical action $S[\phi]$ in the first iteration step. Thus the nth iteration step is

$$V'_{(n)} = S' - \frac{\lambda}{8\pi}\phi\sqrt{V''_{(n-1)}} + \frac{\lambda V^{(3)}_{(n-1)}}{192\pi^2}\ln\left(V''_{(n-1)}\right), \tag{F.12}$$

wherein the subscripts denote the iteration step, starting with $V'_{(0)} = S'$. Note that this methods also suffers from the instability around $\phi = 0$ at criticality. So solving eq. (F.10) entirely with iteration is not an option either. This issue has to be respected in the choice of ϕ_m too, where both, the solution in the upper half and the solution for the lower half, respectively, must solve the differential eq. (F.10) for the effective potential up to a high accuracy for reasons mentioned above.
The mapping of the classical onto quantum parameters is obtained by varying the input parameters such that the matching conditions are fulfilled. Keep in mind that these input parameters differ for the two types of solutions, as the iteration starts with m and λ, whereas the differential equation needs μ and $\bar{\lambda}$ as input. For the matching there are two

constraints, at ϕ_m the two equations

$$\begin{aligned} V'_{ode}[\phi_m] &\stackrel{!}{=} V'_{it}[\phi_m] \\ V''_{ode}[\phi_m] &\stackrel{!}{=} V''_{it}[\phi_m] \end{aligned} \tag{F.13}$$

must simultaneously be true. In order get the values of m related to the effective mass μ is kept fixed in V_{ode} and m is varied. In V_{it} the coupling λ is kept fixed. So the variation of m and $\bar{\lambda}$ for chosen values of μ and λ is done such that both matching constraints are true. This yields sets of related values of m, μ, λ and $\bar{\lambda}$. In practice this is done on a two-dimensional grid for the varied parameters and with an interpolation of the functions at ϕ_m, because the computing time for the iterated solution is quite high. Fig. (F.1) shows a sketch of the matching procedure.

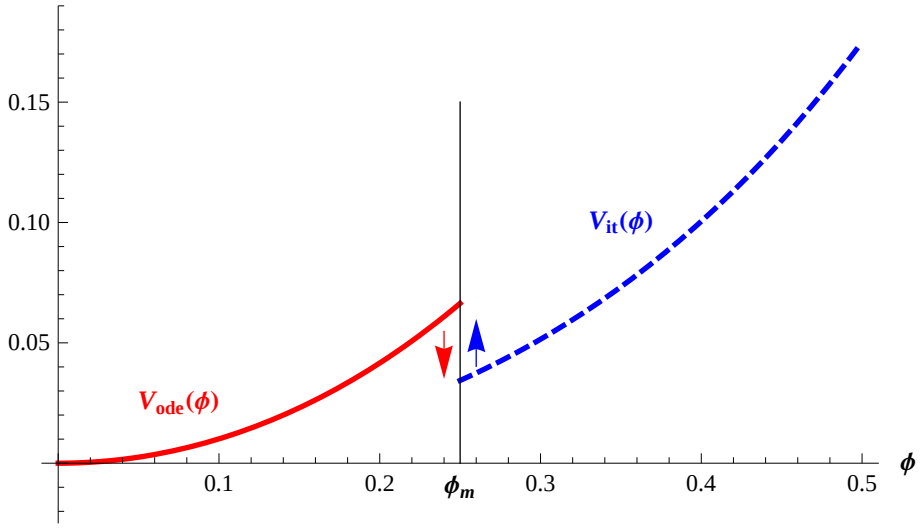

Figure F.1.: Sketch of the matching procedure that is done in order to get a proper map of the input parameters $\{m, \lambda\}$ onto the effective parameters $\{\mu, \bar{\lambda}\}$ (here the parameter-set is chosen arbitrarily).

Note again that in principle there are not two different quantities that describe the phase transition, but rather only one order parameter $\sqrt{m^2/\lambda}$, as described in section F.1. In fig. (F.2) the evolved value $\mu^2/\bar{\lambda}$ of the squared order parameter is plotted against the bare value m^2/λ. In the vicinity of the phase transition the order parameter scales like

$$\sqrt{\frac{\mu^2}{\bar{\lambda}}} \propto |m - m_*|^\nu \,. \tag{F.14}$$

This can be decomposed via

$$\begin{aligned} \frac{\mu^2}{\bar{\lambda}} &\propto \left|\frac{m - m_*}{\lambda}\right|^{2\nu} = \left|\left(\frac{m - m_*}{\lambda}\right)\left(\frac{m + m_*}{\lambda}\right)\right|^\nu \\ &= \tilde{c}\left|\frac{m - m_*}{\lambda}\right|^\nu , \end{aligned} \tag{F.15}$$

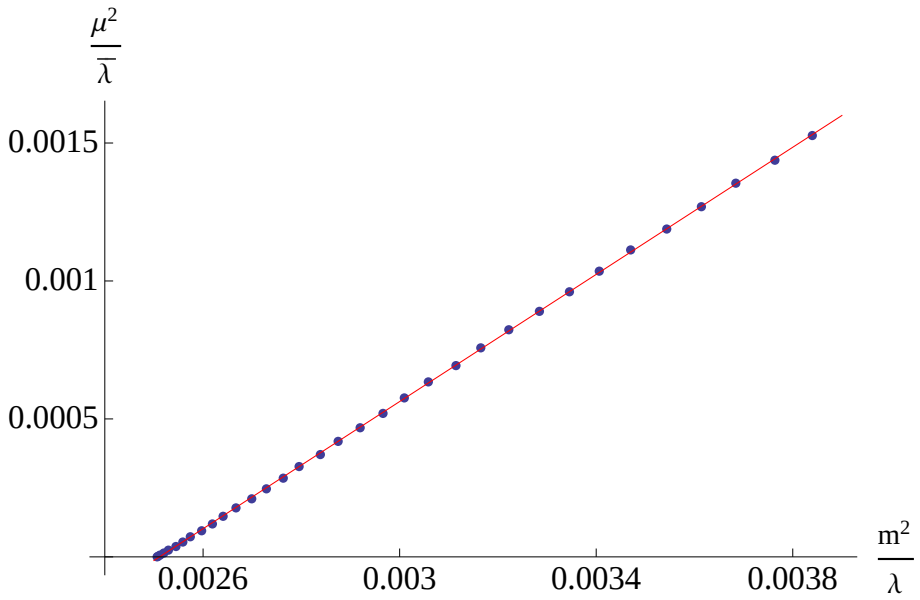

Figure F.2.: Mapping of the bare order parameter onto the effective order parameter. The phase transition is at $\sqrt{\frac{m^2}{\lambda}} \approx 0.051$.

wherein m_* is the value of the mass at the phase transition, and the positive value $m + m_*$ (in the symmetric phase) is absorbed into the constant. This yields a relation from which one can read off the critical exponent of the mapping. The graph shows vanishing curvature, thus it gives the value $\nu \approx 0.5$. So the result of this simple case, where the propagator is taken as bare, yields the mean-field exponent.

F.4. Improving the Scheme

In the preceeding calculation the two-point function is taken as bare. The scheme presented above can be refined by considering the effects of the dressed scalar propagator, so the dressing function $Z(p^2)$ is taken into account that encodes the quantum corrections to the bare propagator. Here, the dressing function is calculated via its DSE, given diagrammatically in fig. (F.3). Note that in the symmetrically broken phase additional diagrams with three-point functions would contribute. For the calculations of such quan-

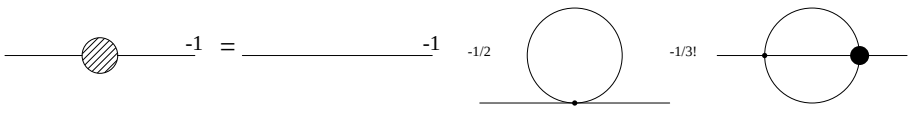

Figure F.3.: Dyson-Schwinger equation for the scalar two-point function in the symmetric phase. Internal propagators are dressed.

tities Chebyshev polynomials have turned out to be a reliable tool, because firstly the included error is smeared out over the total momentum interval, and secondly the point density is highest in the middle of the interval, i.e. where the physics happens, see ap-

pendix C. Thus employing the DSE for the two-point function $Z(p^2)$ can be computed numerically via expanding it in Chebyshev polynomials. Of course the analytical solution of the two integrals in eq. (F.3) is not possible any more, as soon as one plugs the numerical expressions of $Z(p^2)$ into the propagator. Thus the particular contributions from the two integrals in eq. (F.3) must be determined numerically.
From this point on one has to face the same problems that arose already in the approximation in section F.3. Also for a non-trivial dressing function for the scalar propagator the system is unstable around the phase transition. The same stabilisation procedure as in the case with bare propagators is applied here too, i.e. the solution of the differential equation in the lower half of the interval is matched with the solution in the upper half obtained by iteration at intermediate field expectation values. Considering the dressing function this gives that the phase transition is shifted and happens at a higher value of the (bare) order-parameter $\sqrt{m^2/\lambda} \approx 0.054$, see fig. (F.4) for the plot after the first iteration, which is already stable. Surprisingly, the value for the critical exponent is not changed it remains $\nu \sim 0.5$ up to numerical precision. As a result, the critical exponent is still similar to the one obtained in Landau theory.

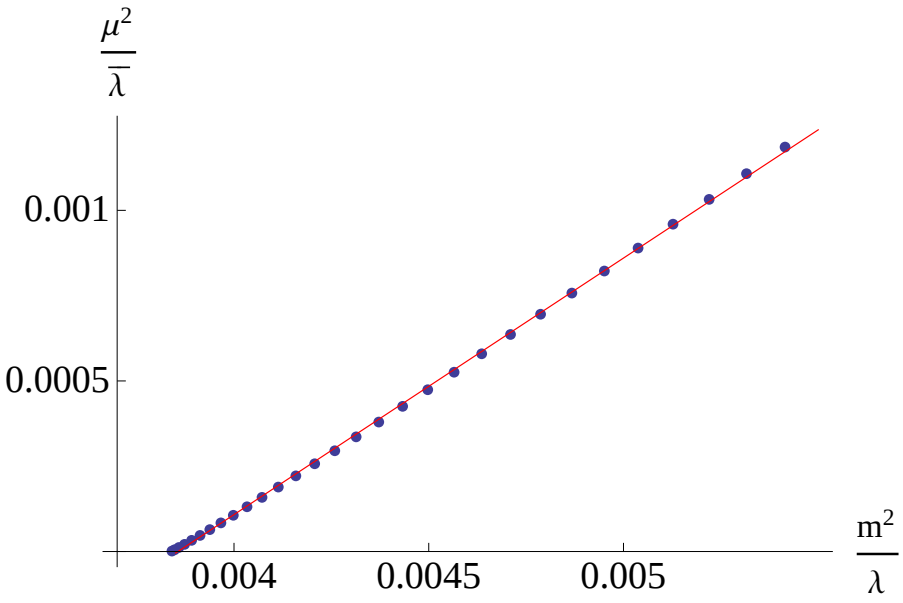

Figure F.4.: Mapping of the bare order parameter onto the effective order parameter under consideration of the dressing function of the scalar propagator.

List of Tables

List of Figures

Acknowledgments

First of all I want to multiply thank Prof. Dr. Jan Pawlowski. I am very grateful for having been able to do my doctoral studies in his research group where I could deal with modern and fundamental aspects of physics. Especially, I thank him for the extraordinarily extensive supervision, for taking a lot of time to share his expertise with me in numerous discussions of my problems and providing always valuable ideas how to proceed. Apart from his expert knowledge, his motivating attitude has made my doctoral studies much easier. In addition to the local supervision, I am grateful for the support concering being given the possibility to participate at many conferences where I could also present my work and for his assistance with respect to applying for postdoc positions.
Furthermore, I am very thankful to Prof. Dr. Michael Schmidt for showing interest in my work and for kindly accepting the laborious task of being the second referee for my thesis.
At this point I finally have the appropriate possibility to thank the people with whom I could collaborate. I thank Jens Braun, Nicolai Christiansen, Christian Fischer, Lisa Haas, Jan Lücker, Florian Marhauser, Sergei Nedelko, Jan Pawlowski, Fabian Rennecke and Andreas Rodigast for the cooperations.
I have enjoyed discussions with many scientists. In particular, I have benefitted from inspirations given by Reinhard Alkofer, Christian Fischer, Axel Maas and Lorenz von Smekal. Furthermore, I appreciate the lattice data that have been provided by Szabolcs Borsanyi, Axel Maas and André Sternbeck.
I am very grateful for various opportunities to present my work to the scientific community. In particular, I want to thank Reinhard Alkofer for the invitation to Graz, Jonivar Skullerud for my visit in Maynooth, Christian Fischer for being given the possibility to talk in Gießen, Lorenz von Smekal for inviting me to Darmstadt, Sergei Nedelko for my stay in Dubna and Andreas Ipp for the opportunity to present this work in Vienna.
Moreover, I have enjoyed the atmosphere at the institute a lot, mainly due to my colleagues: For this I thank Conrad Albrecht, Igor Böttcher, Nicolai Christiansen, Stefan Flörchinger, Naseemuddin Khan, Lisa Haas, Michael Haas, Florian Marhauser, Stephen Mathey, Sergej Moroz, Dorival Goncalves Netto, Boris Nowak, Fabian Rennecke, Andreas Rodigast, David Schnörr, Fabian Spallek, Daniel Spielmann, Martin Trappe and Christian Zielinski.
Decisive contributions have also been made from outside the physics institute, however, words can not fully cover the importance of the following people for the existence of my thesis.
I am deeply thankful to Martina Laura for her love and friendship, her support, understanding and endurance.
In addition, I am truly grateful to my family, my parents Elisabeth and Helfried, my brother Mathis, and my grandparents Karla and Gustav for their support and assistance in all possible ways.
Last but not least I thank the second major source of welcome distraction after Martina Laura, Thomas Nittel for his friendship and numerous cooperations.

Bibliography

[1] M. Gell-Mann, Phys.Rev. **125**, 1067 (1962).

[2] M. Gell-Mann, Phys.Lett. **8**, 214 (1964).

[3] H. Fritzsch, M. Gell-Mann, and H. Leutwyler, Phys.Lett. **B47**, 365 (1973).

[4] Y. Nambu, Phys.Rev. **D10**, 4262 (1974).

[5] W. A. Bardeen and R. Pearson, Phys.Rev. **D14**, 547 (1976).

[6] O. Greenberg, Phys.Rev.Lett. **13**, 598 (1964).

[7] M. Han and Y. Nambu, Phys.Rev. **139**, B1006 (1965).

[8] D. Gross and F. Wilczek, Phys.Rev.Lett. **30**, 1343 (1973).

[9] H. D. Politzer, Phys.Rev.Lett. **30**, 1346 (1973).

[10] C.-N. Yang and R. L. Mills, Phys.Rev. **96**, 191 (1954).

[11] J. Braun, H. Gies, and J. M. Pawlowski, Phys. Lett. **B684**, 262 (2010), 0708.2413.

[12] J. Braun, A. Eichhorn, H. Gies, and J. M. Pawlowski, Eur.Phys.J. **C70**, 689 (2010), 1007.2619.

[13] L. Fister and J. M. Pawlowski, (2011), 1112.5440.

[14] L. Fister and J. M. Pawlowski, (2011), 1112.5429.

[15] S. Hands, Contemp.Phys. **42**, 209 (2001), physics/0105022.

[16] O. Philipsen, Prog.Theor.Phys.Suppl. **174**, 206 (2008), 0808.0672.

[17] J. M. Pawlowski, AIP Conf.Proc. **1343**, 75 (2011), 1012.5075.

[18] K. Fukushima and T. Hatsuda, Rept.Prog.Phys. **74**, 014001 (2011), 1005.4814.

[19] K. Fukushima, J.Phys.G **G39**, 013101 (2012), 1108.2939.

[20] O. Philipsen, (2012), 1207.5999.

[21] P. Braun-Munzinger, K. Redlich, and J. Stachel, (2003), nucl-th/0304013.

[22] STAR Collaboration, J. Adams *et al.*, Nucl.Phys. **A757**, 102 (2005), nucl-ex/0501009.

[23] PHENIX Collaboration, K. Adcox *et al.*, Nucl.Phys. **A757**, 184 (2005), nucl-ex/0410003.

[24] BRAHMS Collaboration, I. Arsene *et al.*, Nucl.Phys. **A757**, 1 (2005), nucl-ex/0410020.

[25] B. Back *et al.*, Nucl.Phys. **A757**, 28 (2005), nucl-ex/0410022.

[26] ALICE Collaboration, K. Aamodt *et al.*, Phys.Rev.Lett. **105**, 252302 (2010), 1011.3914.

[27] B. Muller, J. Schukraft, and B. Wyslouch, (2012), 1202.3233.

[28] M. Cheng *et al.*, Phys.Rev. **D74**, 054507 (2006), hep-lat/0608013.

[29] HotQCD Collaboration, C. E. Detar and R. Gupta, PoS **LAT2007**, 179 (2007), 0710.1655.

[30] F. Karsch, PoS **LAT2007**, 015 (2007), 0711.0661.

[31] RBC Collaboration, HotQCD Collaboration, F. Karsch, J.Phys.G **G35**, 104096 (2008), 0804.4148.

[32] A. Bazavov *et al.*, Phys.Rev. **D80**, 014504 (2009), 0903.4379.

[33] M. Cheng *et al.*, Phys.Rev. **D81**, 054504 (2010), 0911.2215.

[34] Y. Aoki, Z. Fodor, S. Katz, and K. Szabo, Phys.Lett. **B643**, 46 (2006), hep-lat/0609068.

[35] Y. Aoki *et al.*, JHEP **0906**, 088 (2009), 0903.4155.

[36] Y. Aoki, G. Endrodi, Z. Fodor, S. Katz, and K. Szabo, Nature **443**, 675 (2006), hep-lat/0611014.

[37] HotQCD Collaboration, A. Bazavov and P. Petreczky, PoS **LAT2009**, 163 (2009), 0912.5421.

[38] HotQCD collaboration, A. Bazavov and P. Petreczky, J.Phys.Conf.Ser. **230**, 012014 (2010), 1005.1131.

[39] A. Bazavov *et al.*, Phys.Rev. **D85**, 054503 (2012), 1111.1710.

[40] Z. Fodor, PoS **LAT2007**, 011 (2007), 0711.0336.

[41] Wuppertal-Budapest Collaboration, S. Borsanyi *et al.*, JHEP **1009**, 073 (2010), 1005.3508.

[42] S. Borsanyi *et al.*, JHEP **1011**, 077 (2010), 1007.2580.

[43] S. Borsanyi *et al.*, (2012), 1204.6710.

[44] G. Boyd *et al.*, Nucl.Phys. **B469**, 419 (1996), hep-lat/9602007.

[45] J. Engels, J. Fingberg, F. Karsch, D. Miller, and M. Weber, Phys.Lett. **B252**, 625 (1990).

[46] B. Beinlich, F. Karsch, E. Laermann, and A. Peikert, Eur.Phys.J. **C6**, 133 (1999), hep-lat/9707023.

[47] B. Lucini, M. Teper, and U. Wenger, JHEP **01**, 061 (2004), hep-lat/0307017.

[48] B. Lucini, M. Teper, and U. Wenger, JHEP **02**, 033 (2005), hep-lat/0502003.

[49] S. Borsanyi, G. Endrodi, Z. Fodor, S. Katz, and K. Szabo, JHEP **1207**, 056 (2012), 1204.6184.

[50] M. Panero, Phys. Rev. Lett. **103**, 232001 (2009), 0907.3719.

[51] S. Datta and S. Gupta, Phys.Rev. **D80**, 114504 (2009), 0909.5591.

[52] J. Berges and I.-O. Stamatescu, Phys.Rev.Lett. **95**, 202003 (2005), hep-lat/0508030.

[53] J. Berges and D. Sexty, Nucl.Phys. **B799**, 306 (2008), 0708.0779.

[54] G. Parisi and Y.-s. Wu, Sci.Sin. **24**, 483 (1981).

[55] G. Parisi, Nucl.Phys. **B180**, 378 (1981).

[56] G. Parisi, Nucl.Phys. **B205**, 337 (1982).

[57] H. Rothe, World Sci.Lect.Notes Phys. **43**, 1 (1992).

[58] C. Schmidt, PoS **LAT2006**, 021 (2006), hep-lat/0610116.

[59] P. de Forcrand, PoS **LAT2009**, 010 (2009), 1005.0539.

[60] C. Gattringer and C. B. Lang, *Quantum chromodynamics on the lattice* (Lect. Notes Phys., 2010).

[61] F. Karsch, Lect.Notes Phys. **583**, 209 (2002), hep-lat/0106019.

[62] A. M. Ferrenberg and R. H. Swendsen, Phys.Rev.Lett. **63**, 1195 (1989).

[63] I. M. Barbour, S. E. Morrison, E. G. Klepfish, J. B. Kogut, and M.-P. Lombardo, Nucl.Phys.Proc.Suppl. **60A**, 220 (1998), hep-lat/9705042.

[64] Z. Fodor and S. Katz, Phys.Lett. **B534**, 87 (2002), hep-lat/0104001.

[65] Z. Fodor and S. Katz, JHEP **0203**, 014 (2002), hep-lat/0106002.

[66] Z. Fodor and S. Katz, JHEP **0404**, 050 (2004), hep-lat/0402006.

[67] C. Allton *et al.*, Phys.Rev. **D66**, 074507 (2002), hep-lat/0204010.

[68] S. Ejiri *et al.*, Prog.Theor.Phys.Suppl. **153**, 118 (2004), hep-lat/0312006.

[69] R. Gavai and S. Gupta, Phys.Rev. **D71**, 114014 (2005), hep-lat/0412035.

[70] C. Allton *et al.*, Phys.Rev. **D71**, 054508 (2005), hep-lat/0501030.

[71] R. Gavai and S. Gupta, Phys.Rev. **D78**, 114503 (2008), 0806.2233.

[72] P. de Forcrand and O. Philipsen, Nucl.Phys. **B642**, 290 (2002), hep-lat/0205016.

[73] P. de Forcrand and O. Philipsen, Nucl.Phys. **B673**, 170 (2003), hep-lat/0307020.

[74] P. de Forcrand and O. Philipsen, Phys.Rev.Lett. **105**, 152001 (2010), 1004.3144.

[75] O. Philipsen and P. de Forcrand, PoS **LATTICE2010**, 211 (2010), 1011.0291.

[76] M. D'Elia and F. Sanfilippo, Phys.Rev. **D80**, 014502 (2009), 0904.1400.

[77] T. Takaishi, P. de Forcrand, and A. Nakamura, PoS **LAT2009**, 198 (2009), 1002.0890.

[78] A. Nakamura, Phys.Lett. **B149**, 391 (1984).

[79] S. Hands, J. B. Kogut, M.-P. Lombardo, and S. E. Morrison, Nucl.Phys. **B558**, 327 (1999), hep-lat/9902034.

[80] S. Hands *et al.*, Eur.Phys.J. **C17**, 285 (2000), hep-lat/0006018.

[81] S. Hands, I. Montvay, L. Scorzato, and J. Skullerud, Eur.Phys.J. **C22**, 451 (2001), hep-lat/0109029.

[82] S. Muroya, A. Nakamura, and C. Nonaka, Nucl.Phys.Proc.Suppl. **119**, 544 (2003), hep-lat/0208006.

[83] S. Chandrasekharan and F.-J. Jiang, Phys.Rev. **D74**, 014506 (2006), hep-lat/0602031.

[84] S. Hands, S. Kim, and J.-I. Skullerud, Eur.Phys.J. **C48**, 193 (2006), hep-lat/0604004.

[85] S. Hands, S. Kim, and J.-I. Skullerud, Phys.Rev. **D81**, 091502 (2010), 1001.1682.

[86] S. Hands, P. Kenny, S. Kim, and J.-I. Skullerud, Eur.Phys.J. **A47**, 60 (2011), 1101.4961.

[87] S. Hands, S. Kim, and J.-I. Skullerud, Phys.Lett. **B711**, 199 (2012), 1202.4353.

[88] J. Luecker and C. S. Fischer, Prog.Part.Nucl.Phys. **67**, 200 (2012), 1111.0180.

[89] N. Strodthoff, B.-J. Schaefer, and L. von Smekal, Phys.Rev. **D85**, 074007 (2012), 1112.5401.

[90] J. Kogut, M. A. Stephanov, and D. Toublan, Phys.Lett. **B464**, 183 (1999), hep-ph/9906346.

[91] J. Kogut, M. A. Stephanov, D. Toublan, J. Verbaarschot, and A. Zhitnitsky, Nucl.Phys. **B582**, 477 (2000), hep-ph/0001171.

[92] K. Splittorff, D. Son, and M. A. Stephanov, Phys.Rev. **D64**, 016003 (2001), hep-ph/0012274.

[93] K. Splittorff, D. Toublan, and J. Verbaarschot, Nucl.Phys. **B620**, 290 (2002), hep-ph/0108040.

[94] K. Splittorff, D. Toublan, and J. Verbaarschot, Nucl.Phys. **B639**, 524 (2002), hep-ph/0204076.

[95] G. V. Dunne and S. M. Nishigaki, Nucl.Phys. **B654**, 445 (2003), hep-ph/0210219.

[96] G. V. Dunne and S. M. Nishigaki, Nucl.Phys. **B670**, 307 (2003), hep-ph/0306220.

[97] T. Brauner, Mod.Phys.Lett. **A21**, 559 (2006), hep-ph/0601010.

[98] T. Kanazawa, T. Wettig, and N. Yamamoto, JHEP **0908**, 003 (2009), 0906.3579.

[99] T. Kanazawa, T. Wettig, and N. Yamamoto, Phys.Rev. **D81**, 081701 (2010), 0912.4999.

[100] T. Kanazawa, T. Wettig, and N. Yamamoto, JHEP **1112**, 007 (2011), 1110.5858.

[101] L. Kondratyuk, M. Giannini, and M. Krivoruchenko, Phys.Lett. **B269**, 139 (1991).

[102] L. Kondratyuk and M. Krivoruchenko, Z.Phys. **A344**, 99 (1992).

[103] R. Rapp, T. Schafer, E. V. Shuryak, and M. Velkovsky, Phys.Rev.Lett. **81**, 53 (1998), hep-ph/9711396.

[104] C. Ratti and W. Weise, Phys.Rev. **D70**, 054013 (2004), hep-ph/0406159.

[105] G.-f. Sun, L. He, and P. Zhuang, Phys.Rev. **D75**, 096004 (2007), hep-ph/0703159.

[106] T. Brauner, K. Fukushima, and Y. Hidaka, Phys.Rev. **D80**, 074035 (2009), 0907.4905.

[107] J. O. Andersen and T. Brauner, Phys.Rev. **D81**, 096004 (2010), 1001.5168.

[108] M. Harada, C. Nonaka, and T. Yamaoka, Phys.Rev. **D81**, 096003 (2010), 1002.4705.

[109] T. Zhang, T. Brauner, and D. H. Rischke, JHEP **1006**, 064 (2010), 1005.2928.

[110] L. He, Phys.Rev. **D82**, 096003 (2010), 1007.1920.

[111] J. Braun and H. Gies, JHEP **0606**, 024 (2006), hep-ph/0602226.

[112] J. Braun, L. M. Haas, F. Marhauser, and J. M. Pawlowski, Phys.Rev.Lett. **106**, 022002 (2011), 0908.0008.

[113] L. M. Haas, J. Braun, and J. M. Pawlowski, AIP Conf.Proc. **1343**, 459 (2011), 1012.4735.

[114] C. S. Fischer and J. A. Mueller, Phys. Rev. **D80**, 074029 (2009), 0908.0007.

[115] C. S. Fischer, A. Maas, and J. A. Muller, Eur.Phys.J. **C68**, 165 (2010), 1003.1960.

[116] C. S. Fischer, J. Luecker, and J. A. Mueller, Phys.Lett. **B702**, 438 (2011), 1104.1564.

[117] C. S. Fischer and J. Luecker, (2012), 1206.5191.

[118] C. S. Fischer, Phys. Rev. Lett. **103**, 052003 (2009), 0904.2700.

[119] C. Gattringer, Phys. Rev. Lett. **97**, 032003 (2006), hep-lat/0605018.

[120] F. Synatschke, A. Wipf, and C. Wozar, Phys.Rev. **D75**, 114003 (2007), hep-lat/0703018.

[121] E. Bilgici, F. Bruckmann, C. Gattringer, and C. Hagen, Phys.Rev. **D77**, 094007 (2008), 0801.4051.

[122] B. Zhang, F. Bruckmann, C. Gattringer, Z. Fodor, and K. K. Szabo, AIP Conf.Proc. **1343**, 170 (2011), 1012.2314.

[123] Y. Nambu and G. Jona-Lasinio, Phys.Rev. **122**, 345 (1961).

[124] U. Vogl and W. Weise, Prog.Part.Nucl.Phys. **27**, 195 (1991).

[125] T. Hatsuda and T. Kunihiro, Phys.Rept. **247**, 221 (1994), hep-ph/9401310.

[126] P. N. Meisinger and M. C. Ogilvie, Phys.Lett. **B379**, 163 (1996), hep-lat/9512011.

[127] K. Fukushima and K. Ohta, J.Phys.G **G26**, 1397 (2000), hep-ph/0011108.

[128] K. Fukushima, Phys.Rev. **D68**, 045004 (2003), hep-ph/0303225.

[129] K. Fukushima, Phys.Lett. **B591**, 277 (2004), hep-ph/0310121.

[130] A. Dumitru, Y. Hatta, J. Lenaghan, K. Orginos, and R. D. Pisarski, Phys.Rev. **D70**, 034511 (2004), hep-th/0311223.

[131] E. Megias, E. Ruiz Arriola, and L. Salcedo, Phys.Rev. **D74**, 065005 (2006), hep-ph/0412308.

[132] C. Ratti, M. A. Thaler, and W. Weise, Phys.Rev. **D73**, 014019 (2006), hep-ph/0506234.

[133] C. Sasaki, B. Friman, and K. Redlich, Phys.Rev. **D75**, 074013 (2007), hep-ph/0611147.

[134] R. D. Pisarski, Phys.Rev. **D74**, 121703 (2006), hep-ph/0608242.

[135] S. Roessner, C. Ratti, and W. Weise, Phys.Rev. **D75**, 034007 (2007), hep-ph/0609281.

[136] T. Hell, S. Roessner, M. Cristoforetti, and W. Weise, Phys.Rev. **D79**, 014022 (2009), 0810.1099.

[137] T. Hell, S. Rossner, M. Cristoforetti, and W. Weise, Phys.Rev. **D81**, 074034 (2010), 0911.3510.

[138] T. Hell, K. Kashiwa, and W. Weise, Phys.Rev. **D83**, 114008 (2011), 1104.0572.

[139] Y. Sakai, K. Kashiwa, H. Kouno, and M. Yahiro, Phys.Rev. **D77**, 051901 (2008), 0801.0034.

[140] K. Kashiwa, T. Hell, and W. Weise, Phys.Rev. **D84**, 056010 (2011), 1106.5025.

[141] B.-J. Schaefer and J. Wambach, Nucl.Phys. **A757**, 479 (2005), nucl-th/0403039.

[142] B.-J. Schaefer and J. Wambach, Phys.Part.Nucl. **39**, 1025 (2008), hep-ph/0611191.

[143] B.-J. Schaefer, J. M. Pawlowski, and J. Wambach, Phys.Rev. **D76**, 074023 (2007), 0704.3234.

[144] T. K. Herbst, J. M. Pawlowski, and B.-J. Schaefer, Phys.Lett. **B696**, 58 (2011), 1008.0081.

[145] V. Skokov, B. Stokic, B. Friman, and K. Redlich, Phys.Rev. **C82**, 015206 (2010), 1004.2665.

[146] V. Skokov, B. Friman, and K. Redlich, Phys.Rev. **C83**, 054904 (2011), 1008.4570.

[147] K. Morita, V. Skokov, B. Friman, and K. Redlich, Phys.Rev. **D84**, 076009 (2011), 1107.2273.

[148] V. Skokov, Phys.Rev. **D85**, 034026 (2012), 1112.5137.

[149] W. Weise, Prog.Part.Nucl.Phys. **67**, 299 (2012), 1201.0950.

[150] R. Alkofer and J. Greensite, J. Phys. **G34**, S3 (2007), hep-ph/0610365.

[151] R. Hagedorn, Lect.Notes Phys. **221**, 53 (1985).

[152] J. Cleymans and D. Worku, Mod.Phys.Lett. **A26**, 1197 (2011), 1103.1463.

[153] C. Caso *et al.*, Eur. Phys. J. C **3**, 1 (1998).

[154] E. Shuryak, Prog.Part.Nucl.Phys. **62**, 48 (2009), 0807.3033.

[155] T. Schafer and D. Teaney, Rept.Prog.Phys. **72**, 126001 (2009), 0904.3107.

[156] D. A. Teaney, (2009), 0905.2433.

[157] E. Iancu, (2012), 1205.0579.

[158] A. Adams, L. D. Carr, T. Schaefer, P. Steinberg, and J. E. Thomas, (2012), 1205.5180.

[159] P. Steinberg, New J.Phys. **14**, 035006 (2012).

[160] R. Snellings, New J.Phys. **13**, 055008 (2011), 1102.3010.

[161] J. L. Nagle, I. G. Bearden, and W. A. Zajc, New J.Phys. **13**, 075004 (2011), 1102.0680.

[162] Particle Data Group, K. Nakamura *et al.*, J.Phys.G **G37**, 075021 (2010).

[163] M. G. Alford, A. Schmitt, K. Rajagopal, and T. Schafer, Rev.Mod.Phys. **80**, 1455 (2008), 0709.4635.

[164] B. C. Barrois, Nucl.Phys. **B129**, 390 (1977).

[165] H. Heiselberg and M. Hjorth-Jensen, Phys.Rept. **328**, 237 (2000), nucl-th/9902033.

[166] D. Bailin and A. Love, Phys.Rept. **107**, 325 (1984).

[167] K. Rajagopal and F. Wilczek, (2000), hep-ph/0011333.

[168] M. Huang, (2010), 1001.3216.

[169] A. Schmitt, Lect.Notes Phys. **811**, 1 (2010), 1001.3294.

[170] L. McLerran and R. D. Pisarski, Nucl.Phys. **A796**, 83 (2007), 0706.2191.

[171] L. Y. Glozman and R. Wagenbrunn, Mod.Phys.Lett. **A23**, 2385 (2008), 0802.0276.

[172] A. Andronic *et al.*, Nucl.Phys. **A837**, 65 (2010), 0911.4806.

[173] Y. Hidaka, L. D. McLerran, and R. D. Pisarski, Nucl.Phys. **A808**, 117 (2008), 0803.0279.

[174] GSI Darmstadt, URL: `http://www.gsi.de/forschung/fair_experiments/CBM/1intro.html`, 2012 (accessed April 28, 2012).

[175] F. R. Brown *et al.*, Phys.Rev.Lett. **65**, 2491 (1990).

[176] R. D. Pisarski and F. Wilczek, Phys.Rev. **D29**, 338 (1984).

[177] M. Fukugita, M. Okawa, and A. Ukawa, Nucl.Phys. **B337**, 181 (1990).

[178] M. Cheng *et al.*, Phys.Rev. **D77**, 014511 (2008), 0710.0354.

[179] M. Cheng *et al.*, Phys. Rev. **D81**, 054510 (2010), 0911.3450.

[180] C. DeTar and U. Heller, Eur.Phys.J. **A41**, 405 (2009), 0905.2949.

[181] M. Asakawa and K. Yazaki, Nucl.Phys. **A504**, 668 (1989).

[182] A. Barducci, R. Casalbuoni, S. De Curtis, R. Gatto, and G. Pettini, Phys.Lett. **B231**, 463 (1989).

[183] F. Wilczek, Int.J.Mod.Phys. **A7**, 3911 (1992).

[184] J. Berges and K. Rajagopal, Nucl.Phys. **B538**, 215 (1999), hep-ph/9804233.

[185] M. A. Stephanov, K. Rajagopal, and E. V. Shuryak, Phys.Rev.Lett. **81**, 4816 (1998), hep-ph/9806219.

[186] M. A. Stephanov, K. Rajagopal, and E. V. Shuryak, Phys.Rev. **D60**, 114028 (1999), hep-ph/9903292.

[187] J. Greensite, Prog. Part. Nucl. Phys. **51**, 1 (2003), hep-lat/0301023.

[188] R. Alkofer *et al.*, AIP Conf.Proc. **1343**, 17 (2011), 1012.3192.

[189] G. S. Bali, Phys.Rept. **343**, 1 (2001), hep-ph/0001312.

[190] A. M. Polyakov, Phys.Lett. **B72**, 477 (1978).

[191] L. Susskind, Phys.Rev. **D20**, 2610 (1979).

[192] B. Svetitsky and L. G. Yaffe, Nucl.Phys. **B210**, 423 (1982).

[193] B. Svetitsky, Phys.Rept. **132**, 1 (1986).

[194] L. D. McLerran and B. Svetitsky, Phys.Rev. **D24**, 450 (1981).

[195] S. Nadkarni, Phys.Rev. **D33**, 3738 (1986).

[196] S. Nadkarni, Phys.Rev. **D34**, 3904 (1986).

[197] L. Faddeev and V. Popov, Phys.Lett. **B25**, 29 (1967).

[198] C. Becchi, A. Rouet, and R. Stora, Commun.Math.Phys. **42**, 127 (1975).

[199] C. Becchi, A. Rouet, and R. Stora, Annals Phys. **98**, 287 (1976).

[200] I. Tyutin, (1975), 0812.0580.

[201] M. Iofa and I. Tyutin, Teor.Mat.Fiz. **27**, 38 (1976).

[202] D. Zwanziger, Nucl.Phys. **B209**, 336 (1982).

[203] M. A. L. Capri, A. J. Gomez, M. S. Guimaraes, V. E. R. Lemes, and S. P. Sorella, J. Phys. **A43**, 245402 (2010), 1002.1659.

[204] I. M. Singer, Commun. Math. Phys. **60**, 7 (1978).

[205] V. N. Gribov, Nucl. Phys. **B139**, 1 (1978).

[206] N. Vandersickel and D. Zwanziger, (2012), 1202.1491.

[207] D. Zwanziger, Phys. Rev. **D69**, 016002 (2004), hep-ph/0303028.

[208] G. Dell'Antonio and D. Zwanziger, Commun. Math. Phys. **138**, 291 (1991).

[209] G. Dell'Antonio and D. Zwanziger, (1989).

[210] P. van Baal, Nucl.Phys. **B369**, 259 (1992).

[211] P. van Baal, (1997), hep-th/9711070.

[212] T. Kugo and I. Ojima, Prog. Theor. Phys. Suppl. **66**, 1 (1979).

[213] S. N. Gupta, Proc.Phys.Soc. **A63**, 681 (1950).

[214] K. Bleuler, Helv.Phys.Acta **23**, 567 (1950).

[215] N. Alkofer and R. Alkofer, Phys.Lett. **B702**, 158 (2011), 1102.2753.

[216] D. Zwanziger, Nucl. Phys. **B412**, 657 (1994).

[217] D. Zwanziger, Nucl. Phys. **B364**, 127 (1991).

[218] D. Zwanziger, Phys.Rev.Lett. **90**, 102001 (2003), hep-lat/0209105.

[219] A. P. Szczepaniak and E. S. Swanson, Phys.Rev. **D65**, 025012 (2002), hep-ph/0107078.

[220] J. Greensite and S. Olejnik, Phys.Rev. **D67**, 094503 (2003), hep-lat/0302018.

[221] J. Greensite, S. Olejnik, and D. Zwanziger, Phys.Rev. **D69**, 074506 (2004), hep-lat/0401003.

[222] D. Zwanziger, Phys.Rev. **D70**, 094034 (2004), hep-ph/0312254.

[223] C. Feuchter and H. Reinhardt, Phys.Rev. **D70**, 105021 (2004), hep-th/0408236.

[224] A. Nakamura and T. Saito, Prog.Theor.Phys. **115**, 189 (2006), hep-lat/0512042.

[225] J. Greensite and S. Olejnik, Phys.Rev. **D81**, 074504 (2010), 1002.1189.

[226] R. Haag, *Local quantum physics: Fields, particles, algebras* (Springer, Berlin, 1992), Berlin, Germany: Springer (1992) 356 p. (Texts and monographs in physics).

[227] K. Osterwalder and R. Schrader, Commun.Math.Phys. **31**, 83 (1973).

[228] K. Osterwalder and R. Schrader, Commun.Math.Phys. **42**, 281 (1975).

[229] A. Eichhorn, H. Gies, and J. M. Pawlowski, Phys.Rev. **D83**, 045014 (2011), 1010.2153.

[230] S. Mandelstam, Phys. Rev. **D20**, 3223 (1979).

[231] N. Brown and M. Pennington, Phys.Rev. **D39**, 2723 (1989).

[232] A. Hauck, L. von Smekal, and R. Alkofer, Comput.Phys.Commun. **112**, 149 (1998), hep-ph/9604430.

[233] J. E. Mandula and M. Ogilvie, Phys. Lett. **B185**, 127 (1987).

[234] P. Marenzoni, G. Martinelli, and N. Stella, Nucl.Phys. **B455**, 339 (1995), hep-lat/9410011.

[235] P. Marenzoni, G. Martinelli, N. Stella, and M. Testa, Phys.Lett. **B318**, 511 (1993).

[236] C. W. Bernard, C. Parrinello, and A. Soni, Phys.Rev. **D49**, 1585 (1994), hep-lat/9307001.

[237] L. von Smekal, R. Alkofer, and A. Hauck, Phys. Rev. Lett. **79**, 3591 (1997), hep-ph/9705242.

[238] L. von Smekal, A. Hauck, and R. Alkofer, Ann. Phys. **267**, 1 (1998), hep-ph/9707327.

[239] R. Alkofer and L. von Smekal, Phys. Rept. **353**, 281 (2001), hep-ph/0007355.

[240] P. Watson and R. Alkofer, Phys. Rev. Lett. **86**, 5239 (2001), hep-ph/0102332.

[241] C. Lerche and L. von Smekal, Phys. Rev. **D65**, 125006 (2002), hep-ph/0202194.

[242] C. S. Fischer, R. Alkofer, and H. Reinhardt, Phys. Rev. **D65**, 094008 (2002), hep-ph/0202195.

[243] C. S. Fischer and R. Alkofer, Phys. Lett. **B536**, 177 (2002), hep-ph/0202202.

[244] R. Alkofer, C. S. Fischer, and F. J. Llanes-Estrada, Phys. Lett. **B611**, 279 (2005), hep-th/0412330.

[245] W. Schleifenbaum, A. Maas, J. Wambach, and R. Alkofer, Phys. Rev. **D72**, 014017 (2005), hep-ph/0411052.

[246] W. Schleifenbaum, M. Leder, and H. Reinhardt, Phys. Rev. **D73**, 125019 (2006), hep-th/0605115.

[247] C. S. Fischer, J.Phys.G **G32**, R253 (2006), hep-ph/0605173.

[248] C. S. Fischer and J. M. Pawlowski, Phys.Rev. **D75**, 025012 (2007), hep-th/0609009.

[249] C. S. Fischer and J. M. Pawlowski, Phys. Rev. **D80**, 025023 (2009), 0903.2193.

[250] P. Boucaud *et al.*, JHEP **06**, 001 (2006), hep-ph/0604056.

[251] A. Aguilar and J. Papavassiliou, Phys.Rev. **D77**, 125022 (2008), 0712.0780.

[252] D. Binosi and J. Papavassiliou, Phys.Rev. **D77**, 061702 (2008), 0712.2707.

[253] D. Binosi and J. Papavassiliou, Phys. Rept. **479**, 1 (2009), 0909.2536.

[254] R. Alkofer, M. Q. Huber, and K. Schwenzer, Phys.Rev. **D81**, 105010 (2010), 0801.2762.

[255] A. C. Aguilar, D. Binosi, and J. Papavassiliou, Phys. Rev. **D78**, 025010 (2008), 0802.1870.

[256] P. Boucaud *et al.*, JHEP **06**, 012 (2008), 0801.2721.

[257] P. Boucaud *et al.*, JHEP **06**, 099 (2008), 0803.2161.

[258] D. Zwanziger, (2009), 0904.2380.

[259] M. Q. Huber, R. Alkofer, and S. P. Sorella, Phys. Rev. **D81**, 065003 (2010), 0910.5604.

[260] R. Alkofer, C. S. Fischer, M. Q. Huber, F. J. Llanes-Estrada, and K. Schwenzer, PoS **CONFINEMENT8**, 019 (2008), 0812.2896.

[261] M. Q. Huber, (2010), 1005.1775.

[262] L. Fister, (2010), 1002.1649.

[263] L. Fister, R. Alkofer, and K. Schwenzer, Phys.Lett. **B688**, 237 (2010), 1003.1668.

[264] R. Alkofer, L. Fister, A. Maas, and V. Macher, AIP Conf.Proc. **1343**, 179 (2011), 1011.5831.

[265] A. C. Aguilar, D. Binosi, and J. Papavassiliou, Phys. Rev. **D81**, 125025 (2010), 1004.2011.

[266] P. Boucaud *et al.*, Phys.Rev. **D82**, 054007 (2010), 1004.4135.

[267] P. Boucaud *et al.*, (2011), 1109.1936.

[268] M. Hopfer, R. Alkofer, and G. Haase, (2012), 1206.1779.

[269] U. Ellwanger, M. Hirsch, and A. Weber, Z.Phys. **C69**, 687 (1996), hep-th/9506019.

[270] U. Ellwanger, M. Hirsch, and A. Weber, Eur.Phys.J. **C1**, 563 (1998), hep-ph/9606468.

[271] B. Bergerhoff and C. Wetterich, Phys.Rev. **D57**, 1591 (1998), hep-ph/9708425.

[272] J. M. Pawlowski, D. F. Litim, S. Nedelko, and L. von Smekal, Phys. Rev. Lett. **93**, 152002 (2004), hep-th/0312324.

[273] C. S. Fischer and H. Gies, JHEP **10**, 048 (2004), hep-ph/0408089.

[274] J. Pawlowski, D. Litim, S. Nedelko, and L. von Smekal, AIP Conf.Proc. **756**, 278 (2005), hep-th/0412326.

[275] J. Kato, (2004), hep-th/0401068.

[276] C. S. Fischer, A. Maas, and J. M. Pawlowski, Annals Phys. **324**, 2408 (2009), 0810.1987.

[277] D. F. Litim and J. M. Pawlowski, World Sci. , 168 (1999), hep-th/9901063.

[278] J. M. Pawlowski, Annals Phys. **322**, 2831 (2007), hep-th/0512261.

[279] H. Gies, (2006), hep-ph/0611146.

[280] M. Leder, J. M. Pawlowski, H. Reinhardt, and A. Weber, Phys.Rev. **D83**, 025010 (2011), 1006.5710.

[281] A. Weber, (2012), 1205.0491.

[282] D. Zwanziger, Phys. Rev. **D65**, 094039 (2002), hep-th/0109224.

[283] D. Zwanziger, Phys. Rev. **D67**, 105001 (2003), hep-th/0206053.

[284] F. J. Llanes-Estrada and R. Williams, (2012), 1207.5950.

[285] D. Dudal, R. F. Sobreiro, S. P. Sorella, and H. Verschelde, Phys. Rev. **D72**, 014016 (2005), hep-th/0502183.

[286] M. A. L. Capri *et al.*, Eur. Phys. J. **C52**, 459 (2007), 0705.3591.

[287] D. Dudal, J. A. Gracey, S. P. Sorella, N. Vandersickel, and H. Verschelde, Phys. Rev. **D78**, 065047 (2008), 0806.4348.

[288] D. Dudal, S. P. Sorella, and N. Vandersickel, Eur. Phys. J. **C68**, 283 (2010), 1001.3103.

[289] D. Dudal and N. Vandersickel, Phys.Lett. **B700**, 369 (2011), 1010.3927.

[290] D. Dudal, S. Sorella, and N. Vandersickel, Phys.Rev. **D84**, 065039 (2011), 1105.3371.

[291] F. D. Bonnet, P. O. Bowman, D. B. Leinweber, and A. G. Williams, Phys.Rev. **D62**, 051501 (2000), hep-lat/0002020.

[292] F. D. Bonnet, P. O. Bowman, D. B. Leinweber, A. G. Williams, and J. M. Zanotti, Phys.Rev. **D64**, 034501 (2001), hep-lat/0101013.

[293] K. Langfeld, H. Reinhardt, and J. Gattnar, Nucl. Phys. **B621**, 131 (2002), hep-ph/0107141.

[294] J. C. R. Bloch, A. Cucchieri, K. Langfeld, and T. Mendes, Nucl. Phys. **B687**, 76 (2004), hep-lat/0312036.

[295] P. J. Silva and O. Oliveira, Nucl. Phys. **B690**, 177 (2004), hep-lat/0403026.

[296] A. Sternbeck, E. M. Ilgenfritz, M. Müller-Preussker, and A. Schiller, Phys. Rev. **D72**, 014507 (2005), hep-lat/0506007.

[297] I. L. Bogolubsky, G. Burgio, M. Müller-Preussker, and V. K. Mitrjushkin, Phys. Rev. **D74**, 034503 (2006), hep-lat/0511056.

[298] E. M. Ilgenfritz, M. Müller-Preussker, A. Sternbeck, A. Schiller, and I. L. Bogolubsky, Braz. J. Phys. **37**, 193 (2007), hep-lat/0609043.

[299] A. Sternbeck, E. M. Ilgenfritz, M. Muller-Preussker, A. Schiller, and I. L. Bogolubsky, PoS **LAT2006**, 076 (2006), hep-lat/0610053.

[300] A. Sternbeck, *The infrared behavior of lattice QCD Green's functions*, PhD thesis, Humboldt-University Berlin, 2006, hep-lat/0609016.

[301] P. Boucaud *et al.*, (2006), hep-lat/0602006.

[302] A. Cucchieri and T. Mendes, Braz.J.Phys. **37**, 484 (2007), hep-ph/0605224.

[303] A. Cucchieri, T. Mendes, O. Oliveira, and P. Silva, PoS **LAT2007**, 322 (2007), 0710.0344.

[304] A. Cucchieri and T. Mendes, PoS **LAT2007**, 297 (2007), 0710.0412.

[305] A. Cucchieri, A. Maas, and T. Mendes, Phys. Rev. **D75**, 076003 (2007), hep-lat/0702022.

[306] I. Bogolubsky, E. Ilgenfritz, M. Muller-Preussker, and A. Sternbeck, PoS **LAT2007**, 290 (2007), 0710.1968.

[307] I. L. Bogolubsky *et al.*, Phys. Rev. **D77**, 014504 (2008), 0707.3611.

[308] O. Oliveira and P. J. Silva, Eur. Phys. J. **C62**, 525 (2009), 0705.0964.

[309] A. Cucchieri and T. Mendes, Phys. Rev. Lett. **100**, 241601 (2008), 0712.3517.

[310] A. Cucchieri and T. Mendes, Phys. Rev. **D78**, 094503 (2008), 0804.2371.

[311] A. Cucchieri and T. Mendes, PoS **CONFINEMENT8**, 040 (2008), 0812.3261.

[312] A. Cucchieri and T. Mendes, (2008), 0809.2777.

[313] A. Sternbeck and L. von Smekal, Eur.Phys.J. **C68**, 487 (2010), 0811.4300.

[314] I. Bogolubsky *et al.*, (2008), 0804.1250.

[315] V. G. Bornyakov, V. K. Mitrjushkin, and M. Müller-Preussker, Phys. Rev. **D79**, 074504 (2009), 0812.2761.

[316] I. L. Bogolubsky, E. M. Ilgenfritz, M. Müller-Preussker, and A. Sternbeck, Phys. Lett. **B676**, 69 (2009), 0901.0736.

[317] I. Bogolubsky, E.-M. Ilgenfritz, M. Muller-Preussker, and A. Sternbeck, PoS **LAT2009**, 237 (2009), 0912.2249.

[318] V. G. Bornyakov, V. K. Mitrjushkin, and M. Müller-Preussker, Phys. Rev. **D81**, 054503 (2010), 0912.4475.

[319] A. Cucchieri and T. Mendes, Phys. Rev. **D81**, 016005 (2010), 0904.4033.

[320] O. Oliveira and P. Silva, PoS **LAT2009**, 226 (2009), 0910.2897.

[321] O. Oliveira and P. Silva, PoS **QCD-TNT09**, 033 (2009), 0911.1643.

[322] A. Maas, J. M. Pawlowski, D. Spielmann, A. Sternbeck, and L. von Smekal, Eur. Phys. J. **C68**, 183 (2010), 0912.4203.

[323] A. Maas, J. M. Pawlowski, L. von Smekal, and D. Spielmann, Phys.Rev. **D85**, 034037 (2012), 1110.6340.

[324] V. Bornyakov and V. Mitrjushkin, Int.J.Mod.Phys. **A27**, 1250050 (2012), 1103.0442.

[325] R. Aouane *et al.*, Phys.Rev. **D85**, 034501 (2012), 1108.1735.

[326] A. Cucchieri and T. Mendes, PoS **QCD-TNT09**, 026 (2009), 1001.2584.

[327] A. Maas, (2011), 1106.3942.

[328] D. Spielmann, *Aspects of confinement in QCD from lattice simulations*, PhD thesis, Heidelberg Univ., 2010.

[329] A. Cucchieri and T. Mendes, PoS **LATTICE2010**, 280 (2010), 1101.4537.

[330] A. Cucchieri and T. Mendes, PoS **FACESQCD**, 007 (2010), 1105.0176.

[331] A. Cucchieri and T. Mendes, PoS **LATTICE2011**, 206 (2011), 1201.6086.

[332] A. Cucchieri, D. Dudal, T. Mendes, and N. Vandersickel, (2012), 1202.0639.

[333] M. Frasca, Phys.Lett. **B670**, 73 (2008), 0709.2042.

[334] M. Frasca, Nucl.Phys.Proc.Suppl. **186**, 260 (2009), 0807.4299.

[335] M. Frasca, Mod.Phys.Lett. **A24**, 2425 (2009), 0903.2357.

[336] A. Weber, Phys.Rev. **D85**, 125005 (2012), 1112.1157.

[337] M. Tissier and N. Wschebor, Phys.Rev. **D82**, 101701 (2010), 1004.1607.

[338] M. Tissier and N. Wschebor, Phys.Rev. **D84**, 045018 (2011), 1105.2475.

[339] W. J. Marciano and H. Pagels, Phys.Rept. **36**, 137 (1978).

[340] J. C. Taylor, Nucl. Phys. **B33**, 436 (1971).

[341] M. Q. Huber, K. Schwenzer, and R. Alkofer, Eur. Phys. J. **C68**, 581 (2010), 0904.1873.

[342] A. Cucchieri, T. Mendes, and A. Mihara, JHEP **12**, 012 (2004), hep-lat/0408034.

[343] E.-M. Ilgenfritz, M. Muller-Preussker, A. Sternbeck, and A. Schiller, (2006), hep-lat/0601027.

[344] L. von Smekal, (2008), 0812.0654.

[345] K. Kajantie, M. Laine, K. Rummukainen, and Y. Schröder, Phys. Rev. **D67**, 105008 (2003), hep-ph/0211321.

[346] U. Kraemmer and A. Rebhan, Rept.Prog.Phys. **67**, 351 (2004), hep-ph/0310337.

[347] N. Su, Commun.Theor.Phys. **57**, 409 (2012), 1204.0260.

[348] B. M. Kastening, Phys.Rev. **D56**, 8107 (1997), hep-ph/9708219.

[349] T. Hatsuda, Phys.Rev. **D56**, 8111 (1997), hep-ph/9708257.

[350] G. Cvetic and R. Kogerler, Phys.Rev. **D66**, 105009 (2002), hep-ph/0207291.

[351] V. Yukalov and E. Yukalova, (2000), hep-ph/0010028.

[352] R. R. Parwani, Phys.Rev. **D63**, 054014 (2001), hep-ph/0010234.

[353] R. R. Parwani, Phys.Rev. **D64**, 025002 (2001), hep-ph/0010294.

[354] J. Blaizot, E. Iancu, and A. Rebhan, Phys.Rev.Lett. **83**, 2906 (1999), hep-ph/9906340.

[355] J. Blaizot, E. Iancu, and A. Rebhan, Phys.Lett. **B470**, 181 (1999), hep-ph/9910309.

[356] J. Blaizot, E. Iancu, and A. Rebhan, Phys.Rev. **D63**, 065003 (2001), hep-ph/0005003.

[357] J. Blaizot, E. Iancu, and A. Rebhan, Phys.Rev. **D68**, 025011 (2003), hep-ph/0303045.

[358] J. O. Andersen, M. Strickland, and N. Su, JHEP **1008**, 113 (2010), 1005.1603.

[359] J. O. Andersen, L. E. Leganger, M. Strickland, and N. Su, Phys.Lett. **B696**, 468 (2011), 1009.4644.

[360] M. Strickland, J. O. Andersen, L. E. Leganger, and N. Su, Prog.Theor.Phys.Suppl. **187**, 106 (2011), 1011.0416.

[361] J. O. Andersen, L. E. Leganger, M. Strickland, and N. Su, JHEP **1108**, 053 (2011), 1103.2528.

[362] N. Su, (2011), 1104.3450.

[363] K. Fukushima and K. Kashiwa, (2012), 1206.0685.

[364] J. Fingberg, U. M. Heller, and F. Karsch, Nucl.Phys. **B392**, 493 (1993), hep-lat/9208012.

[365] J. Engels, F. Karsch, H. Satz, and I. Montvay, Nucl.Phys. **B205**, 545 (1982).

[366] S. Datta and S. Gupta, Phys.Rev. **D82**, 114505 (2010), 1006.0938.

[367] G. 't Hooft, Nucl.Phys. **B75**, 461 (1974).

[368] J. M. Maldacena, Adv.Theor.Math.Phys. **2**, 231 (1998), hep-th/9711200.

[369] J. Erdmenger, N. Evans, I. Kirsch, and E. Threlfall, Eur.Phys.J. **A35**, 81 (2008), 0711.4467.

[370] W. Pauli, Phys.Rev. **58**, 716 (1940).

[371] K. G. Wilson, Phys.Rev. **B4**, 3174 (1971).

[372] K. G. Wilson, Phys.Rev. **B4**, 3184 (1971).

[373] K. Wilson and J. B. Kogut, Phys.Rept. **12**, 75 (1974).

[374] R. Shankar, Rev.Mod.Phys. **66**, 129 (1994).

[375] C. Bagnuls and C. Bervillier, Phys.Rept. **348**, 91 (2001), hep-th/0002034.

[376] J. Berges, N. Tetradis, and C. Wetterich, Phys.Rept. **363**, 223 (2002), hep-ph/0005122.

[377] J. Polonyi, Central Eur.J.Phys. **1**, 1 (2003), hep-th/0110026.

[378] J. M. Pawlowski, Acta Phys.Slov. **52**, 475 (2002).

[379] S. Bogner, T. Kuo, and A. Schwenk, Phys.Rept. **386**, 1 (2003), nucl-th/0305035.

[380] B. Delamotte, D. Mouhanna, and M. Tissier, Phys.Rev. **B69**, 134413 (2004), cond-mat/0309101.

[381] H. Sonoda, (2007), 0710.1662.

[382] B. Delamotte, (2007), cond-mat/0702365.

[383] S. Bogner, R. Furnstahl, and A. Schwenk, Prog.Part.Nucl.Phys. **65**, 94 (2010), 0912.3688.

[384] S. Diehl, S. Floerchinger, H. Gies, J. Pawlowski, and C. Wetterich, Annalen Phys. **522**, 615 (2010), 0907.2193.

[385] M. Salmhofer, *Renormalization: An Introduction,* Theoretical and Mathematical Physics (Springer, 2010).

[386] M. M. Scherer, S. Floerchinger, and H. Gies, (2010), 1010.2890.

[387] O. J. Rosten, Phys.Rept. **511**, 177 (2012), 1003.1366.

[388] P. Kopietz, L. Bartosch, and F. Schutz, *Introduction to the functional renormalization group* (Lect. Notes Phys., 2010).

[389] W. Metzner, M. Salmhofer, C. Honerkamp, V. Meden, and K. Schonhammer, Rev.Mod.Phys. **84**, 299 (2012), 1105.5289.

[390] J. Braun, J.Phys.G **G39**, 033001 (2012), 1108.4449.

[391] I. Boettcher, J. M. Pawlowski, and S. Diehl, (2012), 1204.4394.

[392] D. F. Litim, Phys. Rev. **D64**, 105007 (2001), hep-th/0103195.

[393] C. Wetterich, Phys.Lett. **B301**, 90 (1993).

[394] J.-P. Blaizot, R. Mendez Galain, and N. Wschebor, Phys.Lett. **B632**, 571 (2006), hep-th/0503103.

[395] J.-P. Blaizot, R. Mendez-Galain, and N. Wschebor, Phys.Rev. **E74**, 051116 (2006), hep-th/0512317.

[396] T. R. Morris, Phys.Lett. **B329**, 241 (1994), hep-ph/9403340.

[397] R. Alkofer, M. Q. Huber, and K. Schwenzer, Comput. Phys. Commun. **180**, 965 (2009), 0808.2939.

[398] M. Q. Huber and J. Braun, Comput.Phys.Commun. **183**, 1290 (2012), 1102.5307.

[399] T. Fischbacher and F. Synatschke-Czerwonka, (2012), 1202.5984.

[400] M. Q. Huber and M. Mitter, Comput.Phys.Commun. **183**, 2441 (2012), 1112.5622.

[401] L. M. Haas, *On the QCD Phase Diagram with the Renormalisation Group*, Heidelberg University, Diploma Thesis, 2008.

[402] R. Mertig, M. Bohm, and A. Denner, Comput.Phys.Commun. **64**, 345 (1991).

[403] Y. Igarashi, K. Itoh, and H. Sonoda, Prog.Theor.Phys.Suppl. **181**, 1 (2010), 0909.0327.

[404] D. Binosi and L. Theussl, Comput.Phys.Commun. **161**, 76 (2004), hep-ph/0309015.

[405] U. Ellwanger, Phys. Lett. **B335**, 364 (1994), hep-th/9402077.

[406] F. Freire, D. Litim, and J. Pawlowski, Int.J.Mod.Phys. **A16**, 2035 (2001), hep-th/0101108.

[407] D. F. Litim and J. M. Pawlowski, JHEP **0611**, 026 (2006), hep-th/0609122.

[408] M. Bonini, M. D'Attanasio, and G. Marchesini, Nucl.Phys. **B421**, 429 (1994), hep-th/9312114.

[409] M. D'Attanasio and T. R. Morris, Phys.Lett. **B378**, 213 (1996), hep-th/9602156.

[410] D. F. Litim and J. M. Pawlowski, Phys.Lett. **B435**, 181 (1998), hep-th/9802064.

[411] Y. Igarashi, K. Itoh, and H. So, JHEP **0110**, 032 (2001), hep-th/0109202.

[412] T. R. Morris and O. J. Rosten, J.Phys.A **A39**, 11657 (2006), hep-th/0606189.

[413] O. J. Rosten, Int.J.Mod.Phys. **A21**, 4627 (2006), hep-th/0602229.

[414] O. J. Rosten, Phys.Lett. **B645**, 466 (2007), hep-th/0611323.

[415] J. M. Pawlowski, (2003), hep-th/0310018.

[416] V. Branchina, K. A. Meissner, and G. Veneziano, Phys.Lett. **B574**, 319 (2003), hep-th/0309234.

[417] M. Reuter and C. Wetterich, Nucl.Phys. **B417**, 181 (1994).

[418] M. Reuter and C. Wetterich, Phys.Rev. **D56**, 7893 (1997), hep-th/9708051.

[419] S. Tan, Annals Phys. **323**, 2952 (2008), cond-mat/0505200.

[420] S. Tan, Annals Phys. **323**, 2971 (2008), cond-mat/0508320.

[421] S. Tan, Annals Phys. **323**, 2987 (2008), 0803.0841.

[422] J.-P. Blaizot, A. Ipp, R. Mendez-Galain, and N. Wschebor, Nucl.Phys. **A784**, 376 (2007), hep-ph/0610004.

[423] J. Braun, Phys.Rev. **D81**, 016008 (2010), 0908.1543.

[424] F. Dyson, Phys.Rev. **75**, 1736 (1949).

[425] J. S. Schwinger, Proc.Nat.Acad.Sci. **37**, 452 (1951).

[426] J. S. Schwinger, Proc.Nat.Acad.Sci. **37**, 455 (1951).

[427] R. Rivers, *Path Integral Methods in Quantum Field Theory*Cambridge Monographs on Mathematical Physics (Cambridge University Press, 1988).

[428] C. Kellermann and C. S. Fischer, Phys. Rev. **D78**, 025015 (2008), 0801.2697.

[429] A. Maas, J. Wambach, and R. Alkofer, Eur. Phys. J. **C42**, 93 (2005), hep-ph/0504019.

[430] M. Le Bellac, *Thermal field theory,* Cambridge monographs on mathematical physics (Cambridge Univ. Press, Cambridge, 1996).

[431] M. Q. Huber, A. Maas, and L. von Smekal, (2012), 1207.0222.

[432] D. Dudal, O. Oliveira, and J. Rodriguez-Quintero, (2012), 1207.5118.

[433] J. Braun and H. Gies, Phys. Lett. **B645**, 53 (2007), hep-ph/0512085.

[434] A. Maas, Phys. Rev. **D75**, 116004 (2007), 0704.0722.

[435] C. Itzykson and J. B. Zuber, *Quantum field theory* (McGraw-Hill International Book Co., New York, 1980).

[436] J. S. Ball and T.-W. Chiu, Phys. Rev. **D22**, 2550 (1980).

[437] J. M. Cornwall and J. Papavassiliou, Phys.Rev. **D40**, 3474 (1989).

[438] GSL Project Contributors, GSL - GNU scientific library - GNU project - free software foundation (FSF), http://www.gnu.org/software/gsl/, 2010.

[439] Wolfram Research, Inc., *Mathematica Edition: Version 7.0* (Wolfram Research, Inc., Champaign, Illinois, 2008).

[440] S. Wolfram, *The Mathematica book (5. ed.)* (Wolfram-Media, 2003).

[441] J. Vermaseren, (2000), math-ph/0010025.

[442] T. van Ritbergen, A. Schellekens, and J. Vermaseren, Int.J.Mod.Phys. **A14**, 41 (1999), hep-ph/9802376.

[443] M. Jamin and M. E. Lautenbacher, Comput.Phys.Commun. **74**, 265 (1993).

[444] W. H. Press, S. A. Teukolsky, W. T. Vetterling, and B. P. Flannery, *Numerical Recipes 3rd Edition: The Art of Scientific Computing*, 3 ed. (Cambridge University Press, New York, NY, USA, 2007).

[445] A. Cucchieri, F. Karsch, and P. Petreczky, Phys.Rev. **D64**, 036001 (2001), hep-lat/0103009.

[446] A. Maas, private communication (2011).

[447] J.-P. Blaizot, A. Ipp, and N. Wschebor, Nucl.Phys. **A849**, 165 (2011), 1007.0991.

[448] K. Fukushima and K. Kashiwa, (2012), 1206.0685.

[449] N. Tetradis and C. Wetterich, Nucl.Phys. **B398**, 659 (1993).

[450] S.-B. Liao and M. Strickland, Phys.Rev. **D52**, 3653 (1995), hep-th/9501137.

[451] M. D'Attanasio and M. Pietroni, Nucl.Phys. **B472**, 711 (1996), hep-ph/9601375.

[452] M. D'Attanasio and M. Pietroni, Nucl.Phys. **B498**, 443 (1997), hep-th/9611038.

[453] D. Comelli and M. Pietroni, Phys.Lett. **B417**, 337 (1998), hep-ph/9708489.

[454] B. Bergerhoff and J. Reingruber, Phys.Rev. **D60**, 105036 (1999), hep-ph/9809251.

[455] D. F. Litim, (1998), hep-ph/9811272.

[456] J. O. Andersen and M. Strickland, Phys.Rev. **A60**, 1442 (1999), cond-mat/9811096.

[457] B.-J. Schaefer and H.-J. Pirner, Nucl.Phys. **A660**, 439 (1999), nucl-th/9903003.

[458] F. Freire and D. F. Litim, Phys.Rev. **D64**, 045014 (2001), hep-ph/0002153.

[459] C. Honerkamp and M. Salmhofer, Phys. Rev. B **64**, 184516 (2001).

[460] T. Baier, E. Bick, and C. Wetterich, (2003), cond-mat/0309715.

[461] J. Braun, K. Schwenzer, and H.-J. Pirner, Phys.Rev. **D70**, 085016 (2004), hep-ph/0312277.

[462] J.-P. Blaizot, R. Mendez Galain, and N. Wschebor, Europhys.Lett. **72**, 705 (2005), cond-mat/0412481.

[463] B.-J. Schaefer and J. Wambach, Phys.Rev. **D75**, 085015 (2007), hep-ph/0603256.

[464] S. Diehl, H. Gies, J. Pawlowski, and C. Wetterich, Phys.Rev. **A76**, 021602 (2007), cond-mat/0701198.

[465] F. Marhauser and J. M. Pawlowski, (2008), 0812.1144.

[466] A. Eichhorn, (2011), 1111.1237.

[467] D. Zwanziger, Nucl.Phys. **B518**, 237 (1998).

[468] R. Alkofer, C. S. Fischer, and F. J. Llanes-Estrada, Mod.Phys.Lett. **A23**, 1105 (2008), hep-ph/0607293.

[469] D. Epple, H. Reinhardt, and W. Schleifenbaum, Phys. Rev. **D75**, 045011 (2007), hep-th/0612241.

[470] M. F. Marhauser, *Confinement in Polyakov Gauge and the QCD Phase Diagram*, PhD thesis, Heidelberg University, 2009.

[471] H. Reinhardt, Nucl.Phys. **B503**, 505 (1997), hep-th/9702049.

[472] L. Abbott, Nucl.Phys. **B185**, 189 (1981).

[473] W. Dittrich and M. Reuter, Lect.Notes Phys. **244**, 1 (1986).

[474] J. Berges, S. Borsanyi, U. Reinosa, and J. Serreau, Annals Phys. **320**, 344 (2005), hep-ph/0503240.

[475] N. Weiss, Phys.Rev. **D24**, 475 (1981).

[476] D. J. Gross, R. D. Pisarski, and L. G. Yaffe, Rev.Mod.Phys. **53**, 43 (1981).

[477] M. E. Peskin and D. V. Schroeder, *An Introduction to quantum field theory* (Addison-Wesley, Reading, 1995).

[478] O. Kaczmarek, F. Karsch, P. Petreczky, and F. Zantow, Phys.Lett. **B543**, 41 (2002), hep-lat/0207002.

[479] C. S. Fischer and R. Alkofer, Phys. Rev. **D67**, 094020 (2003), hep-ph/0301094.

[480] R. Alkofer, W. Detmold, C. S. Fischer, and P. Maris, Phys. Rev. **D70**, 014014 (2004), hep-ph/0309077.

[481] C. S. Fischer, *Non-perturbative propagators, running coupling and dynamical mass generation in ghost - antighost symmetric gauges in QCD*, PhD thesis, Tübingen University, 2003, hep-ph/0304233.

[482] C. S. Fischer, D. Nickel, and J. Wambach, Phys. Rev. **D76**, 094009 (2007), 0705.4407.

[483] R. Alkofer, C. S. Fischer, F. J. Llanes-Estrada, and K. Schwenzer, Annals Phys. **324**, 106 (2009), 0804.3042.

[484] C. S. Fischer and J. A. Mueller, Phys.Rev. **D84**, 054013 (2011), 1106.2700.

[485] A. Aguilar, D. Binosi, and J. Papavassiliou, (2012), 1204.3868.

[486] P. O. Bowman, U. M. Heller, D. B. Leinweber, M. B. Parappilly, and A. G. Williams, Phys.Rev. **D70**, 034509 (2004), hep-lat/0402032.

[487] P. O. Bowman *et al.*, Phys. Rev. **D71**, 054507 (2005), hep-lat/0501019.

[488] M. B. Parappilly *et al.*, Phys. Rev. **D73**, 054504 (2006), hep-lat/0511007.

[489] P. Bowman, U. Heller, D. Leinweber, M. Parappilly, and A. Williams, Nucl.Phys.Proc.Suppl. **161**, 27 (2006).

[490] P. O. Bowman *et al.*, Phys. Rev. **D76**, 094505 (2007), hep-lat/0703022.

[491] F. Karsch and M. Kitazawa, Phys. Rev. **D80**, 056001 (2009), 0906.3941.

[492] P. J. Silva and O. Oliveira, PoS **LATTICE2010**, 287 (2010), 1011.0483.

[493] O. Oliveira and P. J. Silva, (2012), 1207.3029.

[494] J. Braun, Eur. Phys. J. **C64**, 459 (2009), 0810.1727.

[495] J. Braun and H. Gies, JHEP **05**, 060 (2010), 0912.4168.

[496] J. Braun, C. S. Fischer, and H. Gies, Phys.Rev. **D84**, 034045 (2011), 1012.4279.

[497] H. Gies and C. Wetterich, Phys.Rev. **D65**, 065001 (2002), hep-th/0107221.

[498] H. Gies and C. Wetterich, Phys.Rev. **D69**, 025001 (2004), hep-th/0209183.

[499] H. Gies and J. Jaeckel, Eur.Phys.J. **C46**, 433 (2006), hep-ph/0507171.

[500] S. Floerchinger, (2009), 0909.0416.

[501] S. Floerchinger and C. Wetterich, Phys.Lett. **B680**, 371 (2009), 0905.0915.

[502] R. Stratonovich, Dokl.Akad.Nauk Ser.Fiz. **115**, 1097 (1957).

[503] J. Hubbard, Phys.Rev.Lett. **3**, 77 (1959).

[504] J. C. R. Bloch, *Numerical investigation of fermion mass generation in QED*, PhD thesis, Durham University, 1995, hep-ph/0208074.

[505] C. W. Clenshaw, Her Majesty's Stationery Office, London Report No. 5, 1962 (unpublished).